Suitability of Dynamic Wake Models for AEP Estimation: A Wind Farm-Scale Validation Study

European Wind Energy Master Thesis

Mathieu Van der Straeten

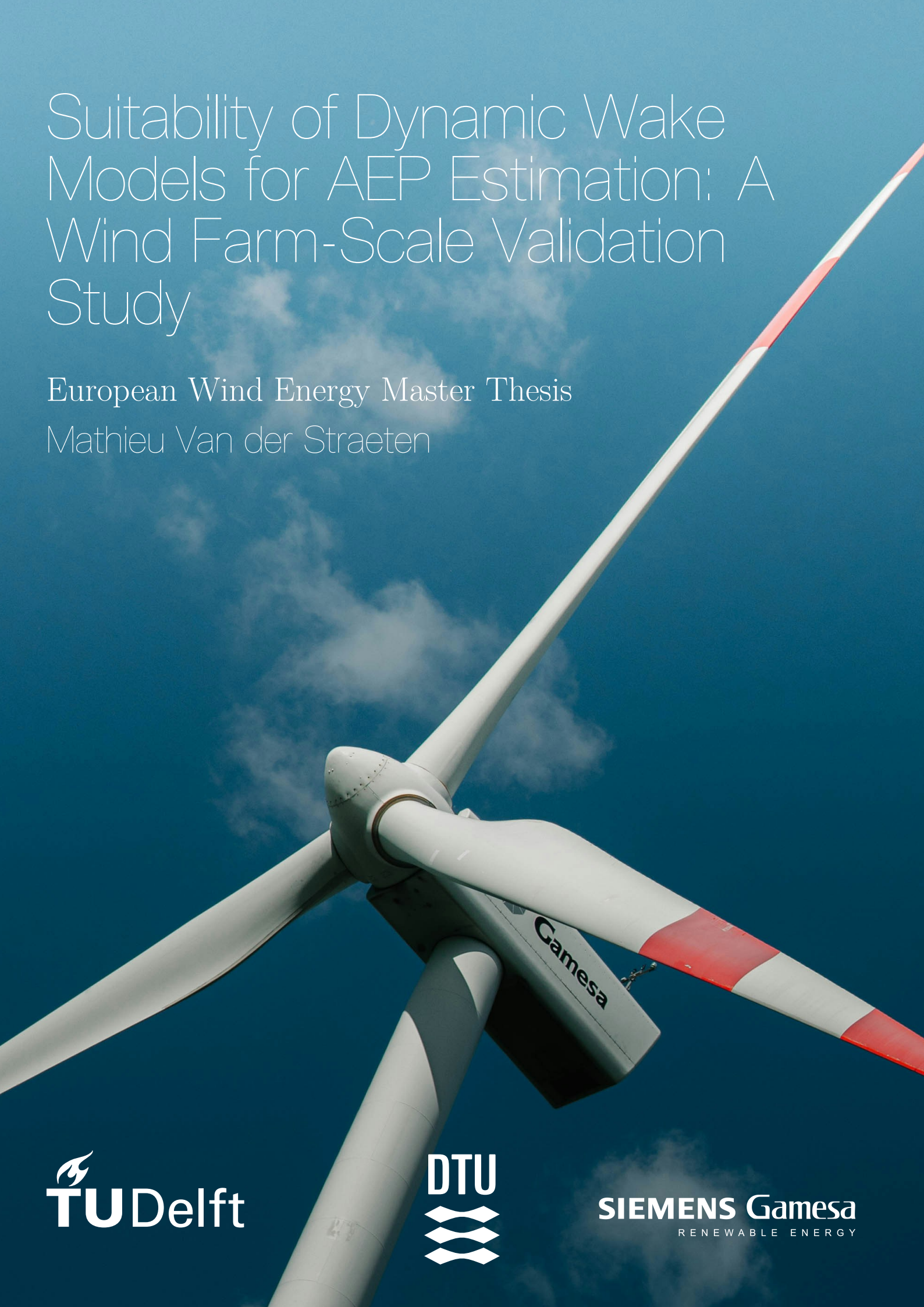

TU Delft

DTU

SIEMENS Gamesa
RENEWABLE ENERGY

Suitability of dynamic wake models for AEP estimation: A wind farm-scale validation study

Author:
Mathieu Van der Straeten
DTU Wind-M-0760
July 2024

Author:
Mathieu Van der Straeten

Title:
Suitability of dynamic wake models for AEP estimation: A wind farm-scale validation study

DTU Wind-M-0760
July 2024

ECTS: 45

Education: Master of Science

Supervisors:
Alexander Raul Meyer Forsting
DTU Wind & Energy Systems

Delphine De Tavernier
TUDelft

Remarks:
This report is submitted as partial fulfillment of the requirements for graduation in the above education at the Technical University of Denmark.

DTU Wind & Energy Systems is a department of the Technical University of Denmark with a unique integration of research, education, innovation and public/private sector consulting in the field of wind energy. Our activities develop new opportunities and technology for the global and Danish exploitation of wind energy. Research focuses on key technical-scientific fields, which are central for the development, innovation and use of wind energy and provides the basis for advanced education at the education.

Technical University of Denmark
Department of Wind and Energy Systems
Frederiksborgvej 399
4000 Roskilde
Denmark
www.vindenergi.dtu.dk

Suitability of Dynamic Wake Models for AEP Estimation: A Wind Farm-Scale Validation Study

by

Mathieu Van der Straeten

to obtain the degrees of

Master of Science
in Aerospace Engineering
at Delft University of Technology

Master of Science
in Wind Energy
at Technical University of Denmark

to be defended publicly on July 29, 2024 at 13:00

Thesis committee:

Chair:	Prof. Dr. S.J. Watson	TU Delft
Supervisors:	Dr. D.A.M. De Tavernier	TU Delft
	Dr. A.R. Meyer Forsting	DTU
	Dr. L. Beaudet	SGRE
Censor:	Dr. L. Landberg	DNV
Place:	Faculty of Aerospace Engineering, Delft	
Project Duration:	November 1, 2023 - July 29, 2024	
Student number:	5008832	TU Delft
	s223215	DTU

Cover photo by Aron Yigin
`https://unsplash.com/photos/white-and-red-wind-turbine-under-blue-sky-during-daytime-9p8Fl4YJtcI`

An electronic version of this thesis is available at
`http://repository.tudelft.nl/` and `https://findit.dtu.dk`

Summary

Wake modelling is crucial in the wind energy industry for optimising wind farm performance and efficiency. Accurately predicting the complex interactions between wind turbines and their wake effects is essential to maximise energy production and minimise losses. More so, effective wake modelling approaches enhance energy yield, support the assessment of new turbine designs, inform wind farm layouts, and refine control strategies, thereby driving the growth and sustainability of the wind energy sector. However, there is currently a lack of consensus in the literature regarding the accuracy of engineering wake models. Various studies employ different validation methods, influencing the perceived accuracy of these models. Additionally, many proposed improvements lack quantitative evaluations, limiting their practical applicability and broader relevance.

This thesis investigates the potential of utilising a dynamic wake model for Annual Energy Production (AEP) estimations in large scale wind farms. Traditional engineering wake models often rely on steady-state assumptions, which can not adequately capture the complex and transient nature of wake interactions in varying wind conditions. In this work, a dynamic wake model, FLORIDyn, is investigated to address these limitations by incorporating time-dependent wake propagation and interaction effects, potentially offering more accurate AEP predictions.

The research commences with an in-depth review of existing wake models and their limitations, highlighting the interest in dynamic modelling approaches. This is followed by a detailed discussion on the functioning of the FLORIDyn model, and the implemented model adjustments. Key achievements include transforming the FLORIDyn model to use C_P-C_T lookup tables and introducing a new implementation to identify influencing turbines, while maintaining the model capabilities to include heterogeneous wind effects.

The calibration findings, based on an inverse Bayesian approach using trained surrogate models, provided a calibrated set of model parameters. These parameters were validated through one-to-one studies comparing FLORIDyn predictions to real-world turbine measurements. The one-to-one validation highlighted that model uncertainty increases with downstream wake accumulation, and that FLORIDyn's assumptions about flow convection are biased towards higher wind speeds and non-physical damping of wind fluctuations, leading to inaccuracies in deep array locations.

Finally, a comparative validation study is conducted on the model evaluations and field data. The validation process includes an assessment of the assumptions related to the suggested methodology, followed by an analysis of the occurrence of dynamic wind events, and a series of comparative analyses between the performance of FLORIDyn and industry-applied steady-state models. These comparative analyses focus on essential metrics such as power output, wake loss predictions, and overall AEP estimations. Despite the comprehensive methodology and calibration approach employed, FLORIDyn evaluations on different levels of complexity did not improve AEP predictions when compared to steady-state models. This thesis identified the need for improved modelling assumptions in the current FLORIDyn model, particularly in the wake superposition and flow convection submodels. It underscores the current limitations of FLORIDyn in large wind farms, recommending further research to enhance dynamic wake modelling.

Overall, while FLORIDyn shows potential for use on small wind farms with large turbine spacings, its current implementation is not robust enough for general industry applications on large wind farms. This thesis concluded with recommendations for future research to address these limitations, suggesting that further refinement of dynamic wake models or the development of new models may lead to improved AEP estimations and more reliable wind farm performance assessments.

Acknowledgements

This thesis represents the work of nine months, during which I have delved into the exploration of wake modelling on wind farms. It has been a journey filled with challenges, learning opportunities, and moments of inspiration. Through these acknowledgements, I aim to provide insight into the journey of this research endeavor, and the most important people that guided me.

I am immensely grateful for the support and guidance provided by my daily supervisor, Laurent Beaudet, whose expertise and encouragement have been invaluable throughout this journey. His insights and feedback have significantly shaped the direction of this thesis and profoundly enriched its content.

Secondly, I extend my heartfelt thanks to my academic supervisors, Delphine De Tavernier and Alexander Forsting, for their continuous guidance throughout this research project. Their critical questions and feedback during the bi-weekly status meetings ensured that I remained on the right track. I also thank Marcus Becker for providing the FLORIDyn model for this research. Monthly meetings with him offered valuable insights into the calibration procedure and feedback on the methodology used within this thesis framework.

Thirdly, I would like to express my gratitude to Simon Watson and Lars Landberg for their interest in this work and for being part of the thesis committee. I look forward to discussing my findings with you.

I also want to thank my colleagues within SGRE for being open and welcoming. A special mention goes out to my fellow interns at the 'kids' table,' who ensured there was always some animation (and, in jest, animosity) on a daily basis. The lively discussions, shared learning experiences, and mutual support at our table made each day enjoyable and enriched my internship experience. Beyond the young core, I deeply appreciate Etienne Muller for his detailed explanations of internal modelling approaches and his assistance with code implementation. I am also grateful to the broader team for their collaboration and willingness to share their knowledge, contributing to the success of this project.

Further, I want to extend my gratitude to my friends, especially Andreas, Jonas, and Kato, who have been with me since day one, for always standing by me throughout my international journey over the past five years. Countless times, you have lifted me out of my lowest moments and brought a smile to my face. Additionally, heartfelt thanks to Hamude, Aditya, Te and Aria for the unforgettable moments we shared in Denmark.

Finally, I want to express my deepest gratitude to my parents, brothers, grandfather and girlfriend, whose unwavering love, guidance, and sacrifices have been the cornerstone of my journey. To my parents and brothers, your endless support has enabled me to pursue my goals with determination and resilience. You have instilled in me the values of perseverance, integrity, and compassion, shaping me into the person I am today. To my grandfather, I am deeply grateful for the wonderful moments we shared. I know you would be the proudest of all, and there is so much I still wish I could tell you about my journey the last three years. To my girlfriend, thank you for your patience and unrelenting support. Through our ups and downs, I am proud of how we have emerged stronger together, and I look forward to our future. Finally, to all of you, I am profoundly grateful for your continuous encouragement, belief in my abilities, and willingness to go above and beyond to ensure my success.

Conducting this research has been rewarding and enlightening, allowing me to delve into wake modelling, expand my knowledge, and develop critical research skills. Along this journey, I have been fortunate to partake in unforgettable experiences, such as climbing a wind turbine, visiting an offshore wind farm, and witnessing the craftsmanship at the blade production plant in Le Havre. Through moments of challenge both within and outside of this project, I have undergone profound personal and professional growth, emerging as a more resilient and skilled individual.

Rouen,
July 15, 2024

Mathieu Van der Straeten

Contents

Nomenclature

List of Abbreviations

ABL	Atmospheric Boundary Layer
AD(M)	Actuator Disc (Method)
AEP	Annual Energy Production
AIES	Affine Invariant Ensemble Sampler
AL(M)	Actuator Line (Method)
AS(M)	Actuator Sector (Method)
BEM	Blade Element Momentum
CFD	Computational Fluid Dynamics
DNV	Det Norske Veritas
DTU	Technical University of Denmark
DWM	Dynamic Wake Meandering
EWEM	European Wind Energy Master
Fastlog	High Frequency SCADA Data
FE	Farm Error
FLORIDyn	Flow Redirection and Induction Dynamics
FLORIS	Flow Redirection and Induction in Steady-State
fw	Far-Wake
GWEC	Global Wind Energy Council
IEA	International Energy Agency
IEC	International Electrotechnical Commission
IRENA	International Renewable Energy Agency
LARS	Least-Angle Regression
LCOE	Levelised Cost of Energy
LES	Large-Eddy Simulation
LHS	Latin Hypercube Sampling
LLM	Lifting-Line Model
LOO	Leave-One-Out
LUT	Look-Up Table
MAE	Mean Absolute Error
MCMC	Markov Chain Monte Carlo
NNI	Nearest Neighbor Interpolation
NSE	Navier-Stokes Equations
nw	Near-Wake
OP	Observation Point
pc	Potential-Core
PCE	Polynomial Chaos Expansion
PDF	Probability Density Function
PSD	Power Spectral Density
RANS	Reynolds Averagd Navier-Stokes
RMSE	Root Mean Square Error
SCADA	Supervisory Control And Data Acquisition
SGRE	Siemens Gamesa Renewable Energy
TI	Turbulence Intensity
TUD	Delft University of Technology
TWF	Temporary Wind Farm
UQ	Uncertainty Quantification
wd	Wind Direction
ws	Wind Speed

Mathematical Operators

$\langle \dots \rangle$	Ensemble Averaging
$\overline{\dots}$	Time Averaging
Π	Product
Σ	Summation

List of Greek Symbols

α^*, β^*	Weight Constants in the Potential Core
α_s	Shear Coefficient
α_s	Wind Shear Coefficient
β	Wake Expansion Factor
Δ	Difference
δ	Wake Centre Line Deflection
ϵ	Eddy Viscosity
ϵ_{LOO}	Leave-One-Out Error
η	Rotor efficiency
$\frac{\Delta u}{u_0}$	Non-Dimensional Wake Deficit
Γ	Circulation
γ	Yaw Misalignment Angle
λ	Tip-speed Ratio
μ	Sample Mean
ν	Kinematic Viscosity
Φ	Self-Similar Flow Property
ϕ	Wind Direction
ϕ_k	Orthonormal set of polynomials
ϕ_x, ϕ_y, ϕ_z	Random Phase Components
$\Phi_{ij}(\vec{k})$	Spectral Velocity Tensor
$\pi()$	Probability Function
Ψ	Inflow Angle
Ψ_k	Multivariate Polynomials
ρ	Air Density
σ	Standard Deviation
σ_y, σ_z	Wake Widths
θ	Wake Deflection Angle
θ_0	Initial Skew Angle
θ_M	Vector of Model Constants

List of Latin Symbols

$\mathbf{CP_w}$	Vector of Weight Factors per Discretised Rotor Point
$\vec{k}$	3D Wavenumber Vector
A	Weibull Scale Parameter
a	Axial Induction Factor
A_r	Rotor Swept Area
c	Chord length
c_l	Lift Coefficient
C_P	Power Coefficient
C_T	Thrust Coefficient
D	Rotor Diameter
d	Wake Convection Speed Scaling Factor
D_r	Rotor Diameter
D_w	Wake Diameter
$E(k)$	Turbulent Energy Spectrum
f	External Body Forces
f_c	Cut-Off Frequency
I	Turbulence Intensity
I_∞	Free-Stream Turbulence Intensity
k	Weibull Shape Parameter
k^*	Wake Growth Rate
k_y, k_z	Wake Growth Rates
$k_{f,a}, \ldots, k_{f,d}$	Parameters for Foreign Wake Turbulence Effects Determination
L	Integral Length Scale
L_x, L_y, L_z	Mann Box Dimensions
N_T	Number of Turbines
N_t	Number of time steps
N_x, N_y, N_z	Mann Box Spatial Discretisation Parameters
P	Power
p	Pressure
p_P	Correction Factor to C_P in Yawed Turbine Conditions
Q	Torque

R	Rotor Diameter
r	Wake Velocity Reduction Factor
R_{ij}	3D Covariance Tensor
R_{ij}	Energy Ratio for Turbine i in Wind Speed Bin j
r_{pc}	Potential Core Radius
$S_i^\top$	Sobol' Index
T	Thrust
t	Time-step
U	Free-Stream Wind Speed
u	Three-dimensional fluid velocity
u_0	Free-Stream Wind Speed
u_r	Wind Speed at the Rotor
u_w	Wake Wind Speed
u_{eff}	Effective Wind Speed at the Rotor
u_{OP}	OP Convection Speed
w_k	Multivariate Polynomial Coefficients
z_h	Hub Height
$\mathrm{TI}_{\mathrm{exp}}$	Wake-Added TI Width Parameter

List of Other Symbols

$\mathcal{K}$	FLORIDyn Coordinate System
$\mathcal{L}$	Likelihood Function
$\mathcal{M}$	Model Evaluation
$\mathcal{N}$	Normal Distribution
$\mathcal{O}$	Order Of Magnitude

List of Figures

List of Tables

1 Introduction

The aim of this chapter is to provide a general overview of this Master's thesis report. In Section 1.1, the larger framework that leads to the motivation and significance of this work is described. This is followed by Section 1.2, in which the general outline of this report is presented.

1.1. Motivation and Background

In the pursuit of a sustainable future and the imperative shift towards electrification, the global energy landscape is undergoing a profound transformation. The pressing need to reduce carbon emissions and mitigate climate change has energised the deployment of renewable energy sources, with wind power playing a crucial role in this global electrification process.

Over the past few decades, wind turbines have not only emerged as iconic symbols of sustainable energy production, but have also emerged as the cheapest source of energy generation on land [1]. Driven by climate change, fossil fuel depletion and energy prices, wind energy has become one of the fastest growing renewable energy sources [2]. Due to the maturity of wind turbine technology, it is widely regarded as a protagonist to achieve the Paris Agreement of limiting global temperature rise to 1.5 degrees and net-zero global carbon emissions by 2050 [3]. To illustrate this, Figure 1.1 shows the projected growth of globally installed wind installations. According to agencies IEA (International Energy Agency) and IRENA (International Renewable Energy Agency), wind power alone is projected to generate up to a third of global energy by 2050 [4, 5].

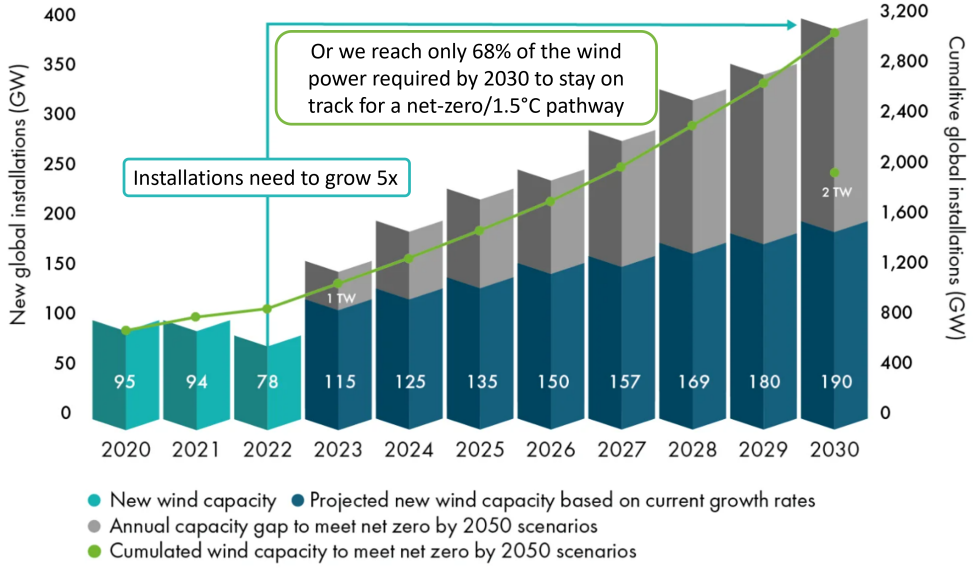

Figure 1.1: Projected new wind capacity from 2023-2030 based on GWECs (Global Wind Energy Council) Q1 2023 Global Outlook [6]. The annual capacity gap indicates that more efforts are required to meet the Paris Agreement targets by 2050.

Despite the rapid growth of total installed wind energy capacity worldwide, Veers et al. [7] identify several monumental obstacles to be overcome in order to reach this forecasted growth rate. Notably, electrical grid design, manufacturing and logistics of offshore turbines, and continuously decreasing LCOE (levelised cost of energy) have shown to be challenging aspects nowadays.

One of the major challenges in wind energy is the fundamental understanding of wind farm flow physics [7, 8]. Most significantly, wake interaction between wind turbines in a wind farm configuration are ill-understood. Wake regions downstream operational turbines are characterised by lower wind speeds and increased turbulence intensities. Turbines operating in wake regions will thus produce less power, while enduring higher loads [9, 10]. In recent years, research has seen increased interest in developing strategies to increase wind farm power output through various wind farm flow control methods, such as wake steering and induction control, among other techniques [11, 12]. Both of these flow control strategies accept power losses of upstream turbines in favour of decreasing the effects of their wake regions, leading to potential benefits at downstream turbines and ultimately increasing the global power output of the wind farm. A case study by Gebraad et al. [13] suggests that AEP (annual energy production) could be increased by as much as 5 to 10% by implementing wake steering and find warm lay-out optimisation techniques.

As discussed by Deng et al. [14], current models reported for optimising wind farm production by wake regulation are mainly static. Typically, these static models assume that the involved time scales are sufficiently large to be neglected. By ignoring the time lag between operational control adjustments or wind changes and responses of downwind turbines, static wake models tend to misjudge the wind farm energy production. Comparison with experimental data suggests that this apparent delay in wake propagation could be one of the primary reasons for inaccuracies in AEP estimations [15]. Therefore, there is a genuine need to better understand and more accurately model the effects of wake propagation delay and dynamically evolving wakes, considering the time-varying operating conditions. Although this has been extensively studied in higher fidelity approaches, it is yet to be considered in faster and computationally less expensive models at wind farm production levels. This necessitates urgent research on dynamic wake modelling, balancing computational complexity [14]. Inspired by this need, this work will investigate the potential use of such a dynamic engineering wake model on AEP computation accuracy.

1.2. Overview of the Report Structure

This thesis report is divided in six chapters. This section aims to give an overview of the discussed topics in each chapter and to provide a high-level overview about the project's workflow.

In Chapter 2, relevant literature work is reviewed. This builds a solid framework for this thesis while helping to establish the research gaps and corresponding research questions to which this work aims to find answers to.

The research methodology to approach the established research questions is discussed in Chapter 3. More specifically, the details of the selected dynamic wake model, numerical set-up, inflow generation and model assessment procedure are detailed.

Before performing the outlined model assessment methodology, Chapter 4 specifies the model calibration and validation framework. As the dynamic wake model is dependent on empirical model constants, a calibration framework is set up using field measurement data to find a set of tuned model parameters. Hence, the calibration procedure, results, and model uncertainty considerations are discussed. This is further accompanied by the identification of the model limitations by means of one-to-one validation simulations.

Based on the set of calibrated model parameters, Chapter 5 will compare the performance of the dynamic wake model against both field measurements and steady-state model results. The chapter begins with an analysis of the assumptions and limitations of the AEP validation study, followed by a data analysis on the significance of dynamic wind change events. This is complemented by the verification of the synthetic wind generation framework presented earlier. Lastly, the chapter presents FLORIDyn evaluations across three levels of input wind complexity in a comprehensive validation study.

Finally, Chapter 6 concludes this thesis by reflecting on the steps taken throughout the report, emphasising the most significant outcomes, and providing answers to the established research questions. It also offers recommendations for future work to build upon this thesis project.

2

Literature Review

This chapter provides an overview of the current state-of-the-art knowledge in the literature regarding wake modelling. It starts with a general description of wind turbine wakes in Section 2.1, followed by a presentation of the governing equations in Section 2.2. Section 2.3 introduces the self-similarity concept, as a basis for the far-wake representation in low-fidelity models. Next, Section 2.4 elaborates on the different rotor representations. This is followed by a discussion of high-, mid- and low-fidelity wake models in Section 2.5, Section 2.6 and Section 2.7 respectively. Consequently, Section 2.8 details the currently implemented wind farm control strategies. Next, Section 2.9 provides an overview of some existing wake modelling frameworks. Finally, the literature review chapter is concluded by Section 2.10, in which the research gap is defined, leading to the formulation of the research objective and research questions.

2.1. Wind Turbine Wakes

As free-stream air traverses a wind turbine, it undergoes alterations in its flow characteristics as energy is extracted by the turbine. The primary feature of a wind turbine wake is evident: a cylindrical zone with diminished streamwise velocity downstream of the wind turbine, encompassing an area larger than the rotor itself. The wake is further characterised by an increase in turbulence intensity resulting from tip vortices, turbulent boundary layers departing from the blades, and mechanical turbulence originating from the blade and tower [16]. When a downstream turbine operates within the wake of an upstream turbine, not only is its power production diminished compared to operating in free-stream air, it will also experience reduced fatigue life due to the increased turbulence [16]. An overview of instantaneous and time averaged wake profiles is shown by Figure 2.1.

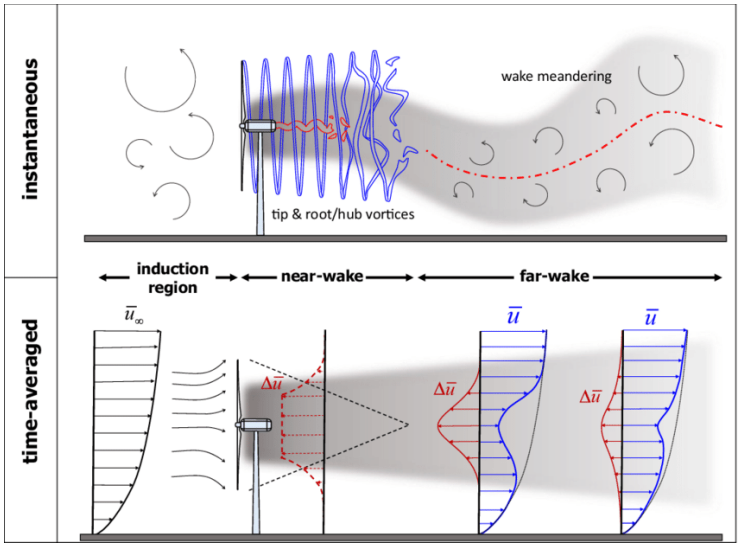

Figure 2.1: Illustrative diagram presenting the flow regions arising from the interaction between a wind turbine and an incoming turbulent boundary layer. The figure illustrates the most distinctive instantaneous features (top) and time-averaged flow characteristics (bottom). Image adapted from Porté-Agel et al. [17]

As indicated by Figure 2.1, the wind turbine wake is typically categorised into two regions: the near-wake and the far-wake. The transition, governed by tip vortex breakdown, occurs between two and five rotor diameters and is influenced by flow characteristics such as turbulence intensity, tip speed ratio and wind speed [16, 17].

The near-wake constitutes the area immediately behind the rotor, where distinct rotor properties can be identified. Consequently, the near-wake is distinguished by a highly intricate, three-dimensional (3D), and heterogeneous flow distribution [17]. The difference in velocity between the air inside and outside the wake gives rise to a shear layer, fostering the formation of turbulent eddies. Depicted in the time-averaged schematic of Figure 2.1, this shear layer expands downstream. As the upper and lower shear layers converge, the far-wake region is established, marked by an approximately self-similar Gaussian velocity-deficit distribution. At this stage, the distinctive properties of the rotor are no longer discernible, and the wake is transported by the ambient flow. Rather than relying on detailed parameters, the mean flow distribution in this region can likely be predicted using global wind turbine parameters, such as the thrust and power coefficients, along with incoming flow conditions [17].

2.1.1. Wake Dynamics

Wind turbine wakes are inherently complex, arising from interactions between physical mechanisms that span a wide range of spatial and temporal scales. Consequently, their structure can vary significantly based on the temporal evolution of inflow characteristics and rotor conditions [18]. This section aims at providing more insight into the dynamic nature related to the flow physics in wind turbine wakes, and how it forms the basis for different modelling approaches.

The initial formation and development of a wind turbine wake is highly sensitive to the characteristics of the ambient flow, and results in a complex velocity field. The aerodynamic forces exerted by the blades on the flow create vortex sheets trailing from the blades. At the hub and tip of each rotating blade, these vortex sheets roll up into vortices, forming a series of vortex filaments as they advect downstream [18, 19]. These highly coherent structures persist until the end of the near-wake region. At further downstream wake locations, the vortex breakdown mechanism indicates the transition between the near- and far-wake regions. Following the energy cascade, continuous vortex breakdown into smaller scales governs the wake recovery process and turbulent expansion [18].

The wake region can vary significantly based on inflow features, wind turbine control strategies, and land topography. Moreover, ambient wind turbulence triggers vortical instabilities, affecting the vortex breakdown mechanism. Additional factors, such as interactions with the hub and rotor, as well as wind phenomena like shear and veer and atmospheric stability, also contribute to wake destabilisation [20]. Additionally, wake advection can occur laterally or vertically, causing the wake to oscillate. This oscillation is referred to as wake meandering, and affects both loads and power production on downstream turbines [18, 21]. Larsen et al. concluded that this meandering is mainly attributed to large atmospheric turbulent scaled in the atmospheric boundary layer [21, 22]. The wake meandering phenomenon is illustrated by Figure 2.2.

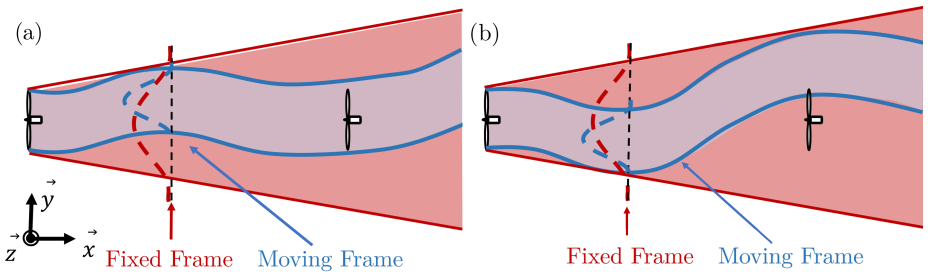

Figure 2.2: Diagram illustrating the dynamic nature of instantaneous wake profiles. The time-averaged wake outline (red) and the instantaneous wake outline (blue) are shown at two different time steps: (a) when the downstream turbine is fully waked conditions and (b) when the downstream turbine is partial waked conditions. The velocity profiles are represented by dashed lines in both the fixed frame (red) and the moving frame (blue). Image adapted from Jézéquel et al. [19]

As highlighted by Figure 2.2, the unsteady wake displacements result in a broader time-averaged wake width and a lower time-averaged maximum velocity deficit. Thus, the evolution of a time-averaged wake can be seen as a combination of two factors: the wake expansion and dissipation due to turbulent diffusion, and the wake meandering caused by large-scale atmospheric boundary layer ABL forcing [19]. As a result, time-averaged wake models often overlook these dynamic features, treating the wake as a static, expanding entity, governed by statistics. This simplification neglects the significant impact of large-scale turbulent structures on the wake's spatial and temporal evolution, and neglects the distinction between meandering and turbulent mixing [19].

In order to model wake dynamics, a major challenge is to determine the range of spatial and temporal scales to consider, since solving the full range from the breakdown of coherent vortical structures to large-scale wake advection is not computationally feasible on large wind farm applications [18, 23]. Nonetheless, the scale separation assumption essentially decouples the large-scale motions imposed on the wake profile from the recovery process. This consideration provides a theoretical framework that simplifies the representation of wake structures, and forms the basis for simplified flow advection approaches that will be discussed in throughout this chapter.

In conclusion, the flow physics of dynamic wakes, driven by the interaction between large-scale and small-scale turbulent eddies, present a complex yet essential aspect of wind turbine wake modelling. This understanding is crucial for developing wake models that can effectively capture the transient nature of wakes and improve the accuracy of predictions in wind farm simulations.

2.2. Governing Equations

The physics of wind turbine wakes can be described by the incompressible Navier-Stokes equations (NSE) as given by Equation 2.1, and form the foundation to describe fluid motion. The NSE are based on the continuum assumption and the conservation of mass and momentum. The incompressibility assumption may be verified due to the operational wind turbine conditions, with atmospheric flow velocities range between 4 m/s and 25 m/s. Except for the blade tip region, flow velocities typically do not exceed 100 m/s, corresponding to the Mach number threshold of 0.3 for incompressible flows and Newtonian fluids [16].

$$\frac{\partial u_i}{\partial x_i} = 0$$

$$\underbrace{\frac{\partial u_i}{\partial t}}_{\text{Acceleration term}} + \underbrace{\frac{\partial u_i u_j}{\partial x_i}}_{\text{Advection term}} = - \underbrace{\frac{1}{\rho}\frac{\partial p}{\partial x_i}}_{\text{Pressure term}} + \nu \underbrace{\frac{\partial^2 u_i}{\partial x_j \partial x_j}}_{\text{Viscous term}} + \underbrace{f_i}_{\text{Body forces}} \tag{2.1}$$

Where u is the three-dimensional velocity, x the velocity vector, p the pressure term, f the external body forces vector, ρ the fluid density and ν the kinematic viscosity. Additionally, t is the time, and i, j represent the directional components.

The NSE pose a challenge in fluid dynamics, lacking analytical solutions, primarily due to the intricate non-linear advection term $\frac{\partial u_i u_j}{\partial x_i}$. This term's influence becomes especially pronounced in complex turbulent flows, dominating the underlying flow physics. The unresolved Navier-Stokes existence and smoothness problem, a Millennium Prize challenge, encapsulates the mathematical intricacies associated with understanding and predicting fluid dynamics at a fundamental level. The non-linear advection term stands as a crucial aspect in this challenge, highlighting its crucial role in shaping the unsolved questions that form the forefront of scientific research. Consequently, the absence of analytical solutions emphasises the need for simplifications in both fluid and blade modelling to understand and predict complex wind turbine flow physics [24]. These simplifications are inherently linked with modelling assumptions, and the resulting models may still be numerically and analytically complex. Therefore, the subsequent sections will primarily encompass these modelling approaches.

2.3. Self-Similarity

As the primary goal of this thesis project is to investigate an engineering wake model, several analytical models will be considered. These models mainly take advantage of the far-wake properties, emphasising the importance of grasping the concept of self-similarity.

A flow variable, denoted as Φ, exhibits self-similarity when its shape remains consistent across various scales [23]. Consider a turbine operating with a constant thrust coefficient C_T and exposed to turbulent flow with a uniform ambient turbulence intensity at hub height, denoted as I_∞. Certain existing analytical wake models express the velocity deficit as a function of the downstream distance from the turbine, denoted as $\hat{x}$, and the radial distance from the turbine's horizontal axis, denoted as $\hat{r}$, using the formula described by Equation 2.2.

$$\Phi(\hat{x},\hat{r}) = \frac{u_0 - u_w(\hat{x},\hat{r})}{u_0} = \frac{\Delta u}{u_0} \tag{2.2}$$

Where u_0 represents the inflow velocity, and u_w is the wake velocity at a specific distance $(\hat{x},\hat{r})$ from the turbine. By introducing the scaled variable: $\xi = \frac{\hat{r}}{\sigma(\hat{x})}$, where σ denotes the characteristic wake width as a function of the downstream distance from the turbine, the velocity deficit $\Phi(\hat{x},\hat{r})$ is considered self-similar if it can be expressed as the product of two independent functions (Equation 2.3), $\mathscr{F}_1$ and $\mathscr{F}_2$, with a dependence on $\hat{x}$ and ξ. Therefore, a self-similar wake profile will generally conserve its shape at any downstream location.

$$\Phi(\hat{x},\xi) = \mathscr{F}_1(\hat{x}) \times \mathscr{F}_2(\xi) \tag{2.3}$$

2.4. Rotor Representations

The aim of this section is to provide an overview of different methods to represent a wind turbine rotor for various numerical modelling approaches. It starts with the most intuitive blade representation when trying to numerically solve the discretised NSE, and ends with a highly simplified rotor representation suitable for wind farm models.

Direct blade modelling involves resolving the detailed geometry of individual blades in the simulation. This approach provides a high-fidelity representation of the aerodynamic effects but comes with increased computational costs. As the blade boundary layers are resolved in direct blade modelling, it is suitable for studies requiring precise details of blade interactions with the flow, but is computationally expensive when considering an entire wind turbine system [25]. Adding to this, the set-up requires special considerations, as the computational mesh generation should be treated with great expertise.

To minimise computational expenses and ease numerical mesh generation, an alternative approach to directly computing blade boundary layers involves representing (modelling) the rotor as body forces, rather than as physical domain elements. These body forces are explicitly incorporated into the weak form of the momentum equation, illustrated by Equation 2.4. The utilisation of the weak form is essential in this context, as the force induces a pressure discontinuity, as discussed by Sanderse et al. [26]. A visual representation of three considered rotor representations as body forces is shown by Figure 2.3.

$$\int_\Omega \frac{\partial \mathbf{u}}{\partial t}\,\mathrm{d}\Omega + \int_{\partial\Omega} \mathbf{u}\,\mathbf{u}\cdot\mathbf{n}\,\mathrm{d}S = -\int_{\partial\Omega} \frac{1}{\rho} p\,\mathbf{n}\,\mathrm{d}S + \int_{d\Omega} \nu\nabla\mathbf{u}\cdot\mathbf{n}\,\mathrm{d}S + \int_{A\cap\Omega} \mathbf{f}\,\mathrm{d}A \tag{2.4}$$

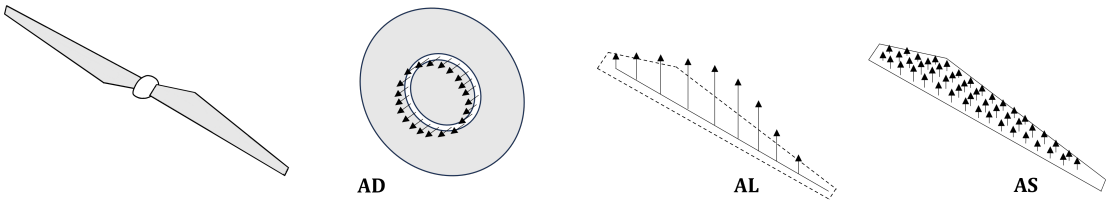

Figure 2.3: Illustrative image showing rotor representation as body forces for the actuator disc (AD), actuator line (AL) and actuator surface (AS) concepts [26].

Actuator Disc Model (ADM)

In an attempt to simplify wind turbine rotor and blade representation, the Actuator Disc Model (ADM)

portrays the rotor as a permeable disc, exerting forces on the surrounding flow [27]. In a blade element approach, the forces are distributed over annual rings, attempting to replicate force distribution over a real blade. The aerodynamic lift and drag forces are obtained from the tabulated aerofoil data, combined with local flow conditions, and result in a force vector at every discretised location along the actuator disc. Mathematical details about this method are provided by Sørensen and Myken [28], but are considered to be outside the scope of this thesis work. Wu and Porté-Agel [29] showed that the development of the far-wake and power production are well predicted, but the ADM cannot capture tip and root vortices in the wake. Hence, ADM may lack precision in capturing near-rotor vortical structures and different methods should be considered to study this flow region. Finally, the ADM can have limitations in terms of load predictions. At high turbulence levels or in partial wake operation, issues with regard to resolving dynamic effects might arise, leading to the need for a more accurate rotor representation.

Actuator Line Model (ALM)
The Actuator Line Model (ALM) represents wind turbine blades as discrete actuator points along their span. Whereas ADM represents the rotor as continuously present, ALM accounts for blade rotation, making it more suitable to model unsteady effects. Another benefit over the ADM is the capability of representing lifting surfaces, without resolving the flow field around it, balancing simplicity and accuracy [30]. Similar to the blade element representation in ADM, lift and drag forces are obtained from tabulated aerofoil polars.

ALM is significantly less complex than direct blade modelling, while its improved geometrical representation of the turbine w.r.t. ADM results in a higher level of fidelity in the representation of near-wake physics, including root and tip vortices. Additionally, ALM can capture helical and asymmetric structures across all wake areas. These phenomena are responsible for an asymmetric roll-up of Kelvin-Helmholtz-like instabilities in the wakes outer shear layer [31].

Actuator Surface Model (AS)
As an extension of the AL method, Shen et al. developed the actuator sector method [32]. The Actuator Sector method enhances fidelity by representing the turbine at a more detailed level, portraying it as a planar surface determined by both blade length and chord [32]. This sector is then overlaid onto the mesh, covering an area equivalent to the blade element during a single time-step. Consequently, the force distribution closely mirrors that attained in a simulation with resolved blades, leading to improved handling of near-wake vortices. However, this method comes with a higher computational cost compared to the ALM [33]. Moreover, the process of force projection demands additional scrutiny, introducing an added layer of complexity and requiring additional information about pressure and skin-friction distributions along the aerofoil [26]. Therefore, the actuator sector method is generally not used, since the benefits in terms of grid requirements compared to fully-resolved computations is only marginal.

ADM - $\mathbf{C_P}$-$\mathbf{C_T}$ Lookup Tables
Finally, the simplest rotor representations are C_P-C_T (Power Coefficient and Thrust Coefficient, defined by Equation 2.5) lookup tables (LUT). In essence, a rotor is represented by the combination of a reference velocity, that yields in a specific C_P-C_T combinations, resulting from nominal turbine operational conditions. Hence, interpolation is required to obtain C_P-C_T properties from the tabulated data for any given reference wind speed in the turbine operational range.

Additionally, models considering these lookup tables also require the rotor size and rotor centre as rotor definition inputs. Essentially, the C_P-C_T values in these tables are derived from operational curves of a wind turbine. These operational curves result from turbine operation strategies and are typically obtained through higher fidelity simulations or experimental data. Similar to AS, AL, and AD methods, the C_P-C_T lookup table representation effectively dynamically adjusts forces applied by the blades based on prevailing wind conditions.

The simplicity of this method does not require large numerical domains, which makes it particularly well suited for fast, low-fidelity engineering models for wind farm applications. Essentially all turbine flow physics are assumed to be modelled using this highly simplified rotor representation. Although the C_P-C_T lookup table approach imposes strong assumptions, it is still possible to extract a relatively realistic global forcing resulting from the blade force distribution. This is obtained by radial force and velocity scaling,

and is regarded as the function that connects the global C_P-C_T properties to the local blade forces at blade elements on the rotor plane.

$$P = 0.5\eta\rho C_P V^3 \pi R^2 \qquad T = 0.5\rho C_T V^2 \pi R^2 \tag{2.5}$$

The synergy of these elements provides a holistic and accurate representation of wind turbine rotor planes in simulations. The choice of rotor representation is a key element in setting up simulations, considering the trade-offs between accuracy, computational cost, and model complexity. Higher accuracy simulations are often coupled with high computational costs and the requirement for more intricate aerofoil data. The dynamic implementation of the ASM and ALM makes them well suited for implementation into Large-Eddy Simulation (LES) cases. The ADM is an attractive solution for Reynolds Averaged Navier-Stokes (RANS) approaches, due to its static nature. Nonetheless, studies of entire wind parks are often carried out given the simplest and least computationally expensive C_P-C_T lookup table representation, given their optimisation and iterative nature. On the other hand, higher fidelity approaches usually consider ALM representations, but limiting the number of considered turbines.

2.5. High-Fidelity Wake Models

High-fidelity wake solvers play a pivotal role in the comprehensive understanding of complex fluid dynamics, particularly in the context of wind turbine wakes. The Direct Numerical Simulation (DNS) approach represents a gold standard for general studies in capturing wake intricacies by numerically solving the discretised Navier-Stokes equations with a resolution sufficient to eliminate modelling errors. This meticulous approach, however, comes at a significant computational cost, rendering it primarily suitable for academic studies with abundant computational resources [34].

Recognising the impracticality of systematically applying DNS to wind turbine applications, especially characterised by high Reynolds numbers $\mathcal{O}(10^6)$, alternative frameworks have been devised. These frameworks involve the integration of physical models aimed at circumventing the need to resolve all spatial scales of turbulence, thereby mitigating the computational burden. In the pursuit of high-fidelity wake solutions, these computational fluid dynamics (CFD) approaches navigate the balance between computational efficiency and accuracy, offering valuable insights into the wake dynamics of wind turbines. Recent advancements in spatial and temporal discretisation techniques contribute to the numerical implementation of Navier-Stokes equations, addressing the challenges posed by the diverse scales influencing wind turbine wakes. As a result, these high-fidelity wake solvers stand at the forefront of research projects, providing nuanced insights into the complex turbulent flow structures around wind turbines [34]. Therefore, this section will briefly present the Large-Eddy Simulation (LES) and Reynolds Averaged Navier-Stokes approached in Section 2.5.1 and Section 2.5.2.

2.5.1. LES

Large-Eddy Simulation (LES) stands out as the most advanced and accurate method feasible for practical implementation in state-of-the-art models. While Direct Numerical Simulations (DNS) might offer even higher accuracy, the computational expenses associated with DNS render it impractical for numerous flow cases, especially on large domains and high Reynolds numbers.

In LES, the computation is centred on numerically resolving large-scale motions (large eddies) while only modelling small-scale motions (sub-grid scale). It primarily revolves around the concept of scale separation, striving for a cut-off frequency/wavelength within the inertial subrange. This focus on small-scale motions is driven by their universal characteristics, which remain independent of flow geometry[23]. This results in a significant reduction in computational costs compared to DNS, as the smallest scales are modelled rather than resolved, while still resolving for the majority of a flow's turbulent kinetic energy. These large eddies contribute significantly to momentum transfer and turbulent mixing, rendering less dependence on turbulence models for LES.

$$\underbrace{\frac{\partial \tilde{u}_j}{\partial t}}_{\text{Acceleration term}} + \underbrace{\frac{\partial \tilde{u}_i \tilde{u}_j}{\partial x_i}}_{\text{Advection term}} = - \underbrace{\frac{1}{\rho}\frac{\partial \tilde{p}}{\partial x_i}}_{\text{Pressure term}} + \underbrace{\nu \frac{\partial^2 \tilde{u}_j}{\partial x_i \partial x_i}}_{\text{Viscous term}} - \underbrace{\frac{\partial \tau_{ij}}{\partial x_i}}_{\text{Sub-filter scale stress tensor}} \tag{2.6}$$

2.5.2. RANS

The Navier-Stokes equation is commonly assessed in a time-averaged manner, leading to the formulation of the Reynolds-Averaged Navier-Stokes (RANS) equation. The derivation involves applying the Reynolds decomposition, separating velocity into its time-averaged and fluctuating components, as presented in Equation 2.7. This time-averaging procedure provides access solely to the static fields by calculating the mean flow field and fully modelling the fluctuating component of the flow. Consequently, none of the scales within the turbulent spectrum are resolved. Incorporating the Reynolds decomposition into the incompressible NSE in Equation 2.1, and performing time-averaging results in Equation 2.8.

$$u(x,t) = \overline{u}(x) + u'(x,t) \qquad \text{Where} \qquad \overline{u}(x) = \frac{1}{T}\int_0^T u(x,t)dt \tag{2.7}$$

$$\underbrace{\overline{u}_j \frac{\partial \overline{u}_i}{\partial x_j}}_{\text{Advection term}} = - \underbrace{\frac{1}{\rho}\frac{\partial \overline{p}}{\partial x_i}}_{\text{Pressure term}} + \underbrace{2\nu \frac{\partial \overline{S}_{ij}}{\partial x_i}}_{\text{Viscous term}} - \underbrace{\frac{\partial \overline{u_i' u_j'}}{\partial x_i}}_{\text{Reynolds stress}} \tag{2.8}$$

Note the creation of a $\overline{u_i' u_j'}$, the Reynolds stress tensor, representing the momentum transfer caused by turbulent fluctuations. It introduces additional unknown variables, leading to the infamous turbulent closure problem [23]. This necessitates additional modelling approaches to ensure closure of the RANS equations, resulting in the emergence of several turbulence models.

One commonly used closure model is the eddy viscosity model. Based on the Boussinesq hypothesis, it represents the Reynolds stress as the product of eddy viscosity and mean strain rate (linear dependence on mean rate of strain, analogous to laminar flows). A generic eddy viscosity definition is shown by Equation 2.9. As a simplification of the Reynolds stress term, it introduces limitations, particularly in accurately capturing anisotropic turbulence and complex flow features. Numerous models are available for estimating this μ_t. However, delving into a detailed discussion of these models was considered beyond the scope of this project.

$$-\rho \overline{u_i' u_j'} = \mu_t \left(\frac{\partial \overline{u}_i}{\partial x_j} + \frac{\partial \overline{u}_j}{\partial x_i} \right) - \frac{2}{3}\rho k \delta_{ij} \tag{2.9}$$

RANS is capable of predicting the time-averaged velocity field in a wind turbine wake, balancing accuracy with a reduction in computational costs compared to LES in which both time and space discretisation are considered. Due to the time-averaging operation, RANS simulations are unable to capture dynamic phenomena. The RANS approach is widely used and appealing to industry applications because it does not necessitate highly detailed meshes and offers short restitution times. For highly unsteady flows and specific interest in temporal flow development, LES simulations should be considered.

Furthermore, the RANS equations can be the starting point for even more simplified models. This report will discuss two such models: Ainslie Eddy Viscosity and Fuga in the following subsections.

2.5.2.1. Ainslie Eddy Viscosity Model

The Ainslie eddy viscosity wake model, rooted in parabolised Reynolds-averaged Navier-Stokes (RANS) equations, stands as one of the oldest field models in its category [35]. Ainslie's approach involves simplifying the RANS equations by assuming axisymmetric flow and assuming the radial gradients are sufficiently larger than the axial counterparts, resulting in a model that can be efficiently and accurately solved. Nevertheless, this simplification comes with a drawback, rendering the model unsuitable for application in the vicinity of the rotor where the pressure gradient holds dominance [36]. Additionally, Ainslie considered a thin shear layer approximation (essentially neglecting viscous terms) and incorporated the eddy-viscosity closure method to model Reynolds stresses [35, 36]. These modelling considerations led to the governing continuity and momentum equations in polar coordinates, as shown by Equation 2.10 and Equation 2.11.

Continuity Equation:
$$\frac{1}{r}\frac{\partial}{\partial r}(r\overline{v}) + \frac{\partial \overline{u}}{\partial x} = 0 \tag{2.10}$$

Momentum Equation:
$$\overline{u}\frac{\partial \overline{u}}{\partial x} + \overline{v}\frac{\partial \overline{u}}{\partial r} = -\frac{1}{r}\left(\frac{\partial\left(r\overline{u'v'}\right)}{\partial r}\right) \tag{2.11}$$

Where $\overline{u}$ and $\overline{v}$ is the Reynolds averaged streamwise and radial velocities, x and r the streamwise and radial directions respectively, and $\overline{u'v'}$ is the Reynolds stress to be modelled by means of an eddy viscosity model, shown by Equation 2.12.

$$-\overline{u'v'} = \varepsilon\frac{\partial \overline{u}}{\partial r} \tag{2.12}$$

The eddy viscosity ε is modelled as a two-fold parameter. Ainslie characterised this eddy viscosity by considering contributions from both turbulent mixing in the wake shear layer and ambient turbulence, as indicated by Equation 2.13 [35].

$$\varepsilon = l_w(x)\overline{u}_w(x) + \varepsilon_a \tag{2.13}$$

Here, the parameters l_w and $\overline{u}_w$ serve as suitable length and velocity scales characterising the wake shear layer, while ε_a represents the ambient turbulence contribution to the eddy viscosity. The chosen length and velocity scales are proportionate to the wake width b and the velocity difference $u_o - u_w$ across the wake shear layer. These scales, indicative of the downstream distance x, remain independent of r [35]. This leads to the following expression for the eddy viscosity:

$$\varepsilon = F\left[k_1 b\left(\overline{u}_0 - \overline{u}_w\right) + K_M\right] \tag{2.14}$$

The filter function F is introduced to account for the apparent build-up of turbulence in the shear layer, as observed in experimental data. It is essential for the treatment of the near-wake region due to the non-equilibrium between the mean velocity field and the turbulence field in the near-wake region [35].

2.5.2.2. Fuga

Fuga was initially developed as a CFD based model for wake effect calculations in offshore wind farm development. Fuga is a linearised flow solver of the steady-state RANS equations [37], employing an actuator-disc approach, and is renowned for its simplicity and robustness in wake modelling [38]. Despite its linearised nature, Fuga's results, specifically in terms of wind-speed deficits, closely align with those obtained from a nonlinear solution of RANS simulations [24, 39].

The linearisation of the simplified Reynolds-Averaged Navier-Stokes (RANS) equations involves employing Taylor expansion, focusing solely on terms of orders zero and one. The zeroth-order equations pertain to a scenario where no perturbations to the flow exist, indicating the absence of turbines [24]. Linearised CFD models mimic the behaviour of full CFD models while offering significant computational speed advantages. Notably, they exhibit relatively high accuracy, particularly in regions with small perturbations, making them substantially faster than their non-linear counterparts and enhancing computational efficiency [38].

Experience with linearised models like Fuga reveals an intriguing feature: despite the potential disruption of momentum balance near the rotor due to linearisation, these models demonstrate a tendency to repair the imbalance and return to reasonable momentum deficits in the far field [38]. Moreover, the ability of linearised models to be solved without a computational grid eliminates issues such as numerical diffusion and spurious mean pressure gradients [39].

2.6. Mid-Fidelity Wake Models

Mid-fidelity wake models were introduced as a means to decrease the computational effort required by the high-fidelity CFD approaches. The primary focus of mid-fidelity wake models is to retain the essential features observed from high-fidelity simulation results, but on a simplified model. This decrease in model

complexity and corresponding computational effort is paired with the use of assumptions, limiting the validity of results in specific wake regions or dependence on specified flow conditions. Therefore, this report will briefly discuss two mid-fidelity wake models: dynamic wake meandering in Section 2.6.1, and vorticity based models in Section 2.6.2.

2.6.1. Dynamic Wake Meandering Model

The dynamic wake meandering (DWM) model has emerged as a leading choice for mid-fidelity wake modelling in various engineering and environmental applications [21]. Unlike traditional approaches, this model dynamically simulates the evolution of wake structures, offering a more accurate representation of the complex interactions between wind turbines and their surrounding flow fields. By accounting for time-dependent factors and considering the evolving behaviour of the wake, the dynamic wake model strikes a balance between computational efficiency and the ability to capture key wake characteristics. This makes it a go-to option for mid-fidelity wake modelling, finding widespread use in the assessment of servo-aeroelastic analysis, and other scenarios where a nuanced understanding of wake dynamics is crucial. Examples of DWM implementations are found in the HAWC2Farm, and FAST.Farm models [40, 41].

The DWM model, which is based on the assumption that the wake behaves as a passive tracer in the turbulent wind field whereby the movement of the passive structure, i.e. the wake deficit, is driven by large turbulence scales [21]. The general structure of the DWM model is divided into three parts and was initially developed by Larsen at the Technical University of Denmark (DTU) [21]. Figure 2.4 illustrates these main model components. Larsen et al. also identified that the unsteady wake meandering treatment is essential as it is the main cause for wake expansion and added turbulence in wake regions.

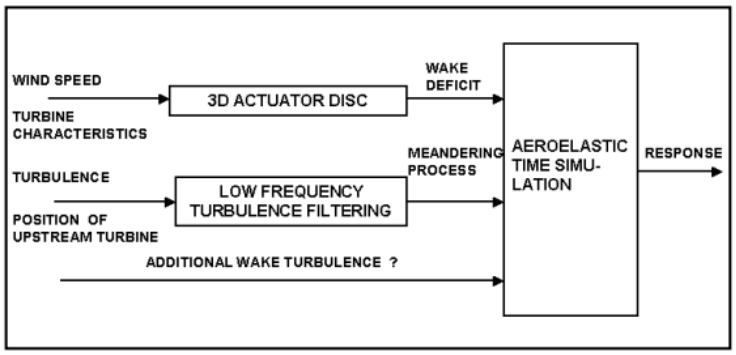

Figure 2.4: Components of the dynamic wake meandering model. Image adapted from Larsen et al. [21].

2.6.1.1. Wake Deficit

As turbulence mixing is the driving factor for wake deficit development, the wake deficit modelling approach is strongly inspired by the Ainslie Eddy Viscosity Model presented in Section 2.5.2.1. The initial deficit is calculated based on the blade element momentum (BEM) theory, more specifically the axial induction factor derived from it. The expansion of the wind speed deficit downstream is computed based on numerically solving the set of differential equations leading from the Ainslie Eddy Viscosity Model.

2.6.1.2. Wake Meandering

The model's second component pertains to meandering, which is derived from the prominent turbulence scales present in the ambient turbulent wind field. The basis of the wake meandering model relies on a core presumption, which states that the transport of wakes in the atmospheric boundary layer can be effectively simulated by envisioning the wakes as passive tracers carried by large-scale turbulence structures. In modelling the meandering process, it becomes imperative to incorporate a suitable representation of the stochastic transport medium. Meandering is computed using the low-pass filtered ambient wind field, generated with a Mann synthetic turbulence model. The cut-off frequency is determined by the wind speed and the rotor size, as outlined in Equation 2.15 [42].

$$f_c = \frac{u_0}{4R} \tag{2.15}$$

By adopting Taylor's frozen turbulence hypothesis, the downstream wake tracer advection is presumed to be influenced by the mean wind speed of the ambient wind field. This formulation ensures that the wake momentum in the direction of the mean flow remains unaffected by the specified longitudinal wake displacement and allows for a straightforward separation of the wake along the wind deficit profile (and its expansion) from the wake transportation process [42].

The lateral and vertical velocity of the wake tracer is assumed to be constant, and taken at the time of emission. The $y(t)$ and $z(t)$ positions of the wake deficits therefore depend linearly depend on the filtered wind speed fluctuations at hub height in horizontal and vertical direction, shown by Equation 2.16. The usage of the filtered wind speed at hub height is thus a considered simplification in this model [42].

$$\frac{\mathrm{d}y(t)}{\mathrm{d}t} = \tilde{v}(t) \qquad \frac{\mathrm{d}z(t)}{\mathrm{d}t} = \tilde{w}(t) \tag{2.16}$$

Both assumptions represent considerable simplifications of the actual underlying physics, neglecting any interaction between the wind field and the wake, as well as disregarding variations in transport velocity across the wake tracer induced by shear. Despite these simplifications, they can be justified as they serve as practical simplifications that do not excessively compromise the results.

2.6.1.3. Wake-Added Turbulence

The additional wake turbulence encompasses contributions from both conventional mechanically generated turbulence induced by the wake shear and the shed blade-bound vorticity, predominantly originating from the tip and root trailing vortices. Initially, these vortices exhibit organised and coherent flow structures. However, over time, they undergo gradual breakdown and tend to adopt characteristics resembling conventional turbulence, albeit with altered turbulence attributes compared to atmospheric turbulence [43].

The model is based on scaling a homogeneous Mann turbulence field [44]. The box cross-sections, hence length scale, are equal to one rotor diameter. This added turbulence refers to a meandering frame of reference, with the turbulence box' centre following the centre of the wake deficit centre positions. The turbulence box scaling factor is assumed to be dependent on the wake deficit depth and radial velocity gradient.

The total wake turbulence is obtained by adding the contributions of the meandering with both the ambient and wake-added turbulence. This addition therefore leads to a locally increased turbulence in the wake region.

2.6.1.4. Wake Superposition

The DWM model is capable of considering the effect of multiple wakes by combining wake effects of individual turbines. It is common practice to make use of the superposition rules formulated in the IEC 61400 standard [45]. Note that two formulations are stated, depending on the magnitude of free wind speed:

Below rated wind speed: The resulting wake contribution is the dominating wake contribution:

$$\vec{u}(\vec{x}, t) = \min_i \left(\vec{u}_i(\vec{x}, t)\right) \tag{2.17}$$

Below rated wind speed: Wake constituted as the sum of all local wake contributions:

$$\vec{u}(\vec{x}, t) = \sum_i \vec{u}_i(\vec{x}, t) \tag{2.18}$$

2.6.2. Vorticity Based Models

The concept of vorticity based models originates from inviscid potential flow theory and a vortex representation of the flow field [46]. The assumption of potential flow theory can be validated for the relatively high Reynolds number in the order of 10^5 in typical wind turbine applications. Compared to CFD models, vortex based models show significantly decreased computational times, at a cost of lower fidelity due to the inherent modelling choices, but are still able to represent wake dynamics and development.

In vorticity based wake models, the rotor is represented by a system of lifting lines or surfaces on the blades in combination with shed and trailing vortex lines in the wake. In this report's discussion, focus will be on the lifting line approach, thus representing the blades as a lifting-line approximation, where the blades are discretised into blade elements, each encompassing a bound vortex line. Conventionally, these bound vortices are located at the aerodynamic centre or quarter chord point [47]. The shed and trailing vortices are a direct result of the Helmholz theorems [48]:

1. The strength of a vortex line is constant along its length;
2. Vortex filaments can not start nor end in a fluid, it must extend to the boundaries of the fluid or form a closed path;
3. Conservation of circulation.

The combination of these theorems lead to a system of vortex rings to model a wind turbine blade, as shown by Figure 2.5. The vorticity sheet containing the shed and trailing vortex filaments originates from the blade trailing edge and propagates downstream, thereby interacting and shaping the wake region. The strength of the vorticity in the shed (Γ_s) and trailing (Γ_t) vortex filaments is dependent on the change in bound circulation (Γ_b), consistent with the third Helmholz theorem. This is mathematically expressed by Equation 2.19, with the shed vorticity dependent on the temporal changes in the bound circulation, and the trailing circulation strength dependent on the radial bound circulation distribution.

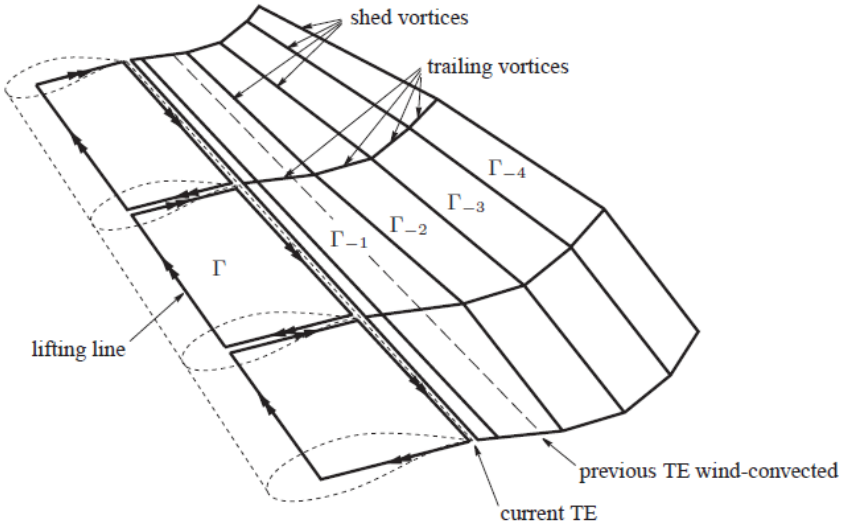

Figure 2.5: Representation of a wake geometry resulting from a wind turbine blade following Prandtl's classical lifting line theory. Image adapted from Van Garrel [46].

$$\Gamma_s(r) = \frac{\partial \Gamma_b(r)}{\partial t} \mathrm{d}t \qquad \text{and} \qquad \Gamma_t(r) = -\frac{\partial \Gamma_b(r)}{\partial r} \mathrm{d}r \tag{2.19}$$

The bound circulation is obtained through the use of the Kutta-Joukowsky theorem in combination with the lift equation [27] as a function of the lift coefficient (c_l), as shown by Equation 2.20. The wake vortices influence the local induced velocity, and thus local wind speed (U_r) on the blade elements, while also dictating the relative angle of attack required for the aerofoil data table lookup.

$$\Gamma_b = \frac{1}{2} c U_r c_l \tag{2.20}$$

The induced velocities at any location can be determined by the Biot-Savart law, given by Equation 2.21 [27]. Equation 2.21 shows the induced velocity vector ($\vec{u}_\Gamma$) at a specified location ($\vec{x}_p$) due to a vortex filament with length dl, at a distance r from the location of interest. Due to the potential flow theory assumptions, linear superposition of this induced wind speed due to all vortex filaments with the undisturbed flow leads to the determination of the global flow field.

$$\vec{u}_\Gamma\left(\vec{x}_p\right) = \frac{-1}{4\pi}\int \Gamma \frac{\vec{r}\times d\vec{l}}{r^3} \tag{2.21}$$

Limitations in modelling accuracy for the vorticity based models lie primarily in the potential flow assumption and use of aerofoil polar data. Although this 2D polar data might include viscous effects, no viscous effects are modelled in the wake model. Additionally, empirical corrections are required in unsteady simulations, with blade sections experiencing dynamic stall, challenging the validity of the shed vortex rings due to the flow separation effects. Finally, the choice of vortex core models introduces singularities in the flow field, potentially causing model instabilities [47], especially for free-vortex models.

Finally, a distinction is made based on how the wake structure is determined. Free wake models enable vortex elements to convect and deform freely in response to the velocity field. This provides the benefit of effectively handling a variety of flow scenarios, including yawed rotor configurations and dynamic inflow conditions [47]. This approach has proven to be computationally expensive due to the calculation of the induced wind speed at all vortex filaments, due to all other vortex filaments, at every simulation time step. Secondly, a sufficient vortex core model should be considered to eliminate model instabilities due to the vortex core singularities.

In an attempt to reduce computational effort and circumvent model instabilities, the prescribed wake model was created. An example of such a wake structure is shown by Figure 2.6. These so-called frozen wake models rely on inherent assumptions on wake expansion, convection speed and wake shape, and show good results for steady-state simulations. Although implementing a frozen wake approach significantly decreases computational effort, it essentially eliminates the model's ability to consider unsteady effects and temporal evolution, and introduces additional uncertainties due to the additional assumptions [47].

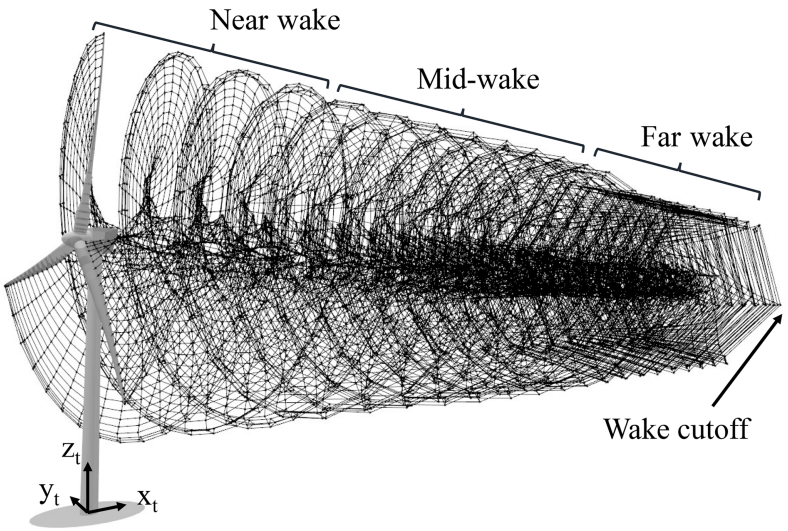

Figure 2.6: Illustrative example of a frozen, non-expanding wake structure, discretised wake representation in the lifting line model [49].

2.7. Low-Fidelity / Engineering Wake Models

The notable benefit of engineering wake models lies in their ability to parametrically predict wind turbine wakes effects, power capture, and consequent AEP for an entire wind farm with significantly lower computational costs compared to more advanced numerical tools. Despite this advantage, the precision of wake and power predictions from engineering wake models may fall short in addressing wind farm optimisation and control challenges [50]. This inadequacy is attributed to the ad hoc tuning of (often empirically determined) model parameters, a process that heavily relies on the specific characteristics of the wind farm site and wind turbines under investigation.

As discussed in previous sections, wake models enclose more than just a velocity deficit. Similarly, engineering wake models should also be able to systematically approximate wake-added turbulence inten-

sities, wake superposition and wake deflection. Especially considering the commonly used C_P-C_T lookup table rotor representation in these models, it is a challenge to retrieve complex flow development from these simple input variables. Whereas these are implicitly accounted for in higher-fidelity models, the severe reduction in resolved flow physics in engineering models explicitly demands modelling techniques to represent for these phenomena. Therefore, the following subsections will provide an overview of the existing analytical engineering wake models, and their subcomponents.

2.7.1. Analytical Wake Velocity-Deficit

Pioneering work in the field of analytical wake velocity-deficit models was carried out by the efforts of Jensen et al. [51] and Katic et al. [52], as they proposed a simple wake representation based on conservation of momentum using a control volume approach. The resulting mass balance between the rotor plane and the downstream flow yields results in Equation 2.22, and forms the basis of the model. Due to its simplicity, practicality and robustness, the Jensen wake model is still widely adopted in engineering applications for wind farm optimisation [24].

$$\left(\frac{D_r}{2}\right)^2 u_r + \left[\left(\frac{D_w}{2}\right)^2 - \left(\frac{D_r}{2}\right)^2\right] u_0 = \left(\frac{D_w}{2}\right)^2 u_w \tag{2.22}$$

The description of the Jensen model is based on the assumption of a top-hat wake profile, together with a linearly expanding wake diameter as a function of the downstream distance, as illustrated by Figure 2.7. Additionally, using the axial induction factor as defined in BEM theory: $u_r/u_0 = (1-2a)$, Equation 2.22 is simplified to Equation 2.23 and represent a wake-velocity deficit expression. Finally, by assuming an ideal axially symmetric flow, no rotation, no turbulence and conic shape wake profile, the axial induction factor is written as a function of C_T. This is shown by Equation 2.24 and highlights the potential use of a C_P-C_T rotor representation [24].

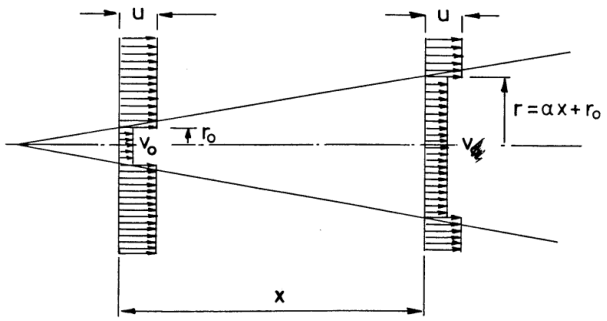

Figure 2.7: Illustrative image displaying the conical (linear) wake expansion and assumed top-hat wake profile. Image adapted from Jensen et al. [51]

$$\frac{u_w}{u_0} = 1 - \frac{2a}{(1+2\alpha x/D_r)^2} \tag{2.23}$$

$$a = \frac{1-\sqrt{1-C_T}}{2} \tag{2.24}$$

Due to the simplified wake representation, this model does not accurately capture wake dynamics. It performs especially poor in the near-wake region and should therefore only be considered for predictions on far-wake properties. This limitation is validated as the model's primary goal is to perform studies on energy losses on wind farm level, rather than representing an instantaneous wake velocity-deficit [24]. This is due to the focus on conserving the average momentum, and thus capturing the averaged momentum loss in the predicted wake profiles. Although reasonable accurate predictions on the maximum velocity-deficit in further downstream regions are obtained using the Jensen model, it tends to underestimate this maximum deficit in downstream regions closer to the turbine.

To address this shortcoming, Frandsen at al. [53] proposed an initial adjustment to the Jensen model, using the same control volume approach and similar wake assumptions, including the top-hat profile. This led to an altered wake velocity-deficit expression:

$$\frac{u_w}{u_0} = \frac{1}{2} \pm \frac{1}{2}\sqrt{1 - 2\frac{A_0}{A_w(x)}C_\mathrm{T}} \tag{2.25}$$

Where A_0 is the rotor area, and $A_w(x)$ the expanded wake area as a function of downstream position. To find this expanded wake area, Frandsen et al. [53] proposed an expansion factor β, as defined by Equation 2.26

$$A_w = \beta A_0, \text{ where } \beta = \frac{1}{2}\frac{1+\sqrt{1-C_\mathrm{T}}}{\sqrt{1-C_\mathrm{T}}} \tag{2.26}$$

Although these adjustments improved some shortcomings of the Jensen model, it remains a top-hat model. This means that the wake velocity-deficit at the wake centre is underestimated, combined with an overestimation of the wake deficit at the wake edges [54].

Gaussian Model

A subsequent model improvement was based on the observation of Gaussian-like self-similar wake profiles in experiments from wind tunnel and field measurements [55]. Therefore, given the assumption of an axis-symmetric Gaussian far-wake model, in combination with applying mass and momentum conservation, Bastankhah and Porté-Agel [54] proposed a new analytical expression for the wake velocity-deficit:

$$\frac{\Delta u}{u_0} = \frac{u_0 - u_w}{u_0} = \left(1 - \sqrt{1 - \frac{C_\mathrm{T}}{8\left(k^* x/D_r + \varepsilon\right)^2}}\right) \times \exp\left(-\frac{1}{2\left(k^* x/D_r + \varepsilon\right)^2}\left\{\left(\frac{z - z_\mathrm{h}}{D_r}\right)^2 + \left(\frac{y}{D_r}\right)^2\right\}\right) \tag{2.27}$$

Where x, y, z are the streamwise, lateral and vertical coordinates, and z_h the hub height. The wake width is defined by $\sigma/D_r = k^* x/D_r + \varepsilon$, where $\varepsilon = 0.25\sqrt{\beta}$ and k^* is the wake growth rate which is linearly proportional to the turbulence intensity TI. Note that this model still assumes linear expansion for the wake region (similar to the Jensen model), with β being a parameter as a function of C_T. As illustrated, the Gaussian model predicts the velocity deficit as the outcome of multiplying the maximum velocity deficit by a shape function dependent on downstream position, thus establishing self-similarity as discussed in Section 2.3.

These adjustments proved to yield in significant improvement when compared to the initial top-hat profile models. The Gaussian model demonstrates consistency and provides reasonably accurate power estimations [54], while top-hat models exhibit lower accuracy and are particularly sensitive to the relative positions of turbines in relation to the wind direction. Nonetheless, the Gaussian model developed by Porté-Agel and Bastankhah still shows issues of robustness and universality, and non-matching profiles in the near-wake range [56]. Therefore, the model should not be considered to represent the near-wake region.

Super Gaussian Model

Both numerical simulations and experimental observations have revealed that the wake velocity profiles do not strictly adhere to a Gaussian distribution, as assumed in the aforementioned model. Instead, as the wind turbine's wake progresses downstream, it has been documented to transition from a top-hat shape to a Gaussian shape in the far-wake [55]. The transformation is attributed to the tip vortices, originating from the blade tips, breaking up as they move downstream of the wind turbine. This phenomenon results in the mixing of the wake with the atmospheric flow, eventually leading to the attainment of a Gaussian-shaped velocity profile. Ensuring an accurate representation of the wake shape is crucial, as an incorrect shape can lead to inaccuracies in estimating power for a rotor operating under full wake or partial wake conditions [57].

In an attempt to improve the prediction of the near-wake velocity deficit, the so-called super Gaussian model was developed as an extension to the Bastankhah and Porté-Agel Gaussian model. The super Gaussian is derived from the general Gaussian deficit equation, but with the addition of the super Gaussian order n, describing the wake evolution [57]. Consistent with the self-similarity concept, the non-dimensional velocity deficit is expressed as a maximum velocity deficit $C(\tilde{x})$ and a shape function $f(\tilde{r})$:

$$\frac{\Delta u}{u_0} = \frac{u_0 - u_w}{u_0} = C(\tilde{x}) f(\tilde{r}), \tag{2.28}$$

with $\tilde{x}$ the axial distance from the turbine, $\tilde{\sigma}$ the characteristic wake width (approaching Gaussian when $n = 2$), and $\tilde{r}$ the radial distance from the wake centre, all three normalised by the wind turbine diameter D_r. The maximum velocity deficit is defined as Equation 2.29, where Γ represents the Gamma function.

$$C(x) = 2^{2/n-1} - \sqrt{2^{4/n-2} - \frac{nC_T}{16\Gamma(2/n)\sigma^{4/n}}} \tag{2.29}$$

Similar to the Bastankah Gaussian model, characteristic wake width σ is a function of the turbulence intensity. An expression for σ is shown:

$$\sigma = (a_s I + b_s)\, x + c_s\sqrt{\beta} \quad \text{with} \quad \beta = \frac{1}{2}\frac{1+\sqrt{1-C_T}}{\sqrt{1-C_T}} \tag{2.30}$$

Here, a_s, b_s, c_s are empirical model constants. Finally, a numerical value for n is required. An analytical expression based on curve fitting is proposed to decrease computational time:

$$n = a_f e^{b_f x} + c_f \tag{2.31}$$

The empirical model parameters $a_s, b_s, c_s, a_f, b_f, c_f$ have been calibrated with particle velocity and LIDAR measurements, with some observed dependencies on I and C_T [58]. Additionally, smooth convergence of n towards 2 is expected for a wake transition to a self-similar Gaussian shape in the far-wake.

In the near-wake, the super Gaussian model shows improved performance when compared to the Gaussian model, predicting larger wake regions. Although the model shows good agreement with measurements and LES results for high turbulence intensities, there is still a mismatch for the low turbulence intensity cases where less turbulence mixing is encountered [57].

The development of engineering wake models is still an ongoing topic in research, with particular challenges to better model the near-wake effects. Since the pioneering work by Jensen et al. [51] in 1983, a vast amount of wake models have been developed, with varying approaches and accuracies. Therefore, Table 2.1 presents a selection of the models implemented in the PyWake framework [59] without specifying the technicalities. Finally, an illustrative example of the model differences is shown by Figure 2.8, showing the predicted wake velocity deficits at different downstream locations for the same turbine in the same operating conditions.

Table 2.1: Short overview of additional engineering models present in the PyWake framework and their most significant differences compared to other models [59].

Model Name	Source	Main Aspects
TurboNOJDeficit	[58]	Modified version of the Jensen and subsequent Park models. The wake expansion rate is made proportional to the local turbulence intensity of the wake.
Niayifar Gaussian	[60]	Modification to the wake expansion parameter in the Bastankah model. The $k*$ varies linearly with local turbulence intensity.
Zong Gaussian	[61]	An adjustment to the Niayifar Gaussian model: a new near-wake width expression, based on a near wake length estimation by Vermeulen [62].
Carbajo Fuertes Gaussian	[63]	Modified version of the Zong model. The model includes an empirical correction for ε, and updated wake expansion constants based on LIDAR measurement observations.
Fuga	[64]	The wake velocity deficit is computed based on a set of lookup tables computed by the Fuga method, as discussed in Section 2.5.2.2. The model also includes blockage effect.

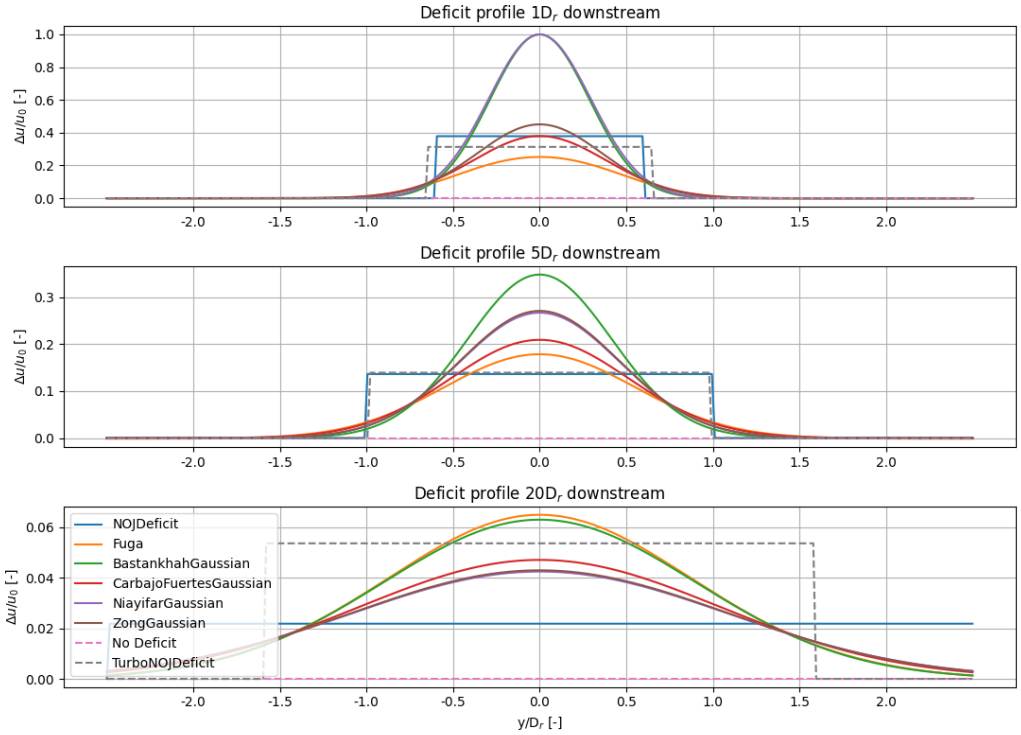

Figure 2.8: Comparison of different steady wake deficit models included in the PyWake framework, applied to the built-in Vestas V80 turbine [59].

2.7.2. Velocity-Deficit Superposition

Wind turbines within wind farms are frequently subjected to numerous wakes from multiple upstream turbines, dependent on the wind direction. Consequently, analytical wind farm wake models must consider the cumulative wake flows generated through the interaction of multiple wakes. To achieve this, wind farm models forecast cumulative wake effects by employing stand-alone wake models for each turbine individually, employing superposition principles to portray the collective impact of overlapping wakes. This section will present four wake superposition models, commonly used in state-of-the-art models. The first considered model considers an analogy with source pollutant dispersion, with wakes being linearly superimposed [65]. This consideration was also used by the Jensen model, and is visualised by Figure 2.9. A mathematical representation is given by Equation 2.32.

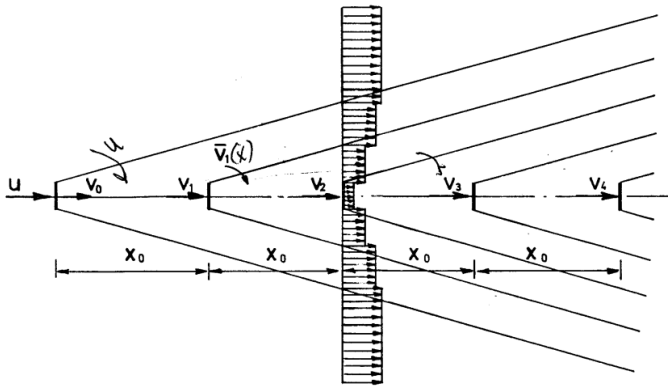

Figure 2.9: Illustrative example of linear wake superposition. Image adapted from Jensen et al. [51]

$$\frac{U_\infty - U_i}{U_\infty} \approx \sum_{k=1}^{N_T} \frac{U_\infty - U_{k,i}}{U_\infty} \tag{2.32}$$

N_T represents the total number of wind turbines, U_∞ is the undisturbed free-stream velocity, U_i is the velocity at turbine i, and $U_{k,i}$ is the velocity deficit of turbine k at the location of turbine i.

Subsequently, a second superposition method is proposed by Katic et al. to conserve the mean kinetic energy deficit [52]. in this second approach, the kinetic energy deficit of a mixed wake is assumed to equal the sum of the energy deficits for each wake at the calculated downwind position, indicated by Equation 2.33.

$$\frac{U_\infty - U_i}{U_\infty} \approx \frac{\sqrt{\sum_{k=1}^{N_T}(U_\infty - U_{k,i})^2}}{U_\infty} \tag{2.33}$$

Up until now, the mentioned superposition models all referred to U_∞. However, accumulation of many wakes can lead to non-physical negative velocities. To prevent this non-physical behaviour, Voutsinas et al. proposed the following linear superposition model [66]:

$$\frac{U_\infty - U_i}{U_\infty} \approx \sum_{k=1}^{N_T} \frac{U_k - U_{k,i}}{U_\infty}, \tag{2.34}$$

where U_k is the velocity immediately upstream of turbine k. In case of small deficits $U_k \approx= U_\infty$, hence providing a more general expression. Similar to the superposition expansion proposed by Katic et al. [52], a quadratic superposition can be imposed, making use of the local velocity U_k at turbine k rather than the absolute free-stream velocity [60]:

$$\frac{U_\infty - U_i}{U_\infty} \approx \frac{\sqrt{\sum_{k=1}^{N}(U_k - U_{k,i})^2}}{U_\infty}. \tag{2.35}$$

2.7.3. Analytical Wake Added Turbulence Intensity

Many wake velocity deficit models commonly rely on the wake width parameter σ, which itself is dependent on the turbulence intensity. Consequently, it becomes crucial to incorporate a model for the additional turbulence intensity to effectively predict the wake velocity deficit.

An initial approach was considered by Crespo and Hernández [67] by fitting a model to the results from RANS simulations of a single turbine wake. Similar to the first velocity deficit model, the added turbulence is assumed to adhere to a top-hat profile, with the intensity decreasing with increasing downstream position:

$$I^+ = 0.73\left(0.5\left(1-\sqrt{1-C_T}\right)\right)^{0.8325} I_\infty^{-0.0325}\left(\frac{\hat{x}}{D_r}\right)^{-0.32} \tag{2.36}$$

Where I^+ is the added turbulence intensity, $\hat{x}$ the downstream location and the exponents can be provided as model constants. Similar to the velocity deficit developments, self-similar Gaussian approaches were considered for further model developments. Eventually, self-similar double Gaussian profiles were considered based on experimental results, to better represent the wake edge regions. Therefore, Ishihara and Qian [56] proposed the following expression for wake added turbulence intensity at the horizontal plane at hub height:

$$\begin{aligned} I^+ =& \frac{1}{C_4\left(C_T\right) + C_5\left(I_0\right)\hat{x} + C_6\left(C_T, I_0\right)\left(1+\hat{x}/D_0\right)^{-2}} \times \\ & \left[k_1\left(\frac{\hat{f}}{D_0}\right)\exp\left(-\frac{1}{2}\frac{\left(\hat{y}/D_0 - 0.5\right)^2}{\sigma^2}\right) + k_2\left(\frac{\hat{r}}{D_0}\right)\exp\left(-\frac{1}{2}\frac{\left(\hat{y}/D_0 + 0.5\right)^2}{\sigma^2}\right)\right], \end{aligned} \tag{2.37}$$

Note the dependence on model constants C_4, C_5, C_6 and k_1, k_2. Whereas the first constants are dependent on C_T and I_∞, the latter constants are dependent on the radial position $\hat{r}$. Nonetheless, all require empirical calibration.

2.7.4. Wake Added Turbulence Intensity Superposition

Opposite to the velocity superposition methods, the superposition of turbulence intensity has seen less attention in literature. The most commonly used methods employ either linear or squared summation. Next to these standard models, some studies suggest only using the imposed turbulence intensity by the immediate upstream turbine, as follows [60, 68]:

$$I_i \approx \sqrt{I_1^2 + I_{2,i}^2} \tag{2.38}$$

where the turbulence intensity in the wake of the ith turbine, I_i, is computed from the ambient turbulence intensity I_1 and the added turbulence intensity of the turbine itself $I_{2,i}$.

Secondly, Wessel et al. propose a turbulence superposition method that accounts for the added turbulence intensities causes by all upstream turbines [69], where N_T is the total number of wind turbines:

$$I_i \approx I_1 + \sqrt{\sum_{j=1}^{N_T} I_{2,j}^2} \tag{2.39}$$

A final modification to this method is proposed to include the ambient turbulent intensity within the square root [70], shown by Equation 2.40. Note that no consensus has been reached yet about the optimal implementation model, different model suggestions are merely representations of different approaches. Therefore, it is advised to consider a sensitivity study based on the considered model in simulations.

$$I_i \approx \sqrt{I_1^2 + \sum_{j=1}^{N_T} I_{2,j}^2} \tag{2.40}$$

2.7.5. Wake Deflection

A wind turbine in yawed operational conditions will not only produce less power, but also the induced wake will be deflected. Therefore, a thorough understanding of this wake deflection would allow for more effective wind farm control strategies. Wake steering by means of yaw misalignment could reduce the reduced wind speed effects on downstream turbines. Thereby, downstream turbines could produce more power, while reducing fatigue loads. Figure 2.10 shows the effect of yaw-misalignment on the wake of a single turbine.

The primary use of engineering wake models is to assess AEP on wind farm level. Therefore, it is vital to have a sufficiently accurate model to predict wake deflections. Jimenez et al. [71] proposed a simple analytical model for a turbine in yawed conditions. The model is based on a top-hat profile, with a wake skew angle θ. Additionally, the model assumes small angle approximation such that $\cos\theta \approx 1$ and $\sin\theta \approx \theta$. The resulting expression for the wake deflection angle is given by Equation 2.41.

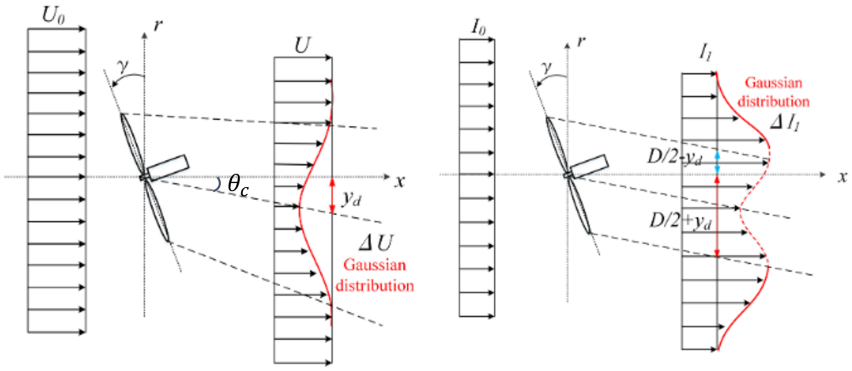

Figure 2.10: Schematic of a Gaussian wake model in yawed condition. Image adapted from Qian and Ishihara [72].

$$\theta = \left(\frac{D_r}{\sigma_w}\right)^2 \cos^2\gamma \sin\gamma \frac{C_T}{2} \tag{2.41}$$

Where σ_w is a measure of the wake width, and γ is the yaw angle. Under the assumption of a linearly increasing wake cross-section with downstream distance, such that $\sigma_w = D_r + \beta x$, Equation 2.41 becomes:

$$\theta = \frac{\cos^2\gamma \sin\gamma C_T}{2\left(1 + \beta\frac{x}{D_r}\right)^2} \tag{2.42}$$

Note that this expression is only valid in the far-wake region, where wake is dominated by ambient turbulence. Additionally, Jimenez et al. [71] argued that the conventional values for β from the unyawed velocity deficit models would not be valid. From comparison with LES results, they suggested using a numerical value in the range from 0.09 to 0.125. Eventually, this initial model was found to underestimate the initial wake skew angle in near-wake regions, but showed good similarity with high-fidelity simulation results in the far-wake.

An extension to this model was proposed by Bastankah and Porté-Agel [73]. They propose to model the near-wake by means of a potential core. The potential core forms a cone-shaped region characterised by a consistent reduction in speed, and originates at the rotor plane [73]. Figure 2.11 visualises this concept. The expressions for the initial skew angle at the rotor plane and the potential core length are given by Equation 2.43 and Equation 2.44 respectively.

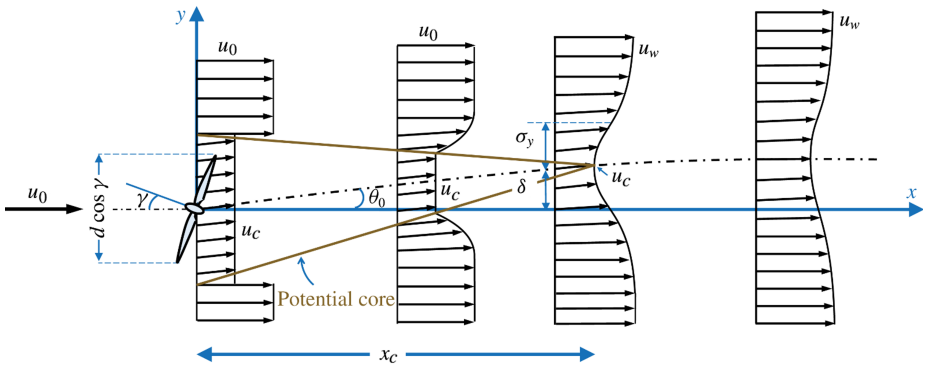

Figure 2.11: Visualisation of potential core definition, and centreline deflection for yawed turbines. Image adapted from Bastankah and Porté-Agel [73].

$$\theta_0 = \frac{0.3\gamma}{\cos\gamma}\left(1 - \sqrt{1 - C_T\cos\gamma}\right) \tag{2.43}$$

$$\frac{x_c}{D_r} = \frac{\cos\gamma\left(1 + \sqrt{1 - C_T\cos\gamma}\right)}{\sqrt{2}\left(\alpha^* I + \beta^*\left(1 - \sqrt{1 - C_T\cos\gamma}\right)\right)} \tag{2.44}$$

Where the empirical constants are tuned to be $\alpha^* = 2.32$ and $\beta^* = 0.154$. Within the potential core region, the wake skew angle is assumed to be constant. The wake radii in the y_1 and z_1 directions of the potential core continuously decrease, and can be formulated as follows (valid for $x_1 \leq x_c$):

$$\begin{aligned} y_{\mathrm{pc}} &= \mathrm{D_r}\sqrt{\frac{C_\mathrm{T}\cos\gamma}{2\left(1 - \sqrt{1 - C_\mathrm{T}\cos\gamma}\right)\sqrt{1 - C_\mathrm{T}}}}\left(1 - \frac{x_1}{x_\mathrm{c}}\right)\cos\gamma \\ z_{\mathrm{pc}} &= \mathrm{D_r}\sqrt{\frac{C_\mathrm{T}\cos\gamma}{2\left(1 - \sqrt{1 - C_\mathrm{T}\cos\gamma}\right)\sqrt{1 - C_\mathrm{T}}}}\left(1 - \frac{x_1}{x_\mathrm{c}}\right) \end{aligned} \tag{2.45}$$

The wake expansion is determined by the Gaussian standard deviation [73]. In the near-wake region, $\sigma_{y,\mathrm{nw}}$ and $\sigma_{z,\mathrm{nw}}$ initiate at 0 for $x_1 = 0$ and progressively increase to their standard deviations at the beginning of the far-wake. Within the near-wake, the Gaussian function attains its minimum at the border adjacent to the potential core. The distinct standard deviations for the near and far-wake regions are explicitly delineated by Equation 2.46.

$$\left.\begin{aligned}\sigma_{y,\mathrm{fw}} &= (x_1 - x_\mathrm{c})\, k_y + \tfrac{\mathrm{D_r}}{\sqrt{8}} \cos\gamma \\ \sigma_{z,\mathrm{fw}} &= (x_1 - x_\mathrm{c})\, k_z + \tfrac{\mathrm{D_r}}{\sqrt{8}}\end{aligned}\right\} x_1 \geq x_\mathrm{c}$$
$$\left.\begin{aligned}\sigma_{y,\mathrm{nw}} &= \tfrac{x_1}{x_\mathrm{c}} \tfrac{\mathrm{D_r}}{\sqrt{8}} \cos\gamma \\ \sigma_{y,\mathrm{nw}} &= \tfrac{x_1}{x_\mathrm{c}} \tfrac{\mathrm{D_r}}{\sqrt{8}}\end{aligned}\right\} x_1 < x_\mathrm{c} \tag{2.46}$$

Combining these equations leads to a simplified expression for the wake expansion parameters, as shown by Equation 2.47.

$$\begin{aligned}\sigma_y &= \max\left(x_1 - x_\mathrm{c}, 0\right) k_y + \min\left(\frac{x_1}{x_\mathrm{c}}, 1\right) \frac{\mathrm{D_r}}{\sqrt{8}} \cos\gamma \\ \sigma_z &= \max\left(x_1 - x_\mathrm{c}, 0\right) k_z + \min\left(\frac{x_1}{x_\mathrm{c}}, 1\right) \frac{\mathrm{D_r}}{\sqrt{8}}\end{aligned} \tag{2.47}$$

The wake growth rates k_y and k_z are described by Equation 2.48. The model directly associates the rate of lateral and vertical wake expansion with the ambient turbulence intensity at a turbine, incorporating two tuned parameters.

$$k_y = k_z = k_a I_{amb} + k_b \tag{2.48}$$

With the constant factors $k_a = 0.38371$ and $k_b = 0.003678$, where I_{amb} is the ambient turbulence intensity [73]. Similar to other analytical models describing wake deficit, the reduction factor is expressed as $r = \Delta u / u_0$. Given this definition, and the defined model parameters, the wind reduction factors in both near and far-wake regions, and the wake deflection in the far-wake region are displayed by Equation 2.49 and Equation 2.50 respectively.

$$\left.\begin{aligned}r_{\mathrm{fw}} &= \left(1 - \sqrt{1 - C_\mathrm{T} \tfrac{\cos\gamma}{8(\sigma_y \sigma_z)/\mathrm{D}^2}}\right) \exp\left[-\tfrac{1}{2}\left(\tfrac{y_1 - \delta}{\sigma_y}\right)^2\right] \exp\left[-\tfrac{1}{2}\left(\tfrac{z_1 - z_h}{\sigma_z}\right)^2\right] \\ r_{\mathrm{nw}} &= \left(1 - \sqrt{1 - C_\mathrm{T}}\right) \exp\left[-\tfrac{1}{2}\left(\tfrac{|y_1 - \delta| - y_{\mathrm{pc}}}{\sigma_y}\right)^2\right] \exp\left[-\tfrac{1}{2}\left(\tfrac{|z_1 - z_h| - z_{\mathrm{pc}}}{\sigma_z}\right)^2\right] \\ r_\mathrm{c} &= \left(1 - \sqrt{1 - C_\mathrm{T}}\right)\end{aligned}\right\} \begin{aligned}x_1 \geq x_c \\ x_1 < x_c\end{aligned} \tag{2.49}$$

$$\frac{\delta}{D_r} = \theta_0 \frac{x_c}{D_r} + \frac{\theta_0}{14.7} \sqrt{\frac{\cos\gamma}{k_y k_z C_T}} \left(2.9 + 1.3\sqrt{1 - C_T} - C_T\right) \times \ln\left(\frac{\left(1.6 + \sqrt{C_T}\right)\left(1.6\sqrt{\frac{8\sigma_y\sigma_z}{D_r^2 \cos\gamma}} - \sqrt{C_T}\right)}{\left(1.6 - \sqrt{C_T}\right)\left(1.6\sqrt{\frac{8\sigma_y\sigma_z}{D_r^2 \cos\gamma}} + \sqrt{C_T}\right)}\right) \tag{2.50}$$

The model by Bastankah and Porté-Agel could not be generally applied in various conditions, as it needs to be tuned from experimental or higher fidelity simulation results [72]. The study also revealed that higher ambient turbulence tends to reduce the length of the potential core region and accelerate flow mixing in the far-wake, resulting in diminished wake deflections. Hence, yaw control strategy proves more effective in conditions of low ambient turbulence, such as those encountered in offshore wind farms, where wake effects remain present over larger downstream distances.

2.8. Wind Farm Control

Wind farm control is a critical aspect of wind energy system optimisation. The application of control algorithms enables wind turbines to adapt to changing wind conditions in order to maximise energy extraction on the entire wind farm, minimise turbine fatigue loads, and mitigate environmental impact. The effectiveness of model-based wind farm control inherently relies on the precision and computational costs associated with the mathematical model employed for the system. From static wake control concepts to emerging dynamic control strategies, ongoing research explores innovative approaches. Therefore, this section will discuss quasi-static and dynamic flow control strategies in Section 2.8.1 and Section 2.8.2, followed by the presentation of two wind farm control algorithms in Section 2.8.3.

2.8.1. Quasi-Static Wind Farm Flow Control

Static wake control concepts operate by influencing the wake through gradual adjustments to the turbine's control degrees of freedom. These adjustments are made in a manner that impacts the time-averaged characteristics of the wake [74]. This form of control has undergone extensive study over the years, resulting in a relatively comprehensive understanding of how the wake responds to control actions. Therefore, the two main industry adapted wake strategies: axial induction control and wake redirection are presented in Section 2.8.1.1 and Section 2.8.1.2 respectively.

2.8.1.1. Axial Induction Control

The axial induction control strategy is designed to mitigate the wake deficit downstream by reducing the axial induction factor of wind turbines located upstream. This reduction can be achieved by adjusting the upstream turbine's operating conditions, either through an increase in the blade pitch angle or by operating at a suboptimal tip-speed ratio [75]. The effect on the upstream turbine's wake is demonstrated by Figure 2.12. On the right side of the figure, axial induction control is demonstrated. While the energy production of the regulated wind turbine decreases, the wind speed in its wake increases, thus leading to a higher power output of the turbine operating in its wake. Although this strategy has been extensively studied, it remains challenging to demonstrate effective power gains in field experiments [74].

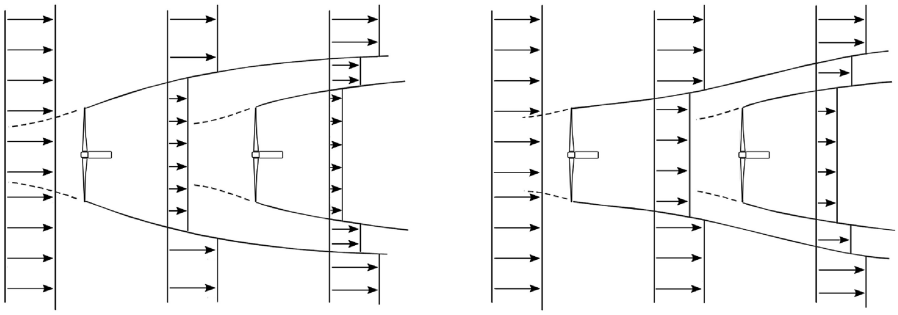

Figure 2.12: Schematic representation of two wind turbines aligned with the wind during regular operation (left) contrasted with axial induction control (right) [76].

2.8.1.2. Wake Redirection

Wake redirection, also known as wake steering, has become the most advanced control approach in terms of commercial use [74]. Especially through recent developments and accuracy improvements in low-fidelity wake models [68, 17], the implementation of wake steering is widely implemented for wind farm layout optimisation and wind farm control.

The goal of the wake redirection strategy is to steer the wake away from the turbine located downstream. In the deliberate yaw misalignment approach, the lateral force generated by the incoming wind is utilised to redirect the wake away from the downstream turbine [77]. Consequently, the downstream turbine has the potential to produce more power, leading to an overall increase in the wind farm's power output. This concept is visualised by Figure 2.13, showing the effect of a deflected wake by means of a yaw offset in a case where two turbines are aligned.

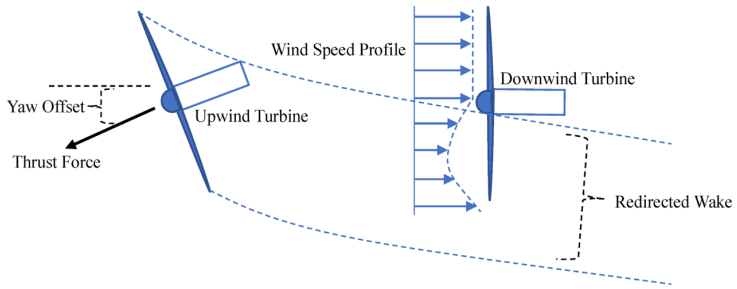

Figure 2.13: Illustrative representation of the wake redirection control strategy implemented in a configuration with two aligned turbines [77].

In addition to increased power production, wake steering could also reduce fatigue loads on downstream turbines [74]. Turbines operating in wake conditions experience higher turbulence intensities, leading to increased fatigue loads. Beyond turbulence intensity, it is the wake meandering and higher flow unsteadiness that contribute to the increased fatigue loads. Therefore, redirecting wakes could benefit both the fatigue life and power production of downstream turbines. However, partial wake conditions (as indicated by Figure 2.13) might also result in increased fatigue loads despite the increase in power output.

The wake redirection strategy has gained widespread adoption in the industry, primarily because it combines increased energy production with added structural loading benefits, and have been validated by field experiments [74]. Ongoing research in the field of wake redirection persists, driven by existing challenges. While the ultimate objective is to enhance accuracy, one of the principal sources of inaccuracy is thought to result from the difficulties in accurately representing the complex dependence on atmospheric conditions, as highlighted in Meyers et al. [74]. These challenges are compounded by secondary wake effects and yaw-based wake recovery, influencing wake steering within extensive arrays of large turbines.

2.8.2. Dynamic Wind Farm Flow Control

Dynamic wind farm flow control strategies are more complex compared to the quasi-steady strategies, as the dynamic nature requires more flow physics to be resolved. The primary idea of such dynamic models is to speed up wake breakdown and increase mixing into the wakes [74]. To achieve this, three main aspects have received attention in research: tip- and root-vortex instabilities, wake meandering and dynamic thrust modulation. This research led to two dynamic flow control strategies: pulse and helix, both visualised by Figure 2.14.

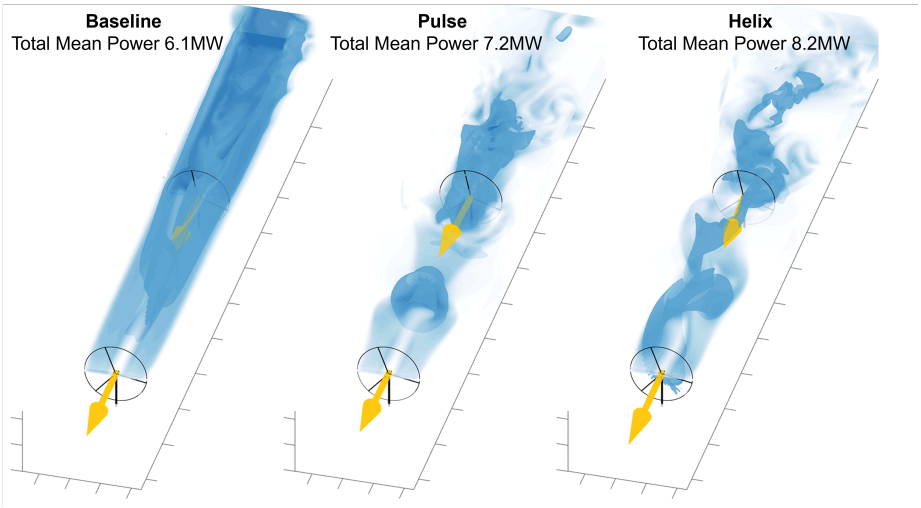

Figure 2.14: Illustration of LES study results for two dynamic flow control strategies (pulse, helix) compared to normal turbine operation [74].

Firstly, the pulsing dynamic flow control strategy will be shortly discussed. By adjusting the turbine

induction in a time-varying manner, a train of vortex rings is created. Because of this vortex ring creation, high speed fluid particles are entrained in the wake centre, leading to an accelerated wake breakdown [74]. Nevertheless, Munters and Meyers [78] could not prove great that the dynamic induction control remained effective beyond the first row of turbines, or in large turbulence (due to the already large turbulent mixing).

More recent developments by Frederik et al. have proposed the helix approach as a novel means to trigger wake helicoidal wake breakup [79]. Through the implementation of dynamic individual pitch control, the rotor undergoes varying tilt and yaw moments, leading to a gradual change in the wake direction over time. When compared to dynamic induction control, the helix approach requires smaller actuation amplitudes, thus reducing structural loading, while potentially inducing a more effective wake breakup [74]. Only limited research has gone into this topic, with more complex and advanced flow analysis expected to follow.

The domain of dynamic control aiming at accelerating the breakup of wakes is still in its early stages. Although theoretical ties to linear stability analysis may prove intriguing, they have not been thoroughly explored [74]. Additionally, current investigations have focused on relatively simple inflow conditions and small arrays of turbines. Finally, the structural impact of such dynamic control approaches needs to be studied in more detail, especially to assess the effects on fatigue loads.

2.8.3. Wind Farm Control Algorithms

Flow models able to capture proposed flow control physics do not suffice to build a wind farm controller. It requires additional logic and algorithms to operate the individual turbines based on the encountered conditions and with a set objective [74]. In order to do so, this section will distinguish between open- and closed-loop control strategies.

The most popular, and achievable current practice for wind farm control is an open-loop control strategy, depending on steady-state engineering models. These models are used to generate optimised control set points (output lookup tables), based on different atmospheric conditions and wind turbine lookup tables [74]. Hence, online (real-time) external conditions (mean wind speed, wind direction, turbulence intensity, etc.) will be used as inputs for these generated control lookup tables to determine the optimal control settings. A visualisation of this open-loop strategy is shown by Figure 2.15. Although open-loop wind farm control is implemented in current industry tools, the static nature of the underlying models introduce uncertainties and model errors that lead to significant safety factors on model predictions, especially on large farm scales.

Alternatively, one can consider a closed-loop control strategy by implementing a feedback loop. The next control policy is determined by implementing measured data in a real-time optimisation framework. The benefit of such a control philosophy is the ability to handle model uncertainty and unknown disturbances, as shown by Figure 2.16 [74]. The downside is the added complexity layer. Ideally, the feedback would be based on a (quasi) dynamic wake model to include wake delays corresponding to mesoscale wind field variability, with the ability to run in real-time. This would allow for continuous control updates to maximise e.g. power output. The identification of these potential benefits have recently sparked interest in developments of quasi dynamic low-fidelity models to capture this dynamic wake development while ensuring low computational efforts.

Presently, research efforts have been focused on validating fundamental concepts rather than demonstrating the feasibility of implementing closed-loop control schemes [74]. Anticipations revolve around the advancement of faster and more precise (quasi) dynamic wake models, coupled with machine learning, which is expected to yield in increased investments in the development of an efficient closed-loop wind farm control strategy.

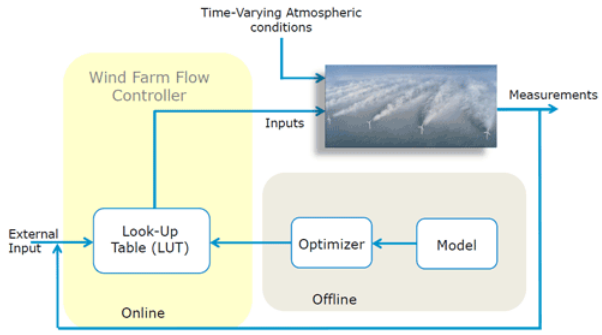

Figure 2.15: Illustration of an open-loop wind farm control scheme, as implemented in current practise [74].

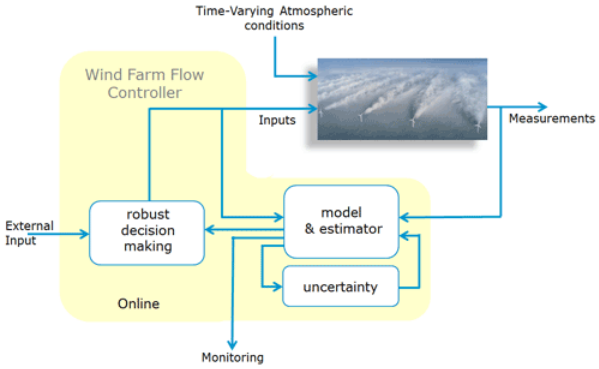

Figure 2.16: Overview of an envisioned closed-loop control scheme for future wind farm control [74].

2.8.4. Engineering Dynamic Wake Models

With the growing need for precise and effective wind farm control, low-fidelity dynamic wake models have gained attention in recent literature. These models help to improve the overall performance of wind farms by incorporating time-dependent factors and providing more accurate predictions of wake effects. Most significantly, they aim to include wake propagation delays responding to mesoscale variability in the flow field and control state changes [74]. Three notable dynamic engineering wake models will be briefly mentioned: FLORIDyn, SPLINTER, and Foxes.

FLORIDyn

Flow Redirection and Induction Dynamic (FLORIDyn) is a quasi-dynamic engineering wake model designed to incorporate temporal dynamics into traditional steady-state wake models. The parametric model is developed at TU Delft, and is primarily intended for to simulate wind farm flow, and to serve as a control-oriented model. FLORIDyn makes use of a framework that leverages FLORIS's steady-state computational efficiency to simulate basic wake dynamics. This is achieved by creating observation points (OPs) at the rotor plane during each time step, inheriting the turbine's state. [80, 81, 82]

SPLINTER

SPLINTER is a dynamic wake model developed at the University of Oldenburg. It originated from a propagation model for LiDAR measurements to correct the temporal distortion and to reconstruct the wind field between the measurements. It was then extended into a comprehensive 2D dynamic wind farm flow model capable of simulating and forecasting wind farm flow at hub-height. Moreover, the semi-Lagrangian structure of the model enables the propagation of multiple parameters or properties alongside the flow, offering versatility for various applications. The model is designed to handle flow estimations derived from SCADA data or to serve as a foundation for wind farm control optimisations [83].

Foxes

Farm Optimization and eXtended yield Evaluation Software (Foxes) is an open source dynamic wake model developed by Fraunhofer IWES. By incorporating high-resolution turbulence data, Foxes can accurately predict the effects of wake interactions on turbine performance. Typical applications include wind farm optimisation (e.g., layout optimisation or wake steering), pre- and post-construction analyses of wind farms, and studies involving wake model analyses. Additionally, Foxes could be implemented to develop control strategies that mitigate the negative impacts of wake turbulence, thereby enhancing the overall efficiency and reliability of wind farms. [84]

Incorporating these dynamic engineering wake models into wind farm control strategies has the potential to develop more effective closed-loop control approaches. This is especially true when accounting for the dynamic inflow conditions and changes in propagation of changes in control states. Optimisation for these models requires balancing modelling accuracy and managing acceptable levels of computational complexity, ensuring that the models can be used efficiently in practical scenarios. This capability of engineering dynamic wake models is crucial for maximising the global wind farm power output and ensuring the sustainable operation of wind farms.

2.9. Synthesis of Varying Fidelity Wake Modelling Frameworks

This section aims to provide an summarising overview of some existing wake modelling frameworks within the considered fidelity classifications. As highlighted throughout this literature review chapter, representing all physical phenomena in wind farm flow models is challenging due to the wide range of spatial and temporal scales governing the flows. Therefore, higher accuracies in representing both rotor and wake representations demand higher computational costs. Conversely, the introduced assumptions related to lower fidelity modelling approaches lead to the omission of complex flow physics, and faster code execution.

To indicate the discussed range variety of modelling approaches, Table 2.2 presents a selection of models, with their respective submodel choices, and allocated fidelity level. It is essential to acknowledge that these fidelity classifications do not follow a universal standard. Nonetheless, they generally indicate model complexity.

Table 2.2: Summarising table indicating examples of different wake modelling approaches on farm level, highlighting the emergence of low-fidelity dynamic wake models.

Framework Name	Flow Propagation	Rotor Representation	Wake Dynamics	Wake Representation	Source
Low-Fidelity					
FLORIS	-	AD - LUT	Steady	Analytic	[82]
PyWake	-	AD - LUT	Steady	Analytic	[59]
FLORIDyn	Linear Convection	AD - LUT	Quasi-Dynamic	Analytic	[81]
Foxes	Linear Convection	AD - LUT	Quasi-Dynamic	Analytic	[84]
UFLORIS	Linear Convection	AD - LUT	Quasi-Dynamic	Analytic	[85]
SPLINTER	2D NSE	AD - LUT	Unsteady	Analytic	[83]
Mid-Fidelity					
FAST.Farm	DWM	AD - BEM	Unsteady	Numeric	[41]
HAWC2Farm	DWM	AD - BEM	Unsteady	Numeric	[40]
High-Fidelity					
Fuga	RANS	AD - BEM	Steady	Numeric	[38]
SOWFA	RANS / LES	AD / AL	Unsteady	Numeric	[86]
EllipSys3D	RANS / LES	AD / AL	Steady / Unsteady	Numeric	[24]
YALES2	LES	AL	Unsteady	Numeric	[87]

2.10. Project Aim and Research Questions

The precision of wind farm AEP prediction relies significantly on the fidelity and accuracy of the underlying wake model for predicting the wind farm flow. However, the high computational cost renders mid- and high-fidelity wake models impractical for large-scale wind farm applications. Consequently, low-fidelity wake models have emerged as the sole viable solution for conducting AEP simulations and optimisation at the scale of entire wind farms.

The currently used industry-standard models for wind farm AEP assessment typically provide steady-state solutions only, assuming that the involved time scales are sufficiently large. However, it is known that changing the operating conditions of an upstream turbine will not instantly result in an increase in power produced by the downstream turbine. There will be a delay as the new wake trajectory needs to propagate downstream. Results indicate that neglecting this delay could be one of the reasons for inaccuracies in AEP estimations. This is especially important when considering the significantly increased rotor sizes over the past years, resulting in increased time-scales on modern wind farms.

Therefore, there is a genuine need for fast dynamic wake models incorporating this time-dependency. This need is particularly important when designing more effective open- and closed-loop wind farm control strategies that can further enhance the wind farm AEP. Therefore, the main research objective for this thesis project is determined to be:

Research Objective

This thesis aims to enhance the accuracy of wind farm Annual Energy Production (AEP) estimation by assessing the suitability of a dynamic wake modelling approach, and to develop a methodological framework for wind farm-scale validation studies.

The research objective naturally flows into the formulation of two main research questions. Both of these research questions are further divided into sub-questions to allow for a systematic and comprehensive approach in answering the main questions.

Research Question 1

How can the inclusion of time-varying wake propagation in engineering wake models contribute to improving the accuracy of Annual Energy Production (AEP) computations?

1.1 What is the significance of accurately estimating wake losses for assessing overall wind farm performance?

1.2 What are the key features and capabilities of low-fidelity engineering tools for wakes?

1.3 How do the limitations of currently used wind farm flow models, particularly in terms of their treatment of wake dynamics, affect the accuracy of AEP predictions?

1.4 How does the assumption of steady-state solutions affect the accuracy of AEP estimations in current state-of-the-art models?

1.5 What is the magnitude of the predicted AEP accuracy gain by implementing time dependency in wake propagation?

1.6 By what amount can the current safety margins on AEP computations be decreased?

1.7 How to design a real-world validation study to assess the suitability of including time-varying wake propagation models in improving AEP accuracy?

1.8 How to develop a suitable methodology to incorporate complexities related to time-varying wind conditions and wake propagation into engineering wake models?

1.9 To what extent is the dynamic wake model considered robust for practical applications in the wind energy industry?

Research Question 2

What are the effects of modelling assumptions on the uncertainty of time-varying engineering wake models?

2.1 How to quantify model sensitivity to empirically tuned constants?

2.2 How to quantify the uncertainties related to modelling assumptions in engineering wake models?

2.3 How does the choice of submodel for representing wake deficits influence the overall uncertainty of time-varying engineering wake models?

2.4 How does the choice of submodel for representing wake added turbulence influence the overall uncertainty of time-varying engineering wake models?

3

Research Methodology

This chapter provides a comprehensive overview of the research methodology employed throughout the thesis project to address the established research questions. Firstly, in Section 3.1, the implementation of the quasi-dynamic engineering wake model, Flow Redirection and Induction Dynamics (FLORIDyn), is explored. This model is chosen for its ability to simulate temporal wake propagation while maintaining computational efficiency compared to high-fidelity models. The discussion covers its main modelling assumptions, approaches, and differences compared to steady-state engineering models. Following this, Section 3.2 outlines the numerical setup adopted for this thesis project, including detailed descriptions of the wind farm and turbine properties. Subsequently, Section 3.3 elaborates on the methodology used to compare the results obtained from the FLORIDyn model evaluation with both field data and steady-state wake model results. It also introduces the approach to generate synthetic wind conditions compatible with FLORIDyn's capabilities and presents comparative model assessment metrics, which will guide post-processing and model comparison procedures. Finally, Section 3.4 synthesises the outlined methodology throughout this chapter.

3.1. FLORIDyn: Quasi-Dynamic Engineering Wake Model

FLORIDyn, a novel control-oriented dynamic wake model, is designed to capture wake interaction effects among wind turbines in a wind farm. In contrast to steady-state engineering models, FLORIDyn not only accounts for wake effects at each wind turbine but also considers the time delay between control-setting adjustments or changing wind conditions and the responses of downstream wind turbines in the wind farm. Hence, changes in wind conditions propagate through the wake instead of instantly affecting turbines downstream [81].

Gebraad and van Wingerden initially introduced the FLORIDyn model in 2014, derived from the steady-state Zone Flow Redirection and Induction in Steady-State (FLORIS) model [80]. Subsequently, in 2020, Becker developed a Gaussian FLORIDyn model based on the Gaussian FLORIS model [88]. Whereas the wake effects are still obtained based on the steady-state Gaussian FLORIS model (derived from the Gaussian model description by Bastankah and Porté-Agel [73]), the dynamics are modelled by the so-called observation points (OPs) at each time step at the rotor plane to inherit the turbine state [82]. In the latest published FLORIDyn model in 2022, Becker et al. revised the distributed OP generation [82]. Instead, only a single OP chain is generated per wind turbine, and propagates along the wake centre line, drastically improving computational effort.

The following seven subsections delineate the latest advancements in the FLORIDyn model architecture. Starting with Section 3.1.1, the discussion unfolds with an exploration of the underlying steady-state Gaussian FLORIS model. Proceeding, Section 3.1.2 delves into the implementation of heterogeneous wind conditions, while Section 3.1.3 details the incorporation of temporal wake dynamics. Following this, Section 3.1.4 elaborates on the models implemented for the convection of free-stream wind conditions. Subsequently, Section 3.1.5 details the implemented model for power computations, while Section 3.1.6 discusses the computation of wake-added turbulence intensity at a turbine of interest. Finally, an overview of the empirical model constants is presented in Section 3.1.7.

3.1.1. Underlying Steady-State Wake Model

The foundational structure of the Gaussian FLORIS model is based on the studies conducted by Bastankhah and Porté-Agel [73], as discussed in Section 2.7.5. The Gaussian FLORIS model introduces a parametric, three-dimensional wake configuration featuring Gaussian-shaped wind speed recovery in the far wake region, combined with a potential core formulation in the near wake. These distinct wake regions are visualised in Figure 3.1. A reduction factor $r = \Delta u/u_0$ is calculated at each of the wake locations. In the potential core, a top-hat profile is considered, thus r is constant. In both the near- and far-wake regions, the wake recovery is governed by the Gaussian standard deviations σ_y and σ_z, indicating the wake diffusion. Finally, wake deflection is obtained from the initial skew angle θ_0 and leads to the centre line deflection δ.

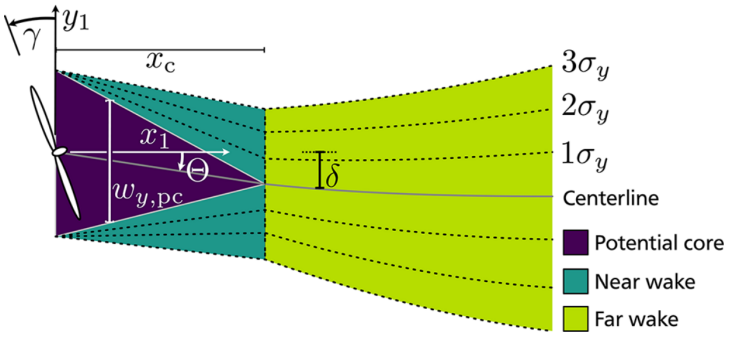

Figure 3.1: Individual turbine wake shape, indicating relevant wake zones and parameters [81].

In the case of overlapping wakes, and to estimate the effective wind speed on the entire domain, the wake effects of several turbines need to be combined. The superposition of wake velocity deficits is governed by Equation 3.1.

$$u_{\text{eff,RP}}\ (u_{\text{free ,RP}}, r_{\text{own}}\ , r_{\text{f,OP}}) = u_{\text{free, RP}}\ (1 - r_{\text{own}}\ ) \underbrace{\prod_{i=1}^{n_{\text{T}}} (1 - r_{\text{i}})}_{r_{\text{f,OP}}} \tag{3.1}$$

Here, $u_{\text{free, RP}}$ represents the free wind speed at the desired reference point (RP) location. Additionally, r_{own} is the RP's own reduction factor (non-zero when the RP is an OP), and r_{i} is the interpolated reduction of an OP for one of the n_{T} upwind turbines. The combination of these parameters thus leads to the determination of an effective wind speed at any location in the wind farm. Hence, the combined reduction effect can be represented by an equivalent r_{f}, that reflects the superimposed reduction effect of the considered OPs.

To calculate an effective wind speed at the rotor plane, the FLORIDyn model considers a distributed set of points across the rotor area. This distributed set of reference points is used to calculate the effective wind speed on distinct locations within the rotor plane.

The latest FLORIDyn version incorporates an isocell rotor discretisation, implemented according to the description by Masset et al. [89]. Within this approach, all discretised cells possess identical areas and shapes. Additionally, this method generates a uniform distribution of cell centres within the circular region. From this rotor discretisation, a weight vector $\mathbf{w}$ is created. It contains the relative weight of every isocell point, depending on the normalised isocell area. Due to the isocell representation, all weights will be equal, but this weight vector allows for different discretisation methods to be implemented. Next, the rotor wind speed is obtained as the product between the weight vector and the elementwise multiplication ($\circ$) of the vector containing the equivalent reduction factors per rotor point ($\boldsymbol{r}_{\text{f,RP}}$) and the free-stream wind speeds at the rotor points ($\boldsymbol{u}_{\text{free,RP}}$). This operation is shown by Equation 3.2. Note that due to the isocell representation, this is essentially a rotor-averaged effective wind speed, since the weights are equal for all discretised points.

$$u_{\text{eff, rotor}} = \boldsymbol{w}^{\top}\ (\boldsymbol{r}_{\text{f,RP}} \circ \boldsymbol{u}_{\text{free,RP}}) \tag{3.2}$$

The Gaussian FLORIS framework has expanded the initial wake deficit model by incorporating an added wake turbulence intensity based on the top-hat formulation by Crespo and Hernández [67]. However, the calculation of the wake-added turbulence intensity is altered, to better match with CFD results [90]. The resulting expression for the I^+ is shown by Equation 3.3.

$$I^+ = \frac{A_{\text{overlap}}}{A_{\text{rotor}}} \left[k_{f,a} a^{k_{f,b}} I_{amb}^{k_{f,c}} \left(\frac{x_1}{D_r} \right)^{k_{f,d}} \right] \tag{3.3}$$

A_{overlap} denotes the area of the wake overlap with that of an upstream turbine, A_{rotor} indicates the area of the considered rotor plane and $k_{f,a}, k_{f,b}, k_{f,c}$ and $k_{f,d}$ are the weight factors of the foreign turbulence influence [90]. The axial induction factor a is obtained based on C_T, as defined by Bastankah and Porté-Agel [73].

The local turbulence intensity I, is obtained by superimposing I_{amb} with the sum of the wake added TI resulting from upstream turbine wakes I_i^+. The Gaussian FLORIS model considers a sum of squares approach as outlined in Section 2.7.4. An adjustment was made to this initial formulation by Becker, since not all upstream and neighbouring turbines are considered. The formulation given by Equation 3.4 considers a number of turbines N_T, that includes all turbines within an arbitrary distance of $15D$ upstream and $2D$ in the spanwise (y) direction [90]. Despite the incomplete understanding of turbulence saturation effects in this context, this formulation has been demonstrated as a more accurate approach for calculating added turbulence intensity. This finding aligns with the experimental results by Chamorro and Porté-Agel [91], indicating that turbulence intensity generally accumulates over two to three turbine rows before reaching an equilibrium.

$$I = \sqrt{\sum_{i=0}^{N_T} \left(I_i^+\right)^2 + I_{amb}^2} \tag{3.4}$$

Similar to the turbulence intensity superposition, the wake deficit superposition is governed by a root sum squared approach, as discussed in Section 2.7.2. Calculated by this approach, an effective velocity reduction factor r_T is obtained at the rotor plane, resulting from the wake deficits caused by upstream turbine wakes. This effective reduction factor is then used to obtain the effective wind speed at the considered rotor plane. Finally, Table 3.1 gives an overview of the subcomponents of the FLORIS model, used as a basis for the wake computations in the FLORIDyn framework.

Table 3.1: Summary of the underlying steady-state Gaussian FLORIS model in the Gaussian FLORIDyn framework.

Model Subcomponent	Gaussian FLORIS Implementation	Report Section	Source
Velocity Deficit	Bastankhah and Porté-Agel	Section 2.7.5	[73]
Velocity Deficit Superposition	$u_\infty \left(1 - r_{\text{own}}\right) \underbrace{\prod_{i=1}^{n_T} \left(1 - r_i\right)}_{r_{\text{f,OP}}}$	Section 3.1.1	[81]
Wake-Added TI	$I^+ = \frac{A_{\text{overlap}}}{A_{\text{rotor}}} \left[k_{f,a} a^{k_{f,b}} I_{amb}^{k_{f,c}} \left(\frac{x_1}{D_r} \right)^{k_{f,d}} \right]$	Section 3.1.1	[90]
TI Superposition	Root Sum Squared	Section 2.7.4	[70]
Centre line Deflection	Bastankhah and Porté-Agel	Section 2.7.5	[73]

3.1.2. Heterogeneous Flow Model

To facilitate a heterogeneous flow representation in both space and time, the wind is represented by a vector ($\mathbf{u}$), rather than a scalar (u) in classical low-fidelity models. This consideration leads to the expression for the wake wind vector as shown by Equation 3.5.

$$\mathbf{u_w} = (1 - r)\mathbf{u_0} \qquad \text{with} \qquad \mathbf{u_0} = \left[u_{x0}, u_{y0}\right]^\top \tag{3.5}$$

Coordinate Systems
Because of the variable wind direction, two coordinate systems are identified: the wake coordinate system $\mathcal{K}_1$ and the world coordinate system $\mathcal{K}_0$. Physically, the $\mathcal{K}_1$ system represents a straight wake on a bent grid. The opposite is true for the world coordinate system, as Figure 3.2 indicates the curved system. In the wake coordinate system, $\mathcal{K}_1, x_1$ describes the downwind direction, y_1 the horizontal crosswind direction and z_1 the vertical crosswind direction. In this coordinate frame, the rotor centre is always located at $[0, 0, 0]^\top$. This coordinate system is not to be confused with the longitudinal (x_0), latitudinal (y_0) and vertical (z_0) world coordinate system $\mathcal{K}_0$.

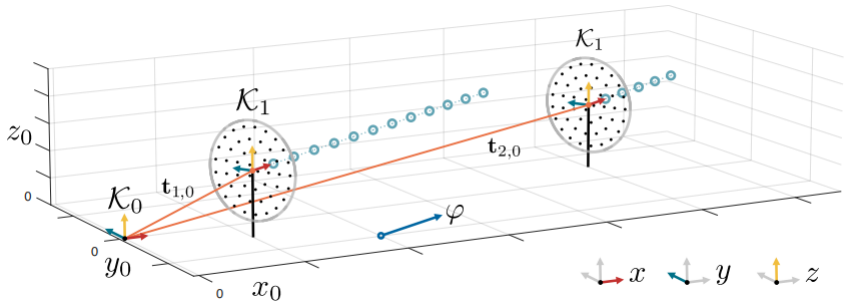

Figure 3.2: Visualisation of the world coordinate system $\mathcal{K}_0$, and two wake coordinate systems $\mathcal{K}_1$ for two considered turbines. Additionally, the downstream propagation OP chains along the wake centre line, the turbine location vectors $\mathbf{t}_{Ti,0}$ and the wind direction vector φ are displayed. Image adapted from Becker et al. [82].

A coordinate transformation to transfer between the two coordinate systems can be determined. $\mathbf{R}_{01} = \mathbf{R}(\mathbf{e}_z, \varphi)$ describes the rotational transformation around the z-axis $\mathbf{e}_z$ from $\mathcal{K}_1$ to $\mathcal{K}_0$ based on the wind direction φ. Any location vector $\mathbf{r}_1$ can be transformed using $\mathbf{r}_0 = \mathbf{R}_{01}(\mathbf{r}_1)\,\mathbf{r}_1$. The transformation is dependent on the location due to the (locally) changing wind direction, allowing for a heterogeneous flow field. In the coordinate system $\mathcal{K}_1$ the known wake model can be evaluated for all $\mathbf{r}_1$. The influence can then be transformed back using $\mathbf{R}_{10} = \mathbf{R}_{01}^{-1} = \mathbf{R}_{01}^\top$.

$$\mathbf{r_0} = \begin{bmatrix} x_0 \\ y_0 \\ z_0 \end{bmatrix} = \mathbf{t_0} + \mathbf{R}_{01}(\varphi)\mathbf{r_1} = \begin{bmatrix} x_{0,\,\mathrm{T}} \\ y_{0,\,\mathrm{T}} \\ z_{0,\,\mathrm{T}} \end{bmatrix} + \begin{bmatrix} \cos\varphi & -\sin\varphi & 0 \\ \sin\varphi & \cos\varphi & 0 \\ 0 & 0 & 1 \end{bmatrix} \begin{bmatrix} x_1 \\ y_1 \\ z_1 \end{bmatrix} \tag{3.6}$$

Here, $\mathbf{r_1}$ is the position vector in $\mathcal{K}_1$, $\mathbf{t_0}$ is the turbine location and $\mathbf{r_0}$ is the position vector in $\mathcal{K}_0$.

Spatial Heterogeneity
Spatial heterogeneous wind conditions are incorporated in the FLORIDyn framework based on the work by Farrell et al. [90]. The essential assumption to incorporate heterogeneity is that knowledge about wind field variables is available at specified locations within the computational domain, represented by OPs in the FLORIDyn framework. These assumptions can be represented either by assumed wind speed and direction gradients, turbulence intensity, or results from measurement data. Within the FLORIDyn analysis, these convecting OPs represent the wind field at discrete, irregular grid locations. Due to this representation of the wind field, the wind field across the entire considered domain is obtained from an interpolation approach.

These wind field measurements stored in OPs allow for the creation of a numerical grid, on which variable interpolation is possible. As interpolation can be computationally inefficient, the more desirable nearest-neighbour interpolation (NNI) is considered at every time step. For points outside the generated mesh, a nearest neighbour extrapolation is considered. Finally, the sparse measurements m are required to be mapped to a denser grid m_g in order to get a sufficient resolution [82]. As this is a static relation, the NNI operation becomes a simple matrix multiplication, shown by Equation 3.7.

$$\mathbf{m}_\mathrm{g} = \mathbf{M}\mathbf{m} \tag{3.7}$$

Where $\mathbf{M}$ is the mapping matrix, $\mathbf{m}$ represent the original sparse grid measurements, and $\mathbf{m}_{\mathrm{g}}$ represents NNI measurements. Note that $\mathbf{M}$ represents a linear interpolation, independent of measurement type. This choice enables that $\mathbf{M}$ can be used to map any measured field variable. Furthermore, the dense grid resolution is a modelling choice, and ensuring a sufficient resolution is a research topic by itself [92]. Nonetheless, this approach allows retrieving heterogeneous wind fields on a specified domain from the sparse measurements stored within the OPs.

The Gaussian wake model was initially developed under the assumption of flat terrain and homogeneous wind conditions, irrespective of atmospheric stability and complex terrain considerations. On the other hand, the heterogeneous model can implicitly model complex terrain by implementing gradients in both wind speed and direction, resulting in a larger application field and possibility to reduce uncertainties related to wind modelling. Although the effects are more significant in complex terrain, large offshore wind farms might also experience heterogeneous wind conditions, which can be included in FLORIDyn simulations.

Wind Shear
Up until this point, the presented framework only considered lateral (x_0 and y_0 directions) and time-varying values. However, the wind speed is also modelled to vary in the vertical (z_0) direction, representing wind shear. Note that only the wind speed is modelled to vary with altitude, and effects of changing wind direction (wind veer) and anisotropy in turbulence intensity are neglected. Following the power law approach by Farrell et al. [90], the vertical wind variation is defined by Equation 3.8.

$$u\left(z_0\right)=\left(\frac{z_0}{z_{0,\mathrm{m}}}\right)^{\alpha_{\mathrm{s}}} u\left(z_{0,\mathrm{m}}\right) \tag{3.8}$$

$z_{0,m}$ represents the height of the wind measurement (equal to the hub height z_h in this work) and α_s is the shear coefficient. The shear coefficient provides an approximation of the joint impact of atmospheric stability and surface roughness. It reflects unstable flow conditions with smaller values. Common values for a_s attributed to different surface roughness conditions are as follows: 0.11 over water, 0.16 over grass, 0.28 over forests, and 0.40 over cities [90].

3.1.3. Temporal Dynamics
Introducing dynamics involves the generation of OPs at the rotor plane at each time step. These OPs carry the turbine states at their creation time, essential for pseudo-steady wake calculations. Over time, they move downstream, representing air masses travelling with the wind, and their trajectory is dictated by the wake centre line. These OPs play a crucial role in describing the local FLORIS wake characteristics at their specific locations, utilising inherited turbine states to ensure accurate wake calculations.

In the most recent FLORIDyn version, a single chain of OPs exists per turbine. Therefore, only one OP per turbine is created at the rotor centre every time step, resulting in the OPs following the centre line [82]. The OPs have three different kinds of states, the first being the OP location, $\mathbf{x}_{\mathrm{OP}}$, in both K_0 and K_1 : $\mathbf{x}_{\mathrm{OP}}=\left[\mathbf{x}_{\mathrm{OP},0}, \mathbf{x}_{\mathrm{OP},1}\right]^{\top}$. The other sets consist of turbine states $\mathbf{x}_{\mathrm{T}}$ and wind field states $\mathbf{x}_{WF}$. The convection model used within the FLORIDyn framework is based on a first order Euler scheme. Therefore, the new downwind location $\mathbf{x}_{\mathrm{OP},1,\mathbf{x}}(k+1)$ depends on the old location, time step Δt, and the OP convection speed (u_{OP}). The crosswind location is described by the deflection function δ, depending on $\mathbf{x}_{\mathrm{OP},1,\mathbf{x}}(k+1), \mathbf{x}_{\mathrm{T}}$ and $\mathbf{x}_{\mathrm{WF}}$. Both the down and crosswind updated locations are described in $\mathcal{K}_1$, as displayed by Equation 3.9.

$$\begin{aligned}\mathbf{x}_{\mathrm{OP},1,x}(k+1) &= \mathbf{x}_{\mathrm{OP},1,x}(k)+u_{OP}\Delta t\\ \mathbf{x}_{\mathrm{OP},1,\mathrm{y,z}}(k+1) &= \delta\left(\mathbf{x}_{\mathrm{OP},1,\mathrm{x}}(k+1), \mathbf{x}_{\mathrm{T}}, \mathbf{x}_{\mathrm{WF}}\right)\end{aligned} \tag{3.9}$$

The updated OP location in K_0 is represented Equation 3.10, and is based on Equation 3.6. Note that the direction step ($[\mathbf{x}_{\mathrm{OP},1}(k+1)-\mathbf{x}_{\mathrm{OP},1}(k)]$) in K_1 needs to be transformed to K_0. This is visually illustrated by Figure 3.3.

$$\mathbf{x}_{\mathrm{OP},0}(k+1)=\mathbf{x}_{\mathrm{OP},0}(k)+\mathbf{R}_{01}\left(\mathrm{x}_{\varphi_{OP}}\right) \underbrace{\left[\mathbf{x}_{\mathrm{OP},1}(k+1)-\mathbf{x}_{\mathrm{OP},1}(k)\right]}_{\text{step in } \mathcal{K}_1}, \tag{3.10}$$

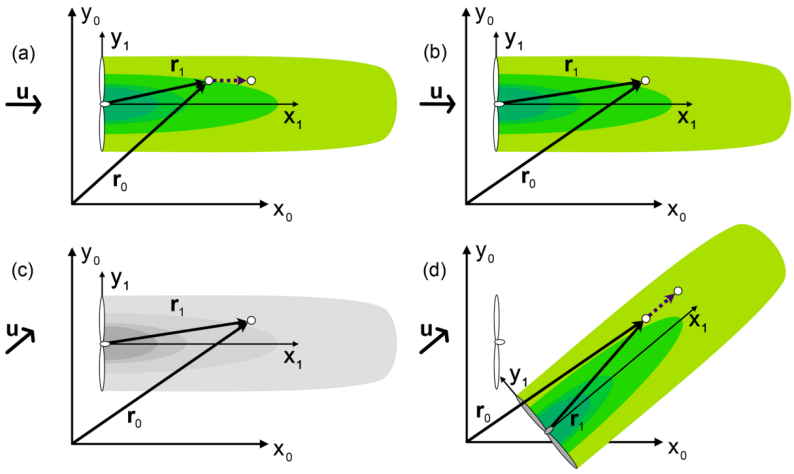

Figure 3.3: This figure illustrates the operation of Equation 3.10, applied to each OP independently. In (a → b), the figure demonstrates the position update of an OP in a time step with a constant wind direction. (c → d) displays the position update when the wind direction changes. In this scenario, the wake coordinate system undergoes rotation around the OP's location to align with the new downstream direction. This rotation causes a shift in the apparent origin of the wake in the world coordinate system, as visualised by the gray turbine [81].

Wake Influence Determination

When compared to older FLORIDyn versions, the latest centre line version considers merely a sparse amount of OPs. Although this is beneficial for computational effort, the lack of high density OPs invalidates the use of an NNI approach to calculate wake influence in the world coordinate system. Therefore, Becker et al. present an alternative method to extrapolate the wake influence on world coordinate system locations $\mathbf{I}_0$, also facilitating heterogeneous wind conditions [82].

Firstly, the two closest OPs per turbine OP chain to $\mathbf{I}_0$ are identified, after which an artificial closest OP* is created on the wake centre line by linear interpolation of the OP states. Next, the $\mathbf{I}_0$ vector is located in $\mathcal{K}_1$ of the considered turbine, through the inverse of rotation transformation matrix presented in Equation 3.6. The resulting $\mathbf{I}_{T_i,1}$ can be calculated for all represented wind turbines. Becker et al. then proceed to generate a temporary wind farm (TWF) to approximate intra wind farm flow at any given location [82]. By doing so, the essential heterogeneous environmental conditions are transformed into a steady-state homogeneous space, in which the Gaussian FLORIS model is evaluated, based on the OP* states. An explanation of the full mathematical framework for the generation of TWFs is given in Appendix A.

It is important to highlight that the TWF framework does not impose specific constraints regarding wake shape or merging methods [82]. With multiple turbines accommodated in a single TWF, it becomes possible to capture secondary wake steering effects. This flexibility ensures that steady-state wake models developed in future research can be tested in this dynamic and heterogeneous environment. Additionally, there's an aspect related to computational efficiency, as the computational load can be scaled by limiting the amount of included wind turbines in the generated TWFs. In cases where downstream turbines do not influence upstream turbines in the applied wake model, or when turbines are significantly distant upwind or crosswind from $\mathbf{I}_0$, they can be neglected. This enables the subdivision of an entire wind farm into numerous smaller wind farms, facilitating parallel evaluation [82].

OP Convection Speed

Becker considered three approaches for the downwind convection speed of the OPs: 1. propagation at local effective wind speed, 2. propagation with free-stream wind speed, 3. propagation with reduced free-stream wind speed, as shown by Equation 3.11.

$$1.\ u_{OP} = |\mathbf{u}_{OP,eff}| \qquad 2.\ u_{OP} = |\mathbf{u}_0| \qquad 3.\ u_{OP} = d\,|\mathbf{u}_0| \tag{3.11}$$

The initial approach to propagate OPs at their local effective wind speed ($u_{OP,eff}$, defined as the local free-stream wind speed, superimposed with the local wind speed deficits) led to a wake propagation that was too slow, when compared to LES results [88]. Additionally, it led to model issues as the OPs in slower wind wake regions transport states at a slower rate, and leads to overlapping wake parts in dynamic conditions.

In order to circumvent these issues, the second approach considers Taylor's frozen turbulence assumption: OPs propagate downstream at the free-stream wind speed [47]. It is based on the assumption that the large turbulent structures are do not change in space and time, and are transported at the average wind speed. This implementation not only solves the issue of overlapping wake regions, but also decreases the model's computational effort, since the local effective wind speed is not required to be calculated for wake propagation, except at the rotor plane.

However, due to the consideration of the free-wind speed, the waked wind region arrives too fast at downstream regions [82, 93]. In order to correct for this effect, the wake advection speed (u_{OP}) can be reduced by an empirical factor. Although this would improve the modelling representation of the dynamic wake propagation, it introduces a new empirical constant d. In the current FLORIDyn model version, this advection constant is a tunable variable, and will be considered as a calibration variable within this work. This consideration is made due to the significant influence of this parameter on the wind field and turbine state propagation.

OP State Corrections

The state correction models in FLORIDyn essentially dictate how the OPs within a single wake chain interact. There are four implemented models in the current FLORIDyn version, with varying complexity and assumptions. In general, there are two main considerations: propagating 'raw' wind states, or propagating 'smoothed' wind states. Both propagation philosophies have two implementations. For the first one, there are the 'Basic' and 'Maximum' models. The latter consideration has the 'Averaged' and 'Weighted' models. Functional descriptions for each of these models are provided in Table 3.2.

Table 3.2: Overview of the available state correction models within FLORIDyn.

State Correction Model	Description
Basic	OP locations and states are updated based on their wind speed, without interaction with foreign OPs.
Maximum	Generally, OPs are updated independently, based on their local wind speed and states. In case of OPs overtaking (due to changing freestream wind conditions), the slower OP (older OP) states are overwritten by those of the faster one that overtakes it.
Averaged	OP states are updated based on interaction with foreign OPs: the new states are weighted averages between current and foreign OPs.
Weighted	Similar to the 'Averaged', but different weights assigned to down- and crosswind directions, and an added time decay factor to consider in the state updates.

Whereas the 'Basic' and 'Maximum' approaches are able to propagate turbulence through the wind farm without considering interactions between OPs, the averaging operation for the 'Averaged' and 'Weighted' approaches essentially smoothen out the turbulent wind input. Since the research in this work is primarily focused on time-averaged power statistics, and less on instantaneous turbulence or loads, the 'Basic' and 'Maximum' settings will not be considered. Additionally, the 'Maximum' interaction setting would lead to a significant model bias towards higher wind speeds, especially on deep array turbine locations. Next, the 'Averaged' setting is preferred over 'Weighted' due to the additional computational expense related to the latter setting. This is especially important for the large number of simulations required for both the required simulations for AEP prediction, and the model calibration procedure, as will be detailed in Section 3.3 and Chapter 4 respectively. Therefore, the results presented in the remainder of this work will be based on the 'Averaged' implementation, as it does not fully neglect interaction within the wind field, and omits the issue of overtaking OPs.

3.1.4. Propagation Model for Free-Stream Wind Conditions

This section will detail the submodels embedded in FLORIDyn to determine the local 'free-stream' wind conditions at any given turbine location. As mentioned in Section 3.1.3, FLORIDyn uses the OPs to store and propagate both wind field, and wake influence information. To propagate upstream wind conditions, the current FLORIDyn model accommodates three settings to model the downstream propagation of time-varying wind conditions based on the convection of OPs, listed from lowest to highest complexity: none, all, and influence. Note that different settings can be specified to model the downstream propagation of wind speed, wind direction and TI within the same simulation run. Effectively, the three different settings differ in how or if the local wind conditions at the considered turbine are altered by surrounding foreign OPs. Functional descriptions are provided by Table 3.3.

Table 3.3: Overview of the available free-stream wind condition propagation models within FLORIDyn.

Free-Stream Wind Propagation Model	Description
None	The local wind conditions at any turbine are considered from the initialisation, effectively indicating no convection of free-stream wind conditions.
All	The local wind conditions are changed for all turbines on the modelled wind farm at once. A prescribed time series for wind direction thus effects the entire wind farm at once. Such events could be attributed to the passing of a weather front or large gust.
Influence	Local wind conditions at a turbine location are determined by the identified influencing OPs. Hence, the information about the wind field captured by the convecting OPs is used as local wind conditions on downstream turbines.

Out of the three submodels for the convection of free-stream wind conditions, only one actually convects the wind field states. The 'None' setting considers only the initialised wind conditions per turbine, and will not be used in this work, as it does not update local wind conditions from convecting OPs. Next, the 'All' effectively instantly propagates a change in wind conditions along the entire farm, however, the wake states captured by the OPs are convecting downstream. This setting thus implements a decoupled convection between free-stream wind conditions and the wake velocity deficits and added TI from upstream turbines. Finally, all the states captured by the OPs are convecting and affecting downstream turbines at the same instant for the 'Influence' setting. In other words, the wake states and local unaffected wind states convect simultaneously, and act simultaneously on downstream turbines.

As the interest in this work lies in the ability to model the encountered timescales on the downstream propagation of wind conditions, the 'Influence' setting is the preferred choice. This setting does bring some additional complexity and computational cost compared to the other settings. More specifically, the FLORIDyn model would need to enclose an identification procedure to determine the OPs that influence the local turbine conditions. Additionally, a given simulation would need to deal with a start-up transient due to the timescale related to the convection of an OP along the dimension of the wind farm.

Determination of Influencing Turbines

Becker's original FLORIDyn model considers a single search area to determine both the influencing OPs to compute the local wind speed reduction factors, and to determine the free-stream wind conditions when using the 'Influence' setting. Although this approach is valid when considering either the 'None' or 'All' convection settings, it is not effective for the 'Influence' setting, as will be discussed in this section.

Ideally, a large search area should be considered to determine the turbine wakes that influence the local wind speed deficit and TI values. Especially when considering that FLORIDyn models the wake effects by using a single OP per time step, located at the wake centre line, the edges of a modelled wake can be distant from this point due to wake expansion. Hence, on a large-scale wind farm, a turbine located in a deep-array location might be affected by the wake of an upstream turbine, without being in proximity to the wake centre line.

On the other hand, enforcing a large search area implicitly counters FLORIDyn's capability to model heterogeneous wind inputs. Since the OPs detected in this search area will all contribute to affect the

local wind conditions, spatial gradients will be removed due to the averaging operator. Additionally, the convection model might be skewed since OPs that are far upstream can be considered to locally influence wind conditions, although convection of those OPs have not yet reached the downstream turbine location.

In order to omit these issues, this work introduced two separate search areas to determine OPs that influence the foreign reduction on the local wind speed, and those that will determine the local wind when using the 'Influence' setting. These search areas are illustrated by Figure 3.4.

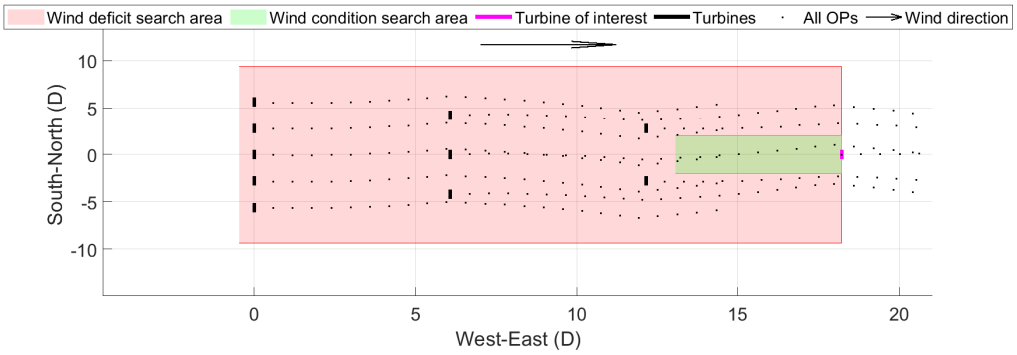

Figure 3.4: Illustrative example of the implemented strategy to separate the identification of OPs determining local wind conditions and OPs influencing the local wind speed deficit.

In the example displayed by Figure 3.4, the search area to identify the OPs influencing the local wind speed deficit spans the entire wind farm width in the upstream region. The OPs in the green search area are eligible to influence the local unaffected wind conditions at a considered turbine. The bounds for this region have been set to a cross-wind distance of 1.5 turbine diameters (total width of 3 turbine diameters), and an upstream distance of 5 diameters within this work.

Start-up Transient

A start-up transient is present in the FLORIDyn model evaluations due to the flow initialisation. More specifically, a FLORIDyn simulation is initialised based on the steady-state wind field at the first time stamp. Consistent with the timescales related to the convection of these OPs, the FLORIDyn model convects these initial states, leading to the transient start-up behaviour. Note that this transient time differs per turbine, and is based on the distance from any given turbine to its aligned most upstream turbine. The first effective model results can thus only be considered once the first OP of the most upstream turbine in the farm has passed the given downstream turbine.

As an initial approach, and for simplicity, a single start-up transient time per simulation is considered in this work, equal for all turbines. Given a mean wind speed, direction and the numerical value for the model constant d. The adjusted FLORIDyn model includes a functionality to estimate and filter out this start-up transient. As a result, the FLORIDyn model outputs can directly be used for processing and comparison purposes.

3.1.5. Thrust and Power Calculation

With the end goal of assessing AEP, it is crucial to understand how the power output of any given turbine is calculated. After applying the wake model to estimate the wake regions, and thus local u_{eff}, the power output for each individual turbine in the wind farm is calculated by Equation 3.12.

$$P = \frac{1}{2}\rho u_{eff}^3 \pi \left(\frac{D_r}{2}\right)^2 C_P\left(u_{eff}, \gamma\right) \tag{3.12}$$

Note that $C_P\left(u_{eff}, \gamma\right)$ is dependent on the yaw angle (γ) and the effective wind speed (u_{eff}). This definition of the power coefficient is dependent on the choice of rotor representation model. In this work, a C_P-C_T lookup table is intended to be used, to directly implement turbine specific thrust and power curves. Therefore, the presented computation differs from the one originally presented by Becker et al. [81, 82], as they proposed to obtain C_P and C_T based on a general actuator disc methodology, indicated by Equation 3.13.

$$\begin{aligned} C_{\mathrm{T}} &= 4a(1-a) \\ C_{\mathrm{P}} &= 4a(1-a)^2 \eta \cos\left(\gamma^{p_P}\right) \end{aligned} \tag{3.13}$$

In Equation 3.13, both C_T and C_P are dependent on the axial induction factor (a). Additionally, C_P is corrected by $\eta \cos^{p_P}(\gamma)$, with η indicating an efficiency factor, and p_P a correction factor applied on $\cos\gamma$ to account for turbine conditions in yaw misalignment.

As mentioned before, this original definition for C_P and C_T has been altered in this work, to facilitate the envisioned C_P-C_T lookup table rotor representation. This choice is justified since most of the equations in the Gaussian FLORIS model are directly dependent on C_T [81], and because of the availability of the lookup table data for steady-state turbine operations. These considerations lead to the ability to interpolate both C_T and C_P from the lookup tables provided as input to the FLORIDyn model, thus omitting the dependency on a:

$$\begin{aligned} C_{\mathrm{T}} &= C_{\mathrm{T,LUT}}\left(u_{eff}\right) \\ C_{\mathrm{P}} &= C_{\mathrm{P,LUT}}\left(u_{eff}\right) \eta \cos^{p_P}(\gamma) \end{aligned} \tag{3.14}$$

3.1.6. Wake-Added TI Weight Influence ($A_{\mathbf{overlap}}$ /$A_{\mathbf{rotor}}$)

The final subcomponent of FLORIDyn to be discussed is the determination of the wake-added TI per coordinate point or set of discretised rotor points. The general mathematical operation is displayed by Equation 3.15, indicating the computation of A_{overlap} /A_{rotor} in Equation 3.3.

$$\mathrm{TI}^{+} = \mathbf{TI}^{+}_{\mathbf{local}} \cdot \mathbf{CP_w} \left(e^{-0.5\cdot((y_{cw}-\cos(\phi_{cw})\cdot y_{\mathrm{pc}}\cdot 0.5)/(\mathrm{TI_{exp}}\cdot\sigma_y))^2} \cdot e^{-0.5\cdot((z_{cw}-\sin(\phi_{cw})\cdot z_{\mathrm{pc}}\cdot 0.5)/(\mathrm{TI_{exp}}\cdot\sigma_z))^2} \right) \tag{3.15}$$

In this equation, $\mathbf{TI}^{+}_{\mathbf{local}}$ is a row vector containing the TI^{+} values at each rotor discretisation point, and $\mathbf{CP_w}$ is a column vector representing the weight factor of each of the discretised points. Note that Equation 3.15 represents a dot product, weighted by a Gaussian function, dependent on the crosswind locations of the (discretised) coordinate point (z_{cw}, y_{cw}) and the relative angle between them (ϕ_{cw}) with respect to the influencing turbine. Next, y_{pc} and z_{pc} represent the potential core dimensions, with σ_y and σ_z representing the wake expansion rates. Note that an additional model constant $\mathrm{TI_{exp}}$ is introduced to scale the wake expansion rate parameters, and thus influence the wake width. With a smaller value indicating a narrower wake. Adversely, a larger value indicates a wider wake, with higher TI^{+} values near the wake edges. In the case where a single coordinate point is considered (thus not a discretised rotor), all parameters in Equation 3.15 are represented by scalar values. Note that the original FLORIDyn model contained an error in the computation of the TI in the wake, which is shortly discussed in Appendix B. In the updated FLORIDyn model, the effect of $\mathrm{TI_{exp}}$ on the wake regions is displayed by Figure 3.5.

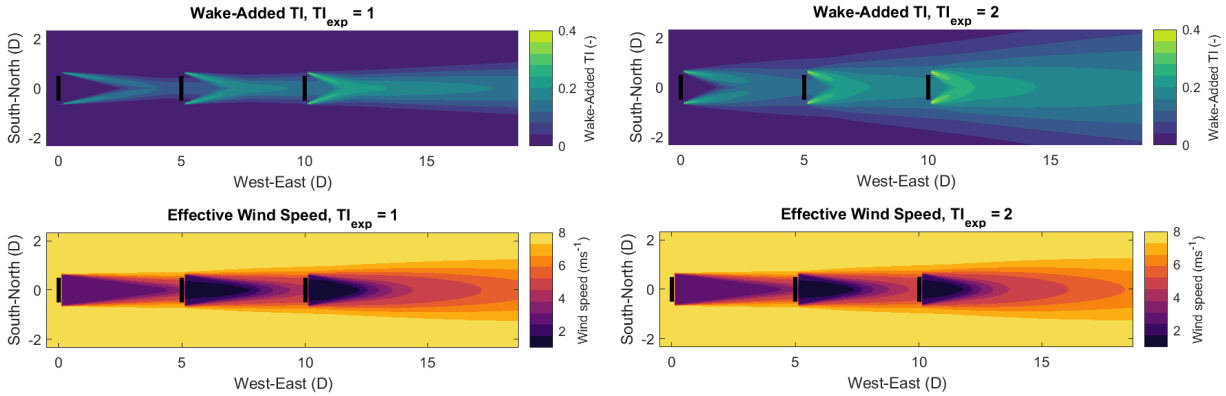

(a) Results for the baseline case $\mathrm{TI}_{exp} = 1$. **(b)** Results for the adjusted case $\mathrm{TI}_{exp} = 2$.

Figure 3.5: Illustrative example displaying the effect of altering the effective wake width parameter for wake-added TI on the effective wind speed and wake-added TI on a three turbine case with 6.1D$_r$ spacing.

Figure 3.5 clearly shows the increased region of influence for the wake-added TI, when increasing TI_{exp}. Not only has the affected region increased in size, also the TI magnitudes show increased values.

These higher TI values indicate more turbulent mixing in the model. As a result, a faster wake wind speed recovery is predicted by FLORIDyn, especially for turbines operating in conditions influenced by superimposed wakes (shown by Figure 3.5b). Within this work, the TI_{exp} will be considered to not be a tuning constant. The reasoning behind this choice is to have a consistent wake width size between the wake-added TI and velocity deficit computations. Therefore, the baseline value for TI_{exp} of 1 is considered in the remaining part of this work.

3.1.7. Overview of Empirical Model Constants

Given the inherently low-fidelity nature of the model, its accuracy is predominantly contingent on the calibration of empirical model constants. The model variables are dependent on turbine states and local wind conditions, such as C_T, γ, and I_0. In total, a set of 12 model parameters is identified, and required to be empirically calibrated. The main influences of these parameters are observed in wake recovery rate, expansion rate, the sensitivity to added turbulence levels and the influence of the yaw misalignment angle [81]. A comprehensive overview of the identified constants is given by Table 3.4, with an overview of literature suggested numerical values in Table 3.5. Note that the value for η is set to 1 due to the implementation of the turbine specific C_P LUT. Finally, TI_{exp} is also set to 1 for consistency between wake velocity deficit and wake-added TI expansion.

Table 3.4: Comprehensive overview of the empirical model constants in the FLORIDyn model [94].

Parameter	Description
α^*, β^*	Potential core length determination coefficients
k_a, k_b	Wake expansion coefficients
$k_{f,a}, \ldots, k_{f,d}$	Parameters for foreign wake turbulence effects determination
d	Wake advection speed scaling factor for temporal dynamics
TI_{exp}	Considered wake width parameter for wake added TI computations
η	Wind turbine efficiency factor
p_p	Correction factor to C_P to account for yawed turbine conditions

Table 3.5: Literature suggested numerical values for the empirical model constants. This set will be referred to as the 'Baseline' parameters

	Potential Core		Wake Expansion		Wake-Added Turbulence					Dynamics	Power	
	$\boldsymbol{\alpha^*}$	$\boldsymbol{\beta^*}$	$\mathbf{k_a}$	$\mathbf{k_b}$	$\mathbf{k_{f,a}}$	$\mathbf{k_{f,b}}$	$\mathbf{k_{f,c}}$	$\mathbf{k_{f,d}}$	TI_{exp}	$\mathbf{d}$	$\boldsymbol{\eta}$	$\mathbf{p_p}$
Value	2.32	0.154	0.38371	0.003678	0.73	0.8325	0.0325	-0.32	1	1	1	2.2
Source	[73]	[73]	[73]	[73]	[90]	[90]	[90]	[90]	[-]	[81]	[-]	[17]

Next to numerical values for the model constants, and submodel choices, the FLORIDyn framework requires two additional input types. Firstly, the wind conditions can be specified. These wind conditions comprise the following parameters: wind speed and direction, wind shear coefficient and turbulence intensity. Ideally, all should be specified as time-series to make use of the full FLORIDyn capacities, but they can also be specified as constants. Secondly, the model requires turbine data on the considered wind farm. These input turbine data comprise not only the individual turbine locations, but also the C_P-C_T LUT, that vary per turbine operational state. Next to the model constants and wind input variables, the FLORIDyn model also requires a specification of the wind turbine locations. Therefore, Section 3.2 details the wind farm that will be considered throughout the remainder of this work.

3.2. Wind Farm Description

For the analysis in this thesis project, the Sheringham Shoal offshore wind farm is selected to conduct the validation studies. The main reason for this choice, is the availability of field data, and results from a benchmarking study with two internal steady-state wake models. The wind farm is a joint venture between Equinor and the Green Investment Group, with Equinor serving as the operator, and officially commissioned in 2012. The Sheringham Shoal wind farm is located approximately 17 to 23 kilometres off

the coast of Sheringham, the United Kingdom, in the North Sea. The geographic location and surrounding wind farms are indicated by Figure 3.6a.

The wind turbines at Sheringham Shoal are organised in rows and columns, forming a grid-like pattern across the wind farm area. The rhombus shaped lay-out has a total area of approximately 35 km^2. The principal axes are located in the south-west > north-east, and north-west > south-east directions. The turbines are organised in 8 rows (8.1 diameter spacing) and 11 columns (6.8 diameter spacing) along axes parallel to the sides of the rhomboid. The minimal turbine spacing is indicated to be 6.1 rotor diameters. In total, 88 Siemens Gamesa Renewable Energy (SGRE) SWT-3.6-107 turbines are operated, resulting in a rated wind farm power output of 317 MW. The wind turbines are labelled according to a combination of a letter and a number, with a letter representing the column, and the number representing a row. Figure 3.6b displays the discussed wind farm lay-out.

(a) Geographic location of the Sheringham Shoal wind farm, and surrounding offshore wind farm [95].

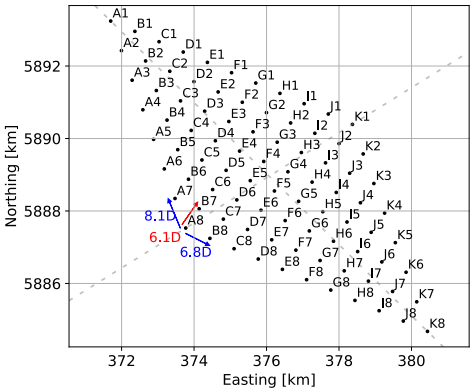

(b) Sheringham Shoal wind farm layout in a regular grid, with turbine spacing indicated by arrows.

Figure 3.6: Visual representations of the Sheringham Shoal geographical location (a) and grid layout (b).

The wind conditions at the Sheringham Shoal wind farm are indicated by a wind rose and a Weibull plot, as shown by Figure 3.7. The prevalent wind is observed to come from the west/south-west direction, i.e. a coastal wind. To conclude, a summary of the general wind farm characteristics is shown in Table 3.6.

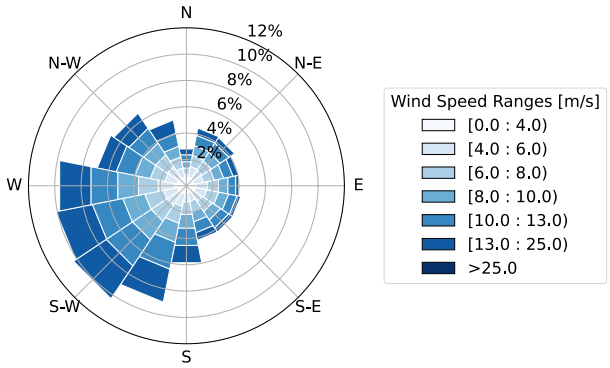

(a) Wind rose indicating a prevailing wind direction from west/south-west directions, i.e. a coastal wind.

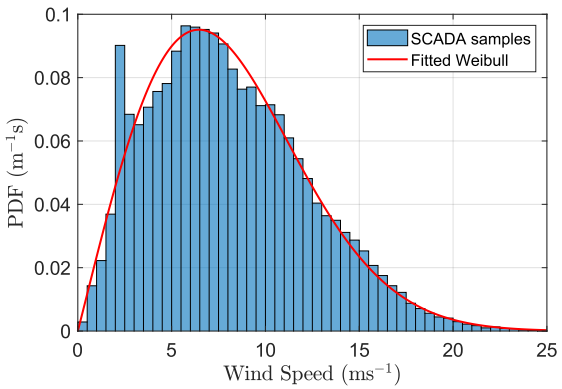

(b) Weibull plot for the Sheringham Shoal site.

Figure 3.7: Wind rose and histogram with fitted Weibull distribution indicating the wind climate on the Sheringham Shoal site location.

Table 3.6: General overview of the Sheringham Shoal wind farm characteristics.

Parameter	Value
Number of Turbines	88
Farm Rated Power	317 MW
Turbine Type	SWT-3.6-107
Turbine Rated Power	3.6 MW
Wind Farm Area	35 km^2
Distance to Shore	17−23 km
Turbine Spacing	6.1 D_r - 6.8D_r - 8.1D_r
Average TI	7.2%

3.3. Model Assessment Procedure

Given the FLORIDyn model, and the available wind farm data, this section outlines the procedure to assess and compare the FLORIDyn model with both field data from SCADA (Supervisory Control And Data Acquisition) measurements, and steady-state wake model results. A general overview of the implemented procedure is displayed by Figure 3.8. Additionally, the study's approach to compare model predictions with field data is elaborated upon, highlighting the criteria and metrics used to gauge model accuracy and reliability.

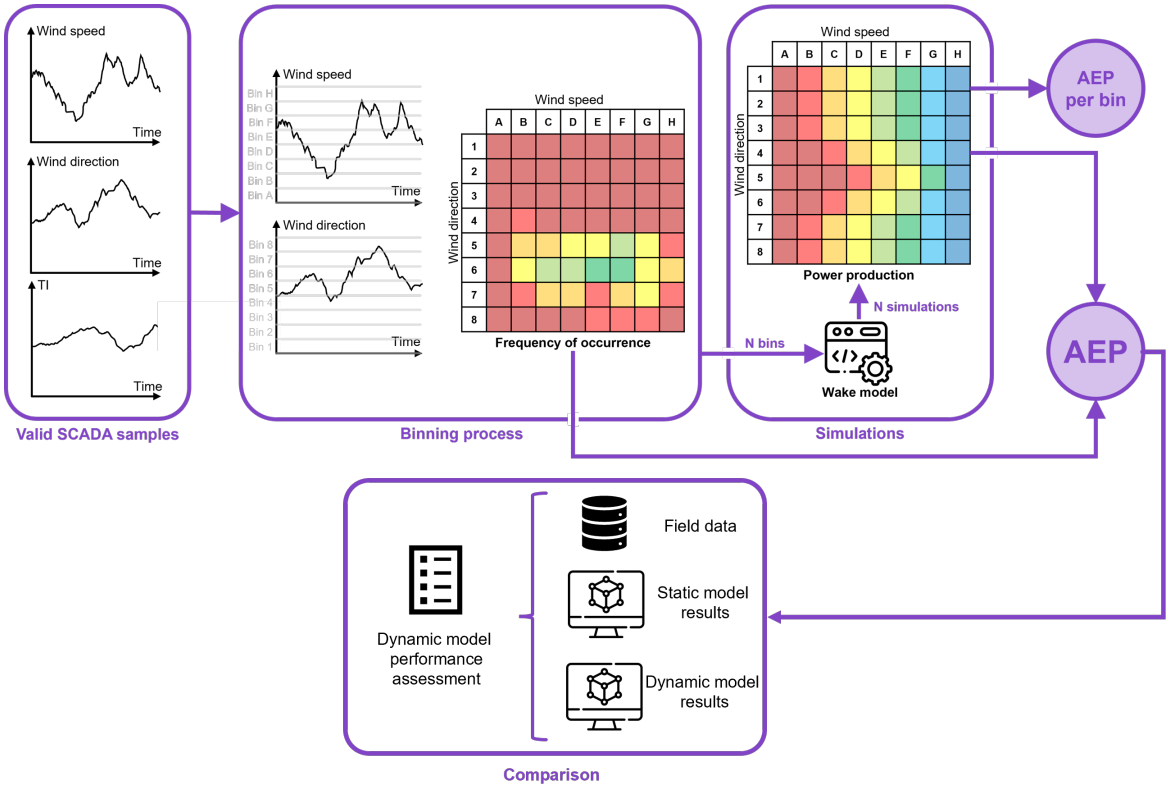

Figure 3.8: Illustrative overview of the AEP computation procedure. Binned data from 10-minute statistics SCADA data serve as input for the model evaluations. These results per wind condition bins are processed into AEP and other comparative metrics to perform a comprehensive validation study.

The comparison framework in this work will consist of three levels of complexity. Firstly, the results of the steady engineering models, and the steady version of FLORIDyn will be compared and analysed. These will be considered as the baseline results to compare the obtained outcomes from dynamic FLORIDyn evaluations with. To facilitate the dynamic capabilities of the FLORIDyn model, a second AEP evaluation

will be carried out on wind fields for which the wind speed is considered constant, but with time-varying wind directions. The final level of complexity considered in this work will be a fully time-varying input for both wind speed and wind direction.

By incorporating this approach of gradually increasing the complexity of input wind conditions, assumptions related to engineering models using steady wind inputs can be checked. Adversely, the modelling assumptions that cause the largest discrepancies with field measurements could be gradually identified. Hence, the most important effects of modelling dynamic wind inputs could be identified.

For the comparative analyses conducted in this work, both a uniform wind rose (equal weighting to wind condition bins) and the actual wind rose will be used to analyse model performance. The reason for this consideration is that wind conditions with a higher relative probability of occurrence in the actual wind rose will severely affect the energy yield predictions. Conversely, a uniform wind rose allows for a straightforward comparison between different models or scenarios without the added complexity of site-specific wind patterns. By removing the variability introduced by the actual wind rose, the focus remains on the core mechanics and assumptions of the wake model. This helps in better understanding and improving the fundamental aspects of the model. Finally, it ensures that all wind directions are given equal importance, which is useful in assessing the directional sensitivity of the wake model.

The first step in the validation study is to subdivide the available SCADA dataset into binned wind conditions. These binned conditions are generated for wind speed, wind direction and TI. This is not only essential to generate the input conditions for both the steady engineering models and the FLORIDyn model, but also allows for thorough model comparison on a selection of wind conditions. An example of this data binning is given by the wind rose presented in Figure 3.7a, which shows the combined binning operation on wind speeds and directions. A more elaborated discussion on the binning process is provided in Section 5.1.

Whereas the current static wake models can directly use these binned wind statistics (speed, direction, and TI) as model input, the FLORIDyn model requires a time-series input to capture dynamic effects. Hence, Section 3.3.1 describes the developed procedure to generate wind conditions per wind bin, to be used as input for the dynamic wake model. The final step in this process is to analyse the simulation results for all the considered binned wind conditions. In order to effectively perform this evaluation, and carry out comparison studies, Section 3.3.2 defines a set of comparison measures to represent the model predictions.

3.3.1. Generation of Synthetic Wind Conditions

In order to perform AEP studies, adequate and site specific input wind conditions should be generated to initialise the simulation runs. Given the dynamic nature of the FLORIDyn model, a time varying wind field should be considered for the model evaluations.

Opposite to steady-state wake models, where the binned wind speeds and directions could immediately be used as model input, the FLORIDyn inputs require more modelling to account for the dynamically changing wind conditions. Therefore, the Mann turbulence model will be used to generate turbulent input wind conditions, per binned wind speed and direction combination. The Mann box is an industry-standard methodology to generate 3D synthetic turbulent wind conditions, and is based on a spectral description of turbulence [44]. The Mann-model enables the synthetic generation of the three velocity components in 3D Fourier space, implicitly modelling the coherences between all components. The Mann turbulence box is generated on a specified numerical grid, with dimensions L_x, L_y, L_z, and corresponding number of grid points N_x, N_y, N_z. These parameters allow deriving the encountered wavenumbers k_i, essential for the spectral evaluation. For a velocity field with homogeneous statistics, the velocity components in Fourier space ($\hat{u}(\vec{k})$) are described by Equation 3.16.

$$\hat{u}(\vec{k}) = \frac{1}{\sqrt{2\pi}^3} \iiint_{-\infty}^{\infty} \vec{u}'(\vec{x}) \mathrm{e}^{-\mathrm{i}\vec{k}\cdot\vec{x}} \, \mathrm{d}^3x \tag{3.16}$$

$\vec{k}$ represents the wavenumber vector, $\vec{u}'(\vec{x})$ is the velocity fluctuation field in physical space ($\vec{x}$), and i represents the imaginary unit. Given the assumptions of homogeneity and incompressible flow, the 3D velocity covariance tensor, indicated by Equation 3.17, is only a function of the separation variable $\vec{r}$.

$$R_{ij}(r) = \langle u_i(x) u_j(x+r) \rangle \tag{3.17}$$

Note that the operator $\langle\ \rangle$ denotes ensemble averaging. The covariance tensor in 3D implies that the diagonal elements are $\sigma_u^2, \sigma_v^2, \sigma_w^2$ when $\mathbf{r} = 0$. Conversely, $R_{ij} = 0$ for $|\mathbf{r}| \to \infty$, that velocity components are uncorrelated when the spatial separation $\vec{r}$ becomes large. From this covariance tensor, a spectral velocity tensor $\left(\Phi_{ij}(\vec{k})\right)$ is derived through its Fourier transfer:

$$\Phi_{ij}(\vec{k}) = \frac{1}{(2\pi)^3} \iiint R_{ij}(r) \mathrm{e}^{-i\vec{k}\cdot\vec{r}}\ \mathrm{d}\vec{r}, \tag{3.18}$$

where $\vec{k} = (k_x, k_y, k_z)$ represents the wavenumber vector. For the case where no shear, and thus spatial isotropic properties are assumed, this spectral tensor in Equation 3.18 is represented by Equation 3.19.

$$\Phi_{ij}(k) = \frac{E(k)}{4\pi k^4} \left(\delta_{ij} k^2 - k_i k_j\right) \tag{3.19}$$

Note that $k = |\vec{k}|$. Von Kármán suggested the following form of the energy spectrum ($E(k)$) spectrum, indicated by Equation 3.20 [96].

$$E(k) = \alpha \varepsilon^{\frac{2}{3}} L^{\frac{11}{3}} \frac{k^4}{\left(1/L^2 + k^2\right)^{\frac{17}{6}}} \tag{3.20}$$

ε represents the rate of viscous dissipation of the turbulent kinetic energy, and L is the integral length scale that depends on large scale phenomena, and represents the distance for which the flow field is spatially uncorrelated. α is an empirical constant with an approximate value of 1.7. Finally, $\left(1/L^2 + k^2\right)^{-17/6}$ ensures that Kolmogorov's -5/3 spectrum is asymptotically matched for $k \longrightarrow \infty$. Substituting the expression in Equation 3.20 back in Equation 3.19 leads to the von Kármán spectral velocity tensor:

$$\Phi_{\mathrm{vK}}(\vec{k}) = \frac{\alpha \varepsilon^{2/3} L^{\frac{11}{3}}/4\pi}{\left(1/L^2 + k^2\right)^{17/6}} \begin{pmatrix} k_y^2 + k_z^2 & -k_x k_y & -k_x k_z \\ -k_x k_y & k_x^2 + k_z^2 & -k_y k_z \\ -k_x k_z & -k_y k_z & k_x^2 + k_y^2 \end{pmatrix} = \frac{\alpha \varepsilon^{2/3} \left(k^2 I_3 - \vec{k}\vec{k}^T\right)}{4\pi \left(1/L^2 + k^2\right)^{17/6}} \tag{3.21}$$

By introducing a random phase spectrum $\left(\mathrm{e}^{\mathrm{i}\varphi_x(\vec{k})}, \mathrm{e}^{\mathrm{i}\varphi_y(\vec{k})}, \mathrm{e}^{\mathrm{i}\varphi_z(\vec{k})}\right)^T$, a full 3D turbulent velocity field in physical space is obtained by performing an inverse Fourier transfer, indicated by Equation 3.22.

$$\vec{u}'(\vec{x}) = \frac{1}{\sqrt{2\pi^3}} \iiint_{-\infty}^{\infty} [\Phi(\vec{k})]^{1/2} \begin{pmatrix} \mathrm{e}^{\mathrm{i}\varphi_x(\vec{k})} \\ \mathrm{e}^{\mathrm{i}\varphi_y(\vec{k})} \\ \mathrm{e}^{\mathrm{i}\varphi_z(\vec{k})} \end{pmatrix} \mathrm{e}^{\mathrm{i}\vec{k}\cdot\vec{x}}\ \mathrm{d}^3 k \tag{3.22}$$

Within the scope of this work, essentially a 2D version of the Mann model is to be derived. Since the vertical velocity component (w) is not modelled within the FLORIDyn model, it is solely represented by a numerical value for the shear component. The lateral velocity components (u, v) on the other hand will be used to generate the wind speed and wind direction inputs for the FLORIDyn model evaluations.

Therefore, the wavenumbers in the vertical dimension can be neglected, reducing the von Kármán tensor to a 2×2 matrix. Additionally, the analytical exponent to match Kolmogorov's -5/3 spectrum should be adjusted to 14/3. This is required since there is no longer an integration over a spherical shell to obtain $E(k)$, but an integration over a 2D circular element, and thus reducing the dimension. Finally, the $\alpha \varepsilon^{2/3} L^{\frac{11}{3}}/4\pi$ term is dropped since the target turbulence standard deviation value is set by the TI and mean wind speed input, as will be detailed later in this section. Implementing these considerations leads to the reduced expression for the 2D von Kármán spectral tensor, as indicated by Equation 3.23.

$$\Phi_{\mathrm{vK}}(\vec{k}) = \frac{1}{\left(1/L^2 + k^2\right)^{14/6}} \begin{pmatrix} k_y^2 & -k_x k_y \\ -k_x k_y & k_x^2 \end{pmatrix} = \frac{k^2 I_2 - \vec{k}\vec{k}^T}{\left(1/L^2 + k^2\right)^{14/6}} \tag{3.23}$$

Similar to the operation in Equation 3.22, Equation 3.24 generates a stochastic wind field along the longitudinal plane for the lateral velocity components. Note that only random phases in the z-dimension need to be generated due to the cross product operation.

$$\vec{u}'(\vec{x}) = \frac{1}{\sqrt{2\pi}^2} \iint_{-\infty}^{\infty} \left[\frac{1}{\left(1/L^2 + k^2\right)^{14/6}} \right]^{1/2} \mathrm{i}\vec{k} \times \begin{pmatrix} 0 \\ 0 \\ \mathrm{e}^{\mathrm{i}\varphi_z(\vec{k})} \end{pmatrix} \mathrm{e}^{\mathrm{i}\vec{k}\cdot\vec{x}} \, \mathrm{d}^2 k \tag{3.24}$$

The result of this procedure is a generated 2D plane containing u, v velocity components. Since the FLORIDyn model requires a time-dependent input, the resulting Mann turbulence field needs to be transferred to the time domain. Similar to the approach discussed in Section 2.6.1, Taylor's frozen turbulence hypothesis is considered. Making use of a strong linearisation assumption for the transport term in the NSE, it is reduced to:

$$\frac{\partial \vec{u}}{dt} = U \frac{\partial \vec{u}}{dx} \qquad \Leftrightarrow \qquad \vec{u}(\vec{x}, t) = \vec{u}(\vec{x} - \vec{U}t) \tag{3.25}$$

Note that this is only valid when $\vec{U} \gg |\vec{U} - \vec{u}(\vec{x}, t)|$, and thus the flow is convected by the mean wind vector, with $\vec{U}$ independent of both $\vec{x}$ and t. Essentially, this assumption allows to map the physical space to time domain.

The frozen turbulence assumption also allows computing the domain size parameter L_x, required to initialise the 2D Mann model. Given the input mean wind speed $\overline{U}$, and the envisioned simulation time T_{Sim}, the domain length can be determined by Equation 3.26.

$$L_x = T_{\mathrm{Sim}} \cdot \overline{U} \qquad \text{and} \qquad T_{\mathrm{FLORIDyn}} = T_{\mathrm{startup}} + T_{\mathrm{Sim}} \tag{3.26}$$

The number of spatial discretisation points (N_x) can then be derived from the model update frequency (f_{FLORIDyn}): $N_x = T_{\mathrm{Sim}}/f_{\mathrm{FLORIDyn}}$. As an initial approach, the lateral dimension (L_y) and discretisation (N_y) are assumed to be equal to the properties of the longitudinal domain. Within the scope of this work, $\overline{U}$ will be obtained from the binned wind conditions. Thus, a synthetic wind generation is performed on all wind speed and direction bins.

The final input parameter to be determined is the integral length scale L. For the case of a full wind farm, the relevant turbulence time and length scales are much larger than those used for load computations on a single turbine. As this work is the first attempt to use the Mann model on a full wind farm analysis, the initial approach in selecting the integral length scale is to consider the minimum turbine spacing from Figure 3.6b. Since it is about $6\mathrm{D}_r$, it is in line with the ABL height, and deemed as a valid initial approach.

The results of the wind field generation by Equation 3.24 are not scaled, and do not correspond to the targeted TI value. Since the spectral scaling factor $\alpha\varepsilon^{2/3}L^{\frac{11}{3}}$ was omitted, the output velocity field is required to be scaled according to the desired standard deviation. For the application in this work, the scaling is based on the target variance method. This method involves simply multiplying the velocity field realisations $\vec{u}'(x, y)$ with the ratio of the standard deviation for the entire flow field (σ_{plane}) to the target standard deviation (σ_{target}). This operation is mathematically expressed by Equation 3.27.

$$\vec{\tilde{u}}'(x, y) = \frac{\sigma_{\mathrm{target}}}{\sigma_{\mathrm{plane}}} \vec{u}'(x, y) \tag{3.27}$$

In this work, σ_{target} is obtained from the binned statistical data. More specifically, by using the TI value attributed to the binned wind speed and wind direction combination, $\sigma_{\mathrm{target}} = \mathrm{TI}_{\mathrm{bin}} U_{\mathrm{bin}}$. The final signal for the wind speed is obtained by adding the scaled longitudinal velocity fluctuations to the mean

wind speed. Additionally, the wind direction is obtained by considering the angle between the scaled longitudinal and lateral velocity components. Mathematically, this is expressed by Equation 3.28. Similar to the scaling with the target standard deviation, the resulting wind speed and direction signals need to be adjusted to correspond to the target input mean properties. This operation is required since the created sample means might not be consistent. Therefore, the computed offsets from the synthetic wind generation results need to be subtracted. This process ensures that the desired mean wind speed and directions are correctly enforced on the desired simulation time.

$$U_{\text{FLORIDyn}} = \tilde{u}' + \overline{U} - \overline{\tilde{u}'} \qquad \phi_{\text{FLORIDyn}} = \overline{\phi} + \arctan\left(\frac{\tilde{v}'}{U_{\text{FLORIDyn}}}\right) - \overline{\arctan\left(\frac{\tilde{v}'}{U_{\text{FLORIDyn}}}\right)} \tag{3.28}$$

The final step in the synthetic wind generation process is to account for the T_{startup}. As the wind is only generated for the desired simulation duration T_{Sim}, the wind signals are manipulated to result in a time series spanning the full T_{FLORIDyn}. In this work, this operation is carried out by mirroring and concatenating the generated signals, until the full T_{FLORIDyn} is reached. This procedure is visualised by Figure 3.9.

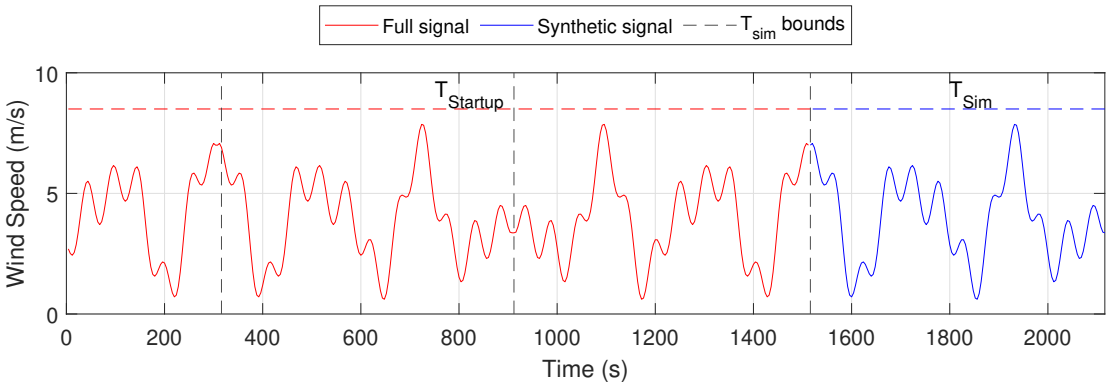

Figure 3.9: illustrative example of the mirroring and concatenation process.

As observed by from Figure 3.9, the outlined approach ensures that the desired wind properties are generated on the interesting time window retained from the simulations. However, the spectral properties of full wind signals at lower frequencies will not be consistent with Equation 3.23 due to the mirroring and concatenation operation. This is an acceptable limitation in this work, both due to the discarded T_{startup}, and since the AEP computations govern the averaged statistical properties, rather than influences of small-scale turbulence.

3.3.2. Model Comparison Metrics

In line with the research questions, the focal points of interest in the FLORIDyn model outputs are primarily the power outputs of the turbines. To assess the model's performance, this section will present two metrics derived from power output, to be evaluated at both farm and turbine levels.

3.3.2.1. AEP

Having established the framework to predict wind farm power output on a time-series basis, the next step is to extrapolate power production on these short time periods results to AEP. Analogous to the approach by Baker et al. [97], Equation 3.29 describes the procedure to extrapolate AEP from 10-minute averaged simulation results in combination with wind speed binning using a wind rose.

$$\text{AEP} = 6 \cdot \left(\sum_{k=1}^{n_{\text{wd}}} \sum_{l=1}^{n_{\text{ws}}} f_k w_{k,l} P_{k,l}\right) \cdot 8760 \frac{\text{hrs}}{\text{yr}} \tag{3.29}$$

Where, n_{wd} denotes the number of wind direction bins, n_{ws} represents the number of wind speed bins. f_k signifies the frequency of occurrence of a wind direction bin, $w_{k,l}$ represents the frequency of occurrence

of a wind speed bin, given a wind direction bin. $P_{k,l}$ indicates the collective wind farm power output for a wind speed and direction combination. Finally, 8760 represents the number of hours in a full year, with a multiplication of 6 to account for the amount of 10-minute windows in one hour.

Note that Equation 3.29 essentially expresses the energy yield as a central metric by AEP. On the other hand, the energy yield can also be expressed per wind condition bin. This information is effectively an evaluation of the model predictions weighted by the wind rose from the site conditions, and gives an insight into the most important wind direction sectors that contribute to the yearly energy yield.

3.3.2.2. Normalised Power Deficit

The normalised power deficit is a metric to indicate wake losses on wind farm level. It simply represents the wake-induced reduction of the power production relative to the gross production in the absence of wake effects [98]. The normalised power deficit or wake loss is defined by Equation 3.30.

$$\varepsilon_{\text{wake}} = 1 - \frac{P_{\text{net}}}{P_{\text{gross}}} \qquad \text{with} \qquad P_{\text{gross}} = \frac{1}{2}\rho U_{\infty}^{3}\pi\left(\frac{D}{2}\right)^{2} C_P(U_{\infty}) \tag{3.30}$$

Where P_{net} is the effective power output of a turbine (either from simulations or field data). On the other hand, the gross energy production $\mathrm{P}_{\text{gross}}$ is obtained by calculating a turbine's power output as if it was operating in free-stream conditions. Defining the gross energy production poses a significant challenge in this analysis. Within this report's framework, the power production of undisturbed turbines is obtained from the reference turbine selection, as briefly discussed in Section 5.2.

In conclusion, the wake loss is a metric that represents the power ratio of a turbine operating in its effective (potentially waked conditions) to its operation in unaffected conditions. Note that this metric can be used on both turbine and wind farm level, by simply considering the power output on the desired scale.

3.4. Research Methodology Synthesis

This chapter provided a comprehensive overview of the research methodology used to address the research questions. The chapter begins with an introduction to FLORIDyn, a quasi-dynamic engineering wake model designed to simulate the temporal propagation of wakes while maintaining computational efficiency. FLORIDyn is significant for capturing the dynamic interactions between wind turbines and the time-lagged wake effects due to changing wind conditions or control settings.

Next, the chapter described the numerical setup, detailing the wind farm layout and turbine properties used in the simulations. This setup includes the specific conditions under which the simulations were conducted, which is crucial for replicating the study and ensuring robust and obtaining relevant results.

The final section outlined the model assessment procedure, which involves comparing FLORIDyn's outputs with field data and results from steady-state wake models. The section also introduced metrics for evaluating the model's accuracy and describes the process for generating synthetic wind conditions. This comparative analysis is essential for validating FLORIDyn and identifying its limitations. In summary, the outlined uniform wind rose strategy in wake modelling applications allows for a more controlled, simplified, and generalised evaluation of the model's performance, facilitating the identification of core strengths and weaknesses that might be masked by site-specific wind patterns.

Overall, Chapter 3 provided a thorough explanation of the research methodology in this work, from the implementation of the dynamic wake model to the numerical setup and comprehensive model assessment procedure, ensuring the credibility and applicability of this study's findings. To achieve this comparison study, the next step is to determine a set of calibrated model constants for the AEP simulation runs. Accordingly, Chapter 4 describes the FLORIDyn calibration and validation framework.

4

Model Calibration and Validation Framework

The aim of this chapter is to present a framework to obtain a calibrated set of FLORIDyn empirical model constants, and validate the FLORIDyn model outputs by means of a direct comparison with real world measurements (referred to as one-to-one simulations). Firstly, Section 4.1 outlines the procedure starting from the FLORIDyn centreline model, generating a surrogate model and arriving at a set of calibrated constants. This is followed by a discussion on the calibration procedure results in Section 4.2. Next, one-to-one model evaluations are performed in Section 4.3. This is achieved by introducing model validation metrics and comparing FLORIDyn model outcomes for both the baseline (provided in Table 3.5) and tuned model constants to field data. Additionally, the uncertainty in tuned model constants is propagated through the FLORIDyn model to give an estimate of the uncertainty in model results. Finally, Section 4.4 discusses the concluding remarks on the calibration and validation framework.

4.1. Model Parameter Calibration Procedure

The calibration framework to be used within this project is based on the UQlab MATLAB package [99], and was created as an open-source, general purpose uncertainty quantification framework. The general calibration procedure to be applied in this work is outlined in Figure 4.1.

As discussed in Section 3.1, the FLORIDyn model is parameterised by several model constants that need to be tuned. Due to the considerable computational expense of the full FLORIDyn model (compared to traditional low-fidelity models), a surrogate model will be created to perform large numbers of model evaluations. This initial conversion is outlined in Section 4.1.1. Once a surrogate model has been obtained, it can be used for the sensitivity analysis, as discussed in Section 4.1.2. Depending on the observed model sensitivity to model constants, a set of variables to be tuned can be established. This tuning is performed as an inverse Bayesian calibration and is the final step in this framework, outlined by Section 4.1.3.

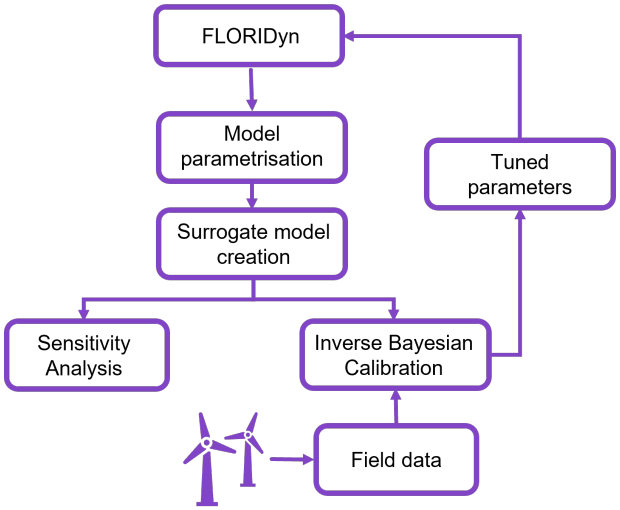

Figure 4.1: Schematic overview of the calibration framework. Image adopted from Sanderse et al. [100].

4.1.1. Polynomial Chaos Expansion Surrogate Model Creation

The primary reason to create a surrogate model for the sensitivity and calibration framework, is the required high number of FLORIDyn model evaluations, and the related computational expense. In an attempt to alleviate this, a polynomial chaos expansion (PCE) surrogate model is constructed to approximate the model predictions. This mathematically expressed as Equation 4.1.

$$Y_i(t) = \mathcal{M}\left(\theta_M, \mathcal{S}\right) \approx \mathcal{M}^{PC}\left(\theta_M, \mathcal{S}\right) \qquad \text{with} \qquad i = 1, \ldots, N_T \tag{4.1}$$

Where $Y_i(t)$ are the FLORIDyn model predictions for turbine i, and N_T is the number of turbines. θ_{M} represents a vector of model constants $(\theta_{\mathrm{M},1}, \ldots, \theta_{\mathrm{M},10})$, and $\mathcal{S}$ represents the inflow conditions. Finally, $\mathcal{M}$ and $\mathcal{M}^{PC}$ are the FLORIDyn and PCE surrogate model evaluations respectively. The latter is defined as a weighted sum of multivariate polynomials, indicated by Equation 4.2.

$$\mathcal{M}^{PC}\left(\theta_M, \mathcal{S}\right) = \sum_{\mathbf{k} \in \mathcal{K}_i} w_{\mathbf{k}} \Psi_k\left(\theta_M, \mathcal{S}\right) \tag{4.2}$$

where the Ψ_k are multivariate polynomials, and the $w_{\mathbf{k}}$ are the corresponding coefficients. The polynomial basis Ψ_k is traditionally constructed from a univariate orthonormal set of polynomials $\phi_k\left(x\right)$ for each model input parameter, and satisfy Equation 4.3. The multivariate polynomials $\Psi_k(\boldsymbol{X})$ are then assembled as the tensor product of their univariate counterparts, as shown by Equation 4.4. From the orthonormality in univariate polynomials, it follows that also the multivariate polynomial set is orthonormal [101].

$$\left\langle \phi_j\left(x\right), \phi_k\left(x\right) \right\rangle = \delta_{jk} \qquad \text{with} \qquad \delta_{jk} = \begin{cases} 0 & \mathrm{j} \neq \mathrm{k} \\ 1 & \mathrm{j} = \mathrm{k} \end{cases} \tag{4.3}$$

$$\Psi_k(\boldsymbol{x}) = \prod_{i=1}^{M} \phi_{k_i}^{(i)}\left(x_i\right) \tag{4.4}$$

Where j and k correspond to the univariate polynomial degree, δ_{jk} is the Kronecker symbol, and i represents the i^{th} model parameter. Within this work, the considered model parameters will be uniformly distributed. Given the PCE implementation in the UQlab framework, this results in a set of Legendre orthogonal polynomials to be used as univariate orthogonal basis functions [101].

The PCE coefficients w_k can be obtained by minimising the difference error between the PCE results and FLORIDyn results. Within this work, the optimisation problem is solved with the least-angle regression (LARS) algorithm [100]. The LARS algorithm in the context of PCE starts with all coefficients set to zero, and then iteratively selects polynomials based on the correlation with the current residual. After every iteration, a cross-validation error, the leave-one-out (LOO) error ϵ_{LOO} , is computed. The definition of ϵ_{LOO} is shown by Equation 4.5.

$$\epsilon_{LOO} = \frac{1}{N} \sum_{n=1}^{N} \left(\mathcal{M}\left(\theta_M^{(n)}, \mathcal{S}\right) - \mathcal{M}^{PC\setminus(n)}\left(\theta_M^{(n)}, \mathcal{S}\right) \right)^2 \tag{4.5}$$

Where N represents the total number of samples of θ_{M}, and $n = 1, \ldots, N$. $\mathcal{M}\left(\theta_M^{(n)}, \mathcal{S}\right)$ indicates the trained surrogate model by leaving the n^{th} sample out. Finally, the set of coefficients for the surrogate model that yields the smallest ϵ_{LOO} are selected as final surrogate model coefficients.

4.1.2. Model Sensitivity

Sensitivity analysis aims at finding which input parameters θ_M of the FLORIDyn model explain the uncertainties or variations in the model predictions [100]. The goal of the sensitivity analysis is to identify the most influential parameters to be considered for the calibration process. In this work, a variance-based Sobol' index approach is considered, and will be briefly described.

The Sobol' index approach is a variance-based analysis that uses a ratio of variances to indicate model sensitivity. In essence, the variation in model predictions is directly related to the variation in model constants through this approach. In this work, the Sobol' index ($S_i^\top$) for each model output (individual turbine power output per discrete time step) is given by Equation 4.6 [102].

$$S_i^\top = \frac{1}{D} \sum_{\mathbf{k} \in \mathcal{K}_i} w_{\mathbf{k}}^2 \qquad \text{with} \qquad i = 1, \ldots, N_\theta \tag{4.6}$$

Here, $\mathcal{K}$ is a set of multivariate polynomials, $w_{\mathbf{k}}$ are the PCE basis function coefficients, N_θ is the number of model constants. Finally, $D = \mathrm{Var}\left[\mathcal{M}^{\mathrm{PC}}(\theta_{\mathrm{M}})\right]$ is the variance of the PCE. A large $S_i^\top$ indicates a strong influence of model constant $\theta_{m,i}$ on the model predictions, and can be considered to be a measure of importance. For a detailed description of the procedure, the reader is referred to the UQlab documentation [103].

The benefit of this approach is that it can be performed without the need to evaluate additional model runs, as it can be directly obtained from the PCE coefficients. Furthermore, the approach is fully model-based and does not require measurement data. Finally, it inherently assumes independence of the parameters $\theta_{\mathrm{M},i}$, which might not be the case in the FLORIDyn model. Within the scope of this work, it is a valid assumption, as the goal of the sensitivity analysis is to identify the model parameters that have the most significant influence on model outputs. Therefore, the sensitivity analysis results will serve as qualitative indicators rather than a quantitative analysis.

4.1.3. Model Calibration

Based on the generated surrogate model, this work considered an inverse Bayesian approach to determine a tuned set of model parameters. Inverse Bayesian calibration is a method used to adjust the parameters of a model to fit observed data, typically by estimating the parameters that maximise the likelihood of the observed data given the model. Practically, a tuned model constant ($\hat{\theta}$) can be considered to be the maximum a posteriori (MAP) estimate, defined as $\hat{\theta}_{\mathrm{MAP}} = \arg\max_{\theta} \pi(\theta \mid y)$. Thus, it represents the point value where $\pi(\theta \mid y)$ is maximum, based on a given validation dataset y.

This procedure implies updating the prior distribution of model constants $\pi(\theta)$, given the observed validation data y to end up with the posterior parameter distributions $\pi(\theta \mid y)$ [102]. Mathematically, this operation is expressed by Equation 4.7.

$$\pi(\theta \mid y) = \frac{\mathcal{L}(\theta|y)\pi(\theta)}{Z} \qquad \text{with} \qquad Z = \int \mathcal{L}(\theta|y)\pi(\theta)d\theta \tag{4.7}$$

Where $\mathcal{L}(\theta|y)$ is the likelihood function and Z is the normalising factor, to ensure that the distribution integrates to 1 [104]. The computation of the high-dimensional integral Z in the equation is typically intractable. This can be circumvented by using Markov Chain Monte Carlo (MCMC) sampling methods, which avoid the need to compute Z [104]. This work will consider the affine invariant ensemble sampler (AIES). AIES is advantageous compared to classical MCMC methods as the algorithm is invariant to affine transformations of the target distribution, which requires little tuning and is suitable for cases where strong correlations exist between the model parameters [100].

In this work, θ represents the combined parameter $\theta = (\theta_M, \theta_E)$, accounting for a discrepancy term θ_E. This term arises due to the FLORIDyn model being a mathematical model representation of real world conditions. In essence, it represents a measurement error and model inaccuracy. This discrepancy term thus explicitly adds uncertainty to the model results, as indicated by Equation 4.8.

$$y = \mathcal{M}(\theta_M, \mathcal{S}) + \varepsilon \qquad \text{with} \qquad \varepsilon \sim \mathcal{N}(\varepsilon \mid 0, \sigma^2) \tag{4.8}$$

As indicated by Equation 4.8, this work assumes a Gaussian distributed discrepancy, with variance σ^2, and 0 mean. For this application, it is assumed to be unbiased, but for controlled environments where the model bias is a known parameter, it can be introduced as the mean of the discrepancy distribution. Additionally, σ^2 is initialised as the UQlab default value of 0.01.

When the prior distributions of the model parameters θ_M and on the discrepancy parameters θ_E are independent, the combined prior distribution $\pi(\theta)$ is defined by Equation 4.9.

$$\pi(\theta) = \pi\left(\theta_M\right)\pi\left(\theta_E\right) \tag{4.9}$$

Finally, the posterior parameter distributions obtained from Equation 4.7 are propagated through the model to obtain the probability of observing the calibrated model outputs $\hat{Y}$ based on the calibrated model parameters. The resulting posterior predictive distribution is expressed by Equation 4.10.

$$\pi(\hat{Y} \mid y) = \int \mathcal{L}(\theta; \hat{Y})\pi(\theta \mid y)d\theta \tag{4.10}$$

Where the likelihood can be computed from either the PCE model evaluations, or from the full FLORIDyn model simulations, given the posterior model constant distributions.

4.2. Calibration Framework Results

This section aims to present the outcomes of the FLORIDyn calibration framework. Firstly, Section 4.2.1 presents the data filtering and preparation operations, in order to set up the calibration runs. These operations are a crucial aspect in setting up the simulations, as data resulting from field measurements must first be cleaned to result in a dataset that can be used for comparison. Next, the results of the surrogate model creation, sensitivity analysis and calibration results will be discussed in Section 4.2.2 to Section 4.2.4 respectively. Note that the reported simulation time is recorded on an Intel Xeon Platinum 8268 CPU. To further investigate the calibration procedure and the model parameter sensitivity to tuning conditions, Section 4.2.5 discusses a repetition of the calibration procedure on multiple farm subsets. Finally, the main differences between the modelled FLORIDyn wakes obtained from the baseline model parameter values (provided in Table 3.5) and the calibrated model parameters are discussed.

4.2.1. Wind Farm Subset Selection, Data Filtering and Pre-Processing

Within this work, the FLORIDyn model calibration procedure is performed based on real-world measurement data. Therefore, the validation dataset is directly generated from operation data. Due to these real-world application, the datasets at hand can not be used directly as model input and require delicate filtering and processing. Therefore, this section outlines the steps taken to clean the dataset at hand, select a suitable set of turbines, and format the data into the required model input.

Firstly, the calibration procedure is not carried out on the full wind farm. The reason for this choice is twofold: 1. Not all turbines operate in nominal conditions at all time (perturbed validation data) 2. Performing a calibration study on the full farm introduces a large number of variables, significantly increasing computational complexity and runtime.

In order to omit some of these difficulties, a farm subset is considered. In essence, it would be beneficial to have as many aligned turbines as possible, ideally resulting in a single line of aligned turbines. However, there are two downsides to this approach. Firstly, the effects from expanding wakes caused by upstream turbines that are not directly in aligned conditions would not be captured. As a result, model parameters calibrated on this single line subset would overcompensate for the wake velocity deficit, caused by the unmodelled upstream turbines. This wake expansion and overlap is indicated by Figure 4.2 for a steady wind input to highlight the wake overlap regions and the need to choose a suitable farm subset. Secondly, the FLORIDyn model facilitates time-varying wind inputs, including direction changes. Therefore, a direction change on a single line subset could deviate from the aligned case, and with no other turbines included in the set-up, all turbines would mistakenly experience unwaked conditions.

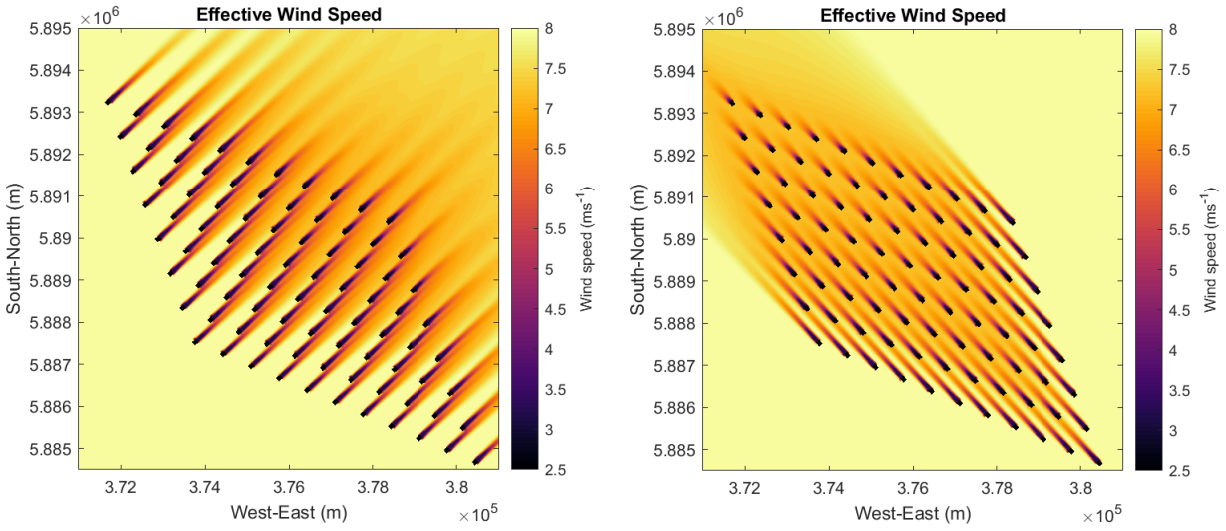

(a) Predicted flow field for an 8 m/s SW input wind. **(b)** Predicted flow field for an 8 m/s SE input wind.

Figure 4.2: Visualisation of FLORIDyn wind farm flow predictions, highlighting the overlap in wake regions at deep array locations for two cases. Especially on wind conditions for which the wind farm is observed as long and narrow, the wake overlap will significantly influence the local wind speeds in deep array locations.

Instead, a wind farm subset array consisting of 11 turbines is selected, as displayed by Figure 4.3. These 11 turbines are chosen due to the alignment with the prevailing SW wind observed in Figure 3.7a. The considered subset consists of 4 rows and 3 columns, and is able to represent the direction of minimum turbine spacing, i.e. the most severe case of turbine alignment, as indicated by the red line in Figure 4.3.

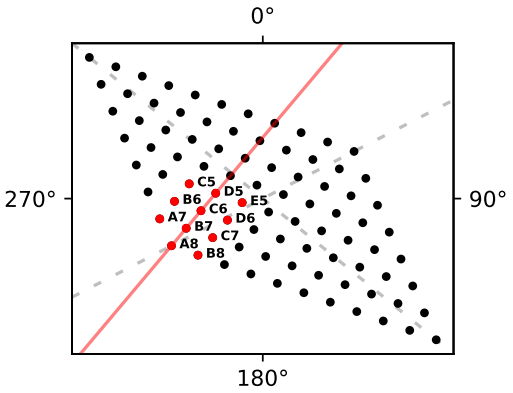

Figure 4.3: Visual representation of the wind farm subset selection, with the axis of minimum turbine spacing indicated in red.

Having established a subset of interest on the original wind farm, a valid time period should be determined to be used as a validation set, and as inflow conditions. This process is carried out based on SCADA data from January 2022 to March 2024, available as 10-minute statistics. This dataset is considered in order to identify the interesting time windows, for which higher frequency time series data can be downloaded (referred to as Fastlog data), and formatted to function as model inputs. However, determining the interested set of turbines and time period first requires adequate data filtering.

The SCADA data set is pre-processed to ensure alignment with the scenarios predicted by the wake models, where all turbines operate in nominal conditions. In order to obtain a filtered, and usable dataset, a collection of filters is applied to only retain valid data points for further analysis. This step is essential to avoid misinterpreting irregular turbine operations as losses resulting from turbine interactions. This filtering procedure is split up into three distinct operations as listed below:

1. **General filters**
   - **1.1.** Wind speed within operational range ($U_{cut-in} < U < U_{cut-out}$);
   - **1.2.** No curtailment / boosted / derated turbine operations;
   - **1.3.** No turbine outages / start-up / shutdown procedure;
   - **1.4.** No faulty or dysfunctional wind measurements;
   - **1.5.** Local outlier detection;
2. **North Calibration**
   - **2.1.** Identification of jumps in turbine wind direction signals;
   - **2.2.** Detect offsets between turbine signals;
   - **2.3.** Correct dataset by obtained direction offsets;
3. **Case specific filters**
   - **3.1.** Selection of turbines in farm subset;
   - **3.2.** Selection of wind directions;
   - **3.3.** All turbines simultaneously operate nominally;
   - **3.4.** Operation in sub-rated wind conditions;

The results of applying the general filter operations are displayed by Figure 4.4. Filters 1.1 to 1.3 ensure that all considered data points result from turbines operating in nominal conditions. Next, filter 1.4 identifies and filters out instances of dysfunctional sensors. On the analysed SCADA dataset, some sensors are reported to indicate the same value on multiple consecutive 10-minute windows. This behaviour is observed as the vertical lines in Figure 4.4a. In this specific case, the wind sensor clearly indicates a faulty value, since the power is significantly fluctuating, resulting in the vertical line appearance. Within this work, such erroneous measurement readings are identified when the standard deviation over five consecutive wind speed measurements is smaller than 0.01 ms^{-1}. The general filtering procedure is concluded by applying a local outlier filter. In this work, local bins are defined with a bin width of 0.5 ms^{-1}. Next, the local mean and standard deviation is computed on the power measurements. Finally, data points identified within a specific wind bin that do not fall within the 99.7% confidence interval $\mu \pm 3\sigma$ are filtered out. A visual representation of this local outlier filter application is provided by Figure 4.4b, resulting in the final set of retained data points in Figure 4.4c. Note that the mean power curve resulting from the data analysis differs from the reference power curve corresponding to a TI value of 7%, consistent with the mean TI of 7.2% at the Sheringham Shoal site (Table 3.6). Finally, Figure 4.4d indicates the amount of data points retained after each filter application in the general set of data filters. In total, 69.7% of the original dataset's data points are retained and available for further analysis and filtering operations.

On this generally filtered dataset, the north calibration procedure was conducted, to properly calibrate the wind direction measurements to a common reference. A brief description of this detection and correction algorithm, along with the results, is provided in Appendix C.

Once the north calibration has been applied, case specific filters are defined. Firstly, a selection of turbines of interest is made according to the targeted alignment of wind direction and turbine spacing, related to the farm layout and targeted wind direction. Next, a check is carried out on the farm subset to identify time periods on which all considered turbines simultaneously operate in a nominal regime. Subsequently, the remaining data points are filtered to operate in sub-rated wind conditions. This filter is applied due to the higher significance of wake effects on lower wind speeds (higher operating C_T) compared to rated power. Furthermore, power losses disappear above rated wind speed as power is limited to its rated value. Ultimately, one time period is selected among the identified potential cases, for which the higher frequency time-series (Fastlog) data is downloaded from the turbine system.

Although an approach using 10-minute windows is standard practice in wind energy applications, the selected time period in this work's calibration framework is selected to be 1 hour. The reason for this choice is twofold. Firstly, including larger time windows increases the available number of data points to train the surrogate model, and run the Bayesian inversion, leading to more converged results. Secondly, a one-hour window captures more distinct wind conditions present at the site, thereby encompassing greater

wind variability. Arguably, the specific selection of a one-hour window can be seen as somewhat arbitrary, but it was ultimately made to strike a balance between maximising the inclusion of data and managing memory constraints in Matlab.

The final step in the data preparation process is to ensure that the validation and input data are compatible with the FLORIDyn model. Therefore, all data was formatted according to Equation 4.11. Thus, matrices of $N_t \times N_T$ (number of time steps $\times$ number of turbines) are created for all model inputs (wind speed, direction, turbine orientation and TI), as well as for the turbine power outputs.

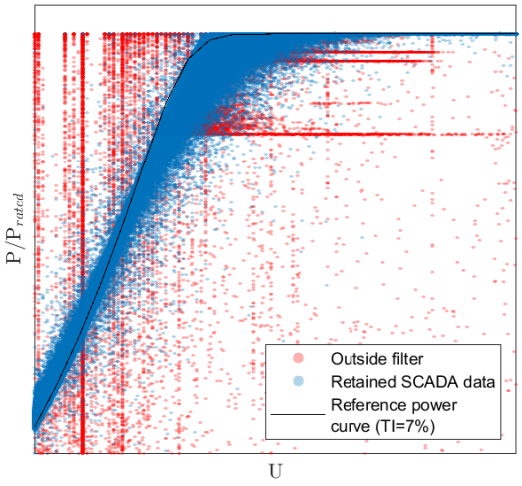

(a) Filter 1.1-1.4.

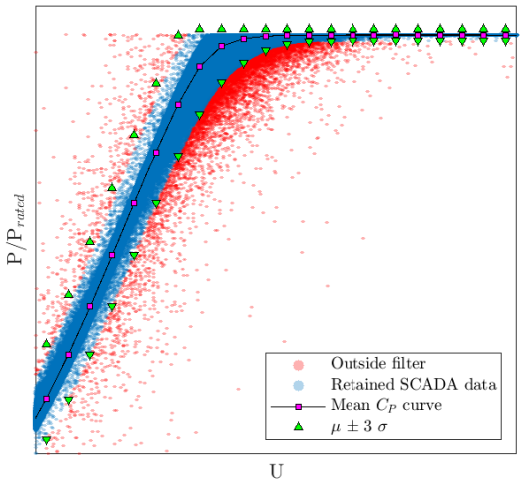

(b) Filter 1.5 (local outlier detection).

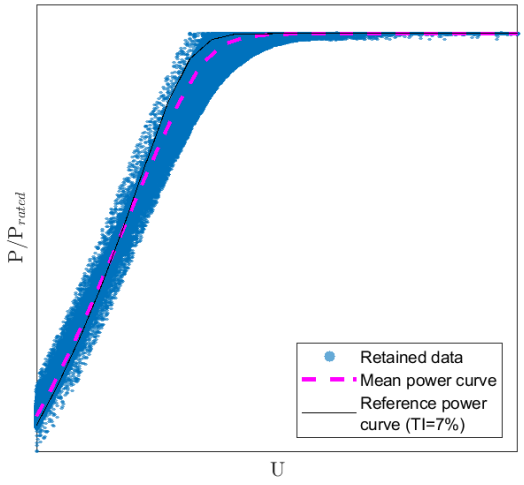

(c) Final set of retained data points.

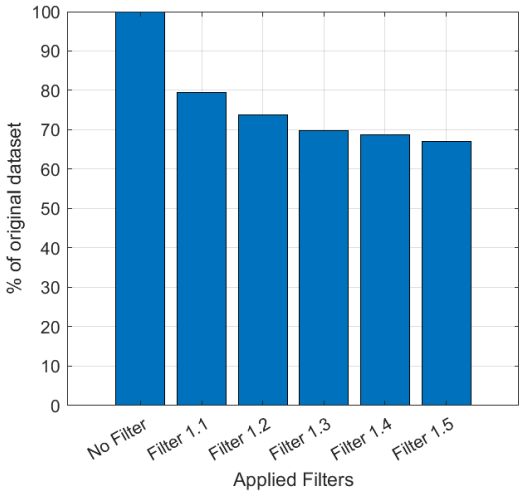

(d) Overview of amount of filtered data.

Figure 4.4: Visualisation of the applied data filtering operations on the available SCADA 10-minute statistics data set, total percentage of retained data and FLORIDyn model output data format.

$$y = \begin{pmatrix} y_1(t_1) & \cdots & y_{N_T}(t_1) \\ \vdots & & \vdots \\ y_1(t_{\text{end}}) & \cdots & y_{N_T}(t_{\text{end}}) \end{pmatrix} \tag{4.11}$$

4.2.2. Surrogate Model Creation Results

Following the theoretical foundation of the PCE surrogate model, this section evaluates its performance. The focus is on assessing the accuracy and reliability of the PCE model, specifically through the leave-one-out error metric. The LOO error provides a robust measure of predictive capability by systematically

excluding individual data points and evaluating the model's performance on the excluded data. This validation process aims to quantify the model's ability to replicate the outcomes of the full FLORIDyn model, thereby establishing its suitability for further use in this work's calibration and validation framework.

Before performing such an analysis, an input range of model parameter values must be specified as an anterior PDF. As mentioned in Section 4.1.1, the input distributions for the model parameters used in the sensitivity analysis are assumed to be uniform. The bounds for the anterior model parameter PDFs are derived from previous literature outcomes [94, 102]. The input sampling ranges are detailed in Table 4.1. Note that ten variable model parameters are set to vary, with the value of η set to one due to the definition of the C_P look-up table (LUT), and the value of TI_{exp} fixed at one to ensure a consistent wake width for both the velocity deficit and wake-added TI computations.

	Potential Core		Wake Expansion		Wake-Added Turbulence					Dynamics	Power	
	$\boldsymbol{\alpha^*}$	$\boldsymbol{\beta^*}$	$\mathbf{k_a}$	$\mathbf{k_b}$	$\mathbf{k_{f,a}}$	$\mathbf{k_{f,b}}$	$\mathbf{k_{f,c}}$	$\mathbf{k_{f,d}}$	$\mathrm{TI_{exp}}$	$\mathbf{d}$	$\boldsymbol{\eta}$	$\mathbf{p_p}$
θ_{min}	1.5	0.15	0.2	-0.005	0.05	0.05	0.05	-0.6	1	0.6	1	1.5
θ_{max}	5	0.45	1	0.005	1	1	0.6	-0.01	1	1	1	2.5

Table 4.1: Assumed uniform distribution bounds for the anterior model parameter PDFs.

Based on the specified anterior distributions, the PCE model design is obtained by using the Latin Hypercube sampling (LHS) method in the UQlab [101]. LHS is preferred over a random sampling method, as it ensures that the generated samples reflect the actual range of variability. In total, 750 FLORIDyn model evaluation are used to perform the PCE coefficient determination. Within this work, the default UQlab settings are used for the estimation, optimisation, and trend methods in determining the model coefficients. Based on these considerations, Table 4.2 indicates the total runtime for the PCE model creation, split into the FLORIDyn runs and ϵ_{LOO} assessment for coefficient determination.

Table 4.2: Runtime overview for the PCE surrogate model creation.

Subcomponent	**Runtime**
FLORIDyn runs	8 h 32 min
Coefficient determination	1 h 31 min
Total	10 h 3 min

As indicated by Table 4.2, the FLORIDyn runs take up the majority of the runtime for the surrogate model creation. Given the even larger number of required model runs for the eventual inverse Bayesian calibration, it justifies the use of a surrogate model. Next, The accuracy of the PCE model is assessed by considering the final ϵ_{LOO} in Figure 4.5, as a time-series for all turbines on the wind farm subset.

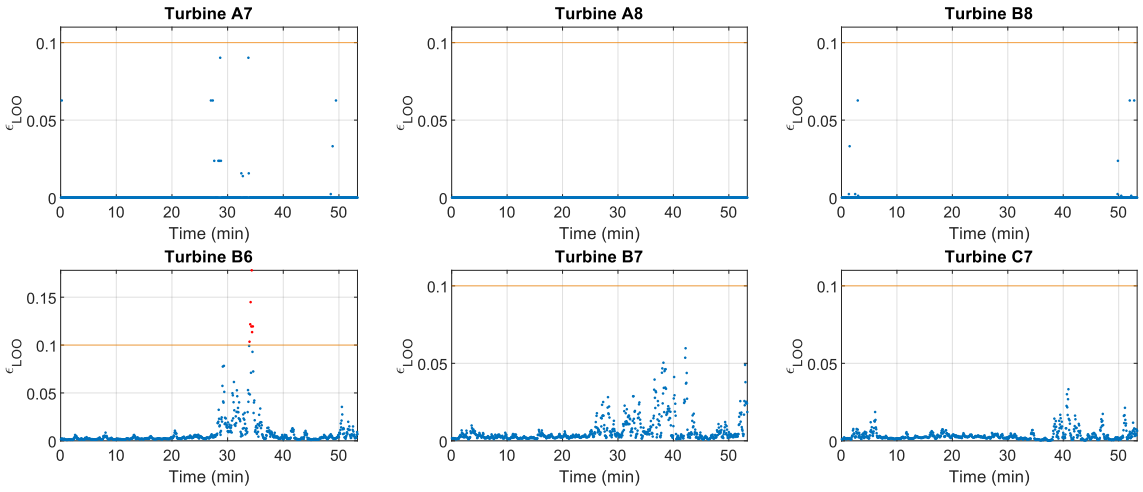

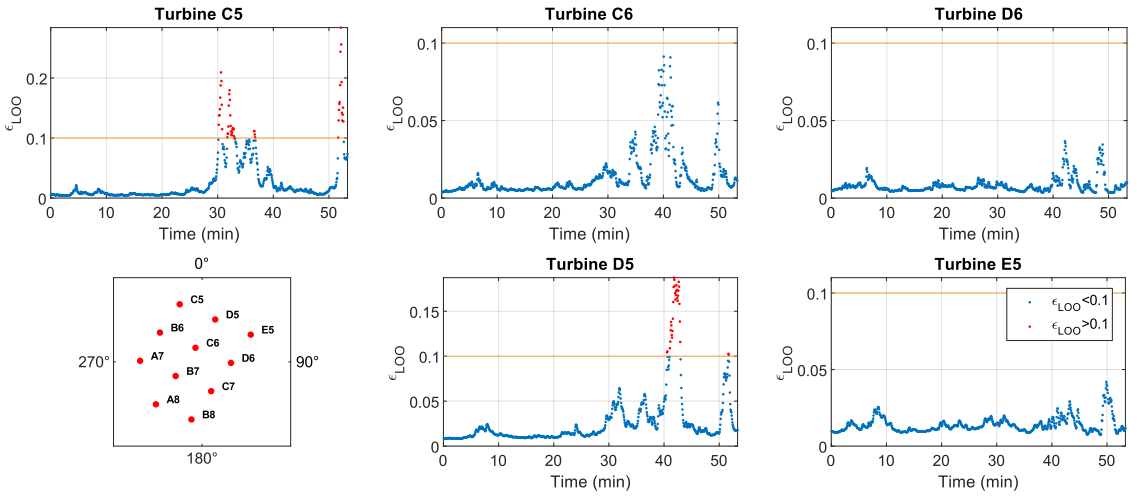

Figure 4.5: Figure displaying the PCE model ϵ_{LOO} per time step per turbine. The horizontal yellow line indicates a set acceptance threshold of 0.1.

Figure 4.5 shows that the resulting ε_{LOO} from surrogate model creation procedure are not always below the acceptance level of 0.1. Whereas the unwaked first row of turbines display ε_{LOO} below 0.1 for all time instants, the surrogate model does not display these favourable outcomes for turbines in waked conditions. However, the acceptance limit is only exceeded at specific time instants, and the majority of ε_{LOO} remain below the set acceptance limit. Essentially, a high value for ε_{LOO} indicates that the determination of the polynomial coefficients in the surrogate model creation has not fully converged yet. Due to the ε_{LOO} only taking on larger values for specific time instants, these occurrences could be hypothesised to be related to significant fluctuations in the input wind conditions, and are further investigated in Section 4.2.3.

As an additional means of verifying the surrogate model performance, a direct comparison to the full FLORIDyn model is carried out. Given the same input wind conditions, farm subset and model parameter values, Figure 4.6 displays two plots indicating the differences between the results on the full FLORIDyn model evaluation and the PCE model outcomes.

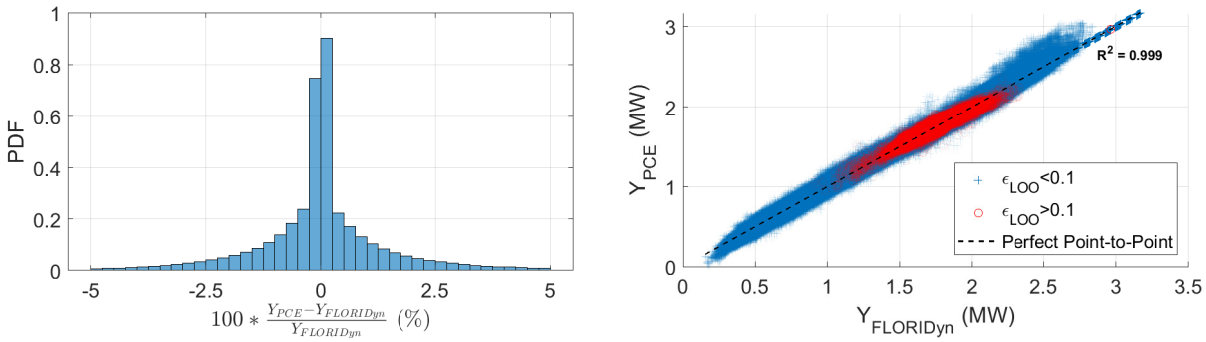

(a) Histogram plot indicating the differences between FLORIDyn and PCE power predictions.

(b) Point to point model output comparison between the PCE and FLORIDyn model results.

Figure 4.6: Additional error metric plots to investigate the surrogate model accuracy.

Figure 4.6a shows an error distribution with the vast majority of errors taking on values close to zero, indicating only a small systematic bias on the PCE results. Neglecting the peak at 0, mostly due to the free-stream turbines, the distribution is slightly negatively skewed, indicating an underestimation of the power production predictions compared to the full FLORIDyn model outcomes, with rare occasions of errors surpassing the 5% error mark. This is further investigated in Figure 4.6b, which indicates a direct

point-to-point comparison of the model outputs. The presented point-to-point comparison indicates a strong correlation between the two models, but also highlights a slight rotation when compared to the perfect point-to-point line. In general, the PCE model tends to overestimate power predictions when FLORIDyn predicts high power output. The opposite is true on lower FLORIDyn power predictions. Note that the red coloured markers indicate results for which $\varepsilon_{LOO} > 0.1$. Interestingly, these instances do not necessarily yield in the largest PCE model residuals. Instead, close agreement with the 0 residual line is observed.

Finally, Figure 4.6b displays an R^2 value as a final metric to assess the surrogate model performance. Since the R^2 metric represents the extent to which the independent variable can explain the variation in the dependent variable, it indicates a numerical value that quantifies how well a model predicts reference outcomes. With numerical values between 0 and 1, a value close to 1 indicates a perfect correlation between two datasets. Hence, the $R^2 = 0.999$ indicated by Figure 4.6b indicates a close match between the PCE and FLORIDyn model results.

In conclusion, while ε_{LOO} exceeds the prescribed threshold at certain simulation time steps for waked turbines, this does not significantly undermine the overall performance of the PCE model. The additional comparison metrics, including the high R^2 value, indicate that the PCE model's predictions are closely aligned with those of the full FLORIDyn model. The strong correlation shown by the R^2 underscores the model's reliability and accuracy in predicting power outcomes. These findings suggest that, despite occasional deviations, the surrogate model effectively captures the essential dynamics of the full model. Consequently, the PCE model is deemed suitable for further use in the calibration procedure. This validation supports its application in subsequent analyses, where a reliable surrogate model is essential for efficient and calibration procedure.

4.2.3. Model Sensitivity Results

Starting from the created surrogate model, the sensitivity analysis is performed using the PCE model coefficients. By decomposing the variance of the PCE model outputs, the Sobol' indices allow for a detailed understanding of the relative importance and interactions of the model parameters. This analysis is crucial for identifying key drivers of model behaviour and for guiding further model refinement and calibration efforts.

The results of the sensitivity analysis are displayed by Figure 4.7, as time dependent Sobol' indices $S_i^{\top}$. Due to the direct use of the PCE model coefficients, the sensitivity analysis only required a runtime of $\mathcal{O}(10^1)$ seconds. The results of the analysis for the 11 considered turbines are displayed in four rows and three columns, with the rows corresponding to the rows in the wind farm array. Hence, the first row corresponds to turbines in free-stream conditions, with further rows representing turbines in waked conditions. On the other hand, turbines represented in the same column are located in the direct waked area of the upstream turbine in a more upstream row.

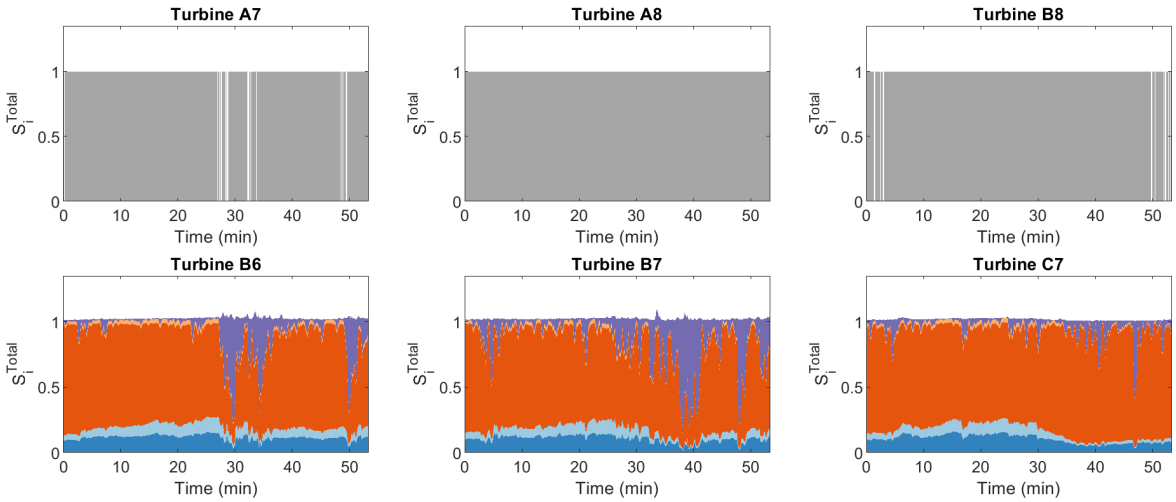

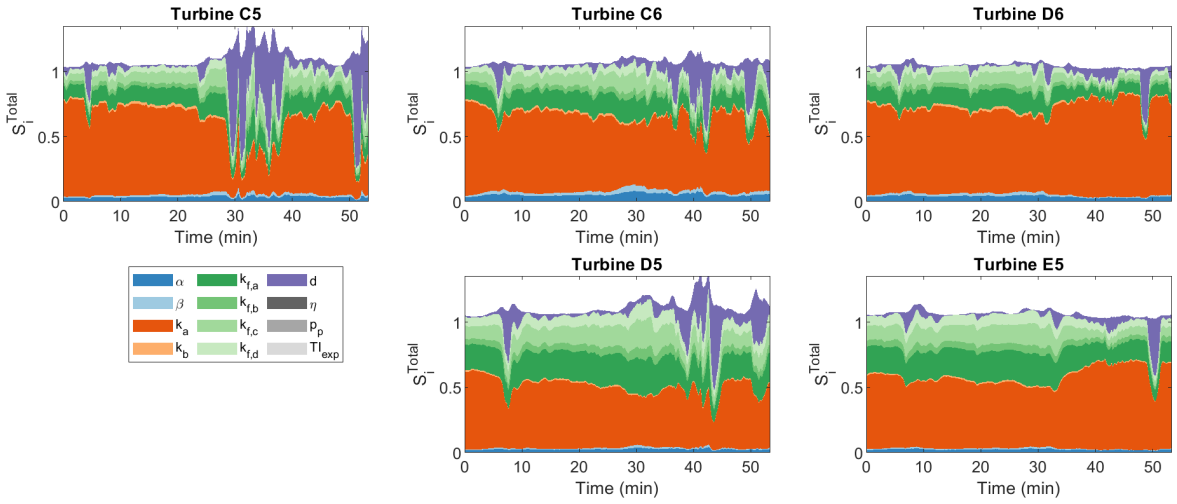

Figure 4.7: Time dependent Sobol' indices $S_i^{\top}$ indicating the relative model sensitivity to the considered model parameters.

Although Figure 4.7 displays legend entries for all twelve model parameters, only ten actually contribute to the variability in model results. This is an expected result since η and TI_{exp} were set to constant values. Additionally, the time periods of increased ε_{LOO} in Figure 4.5 are observed to coincide with time periods that show a significant dependency on the model constant related to wind dynamics. Thus, the increased ε_{LOO} values are suspected to be caused by the variability in input wind conditions. This is further confirmed by Figure 4.8, showing the wind speed and direction time-series at turbine A8.

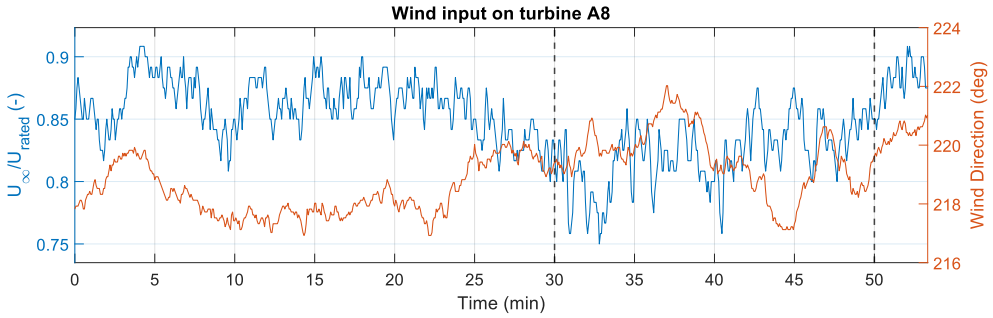

Figure 4.8: Wind speed and direction time-series on unwaked turbine A8, indicating the most significant wind changes between 30 min and 50 min.

Figure 4.8 displays the most significant changes in wind speed and direction between 30 min and 50 min. More specifically, a drop in wind speed is observed in this range, and slowly recovers. This coincides with the time periods that show the largest ε_{LOO} in Figure 4.5, and the largest activation of d in Figure 4.7. It is undesirable that these changing wind conditions cause the largest uncertainty in the PCE model, especially since the FLORIDyn model's additional value lies in its capabilities to model these dynamic effects. It is therefore important to further investigate the robustness of the implemented convection model, which will be revisited in Section 4.3.4.

The first row of turbines in Figure 4.7 (A7, A8, B8) only show a dependency on the variation in p_P. Given that η is considered as an invariant model constant, this is an expected result, since these turbines are experiencing free-stream wind conditions, and are thus not influenced by any wake effects (or any model constant affecting wake computations for that matter). Hence, the power output for these first row turbines is only affected by the yaw misalignment correction factor. Finally, when the turbines are aligned with the incoming wind, the model is observed to be insensitive to any model constants, as no correction is applied, and thus none of the considered model constants affect the power outputs.

The Sobol' indices on the second row of turbines (B6, B7, C7) show the most significant influence of the wake expansion parameter k_a, and both the potential core parameters α^* and β^*. Again, these are expected results. Given the selected inflow conditions, the second row of turbines operates in waked conditions. Hence, a sensitivity on the parameters defining this wake area and the related magnitude in wind speed reduction is expected. Occasionally, the results on this second row are dominated by the convection model constant d. As this parameter affects the propagation speed of the OPs that carry the wind and wake state information, varying this parameter will affect the time of arrival of information at downstream turbines. Interestingly, whereas the potential core and wake expansion parameters retain a relatively constant influence during the simulations, the convection parameter is relatively unimportant, except for a short bursts of time. As displayed by Figure 4.8, these simulations periods are linked with the occurrence of a significant change in the wind field, highlighting the dynamic nature of the wind inflow conditions.

The third and fourth row show the increasing importance of the parameters related to the wake-added turbulence intensity ($k_{f_a}, \ldots, k_{f_d}$). Conversely, on these rows further downstream, the model sensitivity to the potential core parameters significantly decreases. Considering the significant influence of the wake expansion parameter (k_a) on all turbine rows that experience wake effects, it is observed as the most important parameter to tune in order to yield the most accurate model predictions. Conversely, the model is observed to be most sensitive to the calibration of this wake width parameter. This is an expected observation given the influence of k_a in determining the wake width, and its implementation in the Gaussian wake deficit computations displayed by Equation 2.46 to Equation 2.49. Additionally, Equation 2.48 shows that this parameter is dependent on the ambient turbulence intensity. It is thus indirectly related to the wake added turbulence intensity computations, as well as the transport of free-stream wind conditions (free-stream TI), explaining its prevailing influence on model results along all wakes rows of turbines.

Based on the sensitivity analysis results, all considered variable model constants influence the model predictions. Therefore, the entire parameter set θ_{M} will be used for the inverse Bayesian calibration in Section 4.2.4. It should be noted that the wake reduction and added turbulence intensity superposition models also influence the sensitivity analysis results, especially on more downstream turbines. However, the significance of these superposition models can not be captured independently, as there are no parameters that define these submodels. Therefore, model sensitivity to different superposition models should be investigated in future iterations. Due to the limited time for this work, and since the calibration procedure is considered to be a mere step to the end goal of this work, it is not further investigated within this work.

4.2.4. Calibration Results

Following the findings in the sensitivity analysis, the calibration procedure is continued on the set of ten model parameters. Again, the same input anterior ranges are used for θ_M (Table 4.1). Additionally, the discrepancy parameter ε is initialised as a set constant ($\sigma^2 = 0.01$), and accounts for approximation errors between the PCE and FLORIDyn models. In this work, the discrepancy parameters are not calibrated per turbine. Based on the outcomes in Section 4.2.2, the discrepancy between the full FLORIDyn and PCE models is contained within 10%, which closely aligns with $\sigma^2 = 0.01$, and is a valid initial approach.

Based on the prior PDFs, the AIES MCMC is initialised with 100 steps and 500 parallel chains. In advance, it is not possible to provide an answer if this is sufficient to reach convergence in the posterior distributions. Therefore, the validity of these settings will be checked along with the resulting posterior PDF plots. Finally, the calibration data set is obtained from the processed Fastlog field data. The results of the inverse Bayesian calibration are displayed by Figure 4.9 as kernel density estimation (KDE) plots, which will be referred to as the posterior PDFs. For each calibrated model constant, both the prior and posterior distributions are displayed. The total computational time for the Inverse Bayesian process is computed to be 19 hours and 6 minutes.

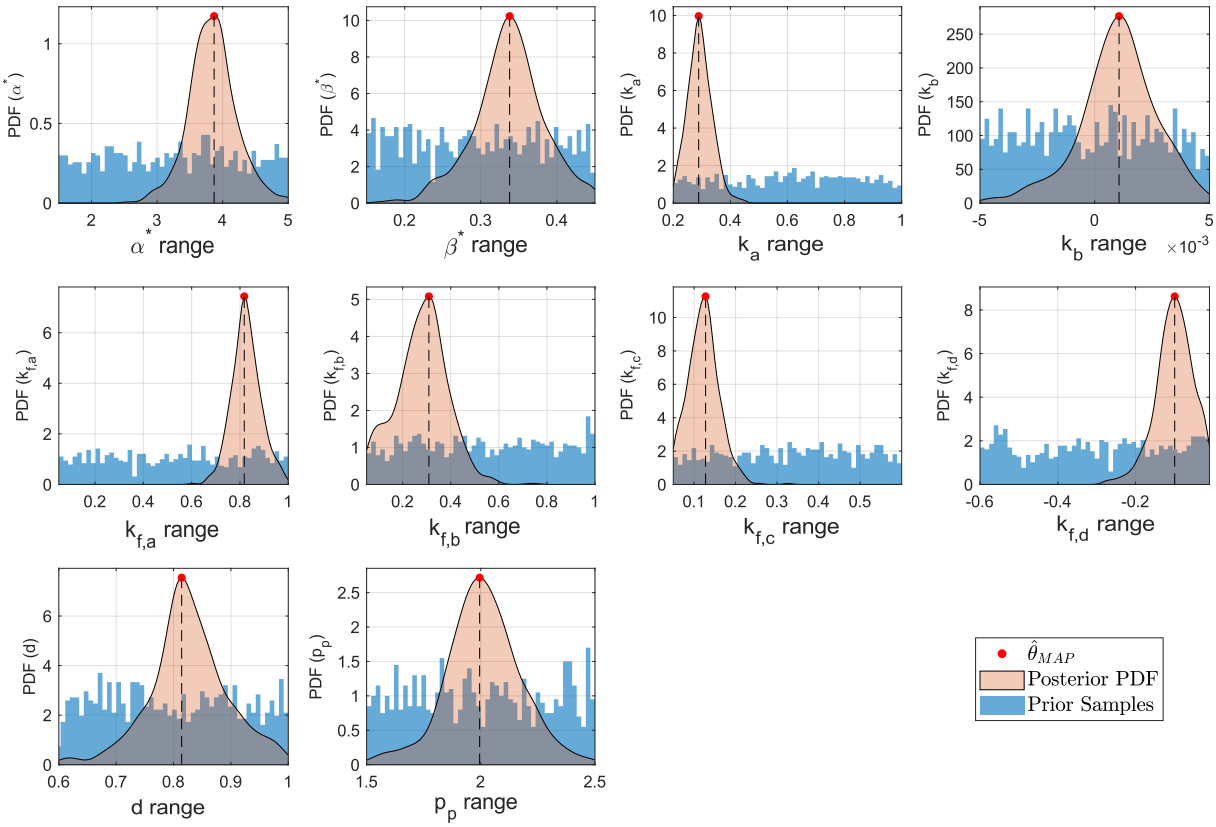

Figure 4.9: Figure illustrating the input samples and the posterior model parameter distributions, with the respective $\hat{\theta}_{MAP}$ point estimates indicated.

The calibration results illustrated by Figure 4.9 show the resulting Gaussian-like shape of the posterior distributions, based on the uniform priors. Although not all distributions are centred around the mid-value of the input range, the calibration results indicate that a convergence is obtained within the specified input range. This convergence is partly observed due to the Gaussian-like shape of the KDE plots, but additional evidence as tracer plots for the MCMC chains is provided in Appendix D. Hence, the chosen number of AIES MCMC steps and chains is sufficient to reach converged posterior PDFs for all calibrated model constants.

The benefit of this calibration procedure is that the posterior distributions essentially provides an uncertainty on the calibrated set of model parameters. Finally, Table 4.3 provides a summary of the $\hat{\theta}_{MAP}$, θ_{mean}, and $\sigma_{\theta_{mean}}$ as indicators of the provided posterior PDFs in Figure 4.9.

	Potential Core		Wake Expansion		Wake-Added Turbulence					Dynamics	Power	
	$\boldsymbol{\alpha^*}$	$\boldsymbol{\beta^*}$	$\mathbf{k_a}$	$\mathbf{k_b}$	$\mathbf{k_{f,a}}$	$\mathbf{k_{f,b}}$	$\mathbf{k_{f,c}}$	$\mathbf{k_{f,d}}$	$\mathrm{TI_{exp}}$	$\mathbf{d}$	$\boldsymbol{\eta}$	$\mathbf{p_p}$
$\hat{\theta}_{MAP}$	3.87	0.338	0.289	0.0106	0.818	0.309	0.128	-0.0994	1	0.814	1	1.99
θ_{mean}	3.84	0.337	0.278	0.0100	0.826	0.303	0.123	-0.100	1	0.827	1	2.01
$\sigma_{\theta_{mean}}$	0.36	0.046	0.042	0.0017	0.060	0.11	0.037	0.048	0	.068	0	0.16

Table 4.3: Key indicators for the posterior model parameter distributions.

As indicated by Table 4.1, the mean and MAP values for the calibrated model constants are in close agreement. This reflects on the Gaussian-like shapes displayed by Figure 4.9. Whereas the numerical values for most of the model parameters presented in Table 4.3 are hard to verify, a simple verification is carried out on the value for d. Based on the power time-series for the upstream turbines and the first row of waked turbines, an estimate on the expected value for d is obtained. In this work, this verification procedure is

based on the cross correlation between a free-stream turbine and its directly waked counterpart. Only this combination of turbines is considered due to the cleanliness of the power signals. On turbines at further downstream locations, significant other wake effects, and wake combination influences the power signals.

Next, the estimate for the effective value of d is made based on the time shift (τ) related to the highest cross correlation, the mean free-stream wind speed ($\overline{U}_\infty$), and the turbine spacing. This estimate is calculated by Equation 4.12, with the results of the cross correlation shown by Figure 4.10.

$$d = \frac{\text{Turbine spacing} \cdot D_r}{\tau_{opt} \cdot \overline{U}_\infty} \tag{4.12}$$

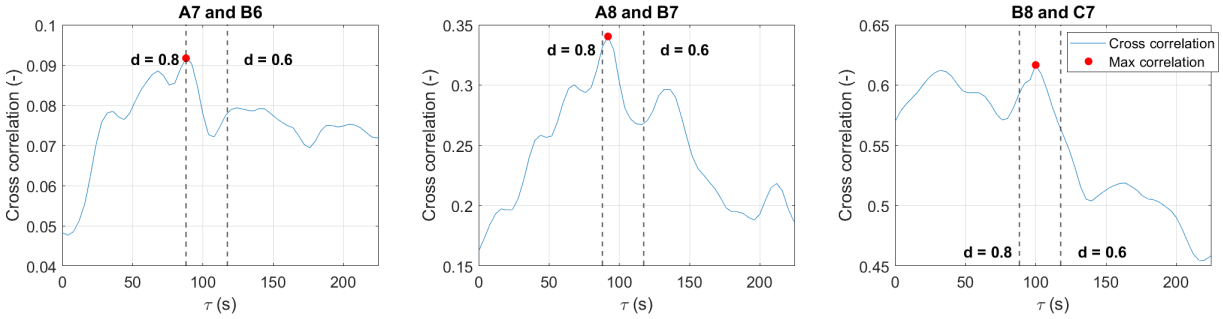

Figure 4.10: Cross correlation plots indicating the estimated value for d.

Figure 4.10 clearly shows that the calibrated value in Table 4.3 closely aligns with the results from the cross correlation analysis. Additionally, the ideal d differs per set of turbine combinations. Due to this variation, it raises interest in performing a sensitivity analysis on the full calibration procedure. Additionally, the outcomes of the calibration procedure might be dependent on other factors than turbine spacing, and will be discussed in Section 4.2.5.

4.2.5. Sensitivity Analysis on the Calibration Results

This section aims at investigating the sensitivity of the calibration results. By considering only a single calibration case, one risks running into overfitting model constants to a single inter-turbine distance. By incorporating multiple turbine alignment cases, and various inter-turbine distances, a more general set of tuned parameters can be obtained. Therefore, the calibration procedure is repeated on multiple wind farm subsets. The advantage of this approach is that the prescribed methodology is run for different turbine alignment cases, and varying input wind conditions, allowing for an analysis of the sensitivity of the calibration results to wind conditions and turbine spacing. This sensitivity analysis will indicate the robustness of the calibration procedure, while also providing insight in the variation of optimal model constant tuning values given different operating conditions.

The different wind farm subsets considered in this calibration sensitivity study are displayed by Figure 4.11, with their respective time periods on which the wind conditions, and validations data are extracted. All farm subset displayed by Figure 4.11 contain between 11 and 16 turbines to limit the computational expense related to creating the surrogate models, and inverse Bayesian calibration. The anterior model constant distributions remain the same as those for the single calibration case, and are tabulated by Table 4.1. Additionally, all other settings for the calibration procedure from PCE creation to the posterior PDF computations are retained.

Note that unlike the original calibration procedure, the analysis presented in this subsection does contain inoperative turbines (but no curtailments or start-up / shutdown operations). Additionally, the considered time periods also contain wind speeds above rated wind speed. These considerations allow for more extensive test cases, also highlighting the relation to potential limitations in the full FLORIDyn model.

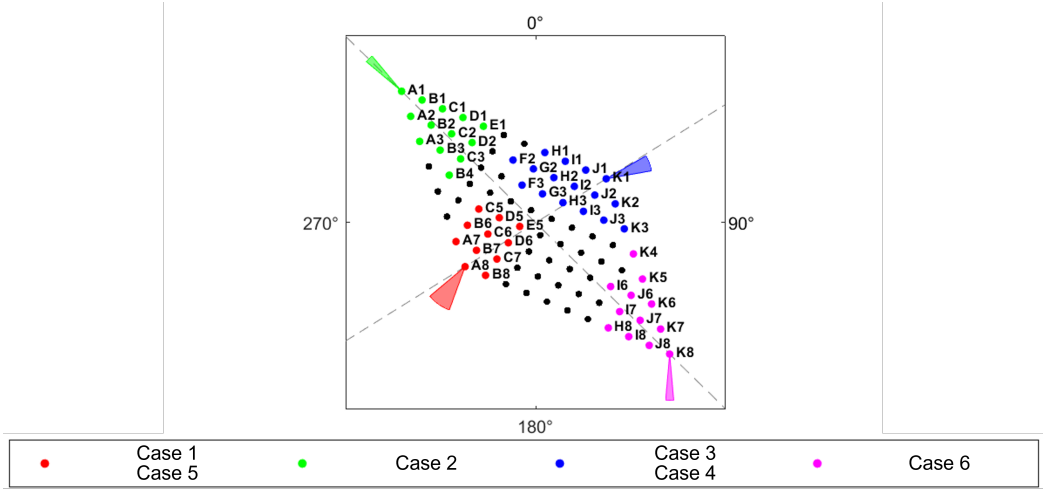

Figure 4.11: Visualisation of the farm subsets used for the multiple calibration runs. The coloured arcs indicate the input wind range along the considered calibration case.

Following the presentation of the various calibration setups, the resulting plots from the calibration sensitivity study are displayed by Figure 4.12. These plots illustrate the impact of each calibration setup on the calibration outcomes. This sensitivity analysis allows gaining key insights into identifying the most critical parameters and setups that drive accurate model calibration. Therefore, Figure 4.12a displays the ensemble-averaged posterior PDFs across the different calibration setups, while Figure 4.12b shows the individual results from all setups, illustrating the driving factors behind the ensemble-averaged results. These figures provide a comprehensive overview of the calibration performance and highlight the variability and consistency across different setups.

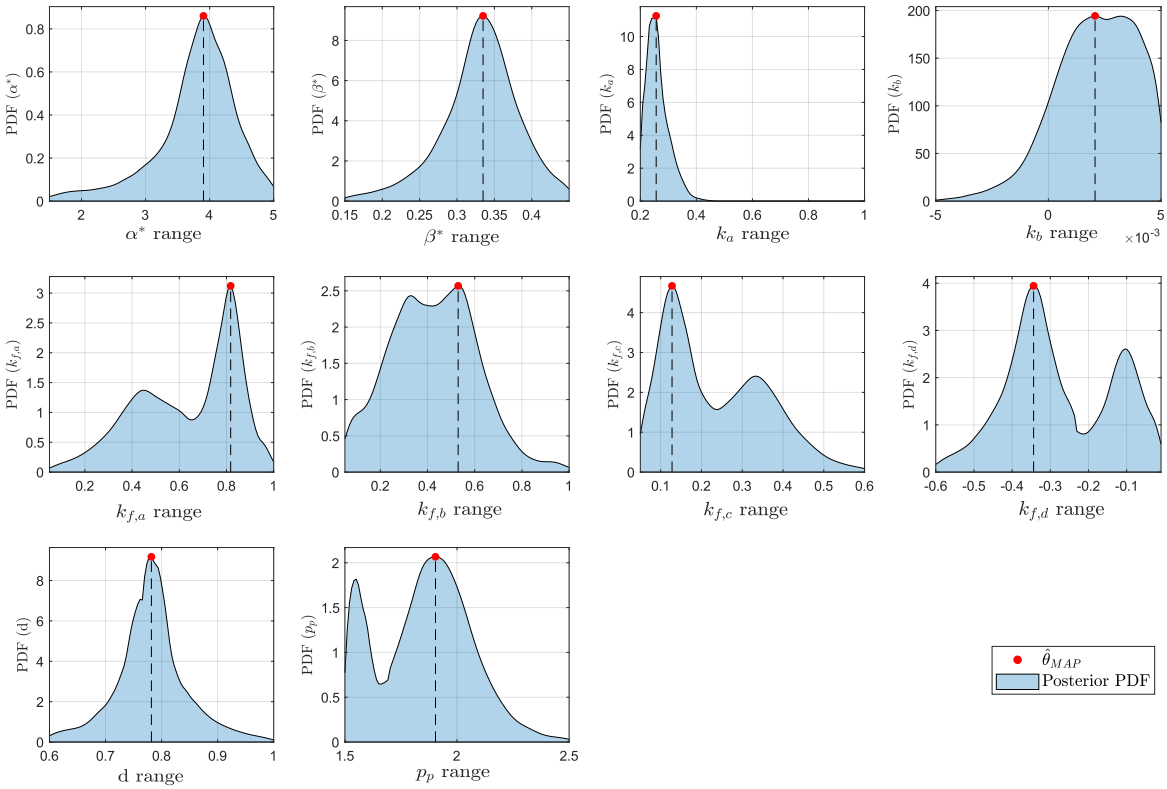

(a) Averaged posterior PDFs on the different calibration case studies.

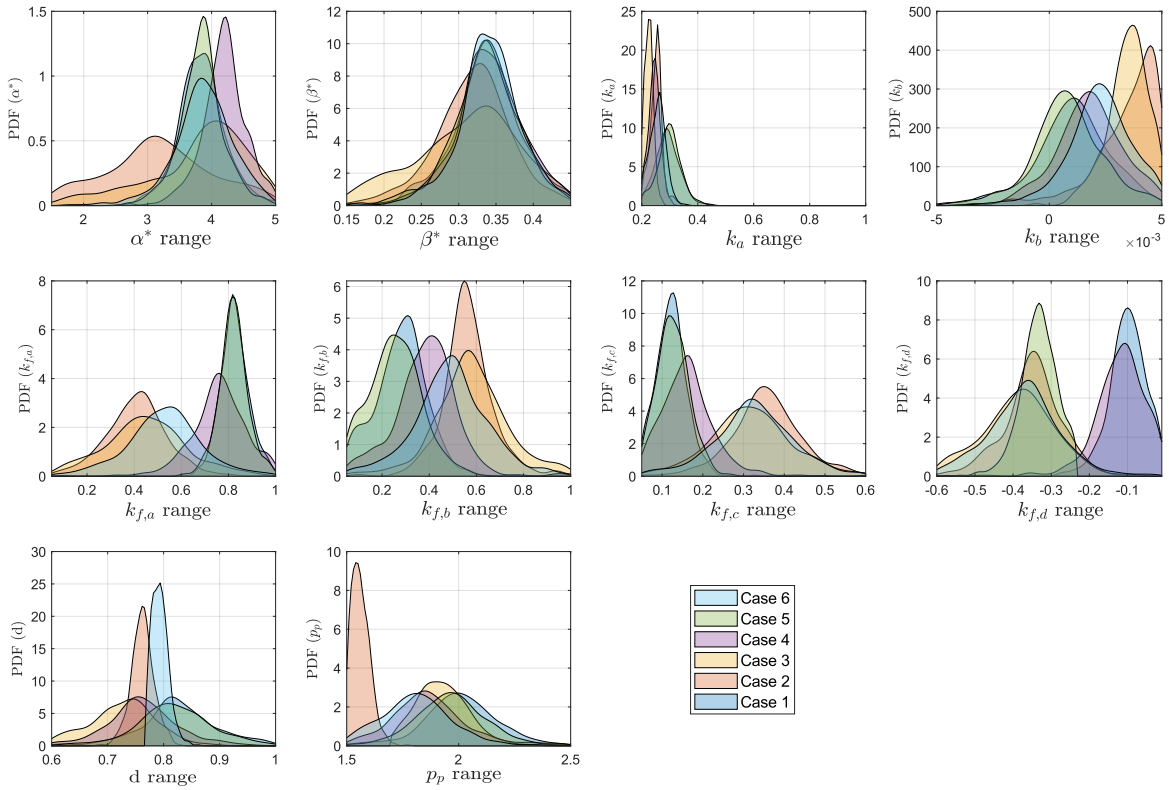

(b) Individual posterior PDFs on the different calibration case studies.

Figure 4.12: Resulting plots from the sensitivity analysis on the calibration procedure.

The results in Figure 4.12 will be discussed per main influence on the wake. Starting with α^* and β^*, the FLORIDyn sensitivity analysis showed that these parameters have the most significant influence on the power output on the first row of waked turbines. Although the ensemble averaged results in Figure 4.12a suggest a good convergence for both parameters, Figure 4.12b shows that the posterior distribution for α^* deviates significantly for one of the calibration sets. Interestingly, $\hat{\theta}_{MAP}$ is observed to be significantly smaller compared to the other calibration sets, and its distribution is wider. This indicates a larger uncertainty of calibration outcomes on this specific case. On this specific case, the largest turbine spacing is encountered. With α^* taking on a smaller value, not only is the length of the potential core increased, also the dependency on ambient TI is reduced.

Secondly, the wake expansion parameters k_a and k_b are discussed. Both of these parameters determine the wake width considered in the Gaussian FLORIS model. Not only do they influence the wake width, also the wake deficit in the far-wake region is governed by these parameters due to the Gaussian weighting (Equation 2.47 to Equation 2.49). Although the initial findings in Section 4.2.4 suggest that the input range was sufficiently large, Figure 4.12b indicates that the real convergence might occur outside the specified input range. Additionally, the k_b factor is observed to vary significantly over the different calibration runs.

Similar to the observation on the posterior PDFs for k_b, the model parameters related to the wake-added TI computations show significant differences between the calibration runs. Figure 4.12a essentially displays combined posterior with double peaks, indicating that the calibration procedure might have converged to two different values over the calibration iterations. Analysis of Figure 4.12b confirms this statement, as the resulting posterior PDFs for $k_{f,a}$, $k_{f,c}$ and $k_{f,d}$ effectively display a split convergence. Half of the considered calibration runs converge to one value, with the other half converging to a distinct value. This observation explains the emerged double peak PDF in Figure 4.12a. To a less extent, this is also observed on $k_{f,b}$. The difference is that one resulting PDF is observed to lay in between the separated other PDFs.

Most notably, there appears to be a general trend: case calibrations resulting in a large $k_{f,c}$ are coupled with a small $k_{f,d}$, and vice versa. Only the results on Case 5 do not follow this trend. Relating this back

to the TI computation $\text{TI}^+ \propto I_{amb}^{k_{f,c}} \left(\frac{x_1}{D_r}\right)^{k_{f,d}}$ (Equation 3.3), $k_{f,c}$ is related to the ambient TI, and $k_{f,d}$ is linked to the downstream wake distance. Interestingly, the combinations appear to invert their influences: a larger value for $k_{f,c}$ leads to a smaller wake-added TI, while a smaller value for $k_{f,d}$ results in a higher wake-added TI prediction. These statements have been made based on $x_1/D > 5$, thus representing the far-wake region. Given this observation, it is clear that the wake-added TI computation is not solely dependent on the considered influences of (a, ambient TI, and x_1/D). As indicated already in Section 2.1.1, wake breakdown and recovery is governed by complex atmospheric physics, that are not represented within FLORIDyn.

It is not unexpected that the largest uncertainty in calibrated model constants is observed in these four parameters related to the TI computations. There are large uncertainties in the computation of the input TI, as this essentially artificial quantity is introduced as a means to represent the turbulence. On average, a wind field can be characterised by this statistical quantity. Therefore, this property can not be measured, only estimated. Within the FLORIDyn model, it is used to indicate wake mixing, and represents the rate at which wake deficits are recovered, playing a key role in the computation of wake velocity deficits in engineering models.

Next, the combined PDF for the convection scaling parameter d displays a converged, Gaussian-like shape. This is mainly caused by two narrow individual PDFs, with the other calibration cases displaying larger uncertainties in the posterior PDFs. In general, although the convection model is based on a strong assumption of frozen turbulence, the results on all calibration cases agree on the most likely value occurring between 0.7 and 0.8. Given this simple convection model, it should be noted that these results have been obtained on relatively small wind farm subsets, where wake interactions on deep array locations could not be included.

Finally, the p_p parameter also shows an interesting double peaked plot. This is mainly caused by a single significantly large peak, away from the other, more or less converged calibration sets. Considering that the analysed simulations did not include samples on which a deliberate yaw offset (yaw steering) is applied, the yaw misalignment values are usually small. Given the $\cos^{p_P}\gamma$ factor to reduce the C_P, a 5% power decrease roughly results from a 13° yaw misalignment. Considering the minimal influence of this parameter on simulations with general turbine and wind direction alignment, obtaining a reliable calibrated value for p_P requires specific conditions. Additionally, considering FLORIDyn's inability to model atmospheric conditions, such as the stability of the atmospheric boundary layer and effects of wind veer, accurate calibration can only be achieved by analysing cases with significant, intentional yaw misalignment.

The final values for the calibrated model constants $\hat{\theta}_{MAP}$ are tabulated in Table 4.4. Additionally, the mean and standard deviations from the combined posterior PDFs are indicated. Unlike the results presented in Table 4.3, the MAP and mean model parameter values can significantly differ. This is a direct result of the observed double peak behaviour in Figure 4.12a, inferring higher uncertainties on the tuned model parameter distributions.

Table 4.4: Key indicators for the posterior model parameter distributions, resulting from the combined calibration runs.

	Potential Core		Wake Expansion		Wake-Added Turbulence					Dynamics	Power	
	$\boldsymbol{\alpha^*}$	$\boldsymbol{\beta^*}$	$\mathbf{k_a}$	$\mathbf{k_b}$	$\mathbf{k_{f,a}}$	$\mathbf{k_{f,b}}$	$\mathbf{k_{f,c}}$	$\mathbf{k_{f,d}}$	TI_{exp}	$\mathbf{d}$	$\boldsymbol{\eta}$	$\mathbf{p_p}$
$\hat{\theta}_{MAP}$	3.90	0.335	0.275	0.00207	0.818	0.530	0.128	-0.344	1	0.782	1	1.904
$\bar{\theta}_{mean}$	3.78	0.331	0.263	0.00204	0.632	0.429	0.236	-0.277	1	0.771	1	1.862
$\sigma_{\theta_{mean}}$	0.63	0.052	0.0402	0.0018	0.21	0.18	0.12	0.14	0	0.063	0	0.20

The obtained calibrated set of model parameters in Table 4.4 influence the wake shape computed in the FLORIDyn model. To visualise this resulting wake shape from the calibrated parameter set, Figure 4.13 shows the effective wind speed and wake-added TI fields on a simple three turbine setup, in an aligned, fully waked configuration, comparing them against those obtained from the baseline set of model parameters.

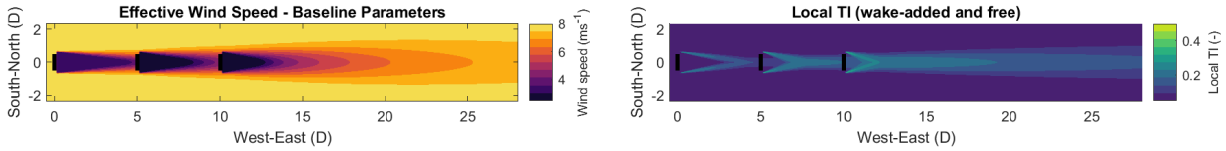

(a) Flow velocity field and TI plots resulting from the baseline set of model parameters.

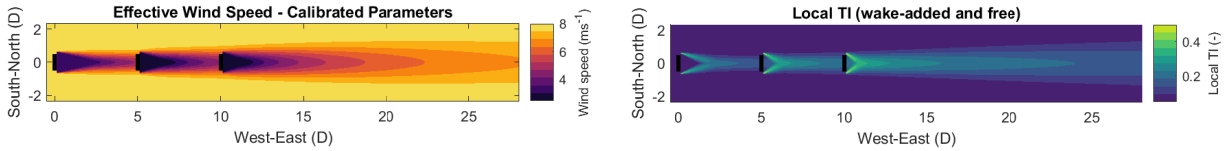

(b) Flow velocity field and TI plots resulting from the calibrated set of model parameters.

Figure 4.13: Comparison between FLORIDyn computed wakes using baseline model parameter settings (a) against calibrated model parameter settings (b).

Given that the calibration procedure aims to identify more accurate model parameter values to better represent quasi-instantaneous wake profiles compared to the time-averaged profiles of the baseline case, specific expectations arise. These include a shorter potential core with a higher velocity deficit, as well as a narrower wake in the far-wake region that maintains higher velocity deficits over a greater distance [105]. These improvements are anticipated to enhance the model's ability to predict wake behaviour more precisely under varying conditions.

Interestingly, Figure 4.13 shows that the wakes resulting from the calibrated model parameters exhibit smaller wind speeds in the near-wake region. This finding is notable because the calibrated model parameters are intended to better represent instantaneous wake profiles, while the baseline model constants reflect time-averaged wake profiles. Given this distinction, achieving lower wind speeds in the potential core region by averaging the wakes from the calibrated model constants over varying wind directions is not feasible. Additionally, the turbine spacing at the Sheringham Shoal layout does not include spacings closer than $6.1\mathrm{D}_r$, which means there are no turbines in the near-wake region. Consequently, the model constants related to the potential core region have been calibrated on a general basis, taking into account their effects on further wake distances, but without a direct comparison in their primary region of influence. This calibration approach highlights the need for further investigation into near-wake dynamics to refine model accuracy.

On the other hand, due to the smaller k_a and the faster decay of wake-added TI in the calibrated set of model constants, a narrower yet more persistent wake is generated compared to the baseline case. Unlike the higher wind speeds in the potential core region, lower wind speeds are maintained over longer distances. This behaviour aligns with expectations, as the analytical wake model represents time-averaged conditions, including fluctuations in wind direction. Thus, longer and more persistent wakes are anticipated in an instantaneous wake profile representation.

Although the expected behaviour in the self-similar far-wake region is observed, the near-wake representation yields counter-intuitive results that do not accurately reflect physical instantaneous wakes. This discrepancy raises questions about the validity of using time-averaged wake profiles in a time-dependent modelling approach. While the large turbine spacing at the Sheringham Shoal wind farm mitigates the impact of these non-physical results in the near-wake region, it is important to note that the current set of calibrated model constants may not be reliable for simulating wind farms with smaller turbine spacing. This limitation underscores the need for further refinement of the model to ensure accurate predictions across different turbine configurations.

4.3. One-To-One Model Validation Studies

This section aims to present a validation study of the FLORIDyn model with the tuned model parameters, and compare to the baseline model. To achieve this, so-called one-to-one simulations will be considered. This essentially means that a wind field deduced from field data is directly fed as model input, with

the goal of predicting the same turbine power outputs as observed in field data. The model validation section starts with the definition of quantitative validation metrics in Section 4.3.1. This is followed by a comparison between the model performance using calibrated and baseline model parameter values. Finally, Section 4.3.3 presents the model uncertainty on power predictions, by propagating the uncertainty in calibrated model parameters (using the posterior predictive distributions). Finally, Section 4.3.4 discusses the findings from FLORIDyn simulation runs on the entire Sheringham Shoal wind farm instead of the considered farm subsets.

4.3.1. Validation Metrics

The metrics introduced in this section will be used throughout the remainder of this work to compare the FLORIDyn model performance to other models, and to indicate how well the field measurements are represented. Therefore, the considered parameters to compute these metrics will be time-averaged properties, rather than the time-series outputs.

Starting with the Farm Error, it indicates the cumulative error of a wind farm collective power output. As shown by Equation 4.13, the difference between the model predicted and Fastlog time-averaged power is summed over all the considered turbines on the considered wind farm.

$$\begin{aligned} \textbf{Absolute Farm Error} &= \sum_{i=1}^{N_T} \left(\bar{P}_i^{\text{model}} - \bar{P}_i^{\text{Fastlog}} \right) \\ \textbf{Relative Farm Error} &= \frac{\sum_{i=1}^{N_T} \left(\bar{P}_i^{\text{model}} - \bar{P}_i^{\text{Fastlog}} \right)}{\sum_{i=1}^{N_T} \bar{P}_i^{\text{Fastlog}}} \end{aligned} \tag{4.13}$$

For these error definitions (represented by ε), the following conclusions are stated:

- $\varepsilon < 0$: The model is overestimating the wake losses, resulting in lower predicted power output, and is thus conservative;
- $\varepsilon > 0$: The model underestimates the wake loss, and is optimistic

Next to the collective farm errors, one could also consider metrics that describe the discrepancies between field data and model outputs on an individual turbine basis. Therefore, Equation 4.14 indicates the relative turbine error, based on the time-averaged power outputs.

$$\textbf{Relative Turbine Error} = \frac{\bar{P}_i^{\text{model}} - \bar{P}_i^{\text{Fastlog}}}{\bar{P}_i^{\text{model}}} \tag{4.14}$$

Additionally, the mean turbine RMSE is introduced as it indicates the variation of observed errors over the included turbines. It has the benefit of not being sensitive to the sign of errors potentially cancelling out, but is more sensitive to outliers when compared to absolute error metrics.

$$\textbf{Mean Turbine RMSE} = \sqrt{\frac{1}{N_T} \sum_{i=1}^{N_T} \left(\overline{P}_i^{\text{model}} - \overline{P}_i^{\text{Fastlog}} \right)^2} \tag{4.15}$$

4.3.2. Calibrated vs Baseline Model Results

This section presents a comparative analysis of the calibrated FLORIDyn model against the baseline model constants. The primary objective is to evaluate the improvements in accuracy and performance achieved through calibration. By assessing key comparison metrics on power output, this analysis aims to highlight the advantages of calibration in enhancing model reliability and predictive capability. The results demonstrate how calibrating the model parameters can lead to an overall increase in model accuracy, thereby supporting better decision-making in wind farm design and operation. Through this comparison, further insights into the strengths and weaknesses of the FLORIDyn model are provided, offering valuable guidance for future model development.

The assessment of the increased model accuracy resulting from the calibration model is first displayed by considering the original, single calibration configuration. For this case, Figure 4.14 displays the results

for both the baseline and calibrated FLORIDyn model runs on the considered farm subset. In total, three comparative metrics are indicated. Firstly, coloured circles on the farm layout display the time-averaged relative errors per turbine. Additionally, the relative farm error and turbine averaged RMSE values are indicated as well.

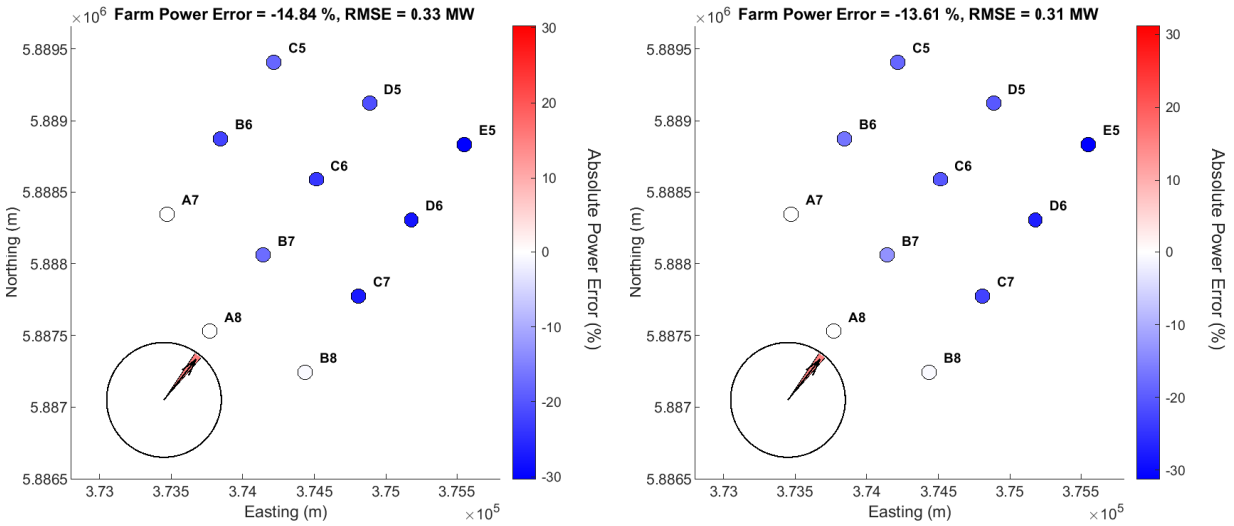

(a) Results for baseline model parameter values.

(b) Results for calibrated model parameter values.

Figure 4.14: FLORIDyn results comparison between baseline and calibrated model parameters generated based on the input wind on Case 1.

The differences between the baseline and calibrated FLORIDyn evaluations in Figure 4.14 indicate that the calibration procedure slightly improved the model predictions. However, the resulting model parameter values were derived from combining the calibration procedure across multiple cases. As such, analysing this single case in detail does not add significant value. To gain a comprehensive understanding, this analysis is extended to the full range of considered calibration cases. Consequently, the turbine averaged RMSE and relative farm errors are compared for all calibration cases between the baseline and calibrated in Figure 4.15 and Figure 4.16 respectively.

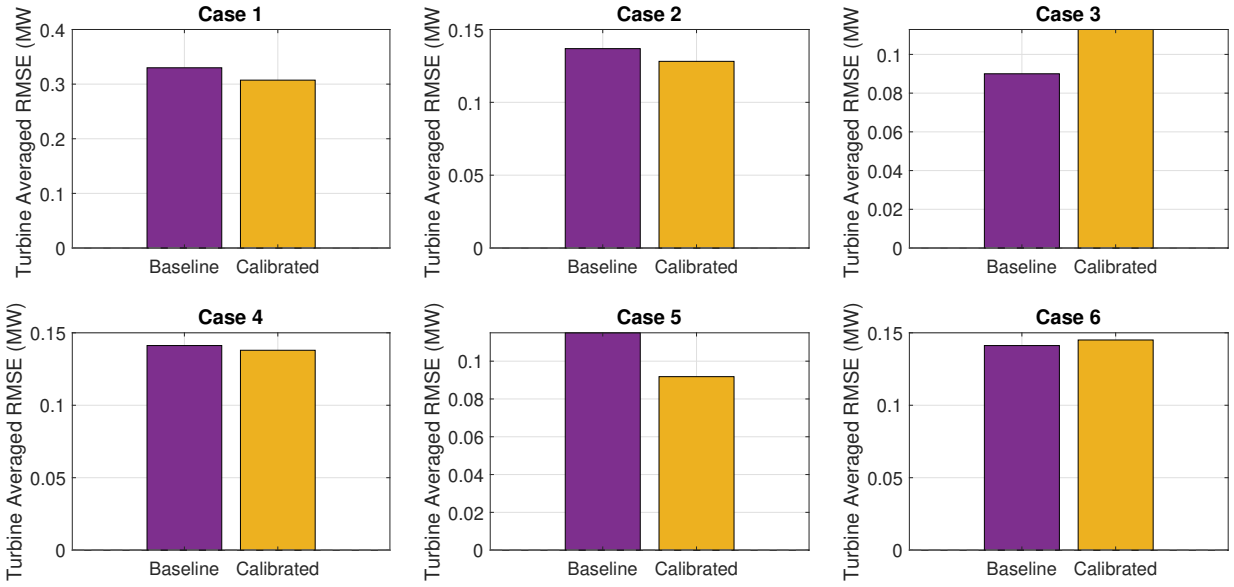

Figure 4.15: Comparison plots of the turbine averaged RMSE between the baseline and calibrated FLORIDyn model evaluations.

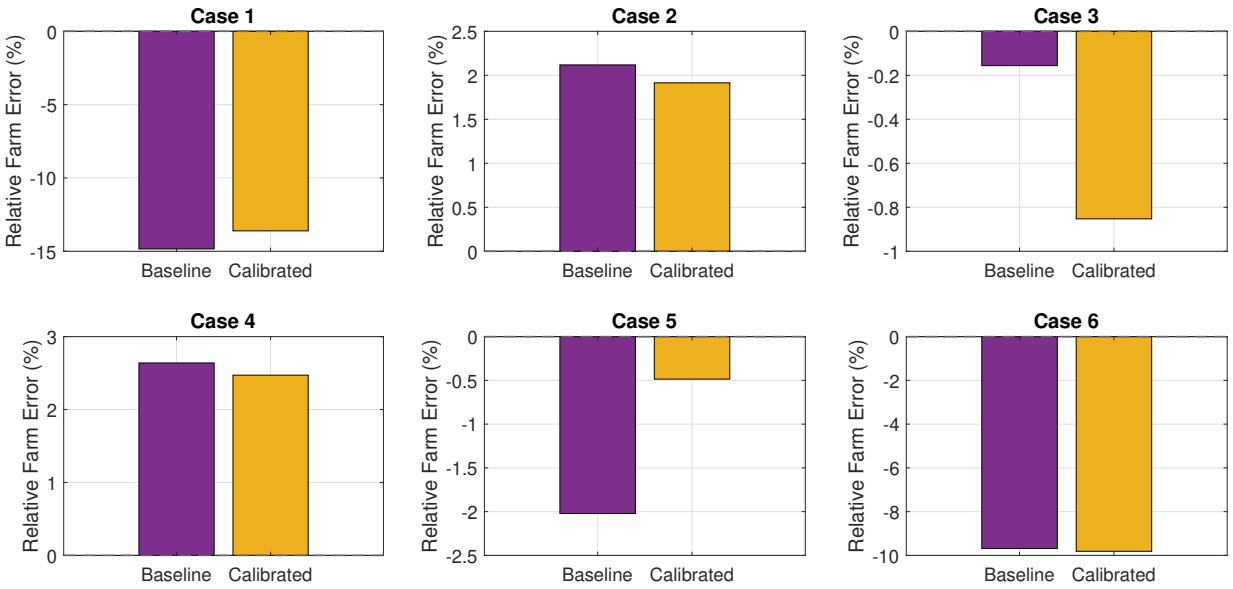

Figure 4.16: Comparison plots of the relative farm error between the baseline and calibrated FLORIDyn model evaluations.

As shown by Figure 4.15 and Figure 4.16, the calibrated FLORIDyn model does not consistently result in more accurate predictions across all calibration cases. While four out of the six cases show improvements with the calibrated set of model constants, the evaluations on Case 3 and Case 6 exhibit slightly increased error metrics.

These results highlight the sensitivity of the calibration procedure again, as the results do not lead to improved model results on all considered subsets. Therefore, no single set of model parameter constants is obtained to improve the FLORIDyn model predictions on all encountered wind conditions and turbine spacing combinations. However, this calibration procedure did find a set of parameters that generally increases the model prediction accuracy on the considered farm subsets. Given the interest in determining the accuracy in predicting AEP, this globally increased modelling accuracy is desired over tailored parameters per specific case, since the AEP predictions are run on all wind farm alignment configurations and in generalised wind conditions. Therefore, the obtained set of calibrated parameters will be considered throughout the remainder of this work.

4.3.3. Uncertainty on FLORIDyn Model Results

The uncertainty in FLORIDyn model results is expressed by the posterior predictive (computed through Equation 4.10). The results from this posterior predictive represent the model outcomes from the propagated posterior model constant predictions. The results of this model uncertainty propagation are displayed by Figure 4.17 on the initial calibration case. The considered curves display the Fastlog field data, the FLORIDyn results given the $\hat{\theta}_{MAP}$, and uncertainty bounds represented by the ensemble averaged power output ($\langle P \rangle$), and a 99.7% confidence interval ($\langle P \rangle \pm 3\sigma$). The results of this evaluation are displayed by Figure 4.17 as a power time-series per considered turbine on the initial 11 turbine farm subset.

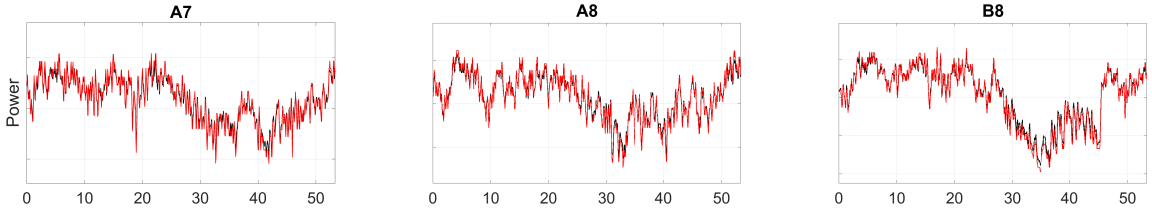

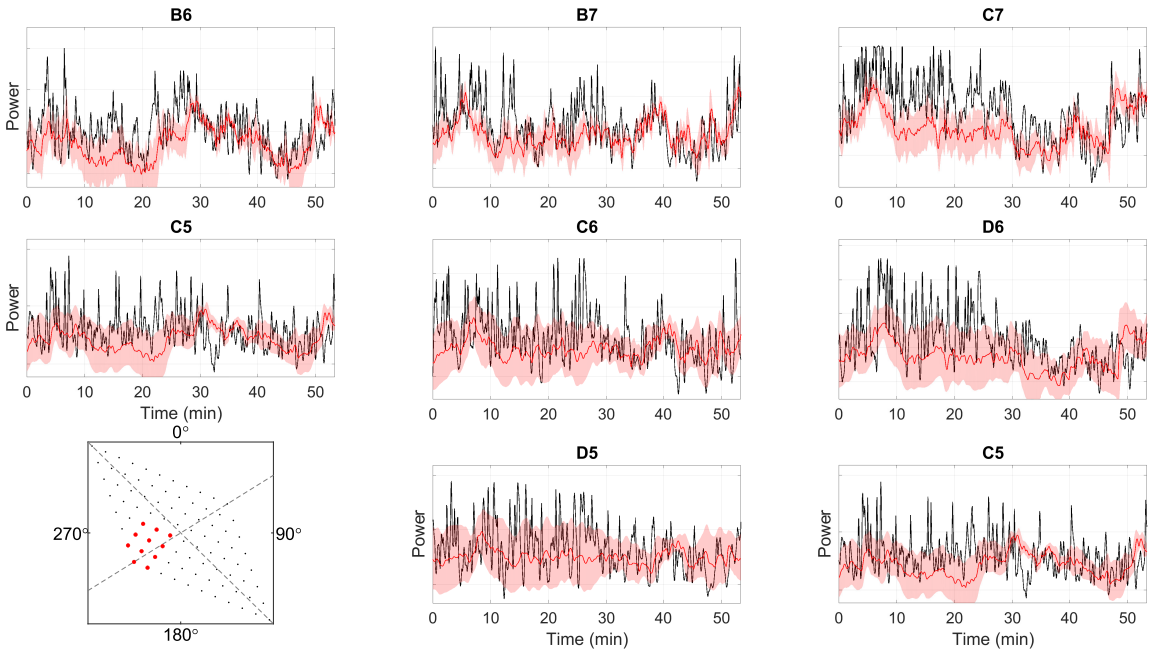

Figure 4.17: Time series plots including uncertainty bounds due to propagating the posterior model constant distributions.

Figure 4.17 shows that the predicted FLORIDyn power time series are essentially low pass filtered power signals that generally follow the trends in the Fastlog signals. Additionally, power fluctuations originating from upstream turbines are convected downstream with an applied time lag that looks to be consistent with field data measurements.

Next, the expected results for the uncertainty bounds are observed. Combining the posterior PDFs from Figure 4.12a with the outcomes of the sensitivity study in Figure 4.7, the largest uncertainties are expected on the most downstream row of turbines. This expectation results from the increased influence of the wake-added TI parameters on the model outputs, combined with the double peak posterior PDFs. As mentioned before, the parameters related to wake-added TI parameters play a role in determining both the wake recovery rate, and the wake width through k_a.

Unsurprisingly, the uncertainty in model outcomes increases with downstream location. This is due to the superposition of upstream wake effects. With multiple wakes interacting, downstream turbines are inherently dependent on the OP propagation of all upstream waking turbines. Therefore, the expected uncertainty in model outcomes is increased as well. Not only is the uncertainty on model outputs increased, also the Fastlog power signals display larger fluctuations on further downstream locations. Due to these larger fluctuations, the model variability does not fully span the Fastlog validation data time-series. Therefore, it might be more interesting to consider a low-pass filtered signal for the validation data for both the calibration procedure, and for the comparison study to have a more comprehensive comparison basis.

Finally, whereas a relatively clean power signal is observed in at the free-stream turbines, significantly large power fluctuations occur on the power signals for the waked turbines. This raises questions on the validity of the averaged wake profile used in FLORIDyn, and on the implemented convection model. This hypothesis is twofold. Firstly, representing wake properties by time-averaged wake fields inherently eliminates the time dependent fluctuations. Hence, the wake meandering effects, and locally increased wind speed fluctuations in the wake, are damped out. Secondly, the implemented OP propagation model ('Averaged') results in a smoothened wind field as it is convected downstream. This is clearly observed from the FLORIDyn power prediction from turbine A8 to D5 in Figure 4.17, and opposes the higher fluctuations observed on the field data measurements.

However, when modelling time-averaged power or even AEP, capturing these higher frequency fluctuations should not the primary objective. Instead of incorporating additional flow physics, models de-

signed for power and AEP predictions focus on improving power predictions while avoiding the increased computational complexity associated with these additional flow physics considerations. Ultimately, the time-averaged power output relies more on statistical properties, with high-frequency fluctuations being less significant compared to their role in load computations.

The uncertainty bounds specified in Figure 4.17 implicitly assume that the results from the model runs attain a normal distribution. In order to check the validity of this assumption, Figure 4.18 depicts the distributions of the power ratios $\langle P(t)\rangle / P_i$, where $\langle P(t)\rangle$ indicates the ensemble average of the model runs at each time instant and P_i indicates the i model runs, for all turbines and time instants on the considered farm subset.

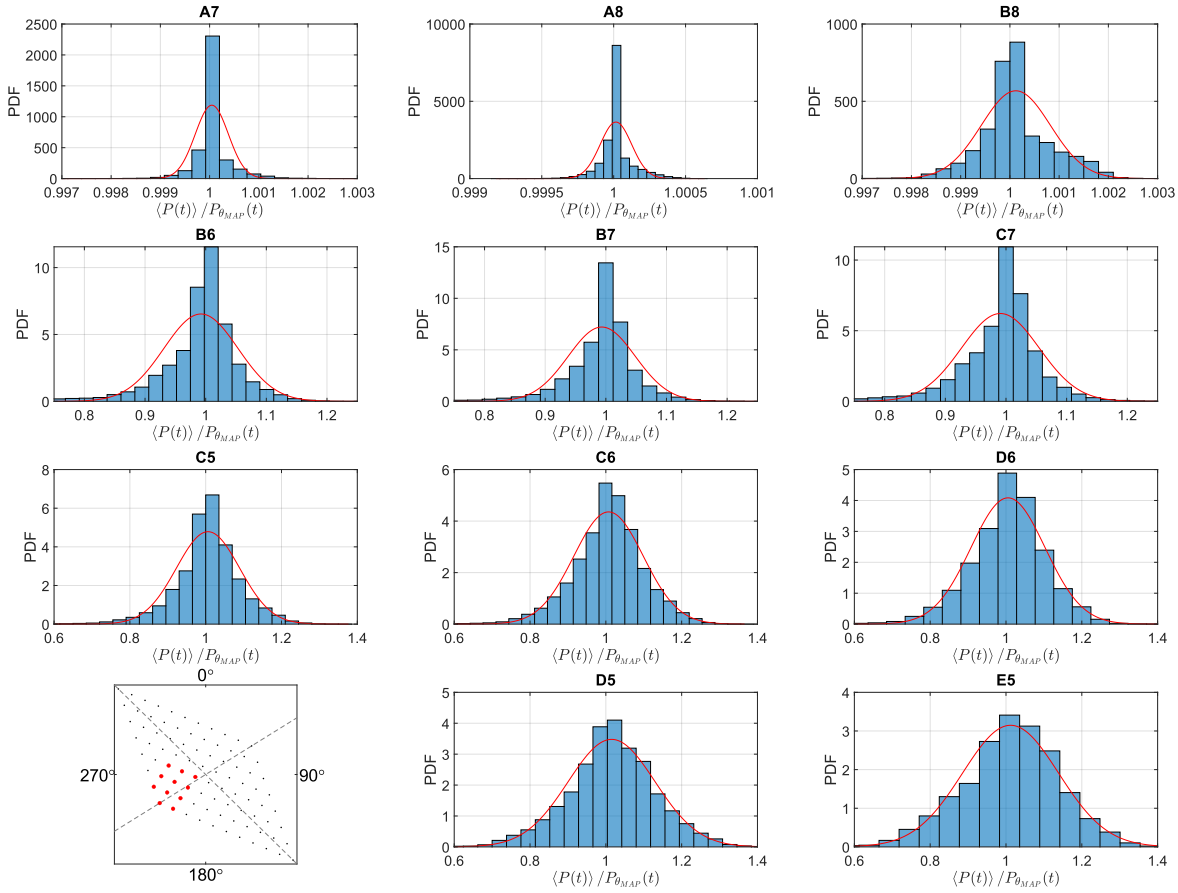

Figure 4.18: Validation plot for the Gaussian model uncertainty distribution assumption.

Consistent with the Gaussian assumption used to generate the uncertainty bounds in Figure 4.17, all histograms display a Gaussian-like distribution centred around 1. This observation validates the uncertainty bounds representation in Figure 4.17.

Not surprisingly, and in line with the observations in Figure 4.17, Figure 4.18 displays almost no variation on the first (unwaked row) of turbines. With effectively only p_P influencing the power production, only small variations are caused both due to the small misalignment values, and the influence of p_P itself. Whereas the first rows show relatively centred and narrow distributions around 1, the distributions become wider on further downstream rows. Especially on the fourth row, wider and larger uncertainty distributions appear, directly resulting from the increased uncertainty in $k_{f,a}...k_{f,d}$.

Finally, the power ratio representation allows for quantitative estimates on the uncertainty on model results. Note that this is a combined uncertainty of FLORIDyn model outputs, ambient environmental conditions, and uncertainty related to the surrogate model creation. Nonetheless, it gives an indication of the range of modelling uncertainties to expect. The final findings are summarised in Table 4.5 for different cases: one including all turbines, and excluding the free-stream turbines, and one on each of the streamwise

turbine rows. This consideration allows having an unbiased estimate of the uncertainty in power predicted by the effective wake modelling computations, and summarises the findings in this section.

Table 4.5: Quantitative results on the uncertainty on FLORIDyn model results.

Case	Uncertainty as std (%)
First row	0.00444
Second row	6.11
Third and fourth rows	11.11
All turbines	8.21
Excluding unwaked turbines	9.62

As the number of downstream aligned turbines increases, the model uncertainty is increasing. However, the performed analyses up to this point only considered limited wind farm sizes, and thus limited rows of waked turbines. Because of these limited wind farm sizes, model performance at deep array locations can not be evaluated. In these regions, the wake accumulation submodels have a significant influence in the determination of wind conditions. Therefore, Section 4.3.4 will elaborate on the findings on FLORIDyn evaluations on the full Sheringham Shoal wind farm.

4.3.4. FLORIDyn Results on the Full Wind Farm Configuration

Up until this section, all FLORIDyn evaluations have been run on subsets of the considered Sheringham Shoal wind farm. This limited scope has allowed for a focused analysis on specific turbine rows and smaller clusters, providing detailed insights into the FLORIDyn model, while allowing for a calibration procedure to be implemented. However, to fully understand the model's performance and applicability, it is essential to extend the evaluation to the entire wind farm, beyond the limited size considered in the calibration procedure. Therefore, this section analyses the results of FLORIDyn simulations compared to field data on the full wind farm configuration, capturing the cumulative and deep-array wake effects that occur in a large farm-scale operational environment. The validation with field data further allows an assessment of the model's accuracy and robustness in real-world conditions, providing a holistic view of its performance across the entire wind farm.

When performing a one-to-one validation simulation on a full wind farm scale, it is inevitable to encounter turbines that do not operate in ideal, nominal conditions. Related to these occurrences, some difficulties arise in handling turbine unavailability and non-nominal turbine operations within simulations. Given the limitation of using a single operational C_P-C_T LUT within this work's framework, corresponding to nominal turbine operation, handling different turbine operational states is currently not available. Therefore, a strategy to represent these special turbine operation cases should be implemented.

In cases where a turbine is detected to be offline, the governing LUT is configured to produce no power or thrust for any wind input. While this assumption is valid for non-operational turbines, it introduces inaccuracies for turbines operating in curtailed or non-nominal regimes, which have altered but non-zero C_P-C_T curves. To mitigate the impact of these altered operating conditions on the FLORIDyn simulation, turbines are categorised as either offline or operating under nominal conditions based on the reference channel. This channel indicates if a turbine is operating under a curtailment regime and is a discrete value that either indicates 1 or 0, for curtailed or nominal operations respectively. Without the operating C_P-C_T curves for curtailed operations available for this study. To minimise the impact on comparison metrics, turbines operating in non-nominal conditions have been excluded from the comparison metrics. However, the insufficiently modelled effects will still influence downstream turbines. Consequently, the turbines operating in downstream regions of such turbines are expected to display larger discrepancies when compared to the validation data.

The results of two FLORIDyn evaluations as one-to-one simulations from real-world wind input data are displayed by Figure 4.19. These correspond with the calibration cases run on the wind inputs on Case 1 and Case 2. Results for the FLORIDyn evaluations on the remaining four calibration cases are additionally provided in Appendix E. Finally, turbines considered to be inoperative within the FLORIDyn simulation

(unavailable power signal / offline / other than nominal operating status) are indicated by yellow coloured circles, with a cross.

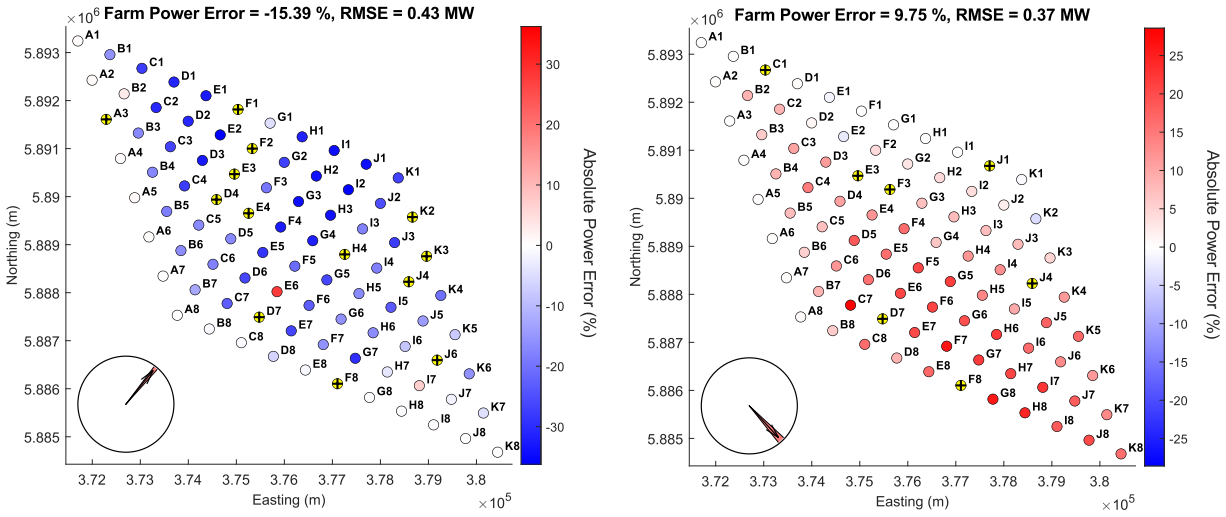

(a) Mapped FLORIDyn power predictions on Case 1. **(b)** Mapped FLORIDyn power predictions on Case 2.

Figure 4.19: One-to-one FLORIDyn simulation results on two distinct inflow conditions initialised from field data measurements. Turbines considered to be inoperative are indicated by yellow circles, with a cross.

Firstly, Figure 4.19 confirms that the insufficient modelling of non-nominally operating turbines induces larger downstream errors. By failing to predict the operating C_T, the wake of a non-nominally operating turbine can not be accurately predicted. Therefore, the absolute largest errors observed in Figure 4.19a result from turbines operating in such conditions (turbines G7 and E6 in Figure 4.19a). These cases will be neglected in subsequent analyses.

In accordance with the expectations outlined in Section 4.3.3, the largest disparities between the actual field data and the model predictions are observed in the deeper field locations. These areas are particularly influenced by intricate dynamics such as complex wake interactions and accumulation effects. Notably, the comparison plots presented in Figure 4.19a and Figure 4.19b highlight significant variations in these specific regions. In Case 1, there is a notable discrepancy characterised by a substantial underestimation of power production, whereas in Case 2, the FLORIDyn model predicts a significant overestimation. This disparity underscores the sensitivity of FLORIDyn model predictions to the specific alignment and spacing of turbines within the wind farm layout.

Both the analysed cases show only small variations on the free-stream turbines in the wind direction over the simulated time window (indicated by the red sector on the wind arrow), highlighting that the main influence on the wakes is caused by wind speed fluctuations. Conversely, the turbine spacing and alignment remain mostly constant throughout the simulations. Consistent with the findings on all cases (Appendix E), the FLORIDyn results accuracy is significantly dependent on the perceived turbine alignment. For cases with strong alignment, the long and strong wakes result in large wake velocity deficits, and accompanying underestimation of power. This is especially the case on wind conditions that display only small variations in wind direction, leading to consistent turbine operation in fully waked conditions.

On the other hand, the partially waked configurations, combined with larger turbine spacings result in relatively accurate power predictions on the first couple of turbine rows, but result in a severe overestimation of power at deep array locations. These differences are more accurately displayed by Figure 4.20, directly comparing the FLORIDyn predicted time-averaged power to the time-averaged Fastlog signals.

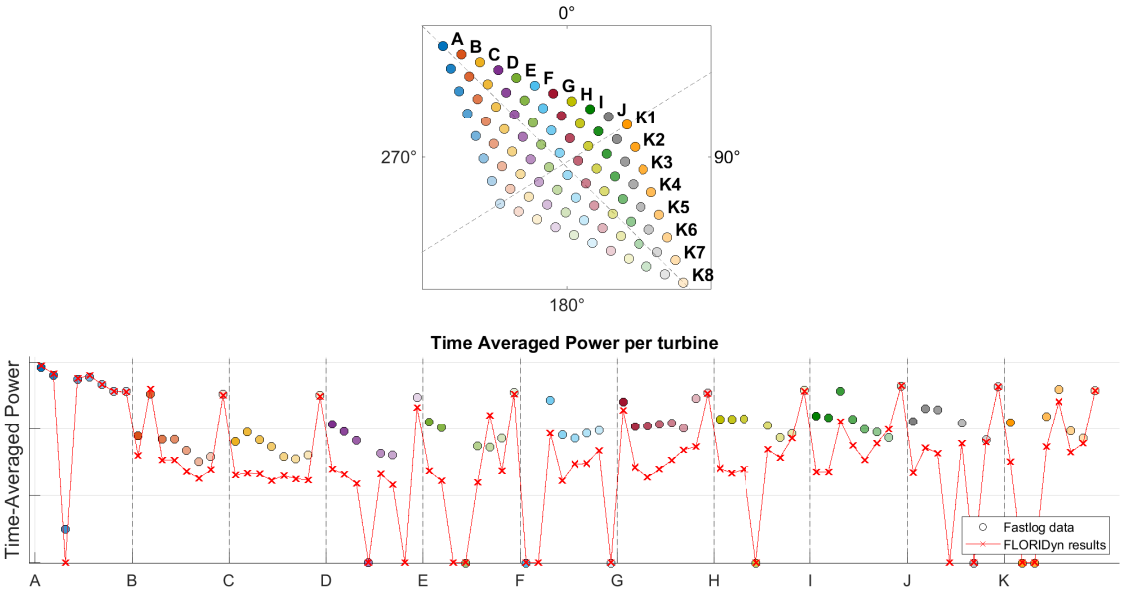

(a) Time-averaged power comparison on Case 1.

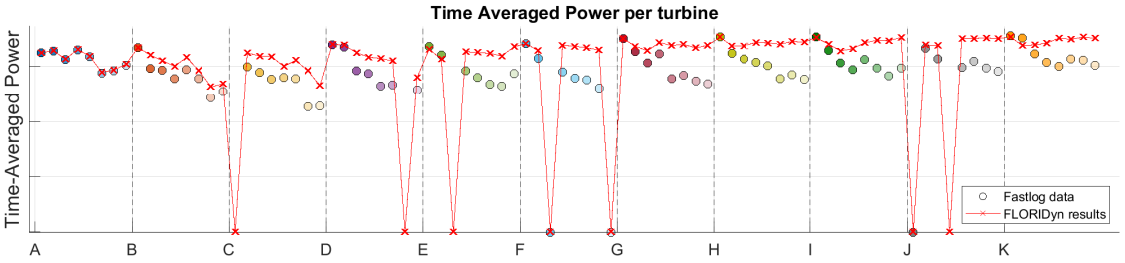

(b) Time-averaged power comparison on Case 2.

Figure 4.20: Direct comparison plots of time-averaged turbine power output on the FLORIDyn results and Fastlog data.

Figure 4.20 confirms the observed differences indicated by Figure 4.19. Neglecting the influence of curtailed and offline turbines, the wake recovery is observed to be inconsistent with the field data observations. Especially in the partial wake and increased turbine spacing configuration, indicated by Section 4.3.4, the predicted wind speed at downstream turbines is overestimated, translating to power overestimations. The differences with the Fastlog results are observed to further increase with downstream turbine location.

The hypothesis on FLORIDyn limitations due to the implemented wake accumulation is further analysed by considering the model predictions in a time series representation. Additionally, the time series representation allows for an investigation of the FLORIDyn convection model, and its related assumptions. Therefore, plots for four turbines on Case 2 at different aligned downstream locations are displayed by Figure 4.21.

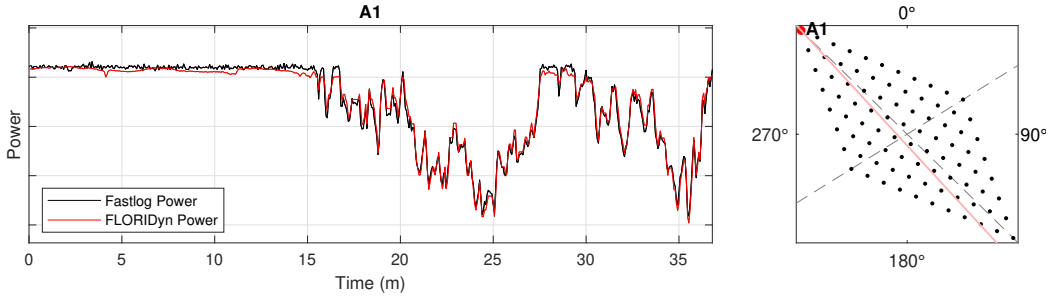

(a) Power time series of turbine A1.

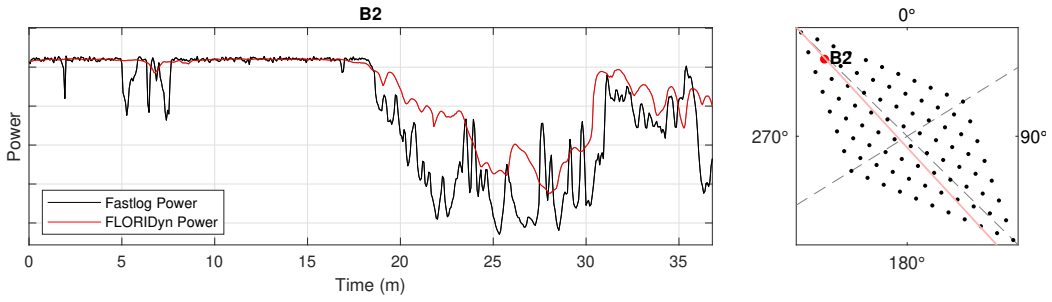

(b) Power time series of turbine B2.

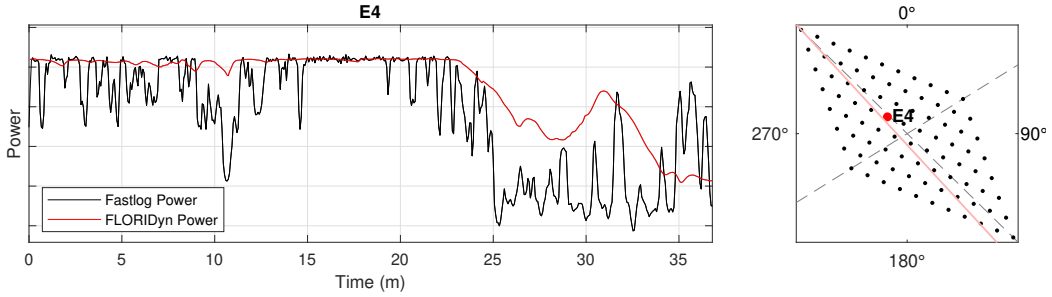

(c) Power time series of turbine E4.

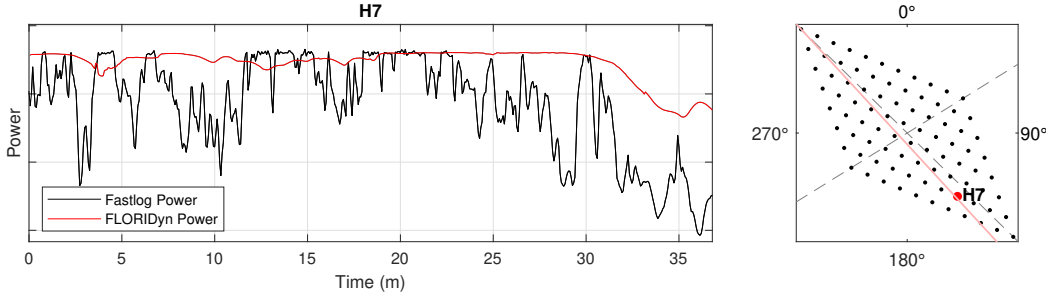

(d) Power time series of turbine H7.

Figure 4.21: Power time series comparison on Case 2 for four turbines at different downstream locations. The mean wind direction is indicated by the red line on the wind farm layout.

By analysing the time series plots in Figure 4.21, definitive conclusions on the FLORIDyn model deficiencies can be stated. It allows validating the hypotheses made based on Figure 4.19 and Figure 4.20.

Starting with the oversimplified convection model, the displayed power time series essentially also indicate the predicted wind speeds at each turbine. Given the small variations in wind directions indicated by Figure 4.19b, this assumption is true as the turbines are aligned with the mean wind direction. Furthermore, Figure 4.21 primarily tracks turbines along the mean wind direction, which is justified by the implementation of the convection model. In this model, only discrete points, or OPs, are convected starting from the upstream turbines. Consequently, turbines located downwind are influenced by the wake and local wind conditions of the upstream turbines. Additionally, OPs interact solely within the wake chain, without interacting with OPs originating from different turbines.

As observed from the downstream development of the power signal, a clear smoothing effect is evident. This is directly attributable to the choice of the 'Averaged' setting on the OP propagation submodel. As a chain of OPs travels downstream, this averaging operator effectively dampens the wind speed fluctuations, resulting in more uniform wind conditions further downstream. Consequently, this smoothing effect had only minor impacts on the smaller wind farms considered in the calibration procedure. In cases with the smallest turbine spacing, the averaging effect was further diminished since the OPs had to convect over shorter distances. Therefore, the evaluation on the wind farm subsets failed to capture this model deficiency, which is most apparent on deep array turbine locations.

Secondly, the accuracy of the time lag predictions decreases with downstream location. While the power

fluctuations for turbine B2 are generally captured at the correct timestamps, this accuracy diminishes for turbines situated further downstream along the mean wind direction. This effect is particularly pronounced for turbines E4 and H7, where the predicted drops in power output, occur significantly later than indicated by the Fastlog curve. Interestingly, the time series for the wind speeds outlined in Appendix F indicate that the time lags are generally well captured by FLORIDyn. However, the overestimation of wind speed magnitude, which remains above the rated speed, primarily leads to less accurate time lag predictions on the power signals.

Next to the limitation imposed by the convection model, Figure 4.21 displays an underestimation in the wake velocity deficits. With increasing downstream distance, a significant overprediction of power is observed due to this effect. For turbines E4 and H7, the predicted power consistently exceeds the field data. At the location of turbine H7, wake accumulation significantly influences the local wind speed. The FLORIDyn model even fails to capture the reduction in power for turbine H7 during the time window between minutes 20-30. This failure to represent the drop in wind speed is partly attributed to the model's bias towards higher wind speeds, and partly to an overly rapid wake recovery.

Wake accumulation significantly impacts the local wind speed deficit and, more importantly, the determination of local TI due to the wake-added TI from upstream turbines. This, in turn, significantly affects the wake recovery and wake width through the parameter k_a, thereby influencing the local wind speed deficits. Again, these effects are most significant on deep array turbine locations, and could hardly be captured on small wind farms or wind farm subsets.

Interestingly, the time lag is also dependent on the wind speed change itself. Figure 4.21 indicates that for a continuous decrease in wind speed, the time lag estimation progressively gets worse. This is most easily observed in between minute 20-25 on the signals on turbine A1 and B2 (Figure 4.21a and Figure 4.21b). Whereas the initial drop in power is well captured, the power prediction is progressively worsening as the wind speed keeps decreasing. This goes along with a wind field that convects too slow, since these even more reduced wind speeds arrive too late at downstream locations. Conversely, the power prediction accuracy improves and better approaches the Fastlog power again, only when a temporary increase in wind speed occurs.

4.4. Concluding Remarks on the Calibration Framework

This section functions as a reflection on the presented calibration and validation procedure. Although the calibration framework proved useful to obtain a set of calibrated model constants, reduce the discrepancies between model results and field data, and to have a more thorough understanding of where to expect the largest model uncertainties, some remarks can be made. Therefore, this section briefly highlights the main points of criticism on the calibration procedure, and the limitations of the FLORIDyn model.

Starting with the surrogate model creation, the PCE models should be created using an increased number of FLORIDyn model evaluations to ensure that ε_{LOO} is below the recommended threshold. Nonetheless, additional analysis highlighted that the differences between the full FLORIDyn model and the surrogate model were small enough to be justified, with a strong correlation between the evaluation results from both models. Based on the generated PCE model, the sensitivity analysis was carried out using Sobol' Indices to indicate the variation in model results caused by the variation in model parameters. The sensitivity analysis provided insight in the most influencing parameters, and indicated a dependency on downstream turbine position. In the end, a set of ten model parameters was selected to be included in the calibration process.

The outlined calibration procedure produced a set of calibrated parameters that generally improved the accuracy of the FLORIDyn model across the six analysed cases. However, not all individual simulations showed increased performance. This variability underscores the sensitivity of model parameters to wind conditions and turbine spacing. Additionally, the calibrated parameter set resulted in a wake shape exhibiting inconsistent near-wake behaviour. Not only did it raise questions on the validity of the assumption to represent quasi-instantaneous wakes by time-averaged profiles, it also limits the applicability of FLORIDyn model evaluations. More specifically, the implementation of the FLORIDyn model with the obtained set of calibrated model parameters is limited to wind farms with a minimum turbine spacing that is larger than the near-wake region. Next, The posterior PDFs allowed for a model uncertainty analysis by propagating parameter uncertainties through FLORIDyn model evaluations. The primary conclusion

from this analysis is that uncertainty in power production increases as wakes accumulate on downstream turbines.

Finally, the one-to-one model evaluations on the full wind farm configuration identified the main FLORIDyn model limitations to be the convection model and the wake accumulation handling. The modelling assumptions related to the implementations generally result in the largest model errors at deep array locations, related to insufficient modelling accuracy in wake recovery and downstream wind evolution. The oversimplified convection model based on discrete OPs proved to dampen the fluctuations in the input wind conditions as the field is convecting downstream. In essence, this poses no issues when targeting AEP studies, but the related model bias towards higher wind speeds does significantly affect the power predictions. As a result of the limitation in the convection model, the predicted time lags show decreased accuracy with increased downstream convection distance.

In conclusion, even with a perfect calibration procedure, simplified physics such as simplified flow convection and wake accumulation, or the exclusion of critical physical phenomena like veer, shear, and atmospheric boundary layer (ABL) stability, cannot be fully accounted for. These factors, however, are invariably present in real-world applications, impacting the accuracy and reliability of the model. The current study did not account for these environmental conditions, and consequently, their associated uncertainties were not explored. Future investigations should address these complexities to improve the model's predictive capabilities under diverse and realistic operating conditions.

Despite the analyses in this work being based on a selection of test cases, a comprehensive overview of the FLORIDyn model's limitations has been achieved. This study highlighted the need to incorporate more realistic flow physics to better reflect actual wind conditions and behaviours, especially on deep-array locations. Future work should focus on addressing these limitations, enhancing the model's ability to simulate complex interactions in atmospheric flows.

5

Model Comparison Results

This chapter provides the results of a case study on the Sheringham Shoal wind farm, comparing the performance of several wake models to SCADA 10-minute statistics data. Not only will the FLORIDyn model be validated against the north calibrated and pre-processed field data, it will also be compared to results obtained from other low-fidelity engineering models.

To fully understand and describe both the model predictions and discrepancies with comparison data, this chapter is organised as follows. First, Section 5.1 describes the general set-up for the AEP comparison study. Then, Section 5.2 outlines and justifies the necessary assumptions required to perform the validation study. Next, Section 5.3 displays the results of a data analysis on wind ramp events, aiming to better understand events of dynamic changes in wind conditions. This includes both changes in wind speed and direction. In the following section, Section 5.4, the verification of the synthetic wind generation is discussed. The outlined findings in Section 5.2 to Section 5.4 lead to the AEP comparison study results in Section 5.5, where the FLORIDyn model performance on a uniform wind rose is assessed against benchmarking steady-state model results and SCADA data. Finally, Section 5.6 provides a summary of the main findings in this chapter.

5.1. Model Comparison Set-Up

This section details the setup for the model comparison study, outlining the configurations and modelling choices used to evaluate various wake models. By establishing a comprehensive framework, a systematic and consistent evaluation process is ensured. The set-up description includes four considerations: selection of wind speed range, data binning, benchmarking models, and the selection of model constants. This thorough description aims to clarify the processes involved, ensure reproducibility, and lay the groundwork for the subsequent analysis and discussion of the results.

Firstly, the validation and comparison analysis focuses exclusively on the wind speed range of [4.5 - 12.5] m/s, rather than the full wind speed range. This selection reduces the number of required simulation runs, thereby decreasing computational expense. Secondly, this range represents the operational conditions where turbines generate a significant portion of their energy output, experience the largest C_P and C_T values, and produce the most significant wakes. Therefore, accurately representing wake losses within this wind speed range is crucial for implementing effective wind farm control strategies. For wind speeds above the rated speed, wind speed deficits are not directly linked to energy losses due to power limitations.

Furthermore, wind speeds within this range are most relevant for evaluating the practical performance of the turbines under typical operational conditions. Low wind speeds contribute less to overall energy production and are thus less critical for optimising turbine performance. Conversely, higher wind speeds result in higher power outputs but also lower thrust coefficients (C_T), leading to smaller wake effects. By focusing on the [4.5 - 12.5] m/s range, the analysis ensures a balanced evaluation of both energy output and wake dynamics under the most impactful and commonly encountered conditions, as indicated by Figure 5.1.

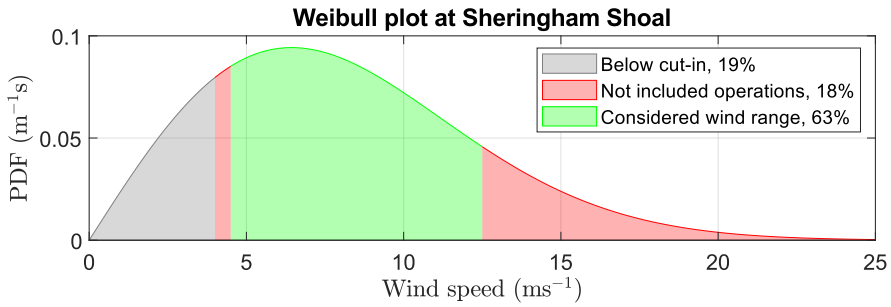

Figure 5.1: Weibull plot indicating the wind conditions at the Sheringham Shoal wind farm, with the interesting wind speed ranges indicated.

The choice to focus the analysis on the wind speed range of [4.5 - 12.5] m/s is further justified by the data presented in Figure 5.1, which indicates that this range encompasses 63% of the wind conditions encountered at the Sheringham Shoal wind farm, representing the majority of the operational conditions. Additionally, wind speeds below the cut-in threshold, which account for 19% of the encountered conditions, are not relevant for energy production as the turbines do not generate power in these scenarios. The remaining 18% of wind speeds, which fall outside the analysed range but are still within operational limits, represent conditions that, while significant for AEP, occur less frequently. To go along with this, the range [4 - 4.5] m/s is significantly close to cut-in conditions and will likely comprise turbine start-up and shut-down operations, which are already filtered out of this work's analysis. Therefore, focusing on this critical [4.5 - 12.5] m/s range ensures that the findings in this analysis are directly applicable to improving the efficiency and reliability of wind farm operations, where accurate wake modelling can have the most substantial impact.

Secondly, the data binning procedure is detailed. Data binning is a crucial step in the model comparison study, ensuring that the wind data is organised systematically for accurate analysis. The choice of an adequate bin width should consider a balance between resolution and data availability. Especially considering the wind direction bin width, it should be fine enough to capture directional variations in the wind, which are critical for wake modelling, yet broad enough to provide sufficient data points within each bin for meaningful statistical analysis.

Similarly, the bin width for wind speed categorisation should be determined. Considering the cubic relation between wind speed and power (Equation 3.12), small variations in wind speed result in significantly larger power variations. Combining the requirements for both the wind speed and direction binning process, bin widths of 1 m/s and 5° were selected. These choices align with the industry standards on wind data binning, and provide a solid foundation for subsequent analyses and extension of this comparison study.

For the final aspect of the binning procedure, the overlap between bins is considered. Non-overlapping bins mean that each data point is assigned to one and only one bin, preventing ambiguity in the categorisation process. This approach simplifies the interpretation of results, as each bin represents a distinct range of conditions, without the smoothening effects of bin overlap. Finally, Table 5.1 summarises the choices related to data binning.

Parameter	Wind direction bin centres	Wind direction bin width	Wind speed bin centres	Wind direction bin width	binning overlap
Choice	[2.5 - 357.5] deg	5 deg	[5 - 12] m/s	1 m/s	0%

Table 5.1: Summarising overview of the data binning choices.

Next, the comparison study in this work comprises six different data origins. Whereas the field data can be directly processed after data filtering operations, model results should be generated according to the same binned wind conditions to allow for a fair comparison. This work will consider five distinct model evaluations: two internal SGRE steady-state models, and three evaluations of the FLORIDyn model. The

SGRE models, labelled as 'Model 1' and 'Model 2' are included to expand the validation study analysis, but remain anonymous in this work for confidentiality purposes.

On the other hand, the FLORIDyn model runs are carried out on three levels of complexity, mainly related to the inflow generation and model dynamics: steady-state, dynamic wind changes, and fully dynamic (both wind speed and direction). These three evaluations allow for a gradual increase in modelling complexity, and the identification of potential increased accuracy or model limitations.

All the steady-state model evaluations, including the steady-state FLORIDyn, are set up to yield in three simulations per wind direction bin, initialised at the bin centre and bin edges respectively. This choice is made to implement a slight smearing out effect of the model predictions due to the bin averaging. The same implementation is not enforced in the dynamic FLORIDyn evaluations due to the significantly increased computational times. Therefore, a single model evaluation is considered on these cases, where the variability in the synthetic wind direction is assumed to cover the smoothing effect related to averaging over multiple simulations. This modelling choice leads to half the required total model evaluations compared to the steady-state models.

Lastly, the used values for the model constants are discussed. The steady-state FLORIDyn model evaluations are run based on the baseline model constants provided in Table 3.5. Given the outlined calibration procedure in this work, the model constants for both the FLORIDyn dynamic wind direction and fully dynamic implementations are carried out based on the $\hat{\theta}_{MAP}$ outcomes tabulated in Table 4.3. Finally, an overview of the configurations used in this work's comparison and validation study are tabulated by Table 5.2.

Model Run	Mean wind speeds	Mean wind directions	Model Constant Tuning	# Simulations
FLORIDyn Steady	[5 : 1 : 12] m/s	[0 : 2.5 : 357.5] deg	Baseline	1152
FLORIDyn Dynamic Wind Direction	[5 : 1 : 12] m/s	[2.5 : 5 : 357.5] deg	Calibrated	576
FLORIDyn Fully Dynamic	[5 : 1 : 12] m/s	[2.5 : 5 : 357.5] deg	Calibrated	576

Table 5.2: Overview of the different considered configurations for the FLORIDyn model evaluations.

5.2. Main Assumptions and Limitations for the Validation Study

In order to effectively evaluate and validate the performance of the wake models on AEP prediction, it is essential to clearly outline the underlying assumptions for the framework employed in this work's comparison study. This section provides a detailed description of the key assumptions that form the foundation of the modelled wind conditions and data analysis, ensuring a transparent and rigorous assessment process. Understanding these assumptions and their implications is crucial for interpreting the results and drawing meaningful conclusions about model capabilities and limitations.

Atmospheric Conditions

Within the scope of this work, the influence of atmospheric conditions is not considered. This includes the effects of temperature change, changes in air density or pressure, atmospheric boundary layer stability, and wind speed profile (shear and veer). Therefore, the comparison study in this work inherently assumes neutrally stable boundary layer stability. Additionally, no boundary layer effects are considered in the model evaluations. This modelling choice stems from the data filtering process. Instead of using the raw wind speed measurements, a channel indicating the rotor equivalent wind speed is used to perform the filtering, binning and model input generation procedures. Additionally, the considered air density is assumed to always be at standard sea level conditions (1.225 kg m^{-3}). Due to its direct influence in C_P and C_T computations, this assumption will result in additional scattering of field data points along the wind speed and direction bins.

Nonetheless, the assumption of neglecting the influence of atmospheric conditions significantly reduces the number of simulations required to be run. Instead of having to set up multiple simulations per wind

speed and direction bin, a single model evaluation suffices, especially for steady-state model evaluations.

Nominal operations of upstream turbines
The analyses in this validation study assume that all turbines are operational on all AEP simulation runs. As mentioned in Section 4.2.1, it rarely occurs that all turbines on a wind farm are simultaneously operating in nominal conditions, especially on large wind farms. Additionally, Section 4.3.4 discussed the limitations in this work related to modelling non-operative / non-nominally operating turbines. In order to omit comparison with erroneous model evaluation results, these data points have been filtered out on an individual turbine basis.

Although the filtering operations outlined in Section 4.2.1 detect and remove non-nominal turbine operations, the results in Section 4.3.4 also highlighted the impact of inadequately modelling non-nominal turbine operations on downstream turbines within their wakes. Therefore, it is essential to mitigate these effects in the validation study, and an additional filter is applied to exclude instances where a turbine operates directly in the (theoretical) wake of an upstream turbine undergoing non-nominal operations. Thus, a SCADA data point is removed if either the turbine of interest is operating non-nominally, or if a turbine directly upstream, causing wake effects, is operating non-nominally. The implementation of this additional filter is depicted by Figure 5.2.

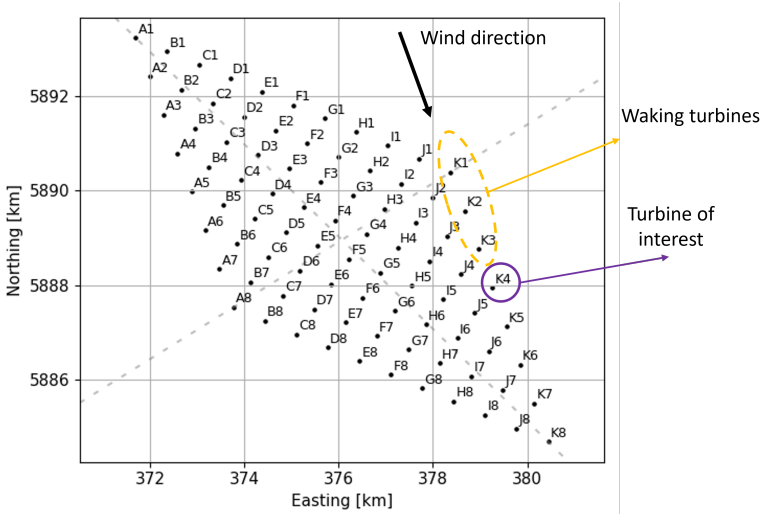

Figure 5.2: Illustrative example of the identification of upstream waking turbines to perform data filtering related to upstream turbine unavailability.

For the illustrative example displayed by Figure 5.2, the data point for turbine K4 is only retained if turbines K1, K2 and K3 all function in nominal operations. If any of the waking turbines, or the turbine of interest, is operating following a different regime, the data point is filtered out.

This assumption not only significantly reduces the number of required simulation runs to represent all turbine operations, but also addresses a critical limitation. The lack of availability of LUTs for curtailed operations within this framework prevents the implementation of a representative turbine initialisation. Therefore, this filtering operation enables a more accurate comparison between field data and model evaluation outcomes for wake losses and power ratios, though it impacts the absolute value of the predicted AEP.

Essentially, a conditional AEP is computed, dependent on the applied filtering operations (nominal operation, signal availability, and waking turbine operations). Consequently, the AEP observed in real-world applications, where continuous nominal turbine operations cannot be assumed, will most likely be lower. Nonetheless, the assumption supports a robust comparison study, yielding quantitative indicators of model performance.

Single C_P-C_T LUT for all simulations
One of the limitations in this study is the use of a single C_P-C_T LUT, due to limited data availability within this study. This work uses a single steady-state LUT that is generated with a reference TI value of 7%. Obviously, TI values vary per wind conditions, and so do the C_P-C_T, with the most significant differences occurring close to the rated wind speed. The qualitative influence of TI on a general C_P curve is indicated by Figure 5.3, and displays a smoothening effect on the sharp edge at rated wind conditions. Therefore, additional uncertainty on the model results is introduced by this limitation of including a single power curve. Nonetheless, this work will not present a quantitative analysis on this added uncertainty.

Next to the influence of TI, discrepancies between the operational C_P-C_T and the theoretical curves can also arise due to blade degradation and wear-down effects, or other environmental conditions. Again, no quantitative estimate on the influence can be detailed in this work. Therefore, it is important to be aware of these effects when analysing simulation results. Finally, model cross-comparison can still be performed since the same assumption is valid for all model evaluations.

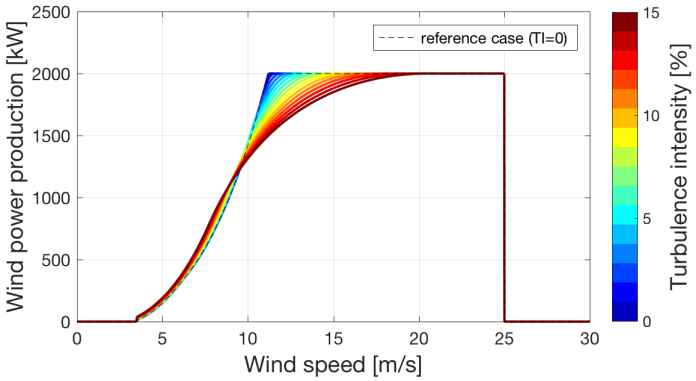

Figure 5.3: Illustrative example to visualise the effect of TI on an operational C_P curve. Imaged adopted from Saint-Drenan et al. [106]

Spatially homogeneous wind conditions
This work's analysis is limited to spatially homogeneous wind conditions. This assumption is primarily imposed to facilitate comparison across multiple models, as not all low-fidelity wake models support heterogeneous wind fields. On the other hand, the implementation of spatial heterogeneity raises additional complexities with the binning process. Firstly, the identification of reference and waking turbines in this analysis would need to be revised. Secondly, additional investigation by means of data analysis would be required to better understand the present gradients and how to include them in the inflow generation procedure.

Finally, this work did not consider applying an additional data filter to identify or remove cases with significant spatial gradients in wind conditions. As a result, a bias could be introduced in the binning process due to these present cases. However, no quantitative estimate on the resulting uncertainty related to these wind conditions is obtained. Therefore, it is key to be aware of this potential influence when drawing conclusions from the comparison results.

Statistically stationary wind conditions
As an initial approach, this work introduces a synthetic wind generation procedure to model the inflow wind conditions, and set up AEP simulations for the FLORIDyn model. In order to obtain a comparison that is consistent with the assumptions for steady-state model results, and with the synthetic wind generation methodology, the assumption of a statistically stationary wind field is introduced. In essence, this means that changes in steady state wind conditions are small enough to be neglected, and thus no significant changes in wind speed or direction occur during the modelled time period.

Since there is no definitive answer regarding the validity of this assumption, further data analysis is necessary to investigate its effects. Therefore, Section 5.3 outlines an additional data analysis study to investigate the magnitude and probability of occurrence of dynamic wind events, and the implications on this work's comparison study.

5.3. Additional Data Analysis on Wind Assumptions

This section outlines the data analysis procedure used to investigate dynamic wind events and verify the assumption of statistically stationary wind conditions. In this work, dynamic wind events are characterised by rapid changes in wind speed or direction as these are the main input parameters for the wake model simulations, and define the SCADA data binning procedure.

Rapid changes in wind conditions can significantly impact power output, especially on a wind farm scale. The analysis in this work involves identifying and characterising these events using SCADA data, as 10-minute averaged statistics, and applying statistical techniques to assess their occurrence, amplitudes, and duration. Additionally, the results are examined to reflect on the assumption of statistically stationary wind conditions, crucial for accurate wake modelling and energy production estimates. This methodology aims to provide a foundation for understanding wind dynamics and improving how to model these effects on wind farm performance predictions.

Given the outlined data binning procedure in Section 5.1, the analysis in this approach will consider a dynamic wind event to occur if the change in the mean statistics over subsequent SCADA data points is larger than the bin width. This procedure is applied to both wind speed and direction analyses in this work, but can be applied to any metric of interest. To track the identification of so-called wind ramp events, an indicator function is expressed by Equation 5.1.

$$\left.\begin{array}{lll} I = 1 & \text{if} & \left|\overline{M}^{t+1}_{\text{SCADA}} - \overline{M}^{t}_{\text{SCADA}}\right| \geq \text{threshold} \\ I = 0 & \text{if} & \left|\overline{M}^{t+1}_{\text{SCADA}} - \overline{M}^{t}_{\text{SCADA}}\right| < \text{threshold} \end{array}\right\} \quad \text{with} \quad \text{threshold} = \text{width}_{bin} \tag{5.1}$$

$\overline{M}$ represents the time averaged metric to be analysed. The indicator equals one for both the instants t and $t+1$ if an event is identified. Note that this approach assumes that the changing wind conditions are represented by a linear change between the mean values of the analysed metric in the samples. With two subsequent SCADA samples spanning a total period of 20 minutes, this methodology can not distinguish between wind changes that occur in shorter time periods. Therefore, it is assumed that the wind ramp takes place in the 10 minutes between the mid-points of the time instants linked to the SCADA data points.

To minimise the influence of wake effects on the data analysis, this detection methodology is solely applied to the turbines operating in free-stream conditions. Therefore, a set of reference turbines is identified per wind direction, as displayed by Figure 5.4 for two distinct inflow directions.

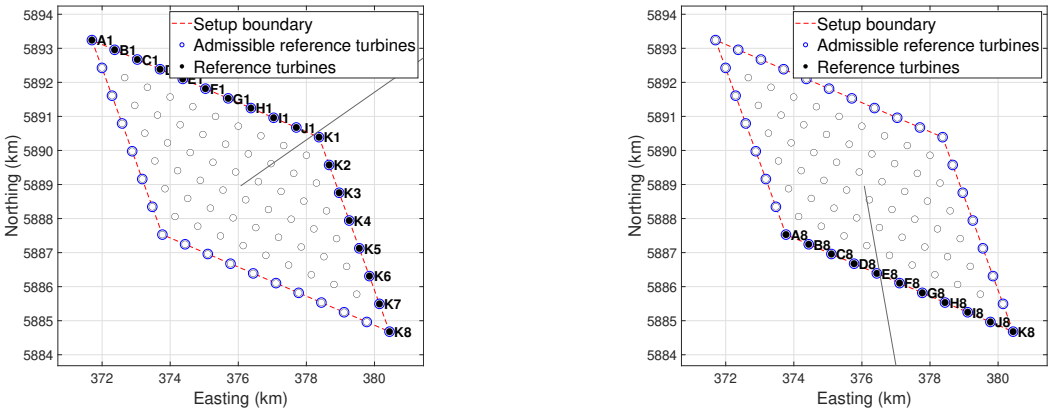

Figure 5.4: Identification of reference turbines for two wind directions: 55° on the left, 170° on the right.

As indicated by Figure 5.4, the number of identified reference turbines is dependent on the wind direction and wind farm layout. Performing the ramp detection procedure on this set of reference turbines by itself would thus naturally create an artificial weighting to the data analysis. In other words, wind directions containing more reference turbines would have larger relative weightings in the statistical analysis. To circumvent this apparent weighting influence, the operation described by Equation 5.1 is applied to all

the identified reference turbines for a given wind direction. However, only if 75% or more of the reference turbines are identified to experience a wind ramp event, the indicator is set to 1 for the corresponding time instant. Additionally, the magnitude of the wind ramp is determined as the ensemble averaged value over the reference turbines. A similar approach is taken for the mean value of the metric of interest. By implementing this approach, the spatial gradients on the wind farm are inherently neglected.

Next, it is interesting to combine subsequent time instants of identified ramp events. Given that these ramp events frequently span multiple consecutive subsets of SCADA data points, subsequent wind ramp events are concatenated and attributed to the same identified event. Not only does this indicate an increased time period on which the observed wind ramp events take place, it also indicates a better estimate on the true magnitude and duration of an identified ramp event. The results of this approach are illustrated by Figure 5.5, displaying identified wind ramp instances on a wind direction time series plot.

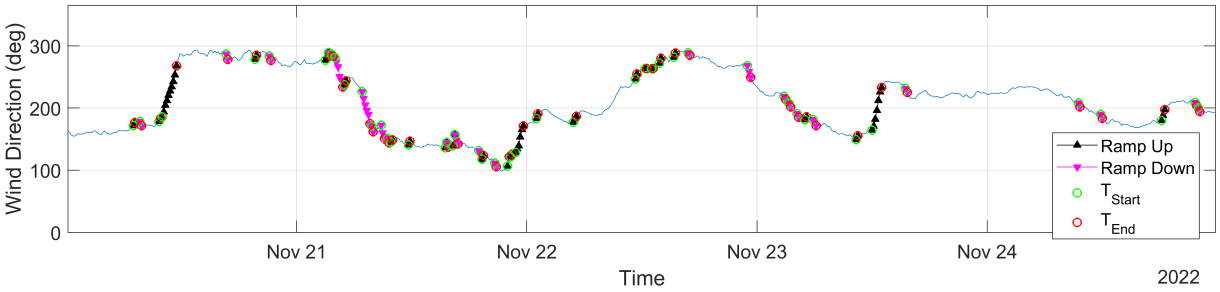

Figure 5.5: Illustration of the wind ramp detection results for a wind direction time series. Note that instances of subsequent ramp detection are concatenated, and start and end points are indicated. A distinction is made between ramp-up (anti-clockwise) and ramp-down (clockwise) wind direction change events.

It is apparent from Figure 5.5 that such ramp event are no rare occurrences. In the analysed SCADA dataset, 15.73% of the data points were identified as wind direction ramp events, while 7.47% were identified as wind speed ramp events. Conversely, 84.27% of the time instants showed statistically stationary wind direction, and 92.53% showed statistically stationary wind speed. Thus, while the assumption of statistically stationary wind fields is generally valid for wind speeds, wind direction ramps occur more frequently and are of greater significance. Therefore, the remainder of this analysis will primarily focus on changes in wind direction.

To gain more insight in the frequency of occurrence, and magnitude of such ramp events, Figure 5.6 displays a histogram plot for the computed wind direction changes over individual pairs of two subsequent SCADA time instants.

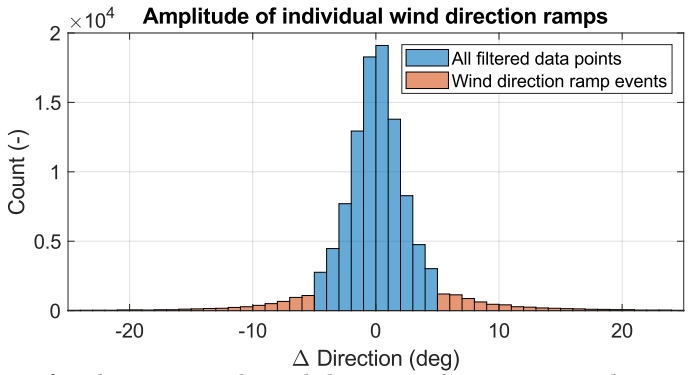

Figure 5.6: Histograms for the computed wind direction changes over subsequent SCADA data points.

Due to the definition of the detection algorithm, the identified wind ramp events represent the tails on the distribution presented by Figure 5.6. Furthermore, a relatively symmetric distribution is observed, with a slight bias towards positive (anti-clockwise) wind direction changes.

Next to the individual wind ramp amplitudes, Figure 5.5 indicates that it is not uncommon to observe identified ramp events that span more than two subsequent SCADA samples. Therefore, it is interesting to investigate the total duration and magnitude when combining subsequent identified time instants. These properties are displayed by Figure 5.7a and Figure 5.7b.

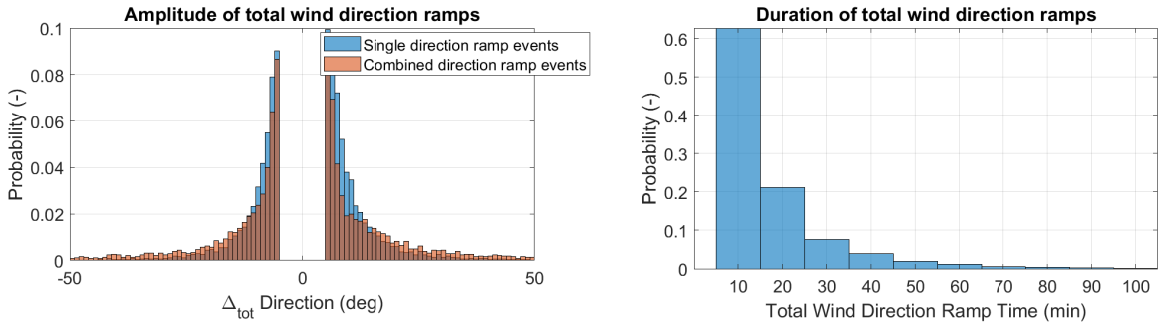

(a) Total wind direction ramp magnitude.

(b) Total wind direction ramp duration.

Figure 5.7: Histogram plots indicating the amplitudes (Figure 5.7a) and duration (Figure 5.7b) of total wind direction changes.

As observed from Figure 5.7b, the time scales involved in the wind direction ramp events can easily span multiple 10-minute windows, combining into a significant total change of wind direction. Whereas this work only considers dynamic FLORIDyn evaluations on statistically stationary 10-minute windows, a strong case can be made to include both longer time periods and wind direction ramp events to capture a wider range of wind conditions in AEP predictions. Additionally, the applied filtering operations on the SCADA dataset do not filter out such dynamic wind events, and will introduce thus additional uncertainty in the model comparison study as the simulation runs do not account for these cases.

Finally, an investigation into the origin of the wind ramp events is outside the scope of this work. The main goal of the data analysis was to highlight the significance of dynamic wind events, and the relation to the modelling assumptions. However, to gain more insight in the underlying physics that drive the identified dynamic wind events, a detailed analysis into weather systems, frontal passing, and relation to high ambient turbulence should be carried out. Additionally, the effects of seasonal variation could be investigated, as winds are generally stronger during the European winter months, characterised by unstable atmospheric conditions and the cyclonic wind storm season [107].

Next to investigating the assumption of statistically stationary wind conditions, a spectral analysis is conducted to verify the validity of the assumed spectrum for the synthetic wind generation procedure (Section 3.3.1). Therefore, Figure 5.8 displays the generated power spectral density (PSD) plot resulting from the ensemble averaged wind speed time series over the reference turbines per wind direction.

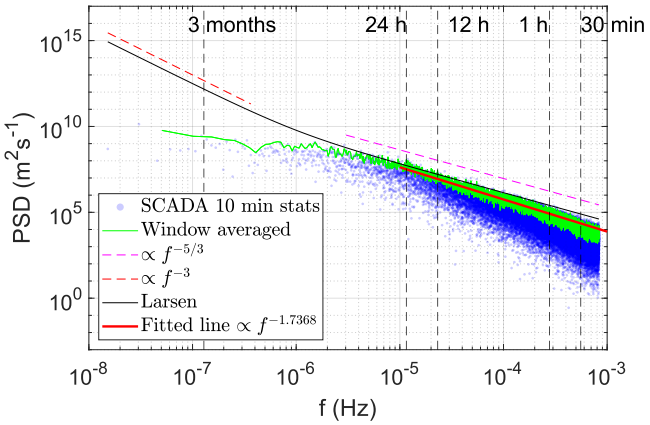

Figure 5.8: PSD plot for the wind speeds ensemble averaged over the reference turbines.

Figure 5.8 displays five curves in total. Note that a window averaged evaluation is made on the SCADA data to obtain a more continuous PSD signal. The downside of this consideration is the loss of information on low frequencies. Even in the raw PSD for the SCADA dataset, limited resolution in the low frequency range is observed. This also explains why the computed spectrum does not follow Larsen's prescribed spectrum in this region. Within the scope of this work however, these low frequencies are not the main interest, and are mainly linked to slow, and large mesoscale effects.

As observed in Figure 5.8, the fitted line to the PSD scales with $f^{-1.7368}$, and is in close correspondence with the considered exponent of -5/3 in the synthetic wind generation. Especially for short time periods, like the 10-minute samples considered in this work, the assumption of using the -5/3 exponent is validated to use for the spectral description in the synthetic wind generation.

5.4. Verification of Synthetic Wind Generation

Synthetic wind generation plays a crucial role in obtaining reliable model outputs, providing a controlled and repeatable dataset for evaluating and optimising model performance. This section discusses the verification of the synthetic wind field generation, following the methodology outlined in Section 3.3.1. Firstly, the correct implementation of the prescribed procedure is verified. Additionally, the section reflects on the anticipated discrepancies with real-world conditions and their effects on the AEP simulation runs. The findings contribute to a better understanding of how synthetic wind data can be utilised to enhance the predictive capabilities of dynamic wake models.

Consistent with the SCADA data, all synthetic wind generations in this work are generated based on a targeted 10-minute simulation time, and manipulated to account for the simulation startup transient time, as described and illustrated in Section 3.3.1. An example of the generated wind field by the derived Mann plane approach is displayed by Figure 5.9 by means of a filled contour plot.

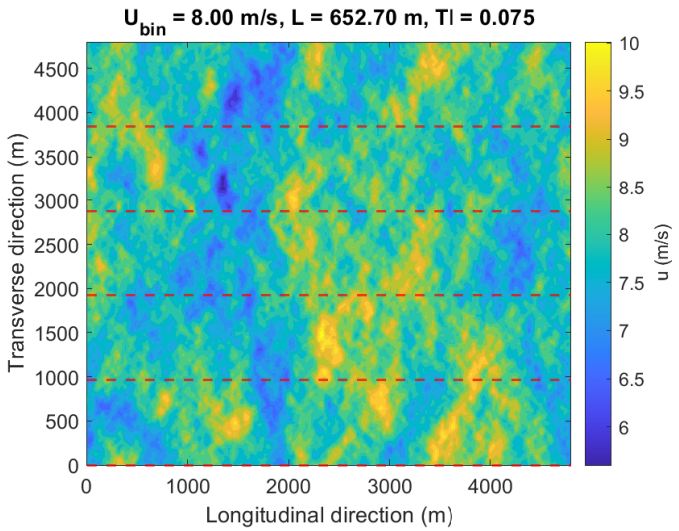

Figure 5.9: Results for six realisations of the synthetic wind generation procedure on an input wind speed of 8 m/s, wind direction of 0 deg and TI = 7.5%.

In order to obtain time series realisations from the velocity field presented by Figure 5.9, the red lines indicate the sampling locations. Due to the cyclic boundary conditions, homogeneous and isotropic assumptions, an equidistant sampling distance is implemented along the transverse direction to minimise the correlation between different samples. As an alternative approach to ensure uncorrelated realisations, different wind fields could be generated, only taking a single sample per generation.

Given the frozen turbulence assumption, these spatial signal realisations are easily transferred into time series. The resulting time series plots for the longitudinal and vertical velocity components, as well as the resulting wind direction and PSD plots on the five realisations, are displayed by Figure 5.10.

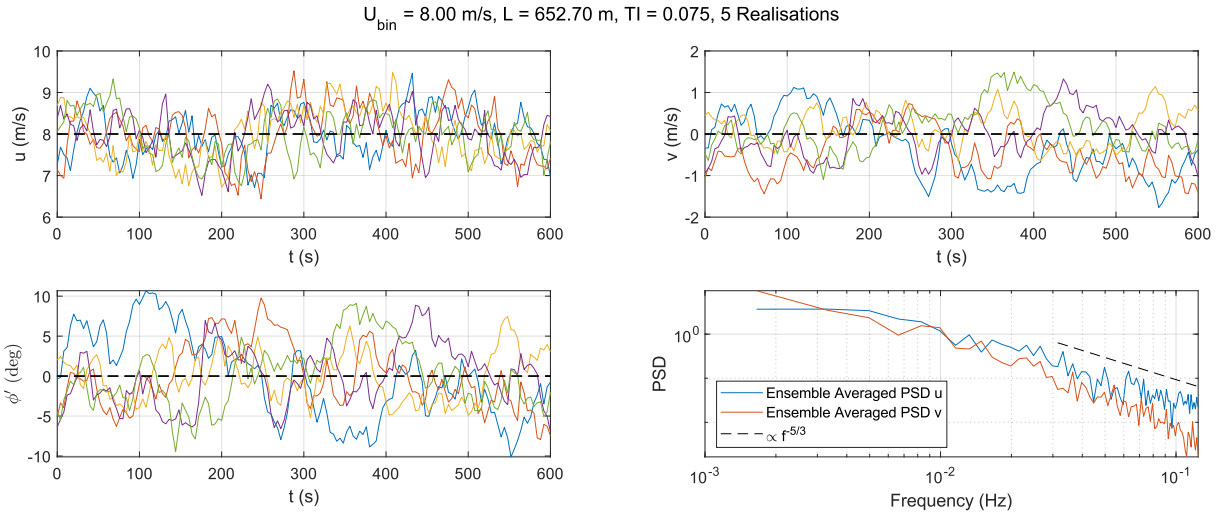

Figure 5.10: Generated wind signals for u, v, ϕ, and PSD of the velocity components.

As indicated by Figure 5.10, time varying wind signals are generated by the adapted 2D Mann method. Consistent with the input spectrum, the PSD curves for the longitudinal and lateral velocity components display the expected behaviour. As an additional check, although the curves in Figure 5.10 look to fluctuate around the correct mean values, Figure 5.11 indicates the time-averaged mean properties per realisation.

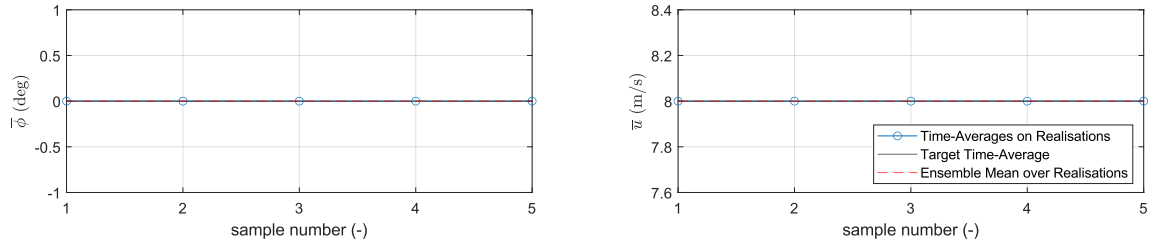

Figure 5.11: Verification plots highlighting convergence between target and generated time-averaged properties.

A correct implementation of the outlined synthetic wind generation is shown by Figure 5.9 to Figure 5.11. For a given set of input binned wind conditions, a desired number of realisations can be generated. For the analysis that will be conducted in Section 5.5, only a single realisation per wind conditions is considered. Despite being a radical approach that doesn't account for the inherent randomness in generating synthetic wind inputs, the resulting FLORIDyn outcomes still offer valuable insights into model performance. Given the increased computational expense associated with FLORIDyn's time-dependent capabilities, this approach serves as a preliminary effort to conduct model comparison studies.

A second limitation of the employed synthetic wind generation procedure is the assumed homogeneity and isotropy. Since the wind direction signal is directly obtained from the computed angle between the longitudinal and lateral velocity components, the resulting wind fluctuations are expected to have amplitudes that might be higher than real-world conditions. However, this hypothesis could not be verified within the scope of this work, and should be considered in future iterations.

The effect of larger wind direction fluctuations (especially in the transverse wind speed component v) is similar to an increased bin width setting in the data binning procedure. As a wider range of wind directions is encountered, the modelled wakes will be convected in different directions as well, leading to more smeared out wake effects.

5.5. Model Comparison Results

This section presents the results of a comprehensive model comparison study aimed at evaluating the performance and accuracy of various wake modelling approaches. The primary objective of this study is to assess the predictive capabilities of different models under diverse conditions, thereby identifying their strengths and limitations. By systematically comparing these models, a better understanding of their applicability and reliability in different scenarios is sought. The comparison study involves rigorous comparison of the FLORIDyn model results against a set of predefined benchmarks, which include both real-world measurement data and results from steady-state model evaluations. Key metrics for this evaluation include accuracy in predicting wake losses (power ratios), error metrics on raw power output, AEP, and computational cost. All metrics, except for computational cost, will be compared for all the considered wake models considered in this work.

Within this model comparison section, all simulated wind conditions, and measurement data are considered to be equally weighted. By applying equally weighted wind condition probabilities (uniform wind rose) in simulations, the comparison remains unbiased by site-specific wind conditions. Therefore, the applied model comparison and validation methodology is robust, and can be applied to any wind farm location and site conditions.

The first metric to be analysed is the raw power prediction. To represent this metric, Figure 5.12 displays the power outputs per model on a polar plot, averaged over the considered wind speed range. Note that due to data confidentiality, no actual power values are indicated, only anonymised results for power production are provided. However, the depicted results still allow for a qualitative analysis to draw relevant conclusions on model performance.

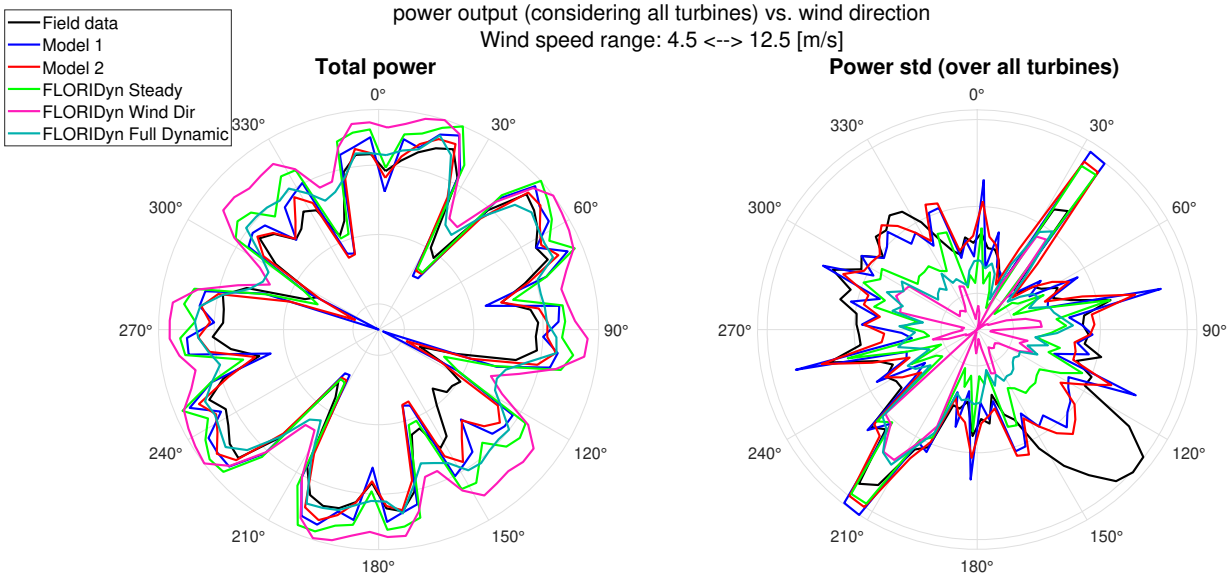

Figure 5.12: Model comparison on the predicted power per wind sector for all models, averaged over the considered [4.5 - 12] m/s wind speed range.

Firstly, Figure 5.12 illustrates that the field data results are generally symmetric on the polar axes, attributable to the regular grid layout of the Sheringham Shoal wind farm. The most significant region of asymmetry is identified in the [120 - 150] degree wind direction sector. A potential cause for this observed dissimilarity is an insufficient modelling approach for the input ambient TI.

TI serves as a crucial statistical indication of the encountered turbulence, and is used in many engineering applications to represent wake mixing. However, in many validation studies like the one presented in this work, the available wind data may not be comprehensive enough to allow for a detailed analysis of TI variations with wind speed and direction. This is partly due to the location of the wind speed sensors on the turbine. Cup or supersonic anemometers are located on the nacelle, downwind of the blades. Therefore, the measurements are significantly affected by blade passing and wake effects. Hence, the computation of $TI = \sigma_u/\overline{u}$ is not reliable due to the increased wind speed variations induced by the blade passing.

Nonetheless, TI is a crucial input parameter for both the steady-state, and FLORIDyn models used in this work. Due to the absence of a reliable turbulence intensity estimator, a simple TI mapping against wind speed was used in this work. This assumption is based on the stronger TI dependency on wind speed than on direction in many offshore environments, particularly in relatively uniform terrain [108]. The used TI mapping in this work is displayed by Figure 5.13.

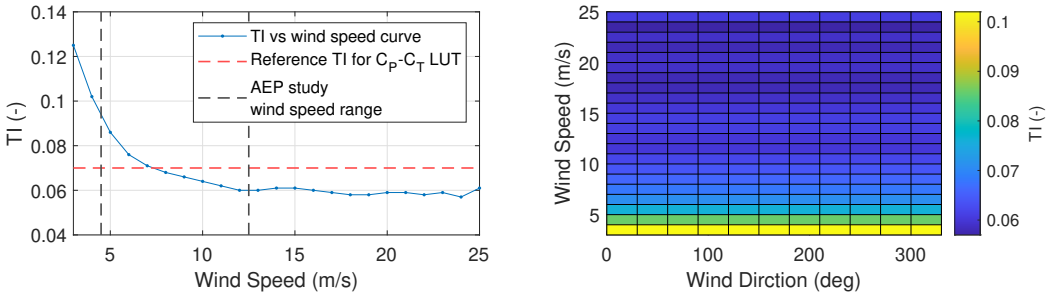

Figure 5.13: TI mapping used to initialise the AEP simulation runs.

Figure 5.13 indicates that within the considered wind speed range in this work, the TI is observed to decrease from around 9% at 4.5 m/s to 6% at 12.5 m/s. Additionally, the used reference TI for the C_P-C_T LUT corresponds to a wind speed of roughly 7 m/s, consistent with the most probable wind speed encountered at the site conditions (Figure 5.1).

The effect of this TI insensitivity to wind speed assumption is that the simulations launched for the AEP comparison study will display symmetry on a wind rose, as observed from Figure 5.12. Although the offshore location exhibits a uniform terrain, neighbouring wind farms are expected to increase the ambient TI from their relevant direction of influence. Observing the site location in Figure 3.6a, especially the NE and NW wind directions are expected to show increased TI compared to their SW and SE counterparts. Given the influence of the shore on SW wind directions, the difference is expected to be less than the NW-SE wind direction set. In this latter case, the SE wind originates from the open sea, rather than from land or influence by other wind farms, and is expected to be paired with both low TI values and a less significant wind shear profile. Therefore, this assumed TI uniformity with wind direction will induce errors related to input wind modelling, and the implemented wake recovery dependency on TI.

This hypothesis is confirmed by analysing the power standard deviation plot in Figure 5.12, which shows higher standard deviations in the field data for the [120 - 150] degree wind direction sector. This indicates larger differences between turbine power outputs, suggesting reduced wake recovery and a lower power output on waked turbines, consistent with the observed reduced power outputs. Across all considered models, TI significantly influences the wake recovery rate. Therefore, the anticipated but uncaptured lower TI values in the [120 - 150] degree wind direction sector lead to a significant overestimation of power prediction in this sector by all models.

Next to the symmetry in model results, Figure 5.12 indicates that the steady-state models generally capture the trends displayed by the field data. In general, steady-state models tend to overestimate the power output of wind farms. However, for wind directions that align with the smallest turbine spacing, these models consistently underestimate power. This indicates that while power is underestimated in conditions with the most severe turbine alignment, the models generally predict wake recovery to be quicker than the field data observations in turbine alignment configurations that are indicated by larger turbine distances and partially waked conditions.

In line with the concluded FLORIDyn model limitations in Section 4.3.4, Figure 5.12 displays a significant power overestimation on the majority of wind directions. Additionally, on farm configurations with the most number of aligned turbines, and thus largest wake accumulation influence, the dynamic FLORIDyn evaluations display small power standard deviations on power. This highlights the convection model and wake-added TI deficiencies, as the input fluctuations are dampened out, and predicted wake recovery is too high. Interestingly, also the steady evaluation of the FLORIDyn model displays significant power overestimation on the entire wind rose, except for the most severe aligned wind directions, corresponding to the smallest turbine spacing. This observation re-iterates the model deficiencies related to wake accumulation.

In order to grasp a more comprehensive understanding of the main limitations of the considered models, an analysis based on power ratios is considered. The evaluated power ratio considers the ratio between the free-stream power and the actual turbine power, defined in Equation 3.30. The results of this analysis are visually displayed by Figure 5.15. Note that the power ratios are plotted against the wind direction bins, averaged over the considered [4.5 - 12.5] m/s wind speed range.

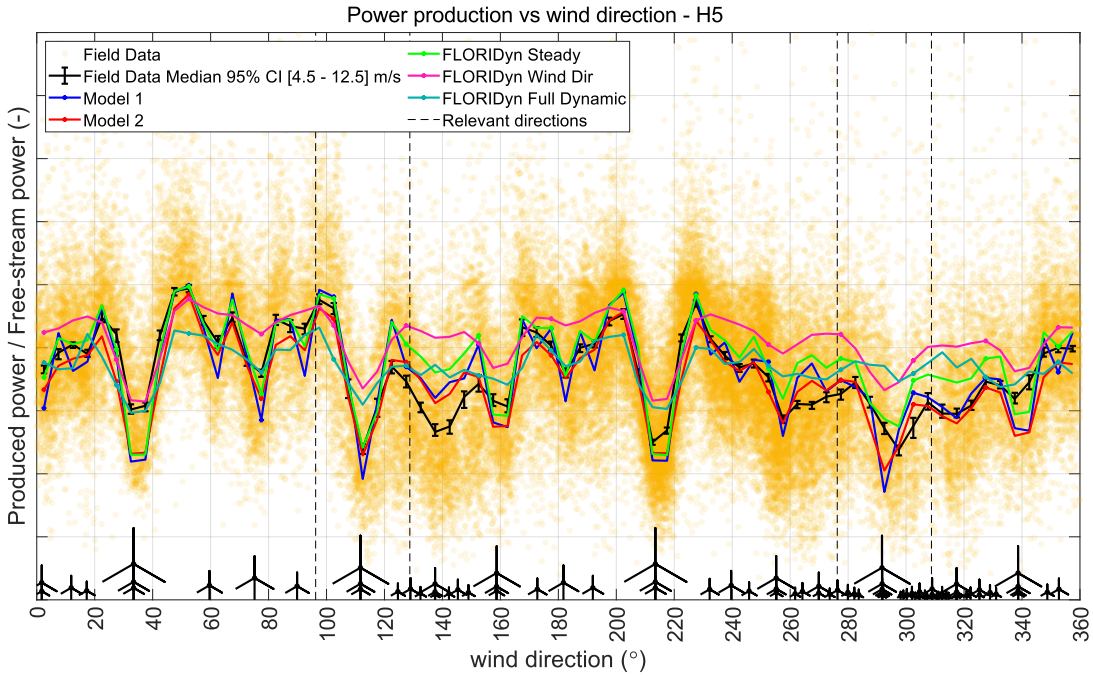

(a) Power ratio along the full wind direction range for turbine H5.

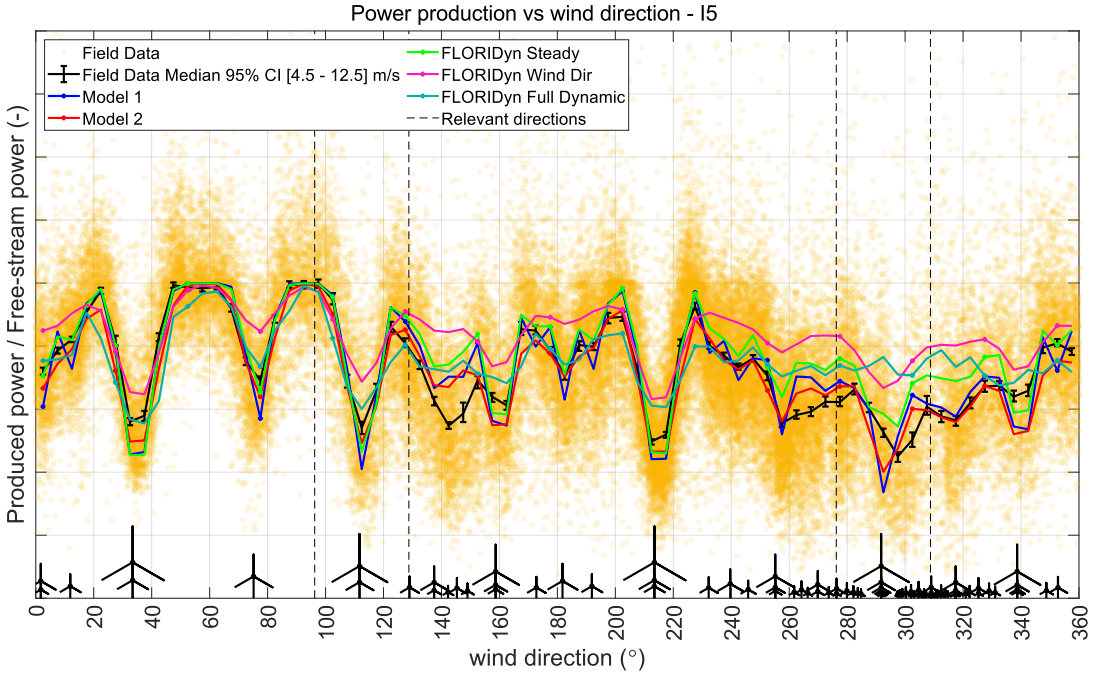

(b) Power ratio along the full wind direction range for turbine I5.

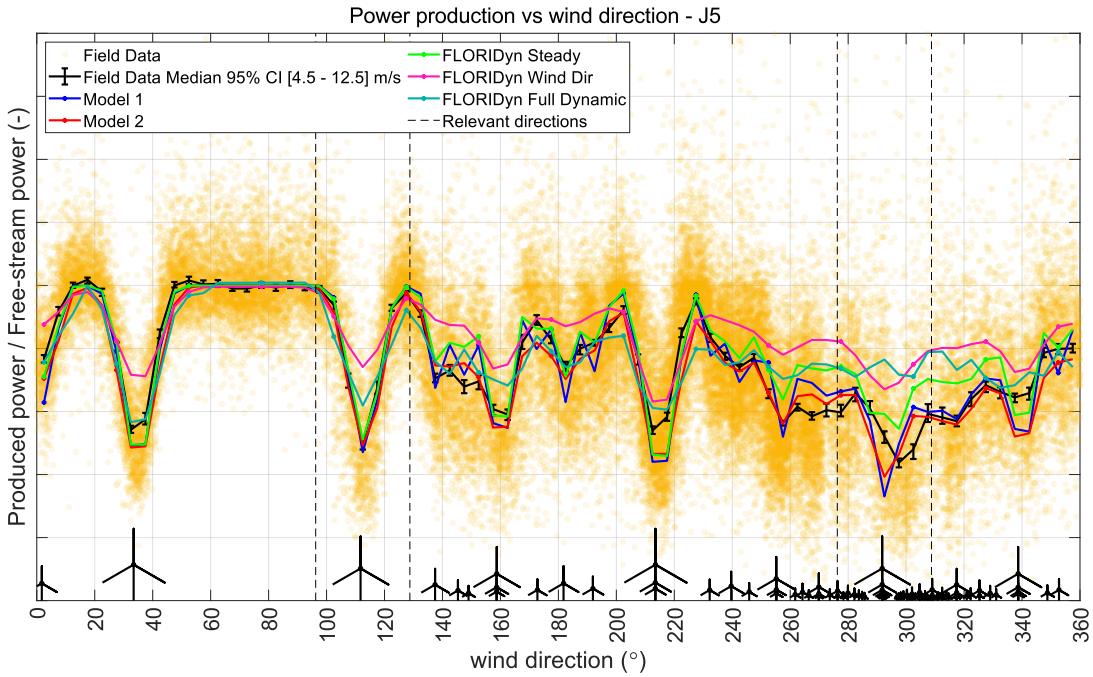

(c) Power ratio along the full wind direction range for turbine J5.

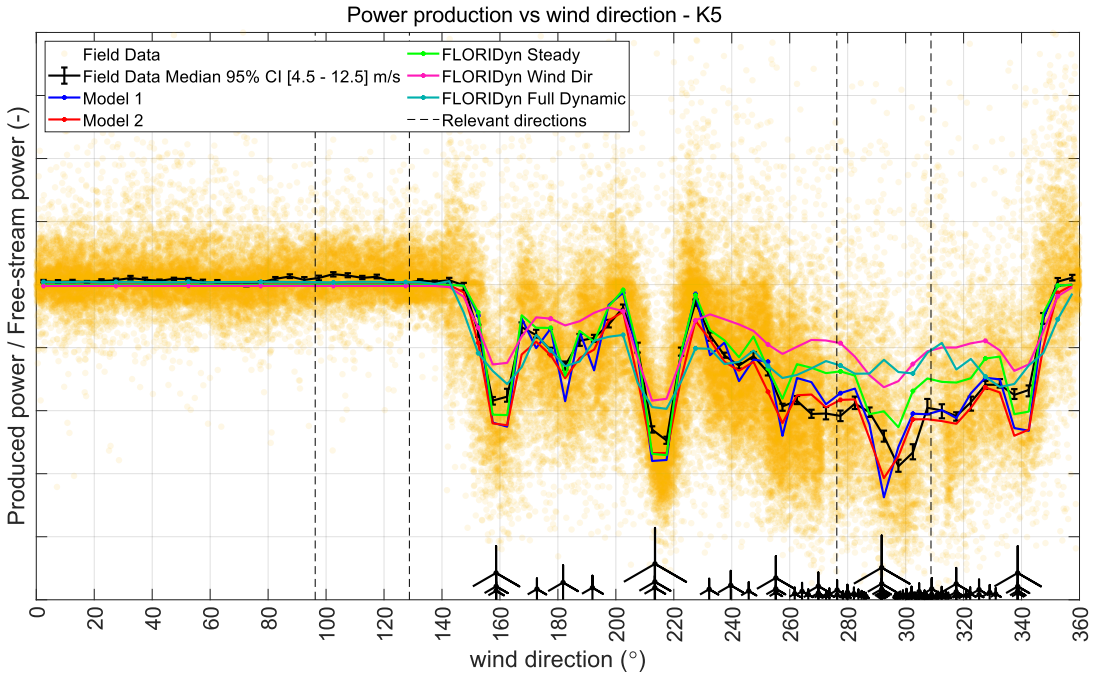

Figure 5.14: Power ratio along the full wind direction range for turbine K5.

Figure 5.15: Effective to free-stream power ratio comparison plots over all wind directions, averaged over the considered wind speeds. The drawn turbines indicate the upstream view of the considered turbine.

The displayed wind turbines on Figure 5.15 indicate the upstream view of the analysed wind turbine per wind direction. A wind turbine that appears larger represents a closer distance to the given turbine when compared to a smaller turbine. This means of representation omits the need to add a wind farm layout plot, and captures both the considered performance metric and turbine location in a single plot.

Firstly, the yellow dots in Figure 5.15 indicate the filtered field data. Note that a scatter is observed around the local median value. This scatter effectively represents the uncertainty on the field data, and mainly results from the different operating wind conditions and measurement uncertainty. Essentially, it represents the combined uncertainty of all external influences.

As expected from the combined power polar plot averaged over all turbines, steady-state models tend to overestimate wake losses in scenarios of full wake conditions and underestimate wake losses in cases of partial wake conditions. However, this is not the case for the dynamic FLORIDyn evaluations. Analysing the FLORIDyn full dynamic power ratio predictions on a 35° input wind on turbines H5, I5 and J5 in Figure 5.14a to Figure 5.14c indicate that the wake deficit is well captured. Therefore, the FLORIDyn full dynamic evaluation yields in the best performance compared to all other considered models, for full waked cases. On this specific wind direction case, the upstream turbines are relatively isolated, and little to no influence from other upstream turbines is encountered, and thus omitting wake accumulation due to partial waked conditions.

Conversely, the least accurate FLORIDyn predictions are observed when a turbine is in partially waked conditions and located deep within the field. This observation is consistent with the findings presented in Section 4.3.4, and is based on the analysis of the wind direction range [280 - 320] degree in Figure 5.15, indicating that especially the dynamic FLORIDyn evaluations predict a significant overestimation in produced power. Note that the influence of the full waked conditions at a wind direction input of 290° do not change this conclusion, where the influence of a smaller turbine spacing is barely captured in deep-array locations.

The final discussion point resulting from Figure 5.15 are the apparent smoother curves for the dynamic FLORIDyn evaluations. Whereas the inclusion of wind direction changes was anticipated to induce smoother curves when compared to the steady-state model outcomes, the modelled wake affects appear to be excessively smeared out. A potential cause of this effect might be related to discrepancies between the synthetic generation of wind direction and measured SCADA.

In this work, simulations are initialised by assuming that all wind turbines are oriented according to the centred wind direction for a given wind condition bin. Additionally, the turbine orientation does not change along the entire simulation duration. Therefore, this assumption states that the encountered yaw misalignment values are small enough to be neglected. To verify this statement, and to check the similarity between the observed yaw misalignment, Figure 5.16 displays the distributions for the observed yaw misalignment on the analysed SCADA dataset, and those observed from the dynamic FLORIDyn evaluations.

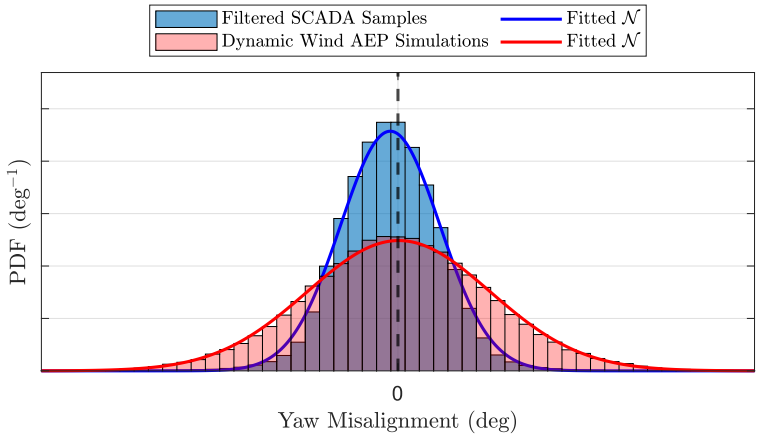

Figure 5.16: Histogram plots and fitted normal distributions indicating the yaw misalignment values for the analysed SCADA measurements and the FLORIDyn model evaluations on synthetic wind generation inputs.

Figure 5.16 shows that the observed yaw misalignment distributions can be approximated by normal distributions. Firstly, the filtered SCADA samples indicate that the assumption of turbine alignment with the incoming wind direction is justified. The systematic offset to perfect alignment is sufficiently small to be neglected, and highlights that the considered data points for analysis do not result from an implemented yaw steering strategy. This small bias is also reflected by the yaw misalignment distribution extracted from the FLORIDyn evaluations.

The primary difference between the two distributions shown in Figure 5.16 lies in their widths. Consistent with the hypothesis of overestimating wind direction fluctuations, the synthetically generated wind inputs exhibit a wider distribution. The fitted Gaussian curves facilitate a quantitative comparison of the differences by examining their respective σ values, revealing a factor of 1.9 between the two distributions. This discrepancy is most likely caused by two factors. First, the implemented Mann model approach assumes isotropy in all wind speed components. Since the wind direction signal in this work is derived from the angle between the lateral u and v wind components, overestimated fluctuations in v lead to larger wind direction fluctuations. This suggests a strong case for including anisotropy in the lateral wind components. Secondly, the fluctuations are scaled by the input TI. As previously indicated, the TI mapping in this study is significantly overestimated in the [120 - 150] degree sector, leading to larger wind direction fluctuations. The combination of these factors results in a wider range of encountered wind directions per simulation, creating an effect similar to increasing the bin width.

Next to the discrepancies on the dynamic FLORIDyn results, the steady FLORIDyn evaluation also indicates an excessive overprediction when compared to Model 1 and 2. This re-iterates the need to revise the wake superposition model embedded in the FLORIDyn model, as it does not solely occur on the dynamic evaluations, and related model limitations imposed by the convection model.

The differences between the implemented wake models are further investigated by looking into distribution of RMSE per turbine. Therefore, Figure 5.17 displays the RMSE distribution per wake model, as violin plots averaged over all considered wind condition bins.

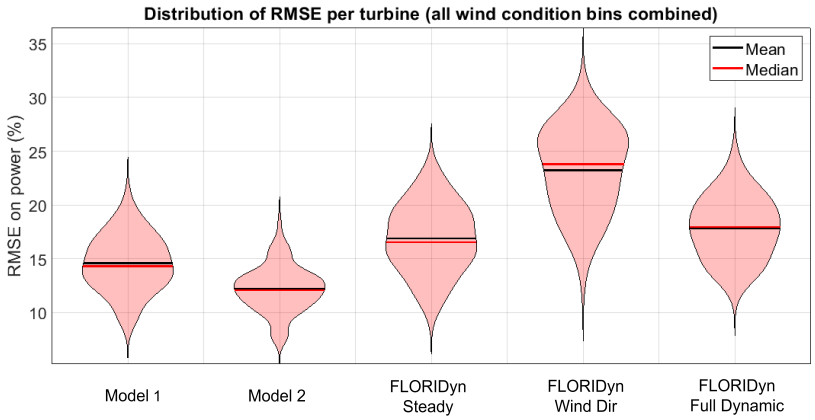

Figure 5.17: RMSE comparison plot for the considered models, combined over all wind bins.

Strikingly, none of the considered model evaluations result a median RMSE values below 10%. This is a direct result of the limitations due to the presented assumptions in Section 5.2 that cause additional uncertainty in the generation of wind input conditions, but also highlights the need for more accurate wake models. As expected from the previous analyses, Figure 5.17 displays that the smallest overall RMSE values result from the Model 2 evaluations, followed by Model 1. Moreover, the FLORIDyn evaluation on only wind direction variations results in the least accurate predictions.

Moreover, the dynamic FLORIDyn evaluations display the largest range of RMSE values over the turbines. This range is anticipated to be reduced when more evaluations on different wind field realisations are run. For the scope of this work however, only a single wind field evaluation is considered due to the required computational effort, as detailed later in this section. However, the obtained RMSE values per turbine already represent the median value over all considered wind conditions (586 data points per turbine in this case), and should already represent a sufficiently large sample size to capture a general trend.

Further investigating the RMSE errors per considered model, Figure 5.18a indicates the sensitivity of RMSE to the wind speed, averaged over all turbines and wind direction bins. Similarly, Figure 5.18b displays the model RMSE sensitivity to wind direction.

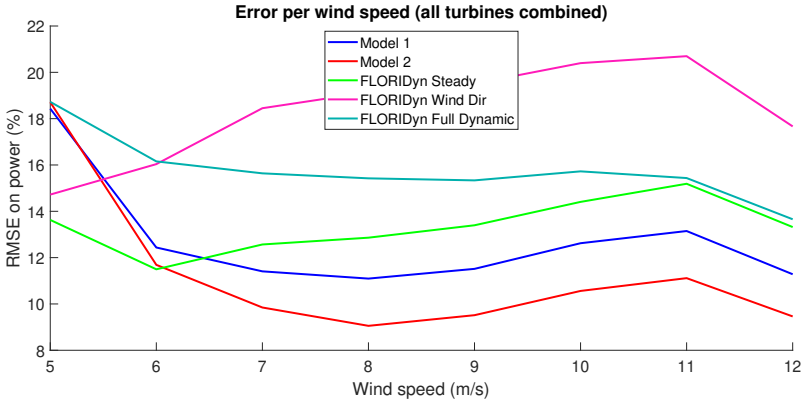

(a) RMSE sensitivity to wind speed per model.

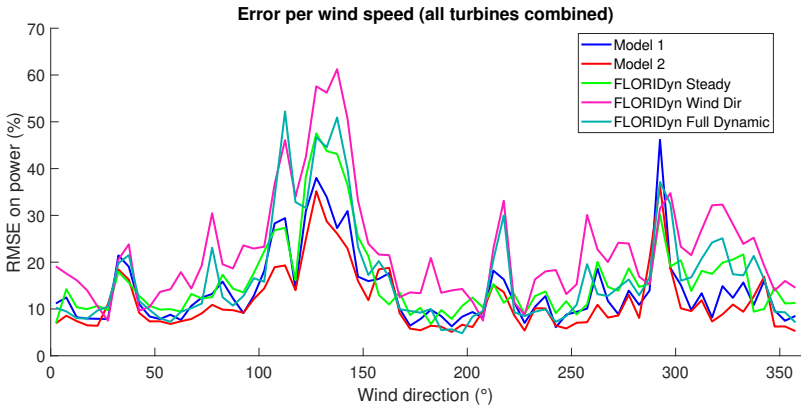

(b) RMSE sensitivity to wind direction per model.

Figure 5.18: RMSE sensitivity to wind direction and wind speed.

Figure 5.18a shows the sensitivity of RMSE to wind speed, averaged over all turbines and wind direction. In general, the highest values for RMSE are observed at the lowest considered wind speed. This is most likely attributed to the on and off-switching of the power curve. Due to the implementation of the steady-state C_P curve, a turbine is not producing power for local wind speeds below 4 m/s. Initialising a simulation at 5 m/s can locally result in wind speeds below 4 m/s at deep field locations on strong turbine alignment wind conditions and small turbine spacing, and thus yield in no power production.

Additionally, the lowest RMSE are observed in the range [7 - 9] m/s for the steady-state models. Relating back to the implemented power curve, Section 5.2 indicated that the corresponding TI value for this reference curve is encountered in this wind speed range. Hence, although a uniform TI mapping is used against wind direction, it still results in the lowest RMSE at the expected wind range.

Interestingly, the steady FLORIDyn model evaluation displays the smallest RMSE on the smallest considered wind speeds. Unlike the other steady-state models, the steady FLORIDyn RMSE does not further reduce on the [7 - 9] m/s wind speed range. For wind speeds $>$ 11 m/s, turbines operate closer to rated conditions, which indicates a smaller C_T, and hence reduced wake effects. Therefore, all wake models show a decrease in RMSE.

Next, a quantitative comparison on the accuracy of AEP prediction is performed. Unlike the comparison results discussed thus far, the AEP results indicate predictions on both a uniform wind and site specific wind rose. The non-dimensional AEP results are tabulated by Table 5.3. The presented analysis on AEP

is normalised by the AEP value resulting from the field data on a uniform wind rose. This representation allows for a direct quantitative interpretation of the over- or underestimations resulting from the model evaluations.

Table 5.3: Comparison of non-dimensional AEP predictions per model.

Normalised AEP	Field data	Model 1	Model 2	FLORIDyn Steady	FLORIDyn Dynamic Direction	FLORIDyn Fully Dynamic
Uniform Wind Rose	1	1.034	1.011	1.076	1.121	1.06
Actual Wind Rose	0.915	0.942	0.922	0.979	1.029	0.964

The values on a uniform wind rose presented in Table 5.3 reveal the expected overestimation of AEP, consistent with the observations made in this chapter. However, the observed differences are much smaller than the range of RMSE values. In general, all model results follow this trend, with Model 2 again resulting in the smallest percentage difference of 1.1% in the estimated AEP, outperforming all other models. The full dynamic FLORIDyn evaluation results in a 6.2% overestimation, marking an improvement over the steady FLORIDyn prediction. Despite the dynamic FLORIDyn evaluations generally generating worse results compared to the steady evaluation, the averaging effect in AEP computations mitigates the largest differences. Thus, this single weighted metric, although based on a uniform wind rose, can not reliably represent the differences in model performance. This highlights the need for additional comparison metrics, as included in this chapter.

Next, the AEP computed from the field data on the actual wind rose is decreased by 8.5% when compared to the uniform wind rose evaluations. This is again an expected result when considering the Weibull plot and wind rose in Figure 3.7, which indicate the highest wind speed probabilities (and thus weighting) occur around 7 m/s, with a prevailing SW wind direction, close to the minimum turbine alignment direction at 215°. Given that this smaller turbine spacing direction is paired with lower power outputs, and that higher wind speeds are weighted less, the decrease in AEP makes sense. Additionally, the AEP computed from the field data on the actual wind rose is 8.5% lower compared to the uniform wind rose evaluations. This result aligns with expectations based on the Weibull plot and wind rose shown in Figure 3.7. These figures indicate that the highest wind speed probabilities (and thus weighting) occur around 7 m/s, predominantly from the southwest direction, which is near the minimum turbine alignment direction at 215°. Given that this direction corresponds to closer turbine spacing and lower power outputs, and higher wind speeds are weighted less, the observed decrease in AEP matches the anticipated outcomes.

Finally, model performance in terms of computational expense is analysed. The findings from a simulation time analysis are summarised by Table 5.4 for the different evaluations of the FLORIDyn model in this work.

Table 5.4: Comparative overview of the simulation time for different FLORIDyn evaluations, evaluated on Intel Xeon Platinum 8268 CPUs.

Model Type	FLORIDyn Steady	FLORIDyn Dynamic Direction	FLORIDyn Fully Dynamic
Average Time per Simulation	4 s	5 min 3 s	12 min 15 s
Total Simulation Time	1 h 23 min	49 h 26 min	119 h 47 min

Table 5.4 clearly indicates that the dynamic evaluations of the FLORIDyn model result in significantly increased computational times when compared to the steady-state evaluation. The simulation times for the dynamic FLORIDyn evaluations are roughly a factor 75 and 170 higher when compared to the steady-state evaluation. Not only is the average time per simulation increased, also the total simulation time is significantly higher, even considering half the number of simulations run. Combining this outcome with the FLORIDyn performance indicators, it can be concluded that the additional computational cost associated with using FLORIDyn for AEP estimations does not result in more accurate AEP predictions. While the computational cost of FLORIDyn can definitely be reduced through a more efficient code implementation, the inherent additional cost due to its time-modelling capabilities will persist. Consequently, unless there

are improvements in the convection and wake superposition submodels, using the dynamic properties embedded in the current FLORIDyn model will not enhance the accuracy of AEP predictions.

5.6. Summary on the AEP Comparison Study

This section aims to summarise the main findings from the model comparison study on AEP estimations presented in this work. The chapter began by outlining the comparison setup. Key assumptions and their related limitations were then highlighted, particularly regarding their influence on the study results. While the evaluation was predominantly qualitative, the assumption of a statistically stationary wind input was investigated in greater detail. The analysis of wind ramp events, considering the bin widths, revealed that such events are no rare occurrences. Additionally, subsequent identified ramp events can span multiple 10-minute windows, leading to significant variations in steady-state wind conditions. As with the qualitative investigation of other assumptions, further detailed analysis is required to deepen the understanding of these influences.

Next, this chapter verified the implementation of the described synthetic wind generation in Section 3.3.1, showing consistency between input variables and model output. Moreover, also the assumption for the spectral tensor was verified by analysing the PSD of the wind speeds resulting from the SCADA data.

Subsequently, the results obtained from the comparison study were discussed in Section 5.5. First, a significant mismatch between the field data and simulation results was observed on the raw power representation on a wind rose. The (a)symmetry was linked to an insufficient TI input mapping, lacking sensitivity to wind direction. Next, the steady-state models were observed to generally underestimate power prediction on wind direction inputs for the most aligned turbine cases. Conversely, power overprediction was observed in partial waked configurations. Additionally, results from dynamic FLORIDyn evaluations yielded smoother power ratio curves. This raised questions about the synthetic wind direction generation. Comparison between FLORIDyn and SCADA yaw misalignment values indicated that the wind direction modelled wind direction changes overestimate those observed in field measurements (factor 1.9 differences between the standard deviations of both distributions). Hence, leading to more smeared out wake effects, similar to increasing the bin width in the binning procedure. This larger wind direction variation is attributed to both the TI mapping, and the isotropy assumption in the Mann model.

Finally, the main findings related to FLORIDyn highlight that while FLORIDyn offers a sophisticated approach by incorporating time-dependent wake effects, its performance does not uniformly surpass traditional steady-state models in all scenarios. In line with the outcomes of Chapter 4, the results in this chapter indicated that FLORIDyns predictions are particularly sensitive to downstream wake accumulation, leading to increased uncertainty and inaccuracies in AEP estimations. Combining these observations with the added computational cost required to run the FLORIDyn simulations, the current FLORIDyn model is concluded to not be sufficiently mature to reduce the currently existing uncertainties in modelling AEP on large scale wind farm applications.

6

Conclusions and Future Work

The concluding chapter of this thesis report encapsulates the key findings and recommendations drawn from an in-depth exploration of the use of FLORIDyn for wind farm AEP estimations. This chapter synthesises the main outcomes of this work, highlighting their implications and significance within the broader context of wake modelling. Additionally, it provides valuable insights for future research directions and practical applications, aiming to contribute to the advancement of dynamic wake modelling.

The chapter is outlined as follows. Section 6.1 summarises the main achievements and steps taken in this work. Next, Section 6.2 outlines the main conclusions and aims to answer the established research questions in Section 2.10. Subsequently, Section 6.3 presents the recommendations and suggestions for future work. Finally, this chapter is concluded by the final words in Section 6.4.

6.1. Main Achievements

With the end goal of investigating the potential use of low-cost dynamic wake models in the wind industry, this thesis project presented a methodology by combining best practices in literature from model calibration up to the comparison of several models and field data. Starting from the baseline quasi-dynamic FLORIDyn model, this work presented its underlying model components to build a thorough understanding. Next, the FLORIDyn model has been transformed to facilitate the use of C_P-C_T LUTs. This implementation also led to a correction to the wake-added TI computations. Additionally, a new implementation to identify influencing turbines was introduced, separating the upstream identified turbines influencing local ambient wind field conditions and velocity deficits.

This thesis first investigated the accuracy and uncertainty of FLORIDyn predictions through a direct one-to-one validation study. in order to obtain the most accurate results, a calibration approach, based on real-world turbine measurements, was proposed. By employing an inverse Bayesian calibration using trained surrogate models, a calibrated set of model parameters was obtained. This work then presented the results of a model validation study based on these calibrated parameters and estimated model uncertainty by propagating the uncertainty in the calibrated parameter values. Finally, the scope of the one-to-one simulations was expanded from small farm array cases to evaluations of the full wind farm configuration, providing a more comprehensive investigation of the limitations of the FLORIDyn model.

Having established a calibrated FLORIDyn model, the second part of this work focused on a comparative study evaluating FLORIDyn's performance in predicting AEP against industry-applied steady-state wake models and field data. This study began by examining the underlying assumptions, conducting an extensive data analysis on the occurrence of wind ramp events, and verifying the presented synthetic wind generation methodology. Finally, the results of the model comparison and validation study were discussed using several comparison metrics.

6.2. Conclusions

The primary objective of this thesis was to assess the suitability of using a dynamic wake model to improve the accuracy of AEP predictions at the wind farm level, and to develop a validation framework. This overarching goal led to the formulation of specific research questions that guided the methodologies employed throughout the thesis. To address these questions, the quasi-dynamic FLORIDyn model was extensively investigated, and a comprehensive framework was developed, starting from model calibration, and leading up to comparison with industry-applied wake models and field data. Throughout this research process, several conclusions were drawn, which are discussed in this section in relation to the initial research questions.

Research Question 1

How can the inclusion of time-varying wake propagation in engineering wake models contribute to improving the accuracy of Annual Energy Production (AEP) computations?

Accurately estimating wake losses is vital for assessing overall wind farm performance because it directly impacts the ability to optimise energy production. Precise wake loss predictions allow for the development of effective control strategies, which can mitigate energy losses caused by turbine interactions. This leads to improved AEP, more efficient operation, and in the end, better financial returns. Additionally, accurate wake loss estimation helps in layout design of wind farms, ensuring optimal placement of turbines to maximise performance.

Currently, wake-steering control strategies are developed using steady-state engineering models. These models employ time-averaged and analytical wake profiles, allowing them to represent wind farm flows using empirical model constants while maintaining low computational demands. Consequently, their primary advantage lies in their ability to efficiently run large numbers of simulations on binned wind statistics.

However, the steady-state engineering models lack the ability to represent wind dynamics. Especially on the continuously increasing rotor and farm sizes, the corresponding time lags related to changes in the wind field become significant. The steady-state engineering models can not represent these time lags, and assume an instantaneous downstream propagation.

As indicated by the data analysis on wind ramp events, about 15.73% of the analysed dataset contained wind direction jumps larger than the considered bin widths. Additionally, 7.47% of the analysed SCADA samples indicated a wind speed ramp event. Relating this back to the assumption of statistically stationary wind fields in the AEP study, it is found to be generally applicable. Since this work did not filter the identified cases out of the validation dataset, these cases added additional uncertainty to the field data, and was highlighted by the large scatter of data points in the power ratio plot (Figure 5.15).

Based on the analyses in this work, the FLORIDyn model was found to not yield in improved predictions on the AEP estimations. As a consequence, there is no apparent gain in considering this quasi-dynamic wake model for AEP estimations. Evidently, the safety factor on AEP predictions can also not be reduced. Finally, although the FLORIDyn model results are comparable to the industry-applied steady-state model results (Model 1), the demanded computational cost is significantly higher. Therefore, the implementation of the current version of the FLORIDyn model does not bring significant benefits to AEP estimations.

The key takeaway from this AEP validation study is the need for improvement on the model assumptions on wake shape (representing instantaneous wakes by time-averaged solutions), wake accumulation, and the simple convection model. Although the FLORIDyn has been extensively validated against high fidelity simulation tools on small wind farm arrays [94, 82, 102], this work highlighted its shortcomings on larger wind farm applications. Therefore, the current FLORIDyn model implementation can not be deemed sufficiently robust for general industry applications for AEP estimation on large wind farms.

Nonetheless, the conclusion in this work does not generally apply to the suitability of dynamic wake modelling approaches. The main reasoning for the negative decision on the suitability assessment is related to the modelling assumptions on the specific FLORIDyn model, such as the wake accumulation, convection, and wake-added TI submodels. Therefore, a more mature FLORIDyn model in which the

identified limitations are addressed, or a different dynamic wake model might result in improved AEP estimations.

Research Question 2

What are the effects of modelling assumptions on the uncertainty of time-varying engineering wake models?

The model uncertainty in this thesis is assessed through the calibration framework, and is based on an Inverse Bayesian calibration implementation. For this procedure, a surrogate PCE model is created from the full FLORIDyn model. Whereas the PCE model creation introduces additional uncertainty, it reduces the computational time related to the large number of required model evaluations. The overall benefit of this calibration procedure is that the calibrated parameters are represented by posterior PDFs, indicating the uncertainty on the predicted values. By iterating this procedure on multiple wind farm subsets, the calibration sensitivity to wind conditions and turbine spacing was investigated.

The uncertainty analysis on the FLORIDyn model was conducted by propagating the uncertainty in calibrated model parameters through FLORIDyn evaluations. Consequently, the posterior predictive distributions reflected the uncertainty in model outputs. Using power ratios, histogram plots illustrated the distribution of the posterior predictions compared to model outputs derived from the maximum a posteriori parameter values. The primary conclusion from this evaluation is that model uncertainty increases as wakes accumulate at turbines located further downstream. This effect was already apparent on the considered wind farm subsets for the calibration study, and was found to be even more apparent on the one-to-one simulations conducted on the full wind farm configuration.

Similar to the limitations of steady-state wake models, FLORIDyn demonstrated pronounced inaccuracies in deep array locations, primarily due to wake superposition. On the one-to-one simulations, the FLORIDyn evaluations resulted in underestimated power predictions in cases with strong turbine alignment and overestimated predictions in partially waked conditions combined with wake accumulation effects. These conclusions were confirmed from both steady and dynamic evaluations of the FLORIDyn model on the AEP simulation results. These findings are further supported by uncertainty assessments on FLORIDyn evaluations, highlighting larger uncertainties on turbines where combined wake effects are encountered.

Secondly, this work highlighted that another significant limitation of the FLORIDyn model lies in its assumptions regarding flow convection. Due to the discrete point representation by OPs and the simplified interactions solely considering OPs in a single wake chain, complex flow evolution is not captured. While this convection model has limited effects on small wind farms, wind fluctuations tend to dampen out in large-scale farms due to the 'Averaged' OP interaction setting. Additionally, the convection model is biased towards higher wind speeds, as decreasing wind speed trends do not convect sufficiently fast downstream, leading to higher perceived local wind speeds at the downstream turbines. Consequently, in deep array locations, changing wind states do not arrive with the correct time lag for decreasing wind speeds. On the other hand, time lags related to events of increasing wind speeds are better captured.

Thirdly, the wake shapes produced by the calibrated model parameters do not align with expectations in the near-wake region. It is important to note that the calibration study analysed cases with turbine spacings that do not correspond to operation in the near-wake regions. Therefore, the potential core determining parameters α^* and β^* could not be calibrated on these cases, but were instead tailored to generally improve model performance. Nonetheless, this discrepancy in near-wake behaviour prompts questions about the validity of using time-averaged wake profiles to model time-dependent properties. However, the calibration process did yield expected behaviour in the far-wake self-similar region, showing a narrower and more persistent wake compared to the baseline case. As a result, the inability to accurately represent wakes in the near-wake region limits the FLORIDyn model's applicability to cases with sufficiently large turbine spacings.

Combining these findings further confirmed the conclusion that the current FLORIDyn model is only suitable on specific configurations. More notably, only reliable FLORIDyn predictions can be obtained on small wind farms, with sufficiently large turbine spacings.

6.3. Future Work

The findings in this thesis represent substantial progress in developing validation and calibration strategies for wake models, while also identifying areas for future research. In order to improve upon the conducted work, recommendations for future work are categorised into four areas: enhancing the FLORIDyn model, improving the sensitivity and calibration framework, revising the synthetic wind generation method, and addressing implications for the model comparison framework.

6.3.1. FLORIDyn Model

The first major limitation in the FLORIDyn model that demands further development is the incorporated convection model. Especially, the downstream propagation of changing wind speeds is ill-represented by the discrete OP convection model. More specifically, only OP interactions within a single wake chain are considered, and all wind field information is stored in these discrete points. Next, they convect with a scaled free-stream wind speed that was encountered at their turbine of origin, following the frozen turbulence assumption. Effectively, there is no split up between the background and wake flow, as they are both governed by the discrete OPs.

Whereas this simple convection model functions on small wind farms, large wind farms characterised by larger time and length scales, and complex wake interactions on deep field locations require more sophisticated modelling techniques. Therefore, it could be beneficial to implement a background flow solver. An approach similar to that used on the SPLINTER dynamic wake model could be considered [83]. Except for the dissipation term, the implemented convection model is similar to the Navier-Stokes equations. The implementation in the SPLINTER model is a discretised flow solver of these advection equations. Additionally, the flow solver allows for the computation of flow velocities, but allows for the propagation of other parameters too, and thus propagating wake states and turbulence intensities.

The second significant FLORIDyn limitation is the implemented wake superposition model. This led to an overestimation on the wake recovery, especially in deep field locations. Whereas the current FLORIDyn model implements a sum root squared approach to obtain the local TI, this approach should be revised. An alternative approach could be to consider only the maximum wake-added TI resulting from all upstream turbines to use in the local TI determination, instead of the combined influence of all upstream turbines. This approach is also present in the PyWake framework [59] to mitigate overestimation of wake recovery on the steady-state models. A second alternative is to adjust the search area to determine OPs influencing the local wind speed reduction and TI computations. By incorporating this latter approach, the cross- and upstream distances of the search area would essentially be additional tunable parameters. However, this increases the complexity of the calibration procedure, and the first suggested approach is therefore preferred.

6.3.2. Sensitivity and Calibration Framework

Future iterations of the sensitivity and calibration framework could explore performing the calibration procedure on a central, combined metric. Rather than considering the power outputs of all turbines at all time instants, a combined metric (e.g. wind farm power) per time instant or a single time averaged metric per turbine (e.g. time-averaged power) could be considered. This consideration would decrease the size of the optimisation (by factors N_T and N_t respectively) in an effort to reduce computational expense.

This reduced computational expense is especially important to run the suggested calibration procedure on larger wind farm (subsets). To include deep array locations and corresponding wake accumulation effects, larger wind farms should be considered to find a set of calibrated model parameters that better represent the deep array wake behaviour.

Finally, a direct improvement to the framework proposed in this study could involve employing low-pass filtered power signals as validation data for the calibration process. Significant power fluctuations were observed on the Fastlog data on waked turbines, underscoring its substantial impact on the calibration procedure. This effect is particularly pronounced when considering the smoothing effects imposed by the constraints of the FLORIDyn flow convection model, and use of time-averaged wake profiles, thus failing to capture these fluctuations. Therefore, the implementation of low-pass filtered validation data is expected to result into more accurate model calibration results.

6.3.3. Synthetic Wind Generation

Future iterations on the synthetic wind generation procedure should incorporate anisotropy in the longitudinal and lateral velocity components. This anisotropy could be determined from a data analysis on LiDAR, and directly implemented in the spectral tensor. An approach similar to the one proposed by Syed and Mann [109] could be considered to represent anisotropy in the variances of longitudinal and transverse wind components. Alternatively, an initial approach could involve scaling the generated wind direction fluctuations by a factor of 1.9. This factor is derived in this work from comparing the standard deviations of SCADA and simulation yaw misalignment distributions.

To address the startup transient in FLORIDyn simulations, this study introduced a method for a synthetic wind generation that omits the creation of a stochastic realisation on the entire required time window. The straightforward approach involving concatenation and mirroring operations, while effective for maintaining desired simulation characteristics over the effective time period, does not accurately replicate real-world wind conditions. This method serves as an initial engineering solution to the issue. However, it alters the power spectral density of the total signal, particularly in the low-frequency spectrum. Therefore, a critical review of this approach is advised for further improvements.

6.3.4. AEP Validation Studies

The presented validation study on AEP estimation in this work is limited by numerous assumptions, for which the results have not been quantified. Therefore, the majority of the recommendations outlined in this section will govern additional research related to enhance the understanding of the influence of individual assumptions on the global comparison results.

Include spatial heterogeneity and wind ramp events

Whereas this study is limited by the assumption of a homogeneous and statistically steady wind conditions, data analysis showed that wind ramp event can not be discarded. Additionally, no investigation on spatially heterogeneous wind fields has been carried out. Therefore, it is of interest to develop a strategy to implement both dynamic wind change, and spatial velocity gradients in the validation study. The first consideration could be implemented by superimposing the synthetic wind speed and direction fluctuations on a linear trend. On the other hand, heterogeneity could be implemented by applying a scaling factor on the wind at turbine locations to represent this spatial heterogeneity. Given FLORIDyn's capability to include spatially heterogeneous wind fields in both steady and dynamic model evaluations, further data analysis on spatial wind heterogeneity could provide valuable input for AEP simulations and wind farm flow control strategies.

Effects of data binning on comparison studies

Within this work, the influence of data binning has not been investigated. Instead, all results in Chapter 5 have been generated using 1 m/s wide bins for wind speed, and 5° bins for wind direction, without bin overlapping. Future work could further investigate how the results' comparison is affected by different bin widths and overlap settings. Especially since the maximum velocity deficit decreases, and wake effects are smeared out as binning widths increase. Therefore, a future iteration on this work could perform a sensitivity study on the wind condition binning procedure, and the resulting model comparison results. Although the conclusions on the general model deficiencies will not change, a more thorough understanding of the binning effects could improve the model comparison procedure

Secondly, dynamic wind events have been observed to span multiple bins due to the changing wind speed or direction and hence invalidating statistically steady wind assumption. Whereas the mean of the SCADA 10-minute data point is attributed to a single bin, the wind ramp event occurs over multiple bins. Therefore, it is advised to track the occurrence of such wind events per considered wind bin. When performing the AEP prediction simulations, this information about the dynamic wind ramps could be used to either indicate uncertainty in field data, or to use as a weighting function to process the results from simulation runs.

Run AEP simulations with surrogate models to estimate model uncertainty and sensitivity

The calibration procedure in this work highlighted the uncertainty in the calibrated numerical values on the FLORIDyn model constants. By propagating these posterior PDFs through the model on one-to-one

simulations, an insight into model uncertainty and sensitivity to the model parameters was gained. A similar approach could be carried out on the model comparison study. Due to the significant computational cost related to running the dynamic evaluations of FLORIDyn, this could be carried out using a surrogate model.

Include multiple C_P-C_T curves
Future iterations of this work should consider implementing multiple C_P-C_T curves to account for variations in operational wind conditions (varying TI), and turbine operation regime. Either a model to dynamically vary the input steady LUT, or a mapping of different C_P-C_T curves to TI could be implemented to reduce model uncertainty. Next to the variation on TI, implementation of different turbine operation regimes should be considered. Especially when performing additional one-to-one simulation analyses, adequate modelling of inoperative and curtailed turbines is essential to obtain reliable results.

Enhanced TI mapping
One of the largest sources of error in the model comparison study is attributed to the simplified TI mapping. The analyses in this work are run on the assumption that TI is independent of wind direction. Considering the wind farm location, and the displayed field data results, a strong case is made for a TI mapping that varies with both wind speed and direction. Future iterations of this work's comparison study should investigate this asymmetry across the wind rose, and implement a suitable TI estimator to create an enhanced TI mapping to be used as input.

Atmospheric stability
The model evaluations in this work did not account for the effects of atmospheric stability and mesoscale influences. Additionally, no shear profile, and a constant air density were assumed throughout this work. Future research should investigate the impacts of wind shear, atmospheric stability, and mesoscale effects over extended time periods in AEP predictions and model comparison. Currently, it is ill-understood how these conditions influence model performance, and represent a significant uncertainty in both field measurements and model initialisation. Especially considering the prevailing coastal wind on the analysed wind farm, unstable atmospheric boundary layer conditions could indicate faster wake recovery [20]. Nonetheless, the current FLORIDyn model does not allow for inputs related to boundary layer stability, and requires more thorough investigation. As suggested by Meyers et al. [74], additional parameterisation of atmospheric conditions are still largely ongoing research topics, for which the resulting implementation might benefit the FLORIDyn model development.

Gaussian weighting on fluctuating wind conditions
Inspired by the time dependent capabilities of FLORIDyn, and the observed modelling limitations in partially waked conditions, an extension to the approach on steady-state simulations is suggested. Rather than considering a single simulation per wind speed and direction bin, multiple runs on slightly altered wind speed and directions could be launched, and weighted by a Gaussian distribution imposed on the mean properties. Although this approach does not take the encountered time lags into account, it does implicitly model the uncertainty in wind speed and direction measurements, and accounts for the non-stationary wind conditions. By doing so on simulation runs with the steady-state wake models, an effect similar to the time-varying wind speed and direction inputs is created as for the dynamic FLORIDyn evaluations, while conserving lower computational times. Hence, a larger range of wind speeds and directions is covered in the simulated results, similar to how the measurement data comprises binned conditions.

This suggested approach is expected to reduce the discrepancies related to the underprediction of power observed in the strongest aligned turbine conditions. Conversely, it is expected that this extended approach also relieves some issues related to overprediction of power at deep array turbine locations due to partially, and accumulated wake conditions. This latter assumption is a pure hypothesis however, since the wake recovery is also significantly influenced by the TI superposition model.

6.4. Final Words

In conclusion, the wake modelling validation studies conducted in this thesis underscore the need to further develop low-fidelity dynamic wake models. These models are valued for their ability to better simulate wake dynamics compared to steady-state engineering models, while maintaining lower computational costs than CFD. This work established the initial steps toward a model calibration framework based on real-world turbine data and highlighted the importance of conducting calibration studies on multiple wind conditions. Additionally, the framework identified the main limitations of the FLORIDyn model, paving the way for further enhancements and continuous model development. The FLORIDyn model shows potential for developing wind farm flow control strategies and potentially improving AEP yield predictions in future applications, but current the current modelling assumptions limit the use cases to small scale wind farms. Ultimately, this thesis has contributed to a better understanding of the uncertainties and limitations related to power prediction by state-of-the-art wake modelling applications. It has quantified predicted wake losses and identified discrepancies with field observations, laying the groundwork for future research. Finally, suggestions were outlined to further investigate and reduce uncertainties associated with modelling assumptions on both the validation study, and FLORIDyn model.

References

[1] W. Turner. "The Cheapest and Cleanest Energy Source". In: *Energy Engineering* 112.5 (2015), pp. 5–6. DOI: 10.1080/01998595.2015.11449887. URL: https://doi.org/10.1080/01998595.2015.11449887.

[2] G. Bangga. "Progress and Outlook in Wind Energy Research". In: *Energies* 15.18 (2022). DOI: 10.3390/en15186527. URL: https://www.mdpi.com/1996-1073/15/18/6527.

[3] P. Shukla et al. *IPCC Climate Change 2022: Mitigation of Climate Change*. Cambridge, UK: Cambridge University Press, 2022. Chap. 1, pp. 155–194.

[4] IEA. "Net Zero by 2050". In: *IEA, Paris* (2021).

[5] IRENA. "World Energy Transitions Outlook 2022: 1.5° C Pathway". In: *International Renewable Energy Agency, Abu Dhabi* (2022).

[6] GWEC. *Global Wind Report 2023*. 2023. URL: https://gwec.net/globalwindreport2023/ (visited on 11/19/2023).

[7] P. Veers et al. "Grand challenges in the science of wind energy". In: *Science* 366.6464 (2019). DOI: 10.1126/science.aau2027.

[8] J. Liew. "Dynamic modelling of wind farms for closed-loop control". PhD thesis. Roskilde, Denmark: DTU Wind and Energy Systems, 2022. DOI: 10.11581/dtu.00000263.

[9] B. Gu et al. "Cooperative multiagent optimization method for wind farm power delivery maximization". In: *Energy* 233 (2021), p. 121076.

[10] M. A. Khan et al. "Optimization of a wind farm by coupled actuator disk and mesoscale models to mitigate neighboring wind farm wake interference from repowering perspective". In: *Applied Energy* 298 (2021), p. 117229.

[11] W. H. Lio et al. "On wind turbine down-regulation control strategies and rotor speed set-point". In: *Journal of Physics: Conference Series*. Vol. 1037. 3. IOP Publishing. 2018, p. 032040.

[12] Á. Jiménez et al. "Application of a LES technique to characterize the wake deflection of a wind turbine in yaw". In: *Wind energy* 13.6 (2010), pp. 559–572.

[13] P. M. Gebraad et al. "Maximization of the annual energy production of wind power plants by optimization of layout and yaw-based wake control". In: *Wind Energy* 20.1 (2017), pp. 97–107.

[14] Z. Deng et al. "Yaw Optimisation for Wind Farm Production Maximisation Based on a Dynamic Wake Model". In: *Energies* 16.9 (2023). DOI: 10.3390/en16093932. URL: https://www.mdpi.com/1996-1073/16/9/3932.

[15] S. Kanev. "Dynamic wake steering and its impact on wind farm power production and yaw actuator duty". In: *Renewable Energy* 146 (2020), pp. 9–15. DOI: https://doi.org/10.1016/j.renene.2019.06.122. URL: https://www.sciencedirect.com/science/article/pii/S0960148119309565.

[16] B. Sanderse. "Aerodynamics of Wind Turbine Wakes: Literature Review". In: *ECN-e-09-016* (Jan. 2009).

[17] F. Porté-Agel et al. "Wind-Turbine and Wind-Farm Flows: A Review". In: *Boundary-Layer Meteorology* 174 (Jan. 2020). DOI: 10.1007/s10546-019-00473-0.

[18] M. Lejeune et al. "A meandering-capturing wake model coupled to rotor-based flow-sensing for operational wind farm flow prediction". In: *Frontiers in Energy Research* 10 (2022), p. 884068.

[19] E. Jézéquel et al. "Breakdown of the velocity and turbulence in the wake of a wind turbine – Part 1: Large-eddy-simulation study". In: *Wind Energy Science* 9.1 (2024), pp. 97–117. DOI: 10.5194/wes-9-97-2024. URL: https://wes.copernicus.org/articles/9/97/2024/.

[20] R. J. Foreman et al. "The Atmospheric Stability Dependence of Far Wakes on the Power Output of Downstream Wind Farms". In: *Energies* 17.2 (2024), p. 488.

[21] G. Larsen et al. *Dynamic wake meandering modeling*. English. Denmark. Forskningscenter Risoe. Risoe-R 1607(EN). Risø National Laboratory, 2007.

[22] G. C. Larsen et al. “Dynamic wake meandering modeling”. In: (2007).

[23] S. B. Pope. *Turbulent flows*. Cambridge University Press, 2000.

[24] T. Göçmen et al. “Wind turbine wake models developed at the technical university of Denmark: A review”. In: *Renewable and Sustainable Energy Reviews* 60 (2016), pp. 752–769.

[25] S. Kalvig et al. “Comparing different CFD wind turbine modelling approaches with wind tunnel measurements”. In: *Journal of Physics Conference Series* 555 (Oct. 2012). DOI: 10.1088/1742-6596/555/1/012056.

[26] B. Sanderse et al. “Review of computational fluid dynamics for wind turbine wake aerodynamics”. In: *Wind energy* 14.7 (2011), pp. 799–819.

[27] M. Hansen. *Aerodynamics of wind turbines: Third edition*. English. Aerodynamics of Wind Turbines: Third Edition. Journal Abbreviation: Aerodyn. of Wind Turbines: Third Ed. Pages: 173 Publication Title: Aerodyn. of Wind Turbines: Third Ed. Taylor and Francis Inc., 2015. DOI: 10.4324/9781315769981. URL: https://www.scopus.com/inward/record.uri?eid=2-s2.0-84942810624&doi=10.4324%2f9781315769981&partnerID=40&md5=c08ad530b6986a344970decae66f6f5f.

[28] J. N. Sørensen et al. “Unsteady actuator disc model for horizontal axis wind turbines”. In: *Journal of Wind Engineering and Industrial Aerodynamics* 39.1 (1992), pp. 139–149. DOI: https://doi.org/10.1016/0167-6105(92)90540-Q. URL: https://www.sciencedirect.com/science/article/pii/016761059290540Q.

[29] Y.-T. Wu et al. “Simulation of turbulent flow inside and above wind farms: model validation and layout effects”. In: *Boundary-layer meteorology* 146 (2013), pp. 181–205.

[30] L. A. Martínez-Tossas et al. “Filtered lifting line theory and application to the actuator line model”. In: *Journal of Fluid Mechanics* 863 (2019), pp. 269–292.

[31] L. Martinez et al. “A comparison of actuator disk and actuator line wind turbine models and best practices for their use”. In: *50th AIAA Aerospace Sciences Meeting including the New Horizons Forum and Aerospace Exposition*. 2012, p. 900.

[32] W. Z. Shen et al. “The Actuator Surface Model: A New NavierStokes Based Model for Rotor Computations”. In: *Journal of Solar Energy Engineering* 131.1 (Jan. 2009), p. 011002. DOI: 10.1115/1.3027502. eprint: https://asmedigitalcollection.asme.org/solarenergyengineering/article-pdf/131/1/011002/5714048/011002_1.pdf. URL: https://doi.org/10.1115/1.3027502.

[33] C. Sibuet Watters et al. “Application of the actuator surface concept to wind turbine rotor aerodynamics”. In: *Wind Energy* 13.5 (2010), pp. 433–447.

[34] F. Houtin-Mongrolle. “Investigations of yawed offshore wind turbine interactions through aero-servo-elastic Large Eddy Simulations”. PhD thesis. Rouen, France: Normandie Université, 2022.

[35] J. Ainslie. “Calculating the flowfield in the wake of wind turbines”. In: *Journal of Wind Engineering and Industrial Aerodynamics* 27.1 (1988), pp. 213–224. DOI: https://doi.org/10.1016/0167-6105(88)90037-2. URL: https://www.sciencedirect.com/science/article/pii/0167610588900372.

[36] H. Kim et al. “Wind turbine wake characterization for improvement of the Ainslie eddy viscosity wake model”. In: *Energies* 11.10 (2018), p. 2823.

[37] A. Peña et al. “On wake modeling, wind-farm gradients, and AEP predictions at the Anholt wind farm”. In: *Wind Energy Science* 3.1 (2018), pp. 191–202.

[38] S. Ott et al. *Linearised CFD models for wakes*. Danmarks Tekniske Universitet, Risø Nationallaboratoriet for Bæredygtig Energi, 2011.

[39] S. Ott et al. “Developments of the offshore wind turbine wake model Fuga”. In: *E-0046 Report* (2014).

[40] J. Liew et al. “Extending the dynamic wake meandering model in HAWC2Farm: a comparison with field measurements at the Lillgrund wind farm”. In: *Wind Energy Science* 8.9 (2023), pp. 1387–1402.

[41] J. M. Jonkman et al. *Fast. farm user’s guide and theory manual*. National Renewable Energy Laboratory Golden, CO, USA, 2021.

[42] T. J. Larsen et al. “Validation of the dynamic wake meander model for loads and power production in the Egmond aan Zee wind farm”. In: *Wind Energy* 16.4 (2013), pp. 605–624.

[43] H. A. Madsen et al. “Calibration and validation of the dynamic wake meandering model for implementation in an aeroelastic code”. In: (2010).

[44] J. Mann. “The spatial structure of neutral atmospheric surface-layer turbulence”. In: *Journal of fluid mechanics* 273 (1994), pp. 141–168.

[45] IEC. *Wind energy generation systems - Part 1: Design requirements*. IEC 61400-1. Vernier, Geneva, Switzerland: International Electrotechnical Commission, 2019.

[46] A. Van Garrel. "Development of a wind turbine aerodynamics simulation module". In: (2003).

[47] E. Branlard. "A Brief Introduction to Vortex Methods". In: *Wind Turbine Aerodynamics and Vorticity-Based Methods: Fundamentals and Recent Applications*. Cham: Springer International Publishing, 2017, pp. 483–492. DOI: 10.1007/978-3-319-55164-7_40. URL: https://doi.org/10.1007/978-3-319-55164-7_40.

[48] J. T. Reid et al. "General approach to lifting-line theory, applied to wings with sweep". In: *Journal of Aircraft* 58.2 (2021), pp. 334–346.

[49] S. Perez-Becker et al. "Is the Blade Element Momentum theory overestimating wind turbine loads? – An aeroelastic comparison between OpenFAST's AeroDyn and QBlade's Lifting-Line Free Vortex Wake method". In: *Wind Energy Science* 5.2 (2020), pp. 721–743. DOI: 10.5194/wes-5-721-2020. URL: https://wes.copernicus.org/articles/5/721/2020/.

[50] L. Zhan et al. "Optimal tuning of engineering wake models through lidar measurements". In: *Wind Energy Science* 5.4 (2020), pp. 1601–1622.

[51] N. O. Jensen. *A note on wind generator interaction*. Risø National Laboratory, 1983.

[52] I. Katic et al. "A simple model for cluster efficiency". In: *European wind energy association conference and exhibition*. Vol. 1. A. Raguzzi Rome, Italy. 1986, pp. 407–410.

[53] S. Frandsen et al. "Analytical modelling of wind speed deficit in large offshore wind farms". In: *Wind Energy: An International Journal for Progress and Applications in Wind Power Conversion Technology* 9.1-2 (2006), pp. 39–53.

[54] M. Bastankhah et al. "A new analytical model for wind-turbine wakes". In: *Renewable Energy* 70 (2014). Special issue on aerodynamics of offshore wind energy systems and wakes, pp. 116–123. DOI: https://doi.org/10.1016/j.renene.2014.01.002. URL: https://www.sciencedirect.com/science/article/pii/S0960148114000317.

[55] L. P. Chamorro et al. "A wind-tunnel investigation of wind-turbine wakes: boundary-layer turbulence effects". In: *Boundary-layer meteorology* 132 (2009), pp. 129–149.

[56] T. Ishihara et al. "A new Gaussian-based analytical wake model for wind turbines considering ambient turbulence intensities and thrust coefficient effects". In: *Journal of Wind Engineering and Industrial Aerodynamics* 177 (2018), pp. 275–292.

[57] F. Blondel et al. "An alternative form of the super-Gaussian wind turbine wake model". In: *Wind Energy Science* 5.3 (2020), pp. 1225–1236.

[58] N. G. Nygaard et al. "Modelling cluster wakes and wind farm blockage". In: *Journal of Physics: Conference Series*. Vol. 1618. 6. IOP Publishing. 2020, p. 062072.

[59] M. M. Pedersen et al. "PyWake 2.5.0: An open-source wind farm simulation tool". In: (Feb. 2023). URL: https://gitlab.windenergy.dtu.dk/TOPFARM/PyWake.

[60] A. Niayifar et al. "Analytical modeling of wind farms: A new approach for power prediction". In: *Energies* 9.9 (2016), p. 741.

[61] H. Zong et al. "A momentum-conserving wake superposition method for wind farm power prediction". In: *Journal of Fluid Mechanics* 889 (2020), A8.

[62] P. Vermeulen. "An experimental analysis of wind turbine wakes". In: *3rd international symposium on wind energy systems*. 1980, pp. 431–450.

[63] F. Carbajo Fuertes et al. "Wind turbine wake characterization with nacelle-mounted wind lidars for analytical wake model validation". In: *Remote Sensing* 10.5 (2018), p. 668.

[64] S. Ott et al. *Developments of the offshore wind turbine wake model Fuga, no. 0046 in DTU Wind Energy E, DTU Wind Energy, Denmark*. 2014.

[65] P. Lissaman. "Energy effectiveness of arbitrary arrays of wind turbines". In: *Journal of Energy* 3.6 (1979), pp. 323–328.

[66] S. Voutsinas et al. "On the analysis of wake effects in wind parks". In: *Wind Engineering* (1990), pp. 204–219.

[67] A. Crespo et al. “Turbulence characteristics in wind-turbine wakes”. In: *Journal of wind engineering and industrial aerodynamics* 61.1 (1996), pp. 71–85.

[68] P. Argyle et al. “Modelling turbulence intensity within a large offshore wind farm”. In: *Wind Energy* 21.12 (2018), pp. 1329–1343.

[69] A. Wessel et al. “Modelling turbulence intensities inside wind farms”. In: *Wind Energy: Proceedings of the Euromech Colloquium*. Springer. 2007, pp. 253–257.

[70] E. H. Lingkan et al. “An assessment of the scalings for the streamwise evolution of turbulent quantities in wakes produced by porous objects”. In: *Renewable Energy* 209 (2023), pp. 1–9.

[71] Á. Jiménez et al. “Application of a LES technique to characterize the wake deflection of a wind turbine in yaw”. In: *Wind energy* 13.6 (2010), pp. 559–572.

[72] G.-W. Qian et al. “A new analytical wake model for yawed wind turbines”. In: *Energies* 11.3 (2018), p. 665.

[73] M. Bastankhah et al. “Experimental and theoretical study of wind turbine wakes in yawed conditions”. In: *Journal of Fluid Mechanics* 806 (2016), pp. 506–541.

[74] J. Meyers et al. “Wind farm flow control: prospects and challenges”. In: *Wind Energy Science Discussions* 2022 (2022), pp. 1–56.

[75] D. van der Hoek et al. “Effects of axial induction control on wind farm energy production-a field test”. In: *Renewable energy* 140 (2019), pp. 994–1003.

[76] G. P. Corten et al. “Heat and Flux. Increase of Wind Farm Production by Reduction of the Axial Induction”. In: (Oct. 2003).

[77] R. K. Balakrishnan et al. “Maximization of the power production of an offshore wind farm”. In: *Applied Sciences* 12.8 (2022), p. 4013.

[78] W. Munters et al. “Towards practical dynamic induction control of wind farms: analysis of optimally controlled wind-farm boundary layers and sinusoidal induction control of first-row turbines”. In: *Wind Energy Science* 3.1 (2018), pp. 409–425.

[79] J. A. Frederik et al. “The helix approach: Using dynamic individual pitch control to enhance wake mixing in wind farms”. In: *Wind Energy* 23.8 (2020), pp. 1739–1751.

[80] P. M. Gebraad et al. “A control-oriented dynamic model for wakes in wind plants”. In: *Journal of Physics: Conference Series*. Vol. 524. 1. IOP Publishing. 2014, p. 012186.

[81] M. Becker et al. “The revised FLORIDyn model: implementation of heterogeneous flow and the Gaussian wake”. In: *Wind Energy Science* 7.6 (2022), pp. 2163–2179. DOI: 10.5194/wes-7-2163-2022. URL: https://wes.copernicus.org/articles/7/2163/2022/.

[82] M. Becker et al. “FLORIDyn-A dynamic and flexible framework for real-time wind farm control”. In: *Journal of Physics: Conference Series*. Vol. 2265. 3. IOP Publishing. 2022, p. 032103.

[83] A. Rott et al. “Dynamic flow model for real-time application in wind farm control”. In: *Journal of Physics: Conference Series*. Vol. 854. 1. IOP Publishing. 2017, p. 012039.

[84] J. Schmidt et al. “FOXES: Farm Optimization and eXtended yield Evaluation Software”. In: *Journal of Open Source Software* 8.86 (2023), p. 5464. DOI: 10.21105/joss.05464. URL: https://doi.org/10.21105/joss.05464.

[85] B. Foloppe et al. “Development of a dynamic wake model accounting for wake advection delays and mesoscale wind transients”. In: *Journal of Physics: Conference Series*. Vol. 2265. 2. IOP Publishing. 2022, p. 022055.

[86] M. Churchfield et al. “Overview of the simulator for wind farm application (SOWFA)”. In: *National Renewable Energy Laboratory* (2012).

[87] S. Gremmo et al. “Large-Eddy Simulation of Deformable Wind Turbines”. In: *WESC2021*. 2021.

[88] M. Becker. *Maturing FLORIS towards a Dynamic Wind Farm Model*. M.Sc. Thesis. TU Darmstadt, Darmstadt, Nov. 2020.

[89] L. Masset et al. *Partition of the circle in cells of equal area and shape*. English. Tech. rep. May 2011.

[90] A. Farrell et al. “Design and analysis of a spatially heterogeneous wake”. In: *Wind Energy Science Discussions* 2020 (2020), pp. 1–25.

[91] L. P. Chamorro et al. “Turbulent flow inside and above a wind farm: a wind-tunnel study”. In: *Energies* 4.11 (2011), pp. 1916–1936.

[92] J. Annoni et al. “Wind direction estimation using SCADA data with consensus-based optimization”. In: *Wind Energy Science* 4.2 (2019), pp. 355–368.

[93] S. Halvorsen. *Identification of a dynamic center line model and its implementation in FLORIDyn*. M.Sc. Thesis. TU Delft, Delft, June 2022. URL: https://repository.tudelft.nl/islandora/object/uuid%3A83e70716-dd62-42dd-b462-695b378a024e.

[94] D. Shi. *Uncertainty Quantification of A Wind Farm Control Model: FLORIDyn*. M.Sc. Thesis. TU Delft, Delft, June 2023. URL: http://resolver.tudelft.nl/uuid:35aebffb-006b-4959-aa78-0451f3174023.

[95] WindEurope. *European Offshore Wind Farms Map*. 2024. URL: https://windeurope.org/intelligence-platform/product/european-offshore-wind-farms-map/ (visited on 01/11/2024).

[96] T. Von Karman. “Progress in the statistical theory of turbulence”. In: *Proceedings of the National Academy of Sciences* 34.11 (1948), pp. 530–539.

[97] N. F. Baker et al. “Best practices for wake model and optimization algorithm selection in wind farm layout optimization”. In: *AIAA Scitech 2019 forum*. 2019, p. 0540.

[98] N. G. Nygaard. “Systematic quantification of wake model uncertainty”. In: *EWEA Offshore conference*. 2015, pp. 10–12.

[99] S. Marelli et al. “UQLab: A framework for uncertainty quantification in Matlab”. In: *Vulnerability, uncertainty, and risk: quantification, mitigation, and management*. 2014, pp. 2554–2563.

[100] B. Sanderse et al. “Efficient Bayesian calibration of aerodynamic wind turbine models using surrogate modeling”. In: *Wind Energy Science* 7.2 (2022), pp. 759–781.

[101] S. Marelli et al. *UQLab user manual – Polynomial chaos expansions*. Tech. rep. Report UQLab-V2.0-104. Chair of Risk, Safety and Uncertainty Quantification, ETH Zurich,Switzerland, 2022.

[102] V. V. Dighe et al. “Sensitivity analysis and Bayesian calibration of a dynamic wind farm control model: FLORIDyn”. In: *Journal of Physics: Conference Series*. Vol. 2265. 2. IOP Publishing. 2022, p. 022062.

[103] S. Marelli et al. *UQLab user manual – Sensitivity analysis*. Tech. rep. Report UQLab-V2.0-106. Chair of Risk, Safety and Uncertainty Quantification, ETH Zurich,Switzerland, 2022.

[104] P.-R. Wagner et al. *UQLab user manual – Bayesian inversion for model calibration andvalidation*. Tech. rep. Report UQLab-V2.0-113. Chair of Risk, Safety and Uncertainty Quantification, ETH Zurich,Switzerland, 2022.

[105] E. Jézéquel et al. “Breakdown of the velocity and turbulence in the wake of a wind turbine–Part 1: Large-eddy-simulation study”. In: *Wind Energy Science* 9.1 (2024), pp. 97–117.

[106] Y.-M. Saint-Drenan et al. “A parametric model for wind turbine power curves incorporating environmental conditions”. In: *Renewable Energy* 157 (2020), pp. 754–768.

[107] P. C. Kalverla et al. “An observational climatology of anomalous wind events at offshore meteomast IJmuiden (North Sea)”. In: *Journal of Wind Engineering and Industrial Aerodynamics* 165 (2017), pp. 86–99.

[108] A. Peña et al. “Ten years of boundary-layer and wind-power meteorology at Høvsøre, Denmark”. In: *Boundary-Layer Meteorology* 158 (2016), pp. 1–26.

[109] A. H. Syed et al. “A model for low-frequency, anisotropic wind fluctuations and coherences in the marine atmosphere”. In: *Boundary-Layer Meteorology* 190.1 (2024), p. 1.

[110] B. M. Doekemeijer et al. “Comparison of the Gaussian wind farm model with historical data of three offshore wind farms”. In: *Energies* 15.6 (2022), p. 1964.

A

Mathematical Framework for TWF Creation

This appendix is an extension on the explained framework in Section 3.1.3, and is adapted from the work by Becker et al. [82] Firstly, consider a set of wind turbines $\mathcal{T}$. For each turbine $T_i \in \mathcal{T}$, the two closed OPs on the wake centreline to a world location $\mathbf{I}_0$ are considered. The linear interpolation to obtain the artificial OP* at the closest distance to $\mathbf{I}_0$ is given by Equation A.1.

$$w = \frac{\left[\mathbf{x}_{\mathrm{OP}^2,0} - \mathbf{x}_{\mathrm{OP}^1,0}\right]^\top \left[\mathbf{l}_0 - \mathbf{x}_{\mathrm{OP}^1,0}\right]}{\left[\mathbf{x}_{\mathrm{OP}^2,0} - \mathbf{x}_{\mathrm{OP}^1,0}\right]^\top \left[\mathbf{x}_{\mathrm{OP}^2,0} - \mathbf{x}_{\mathrm{OP}^1,0}\right]} \tag{A.1}$$

The result of this interpolation is a weight $w \in [0, 1]$. The location of OP* in $\mathcal{K}_0$ is represented as Equation A.2, and illustrated in Figure A.1.

$$\mathbf{x}_{\mathrm{OP}^*,0} = \mathbf{x}_{\mathrm{OP}^1,0} + w\left[\mathbf{x}_{\mathrm{OP}^2,0} - \mathbf{x}_{\mathrm{OP}^1,0}\right] = (1-w)\mathbf{x}_{\mathrm{OP}^1,0} + w\mathbf{x}_{\mathrm{OP}^2,0} \tag{A.2}$$

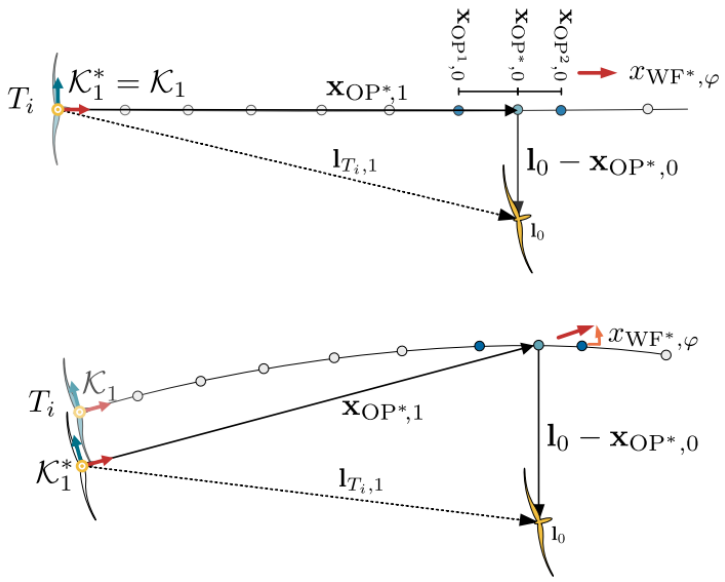

Figure A.1: The upper figure illustrates the interpolation process of OP* and its utilisation to determine the position of $\mathbf{I}_0$ in $\mathcal{K}_1^*$ of T_i. In the case of a steady wind direction where $\mathcal{K}_1$ of the turbine equals $\mathcal{K}_1^*$ of OP*, the wind direction remains constant. However, when there is a change in wind direction, the centre line propagates to its new steady state. The lower figure shows that this results in a shift in $\mathbf{x}^*_{\mathrm{WF},\varphi}$, and consequently, a temporary misalignment between the locations of the origins of $\mathcal{K}_1^*$ and $\mathcal{K}_1$ in the world coordinate system $\mathcal{K}_0$ [82].

The resulting weight is also used to interpolate the OP states $\mathbf{x}_{\mathrm{OP}^*,1}$, $\mathbf{x}_{\mathrm{T}^*}$ and $\mathbf{x}_{\mathrm{WF}^*}$, similar to Equation A.2. Hence, after applying this projection to every turbine in $\mathcal{T}$, all turbines are represented by their respective OP*.

Next, $\mathbf{I}_0$ should be transformed to the $\mathcal{K}_1$ coordinate frame of turbine T_i. This is done by rotating the vector $\mathbf{l}_0 - \mathbf{x}_{OP^*,0}$ (pointing from OP* to $\mathbf{l}_0$) from the world frame $\mathcal{K}_0$ to the wake frame $\mathcal{K}_1$ of T_i with the inverted rotational matrix: $\mathbf{R}_{01}^{-1} = \mathbf{R}_{01}^{\top} = \mathbf{R}_{10}$. This vector is then added to the $\mathcal{K}_1$ position of OP*.

$$\mathbf{l}_{T_i,1} = \mathbf{x}_{\mathrm{OP}^*,1} + \mathbf{R}_{10}\left(x_{\mathrm{WF}^*,\varphi}\right)\left[\mathbf{I}_0 - \mathbf{x}_{\mathrm{OP}^*,0}\right] \tag{A.3}$$

This formulation ensures that $\mathbf{I}_{T_i,1}$ can be generated for all turbines in $\mathcal{T}$. The vector $\mathbf{l}_{T_i,1}$ stems from the origin of $\mathcal{K}_1^*$, the turbine coordinate system of T_i based on the states of OP*. As illustrated by Figure A.1, this means that if the wind field states of OP^1 and OP^2 (which OP* is derived from) have changed since their initialisation, the origins of $\mathcal{K}_1^*$ and $\mathcal{K}_1$ are not at equal locations in $\mathcal{K}_0$.

Subsequently, a TWF is created to approximate the environment around $\mathbf{l}_0$. Using the OP* data, the wind turbine locations in the TWF can differ slightly from those in $\mathcal{K}_0$. This effect is visualised by Figure A.1. Therefore, a new coordinate system $\mathcal{K}_2$ is initialised, with x_2 aligned with the wind direction, y_2 representing the cross wind direction, and z_2 pointing upwards. In $\mathcal{K}_2$, $\mathbf{I}_0$ is represented as $\mathbf{I}_2 = [0, 0, l_{0,z}]^{\top}$. This definition inherits ground level at $z_2 = 0$. The wind turbines can be represented in $\mathcal{K}_2$ by Equation A.4.

$$\mathbf{t}_{T_i,2} = \mathbf{I}_2 - \mathbf{R}_{21}(0)\mathbf{I}_{T_i,1} \tag{A.4}$$

When $\mathcal{K}_1$ and $\mathcal{K}_2$ have the same wind direction, $\mathbf{R}_{21}(0)$ is represented by a 3×3 identity matrix since there is no rotation. Hence, turbine states are directly imposed by OP*. The same is not true for the wind field states, since only the wind direction is fixed. Assuming that wind field states for different OP* are similar due to their local proximity, only the two closest OP* are considered. Finally, the wake influence is obtained as the average between the two closest OP*, weighted by the distance to $\mathbf{I}_0$.

B

Correction to FLORIDyn TI Computations

This appendix aims at clarifying an bug fix to the wake-added TI calculation in the FLORIDyn model. When running initial FLORIDyn simulations, excessively high TI values in wake regions were observed, and indicated by Figure B.1. This led to a thorough investigation of the TI calculation and update computations.

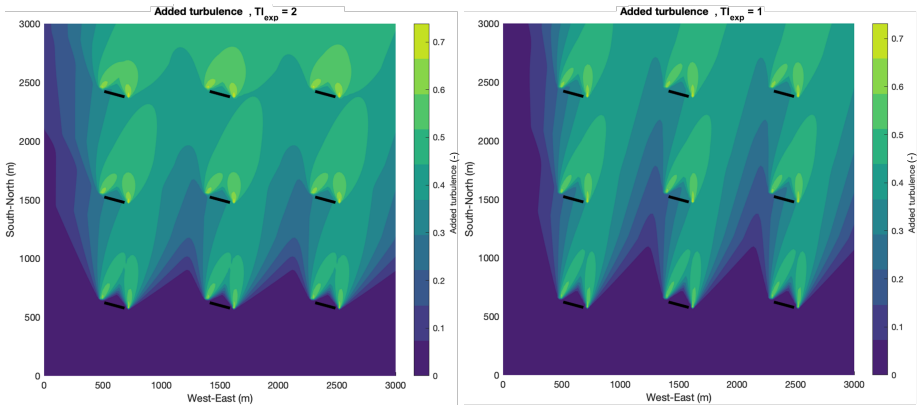

Figure B.1: Wake-Added TI field resulting from the original FLORIDyn model simulation run.

The issue was identified to occur due to a combination of a code implementation bugs in the wake added TI computation (Equation 3.3) and the TI weight influence (Equation 3.15) and the TI superposition implementation (Equation 3.4). Essentially, the square operator from the wake superposition model was already accounted for in the wake-added TI computations. This led to excessively high turbulence values in waked areas. After solving this implementation error, the updated TI fields look more reasonable and display the expected shapes, as illustrated by Figure B.2.

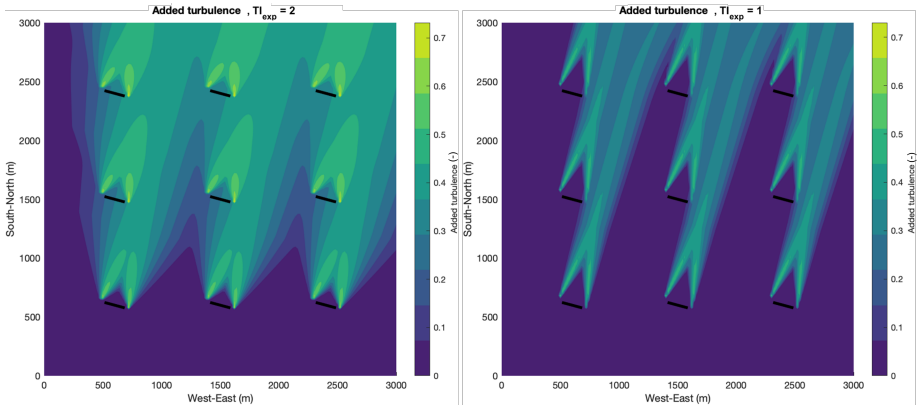

Figure B.2: Wake-Added TI fields resulting from the updated FLORIDyn model simulation run, after solving the TI computation bug.

C

North Calibration

This appendix briefly discusses why a north calibration procedure is required to be carried out on wind farm studies, and how to carry out this operation. To achieve this, the appendix is structured as follows. First, the general need and north calibration procedure is elaborated in Section C.1. The outcomes of the described procedure are discussed in Section C.2.

C.1. General Procedure

The aim of the north calibration procedure is to correct the wind direction signals captured by the turbine sensors. Therefore, the north calibration should provide a set of wind direction offsets to account for sensor malfunctions or calibrations errors arising due to installation or maintenance. It is important to highlight that the measured wind direction is not used to control the turbine. Therefore, any measurement miscalibration, or signal jumps do not affect the performance of the turbines. It is only needed for validation studies, or development of wind farm control strategies.

The necessity for this calibration procedure arises from the common practice of commercial turbine wind direction measurements not being precisely aligned with true north. Instead, they rely on measurements of relative nacelle misalignment to orient themselves into the wind direction. However, for model validation, both the field data and the model must utilise the same reference point and sign convention for wind direction. Wind direction holds significant importance in various applications, with relative wind direction typically being essential for most purposes. Consequently, a series of wind direction offsets must be computed to rectify the measurements. The method employed in this study essentially involves comparing real wake loss profiles with simulated ones, calculated for every direction around a turbine.

In this work, the simulation runs are carried out using a steady-state engineering wake model (FLORIS) to estimate the simulated wake loss profiles. Following the approach proposed by Doekemeijer et al. [110], power ratios for every turbine are compared to the neighbouring turbines along the entire wind direction range. The identification of neighbouring turbines is achieved by setting a predefined search radius, and selecting a specified number of closest turbines. From these identified turbines, the power ratio as a comparison metric is defined by Equation C.1. This metric measures the relative power capture of the selected test turbine of interest compared to the power output of the reference turbine(s). This measure is used to quantify wake effects on wind turbines within a wind farm.

$$R_j = \frac{\sum_{k=1}^{K} P_k\left(T_i, \theta_j\right)}{\sum_{k=1}^{K} P_k\left(T_{\text{ref}}, \theta_j\right)} \tag{C.1}$$

In essence, the power ratio metric can be used with an arbitrary number of reference turbines K. In this work however, a single turbine is considered for both the turbine of interest T_i and reference turbine T_{ref}, indicating that $K = 1$. As the name of the metric suggests, the power output P will be used to obtain the ratios. Finally, j indicates the specific wind direction considered to compute the power ratio.

To determine the optimal wind direction offset, a cost function incorporating the Pearson correlation coefficient is used. The Pearson correlation coefficient reaches 1 when two signals are identical, indicating perfect correlation, and decreases towards zero as the signals become less correlated. A signal is generated by evaluating the computed power ratios for each wind direction. By systematically applying a wind

direction offset ($\Delta\phi$) to the power ratios derived from field data measurements and performing a cross-correlation with the power ratios from the FLORIS simulation results, the offset that maximises the correlation coefficient can be identified. Equation C.2 expresses this as a mathematical operation.

$$\Delta\phi_{\text{bias}} = \arg_{\Delta\phi}\left[\max\left(\text{Corr}\left(\text{R}^{\text{SCADA}}(\phi - \Delta\phi), \text{R}^{\text{FLORIS}}(\phi)\right)\right)\right] \tag{C.2}$$

For the field data, R^{SCADA} contains energy ratios across all wind directions (ϕ), while for the model predictions, R^{FLORIS} holds the corresponding ratios. This process is conducted for every turbine alongside its identified neighbouring turbines. The final wind direction offset is determined by combining the resulting offsets over the set of surrounding turbines, for which the exact process will not be revealed. This averaged wind direction offset is subsequently saved as the calculated calibration offset. The same procedure is iterated for all turbines within a particular wind farm to acquire a comprehensive set of calibration offsets. This systematic and robust approach ensures that a set of wind direction offsets is obtained for all turbines on the considered wind farm

C.2. North Calibration Results

Although the described north calibration methodology in Section C.1 is robust, the implementation is dependent on the quality of the dataset in order to generate sensible results. Although a filtered dataset is already provided as an input to the north calibration algorithm, sudden perceived jumps in measured wind direction signals are identified. These offsets might result from maintenance operations that affected the wind direction sensors. Although the aforementioned jumps can already be observed on signals for a single turbine, this framework considers the difference between the measured wind directions of neighbouring turbines to apply corrections. This jump is identified when the mean of the difference between measured wind directions of neighbouring turbines persists over time. In order to correct the dataset, the jump is corrected by the perceived offset between the mean wind directions. This procedure of data cleaning is visually displayed by Figure C.1.

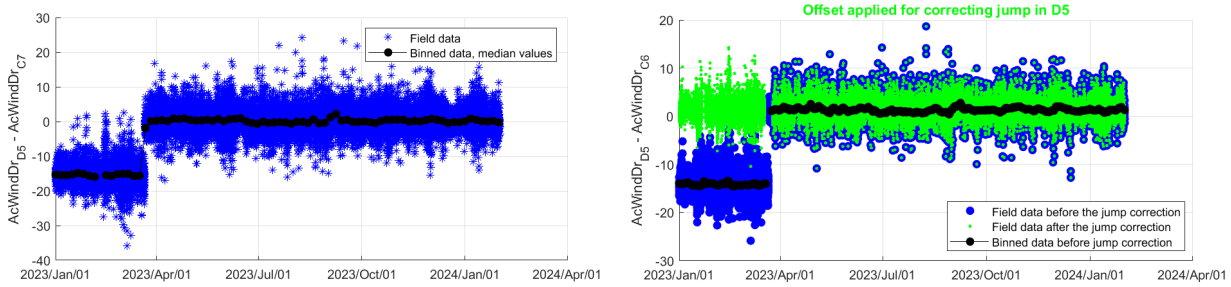

(a) Perceived jump between turbine of interest D5 and neighbouring turbine C7.

(b) Applied jump correction jump to turbine D5 based on neighbouring turbine C6.

Figure C.1: Example of the identification and adjustment of systematic jumps in the wind direction signal.

After adjusting the dataset for identified jumps in wind direction signals, the prescribed north calibration methodology can be applied. An illustrative result of this process is shown in Figure C.2 for a single turbine, depicting all considered properties. Note that this image is generated on artificial signals, and is solely used to present indicative results. Therefore, no model performance can be deduced from the resulting plots.

Firstly, the turbine location in the wind farm, and its neighbouring turbines are displayed on a turbine layout map. Next, the signals of the power ratios plotted against the considered wind directions are shown for three cases: the uncorrected field data, the field data with the applied offset, and the simulation results. In general, the simulation results do not perfectly capture the wake losses, but they do capture the general trends. Since the general trends are captured, especially the largest wake losses on the most aligned wind directions, the algorithm can confidently identify a wind direction offset that maximises the

cross-correlation coefficients. Finally, the cross-correlation results are displayed for wind direction offsets ranging from -180° to 180° as a visual check of the computed optimal offset.

Lastly, the computed offsets can be applied to the wind direction signals of all turbines. This is visualised by Figure C.3. Note that due to the periodicity in wind direction signals (0° = 360°), apparent jumps appear in the plotted signals. In general, the combined turbine signals display a more unified curve for wind direction measurements after applying the north calibration offsets. Therefore, the goal of defining a better reference point is concluded to be achieved.

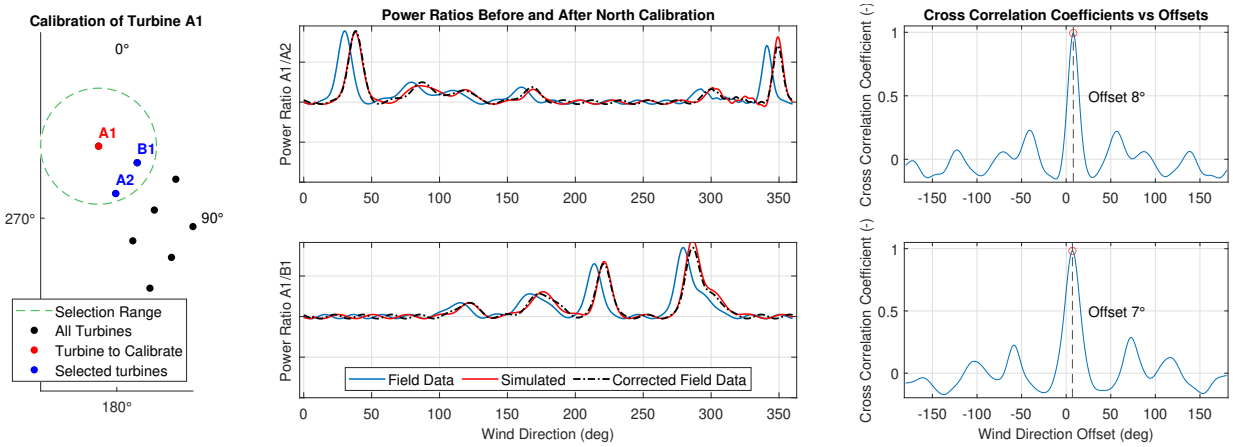

Figure C.2: Example of north calibration results on turbine A1 for artificially generated signals for illustrative purposes. The displayed power ratio curves are artificially generated, and do not reflect model performance, nor real world data.

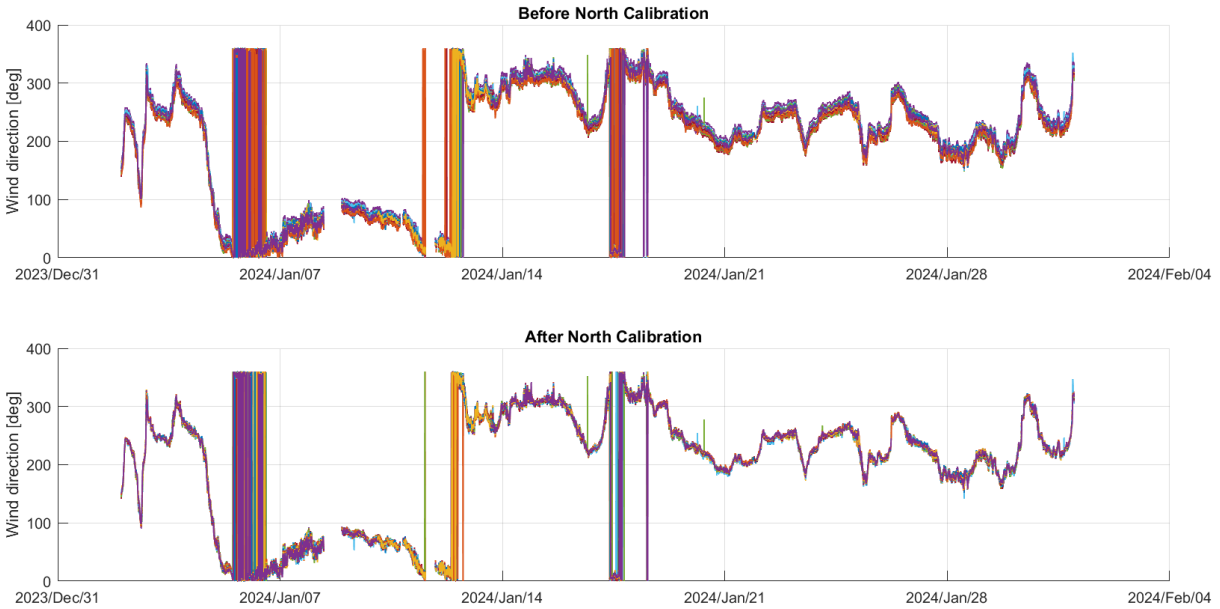

Figure C.3: Combined results of the north calibration offsets applied on the wind direction signals for all turbines along the full time spanned by the available SCADA dataset.

D

Calibration Convergence Assessment

The purpose of this appendix is to extend on the statement of convergence on the posterior PDFs displayed in Figure 4.9. This is achieved by assessing the convergence of the underlying AIES MCMC that determine the final posterior PDFs. In this work, this assessment is made based on the trace plots that contain the MCMC chains. By scrutinising these trace plots, this appendix not only aims to confirm the robustness of the MCMC approach used, but also confirms that the set number of MCMC chains and AIES iterations is sufficient. The resulting tracer plots from the MCMC AIES sampling are displayed by Figure D.1.

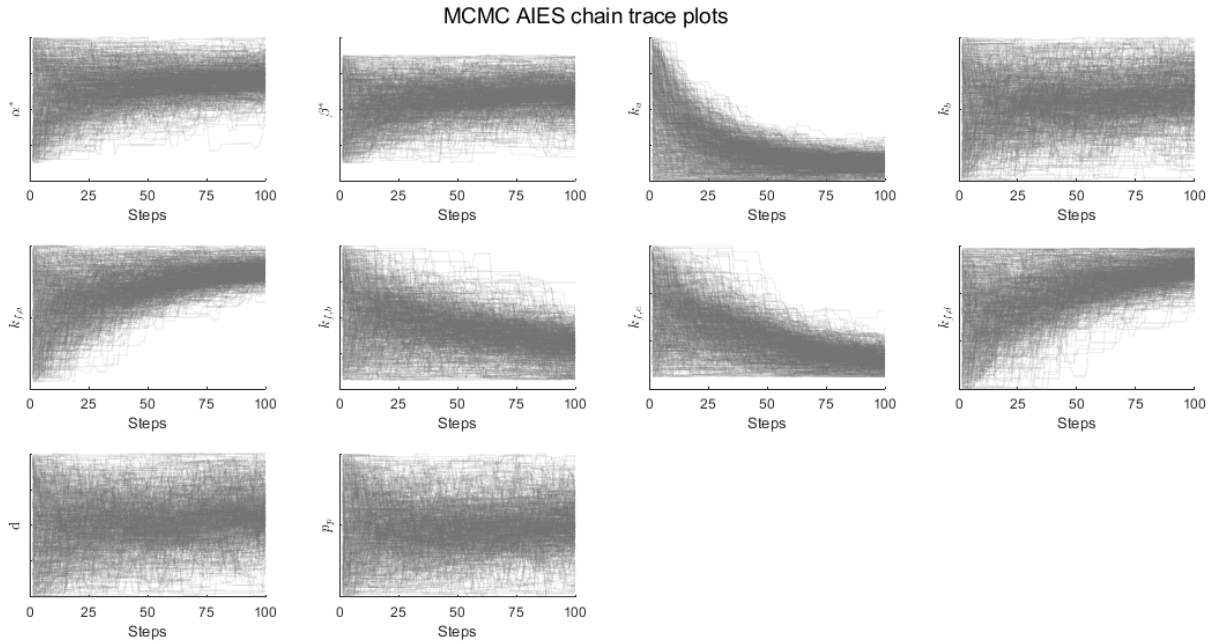

Figure D.1: MCMC AIES trace plots indicating convergence on the calibrated model parameter values.

Figure D.1 shows tracer steps on all AIES iterations, for all model constants. The convergence of the iterations is assessed by evaluating the transparency of the displayed curves. As more chains overlap, a darker area is reached, highlighting convergence on the value for the model constant.

As expected from the general Gaussian-like shapes for the posterior PDFs in Figure 4.9, convergence on the specified number of MCMC AIES steps and iterations is observed in Figure D.1. This statement is made based on the tracer plots displaying a convergence towards a steady-state value. Finally, the tracer plots validate the consistency of the posterior distributions derived from the sampling process. This additional evaluation provides confidence in the results presented in the main body of this work.

E

One-To-One Simulation Results

This appendix aims at providing additional results from the FLORIDyn one-to-one simulations carried out as part of the analysis in Section 4.3.4. More specifically, the results on the full wind farm configuration runs on the input wind conditions of all six calibration cases are displayed.

Therefore, Figure E.1 indicates the errors of the predicted time averaged power outputs on the farm layout, and Figure E.2 displays the time averaged power outputs per turbine, compared to the Fastlog field data measurements. These results are indicated to further support the findings in Section 4.3.4.

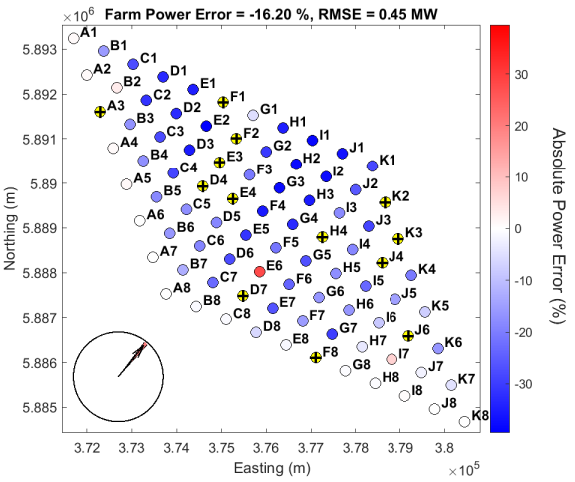

(a) Case 1: mapped power errors.

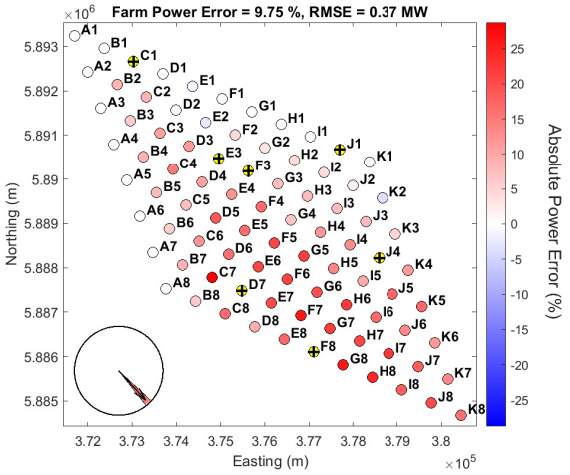

(b) Case 2: mapped power errors.

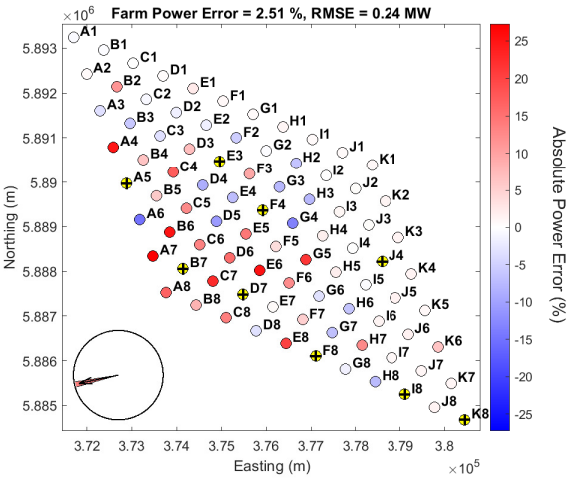

(c) Case 3: mapped power errors.

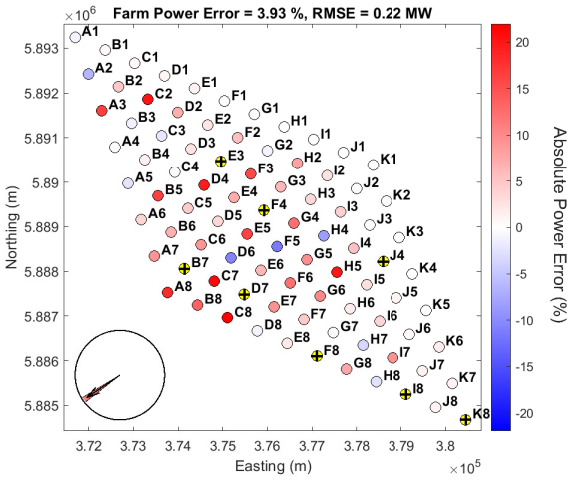

(d) Case 4: mapped power errors.

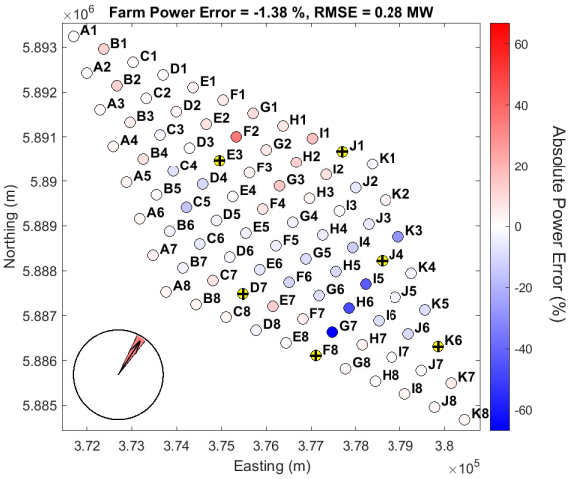

(e) Case 5: mapped power errors.

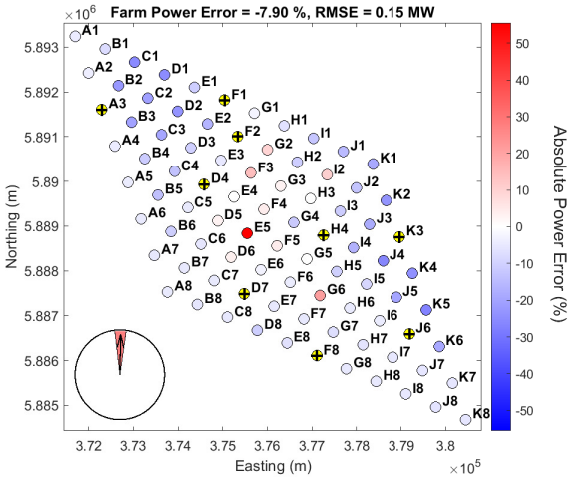

(f) Case 6: mapped power errors.

Figure E.1: 1-to-1 FLORIDyn simulation results on inflow conditions initialised from field data measurements. Turbines considered to be inoperative are indicated by yellow circles, with a cross.

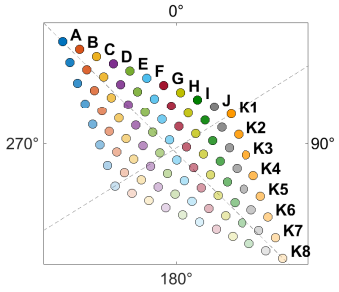

(a) Case 1: Power per turbine.

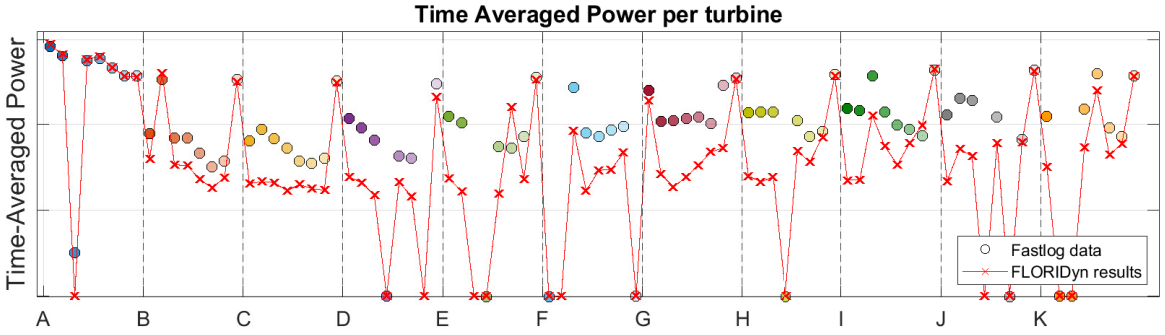

(b) Case 1: Power per turbine.

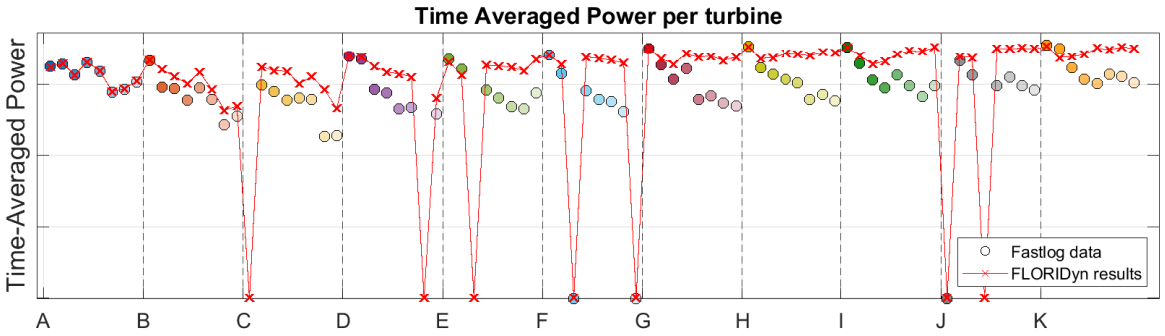

(c) Case 2: Power per turbine.0

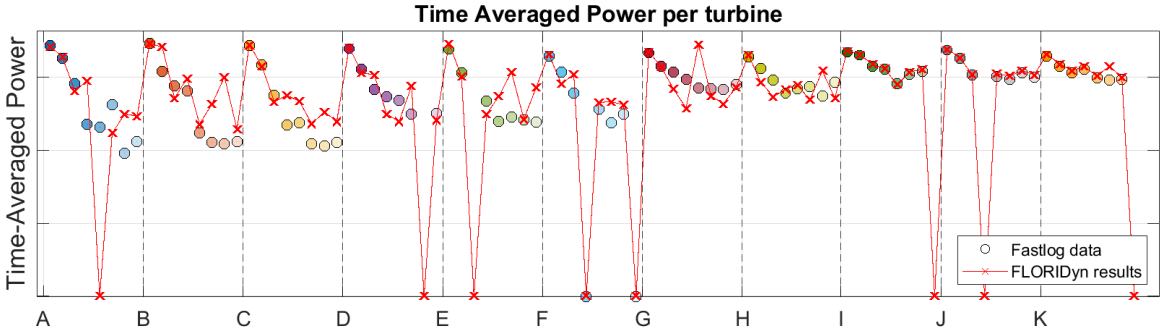

(d) Case 3: Power per turbine.

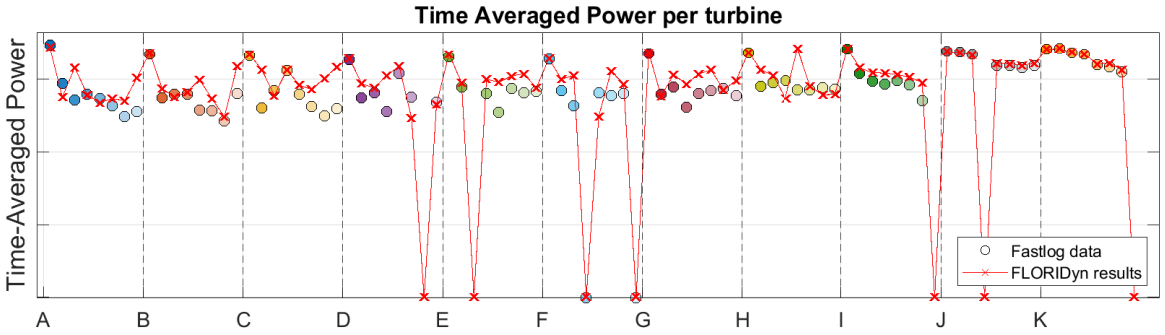

(e) Case 4: Power per turbine.

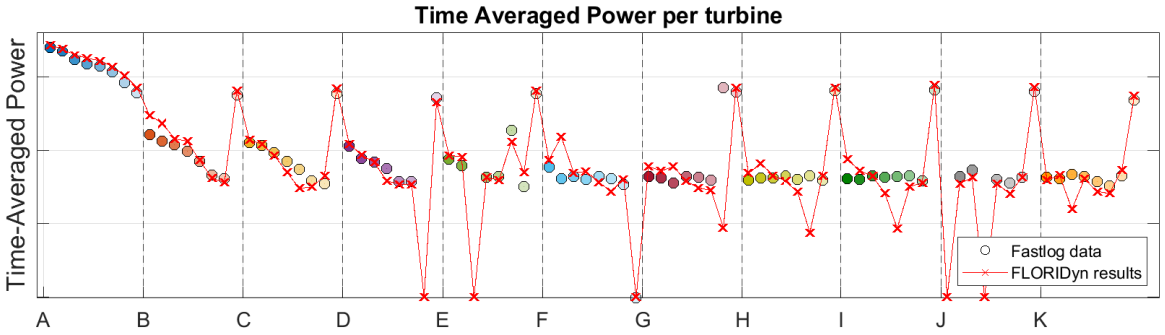

(f) Case 5: Power per turbine.

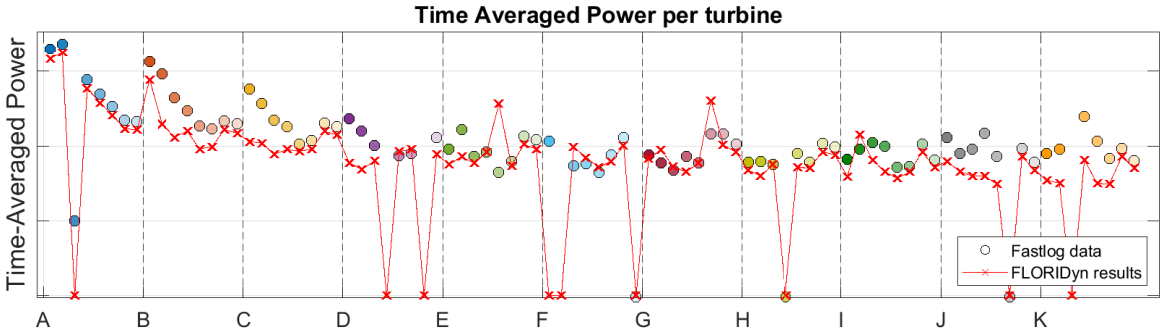

(g) Case 6: Power per turbine.

Figure E.2: Direct comparison plots of time-averaged turbine power output on the FLORIDyn results and Fastlog data.

F

FLORIDyn Limitations Related to Wind Speed Prediction

The aim of this appendix is to provide a more detailed insight in FLORIDyn's bias towards higher wind speeds. Using the C_P-C_T LUT approach, the primary factor in determining power output is the velocity used for LUT interpolation. Consequently, inaccuracies in predicting local wind speeds lead directly to errors in power prediction. Especially considering the $P \propto U^3$ relation, even minor discrepancies in wind speed predictions can result in significant power inaccuracies. Conversely, when small yaw misalignment values are encountered, an accurate wind speed prediction directly leads to reliable power predictions, as highlighted by Figure F.1.

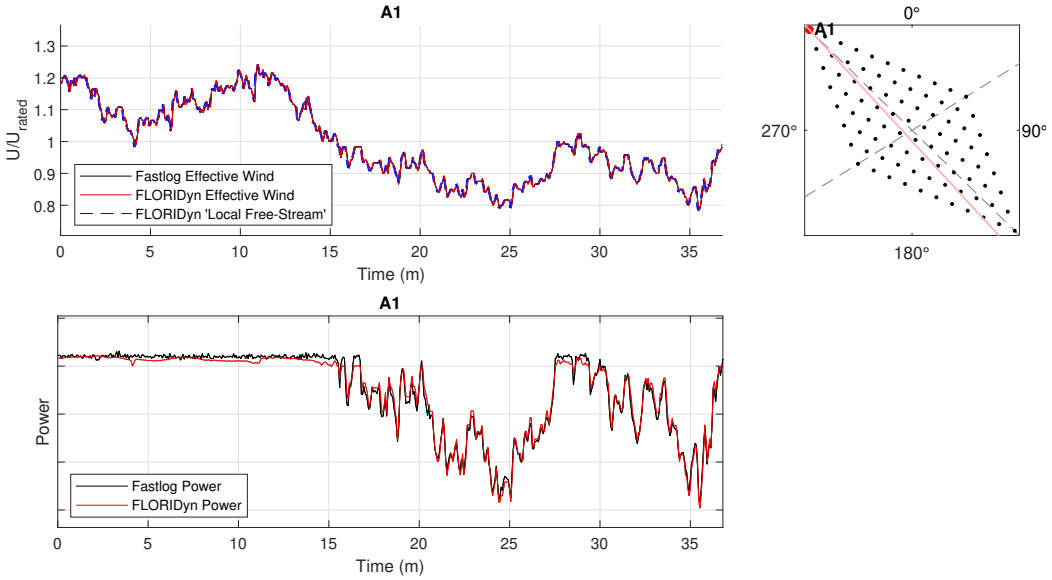

Figure F.1: Wind and power time series on free-stream turbine A1, with input wind conditions from Case 2.

As hypothesised in Section 4.3.4, the mismatch between FLORIDyn power predictions and Fastlog results is primarily attributed to two main causes: 1. Oversimplified convection model; 2. Overprediction of wake recovery in deep-array locations. To further investigate these hypotheses, Figure F.2 displays the Fastlog measured, and FLORIDyn predicted wind speeds on the same turbines considered in Section 4.3.4. Next to the local effective wind speeds, also the apparent 'local free-stream' wind speed predicted by FLORIDyn is indicated.

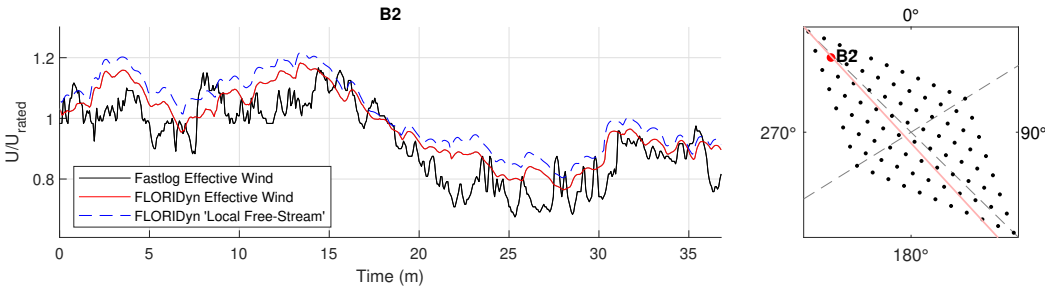

(a) Wind time series of turbine B2.

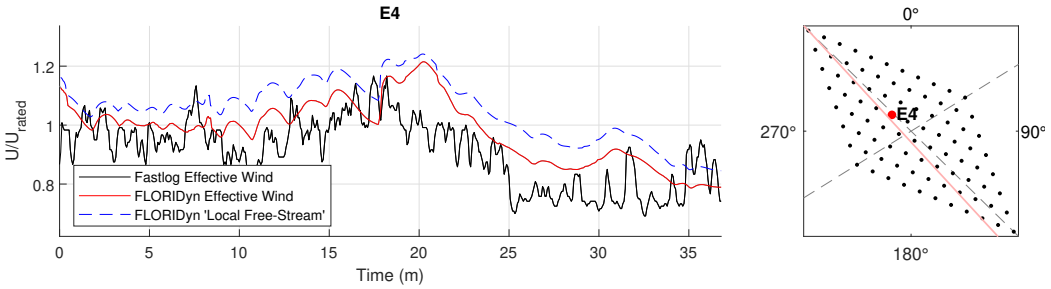

(b) Wind time series of turbine E4.

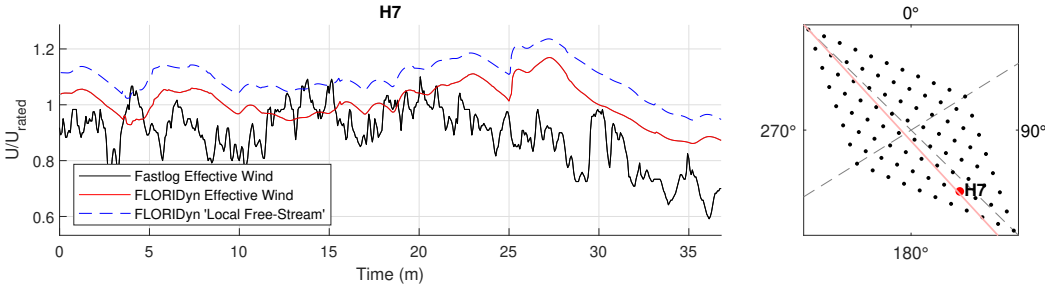

(c) Wind time series of turbine H7.

Figure F.2: Wind speed time series comparison on Case 2 for three turbines at different downstream locations. The mean wind direction is indicated by the red line on the wind farm layout.

Similar to the observations on power prediction in Section 4.3.4, the wind speed is consistently over-predicted in Figure F.2a to Figure F.2c. The use of a simple linear convection model, which considers only interactions between successive OPs within a single wake chain, results in all velocity time series in Figure F.2 being highly similar to, but smoothed versions of, the wind input at the free-stream turbine A1 (Figure F.1). Nonetheless, Figure 4.21b to Figure F.2c generally represent the trend in wind speed time evolution.

Additionally, the wake velocity deficits are observed to be underestimated. This results in the local effective wind speeds being consistently higher than the Fastlog measurements on all cases presented in Figure F.2, getting progressively worse with increasing downstream distance.